

Fundamental Degradation Mechanisms and Materials Optimization of Environmental Barrier Coatings

Mackenzie Ridley

A Dissertation for:

Materials Science and Engineering

University of Virginia

Committee Members: Dr. Jon Ihlefeld (chair), Dr. Prasanna Balachandran, Dr. Patrick Hopkins, Dr. Katherine Faber (CalTech, Pasadena, CA), Dr. Elizabeth Opila (adviser)

Friday, March 26, 2021

Acknowledgements

This work was supported in part by 1. program manager Dr. David Shifler and the Office of Naval Research Award #N000141712280, 2. program manager Adam Chamberlain and Rolls-Royce Inc. through Task Order # 17-UVA-26 “Entropy Stabilized Silicate Investigation” and Task Order # 18-UVA-26 “Characterization of Thermal Properties and Chemical Stability of High Entropy Rare Earth Monosilicates,” 3. the University of Virginia SEAS 2017-2018 Research Innovation Award “Center for Exploring and Tailoring Thermal Conductivity of Defective Oxides,” 4. the National Science Foundation DMREF: Collaborative Research: GOALI: Accelerating Discovery of High Entropy Silicates for Extreme Environments, Award #1921973, and 5. the Virginia Space Grant Consortium 2020-2021 graduate fellowship.

Thank you to my advisor Beth Opila for her guidance, patience, and trust throughout my graduate experience. Thank you to my lab group for all of their comradery and support with research and graduate student life. I also want to thank Dr. Bryan Harder (NASA, Glenn Research Center) for supplying many of the powders for testing, Dr. Jeroen Djiekers for guidance regarding sample processing, Dr. Diane Dickie for single crystal XRD work, Dr. Helge Heinrich for TEM work, and the entire Nanoscale Materials Characterization Facility at the University of Virginia for supplying training, support, and access to various characterization techniques used throughout my research. Finally, I would especially like to thank my family and fiancée Augusta for their unlimited care and support.

Abstract

Environmental barrier coatings (EBCs) are required to mitigate ceramic matrix composite (CMC) degradation in gas engine combustion environments, yet the long-term stability of EBCs in turbine applications is not fully understood. It is known that the primary EBC failure mechanisms include reaction with water vapor, steam oxidation of the silicon bond coat, thermomechanical fatigue, corrosion by ingested debris, erosion, and foreign object damage [1], and that all failure modes are connected through the microstructural evolution of the EBC.

This dissertation attempts to better understand EBC-water vapor degradation mechanisms, long term phase stability, thermochemical stability, and criteria for development of next generation EBC candidates through the following objectives:

1. Uncover fundamental mechanisms for high-velocity steam degradation and microstructural evolution of silicate EBC candidates such as barium strontium aluminosilicate (BSAS, $\text{Ba}_{0.75}\text{Sr}_{0.25}\text{Al}_2\text{Si}_2\text{O}_8$), hafnon (HfSiO_4), and ytterbium disilicate (Yb_2SiO_7)
2. Determine fundamental relationships between rare earth elements and rare earth silicate material properties to tailor improved properties such as thermal expansion, phase stability, steam resistance, thermal conductivity, and Young's Modulus
3. Develop the first figure of merit for a holistic comparison of EBC materials against all major EBC failure modes, for identification and exploration of novel EBC candidates such as ytterbium phosphate (YbPO_4), and for advancement of next-generation EBCs

Table of Contents

Acknowledgements	ii
Abstract	iii
List of Figures	xiii
List of Tables.....	xxviii
1. Motivation.....	1
1.1. History of EBC materials	3
1.2. Volatilization Kinetics for SiO ₂	4
1.3. Thermochemical Stability of Phase Pure Silicates in Steam	6
1.4. Knowledge Gaps.....	7
2. Objective 1. Microstructural Evolution and Quantitative Analysis of Silicates in High-Velocity Steam.....	10
2.1. High-Temperature Water-Vapor Reaction Mechanism of Barium Strontium Aluminosilicate (BSAS)	12
2.1.1. Introduction	12
2.1.2. Methods	13
2.1.2.1. Processing	13
2.1.2.2. Steamjet Experimental Setup and ANSYS Steam Velocity Distribution Model	13
2.1.2.3. Characterization.....	16
2.1.2.4. Thermodynamic Assessment of BSAS.....	17

2.1.3.	Results	18
2.1.4.	Analysis	20
2.1.4.1.	Time Dependence	20
2.1.4.2.	Velocity Dependence	22
2.1.4.3.	Temperature Dependence	24
2.1.4.4.	FactSage Calculations for the BaO-SrO-Al ₂ O ₃ -SiO ₂ system	25
2.1.5.	Discussion	27
2.1.6.	Conclusions	31
2.2.	Thermomechanical and Thermochemical Stability of HfSiO ₄ for Environmental Barrier Coating Applications	33
2.2.1.	Introduction	33
2.2.2.	Methods	35
2.2.2.1.	Processing and Characterization	35
2.2.2.2.	High-temperature XRD	36
2.2.2.3.	High Velocity Steamjet	36
2.2.3.	Results	37
2.2.3.1.	Thermal Expansion and Thermal Expansion Anisotropy	37
2.2.3.2.	X-ray Diffraction of Steam Reaction Layer	39
2.2.3.3.	Plan View SEM of Steam Reaction Layer	39
2.2.3.4.	Cross-section SEM of Steam Reaction Layer	41

2.2.3.5.	Specimen Extended Cross-section	41
2.2.3.6.	Time and Temperature Dependences	42
2.2.4.	Discussion	46
2.2.5.	Conclusions	48
2.3.	Thermochemical Stability and Microstructural Evolution of $\text{Yb}_2\text{Si}_2\text{O}_7$ in High-Velocity High-Temperature Water Vapor	50
2.3.1.	Introduction	50
2.3.2.	Background	50
2.3.3.	Methods	52
2.3.4.	Results	54
2.3.4.1.	X-ray diffraction	54
2.3.4.2.	Plan View SEM.....	55
2.3.4.3.	Cross-section SEM.....	56
2.3.4.4.	Extended SEM Cross-sections	59
2.3.4.5.	Low Gas Velocity Regions	60
2.3.5.	Analysis	61
2.3.6.	Discussion	65
2.3.7.	Conclusions	68
2.4.	Sapphire (0001) Volatility in High-Velocity Steam.....	70
2.4.1.	Introduction	70

2.4.2.	Methods	71
2.4.3.	Results	72
2.4.4.	Analysis	76
2.4.5.	Discussion	77
2.4.6.	Conclusion.....	80
2.5.	Preferred Orientations for Steam Reaction Products of $Y_2Si_2O_7$, Y_2SiO_5 , and $Y_3Al_5O_{12}$	
	Single Crystals.....	81
2.5.1.	Introduction	81
2.5.2.	Methods	82
2.5.3.	Results	83
2.5.3.1.	Single Crystal δ - $Y_2Si_2O_7$ Steamjet Exposure	83
2.5.3.2.	Single Crystal Y_2SiO_5 Steamjet Exposure.....	85
2.5.3.3.	Single Crystal $Y_3Al_5O_{12}$ Steamjet Exposure.....	86
2.5.4.	Discussion	89
2.5.5.	Conclusion.....	89
2.6.	Summary.....	91
3.	Objective 2: Tailoring Rare Earth Silicate Thermal, Mechanical, and Chemical Properties	94
3.1.	High-velocity Steam Resistance of Yb_2SiO_5 and Sc_2SiO_5	98
3.1.1.	Introduction	98
3.1.2.	Methods.....	98

3.1.3.	Results	99
3.1.4.	Conclusion.....	101
3.2.	Tailoring Thermal Properties of Multi-component Rare Earth Monosilicates.....	103
3.2.1.	Introduction	103
3.2.1.1.	Structure	103
3.2.2.	Methods.....	104
3.2.2.1.	Sample Preparation	104
3.2.2.2.	Thermal Expansion and Thermal Conductivity	106
3.2.3.	Results	107
3.2.3.1.	Phase Stability	107
3.2.3.2.	Thermal Expansion and Thermal Expansion Anisotropy	110
3.2.3.3.	Hot Disk Measurements of Thermal Conductivity.....	117
3.2.4.	Discussion	119
3.2.4.1.	Thermal Expansion and Thermal Expansion Anisotropy	120
3.2.4.2.	Thermal Conductivity.....	123
3.2.5.	Conclusions	125
3.3.	High-velocity Steam Resistance of RE ₂ Si ₂ O ₇ (RE = Sc, Nd, Er, Yb, and Lu) at 1400 °C	127
3.3.1.	Introduction	127
3.3.1.1.	High-temperature Stability and Structures of RE ₂ Si ₂ O ₇	128

3.3.1.2.	Steam Reactivity of $\text{RE}_2\text{Si}_2\text{O}_7$	130
3.3.2.	Methods.....	132
3.3.2.1.	Processing	132
3.3.2.2.	Steam Testing.....	133
3.3.3.	Results	133
3.3.3.1.	Initial $\text{RE}_2\text{Si}_2\text{O}_7$ Characterization	134
3.3.3.2.	Steam Exposure of $\text{RE}_2\text{Si}_2\text{O}_7$ (Re = Er, Yb, Lu)	135
3.3.3.3.	Steam Exposure of $\text{Sc}_2\text{Si}_2\text{O}_7$	138
3.3.3.4.	Steam Exposure of $\text{Nd}_2\text{Si}_2\text{O}_7$	141
3.3.4.	Analysis.....	144
3.3.5.	Discussion	147
3.3.6.	Conclusion.....	152
3.4.	Multi-component $\text{RE}_2\text{Si}_2\text{O}_7$: Trends with Thermal Conductivity, Thermal Expansion, Young's Modulus, and High-velocity Steam Resistance	154
3.4.1.	Introduction	154
3.4.2.	Methods.....	156
3.4.3.	Results	157
3.4.3.1.	Starting Microstructure and Phase Stability	157
3.4.3.2.	Thermal Conductivity, Thermal Expansion, and Young's Modulus of Single and Multi-component $\text{RE}_2\text{Si}_2\text{O}_7$	160

3.4.3.3.	Steamjet Exposures.....	163
3.4.4.	Discussion	171
3.4.5.	Conclusion.....	178
3.5.	CTE Prediction for High-temperature Silicate Materials	179
3.5.1.	Introduction	179
3.5.2.	Results	179
3.5.3.	Conclusion.....	181
3.6.	Summary.....	183
4.	Objective 3: Design and Comparison of Next Generation Environmental Barrier Coating Materials.....	185
4.1.	Evaluation of YbPO ₄ as an Environmental Barrier Coating Candidate	187
4.1.1.	Introduction	187
4.1.2.	Methods.....	192
4.1.3.	Results	195
4.1.3.1.	Pre-characterization of the Synthesized YbPO ₄ Powder	195
4.1.3.2.	Thermal Expansion and Thermal Expansion Anisotropy	197
4.1.3.3.	Steamjet Results	198
4.1.3.4.	YbPO ₄ Resistance to CMAS attack	204
4.1.4.	Discussion	210
4.1.4.1.	Thermal Expansion and Thermal Expansion Anisotropy	210

4.1.4.2.	YbPO ₄ Reaction with High-velocity Water Vapor	211
4.1.4.3.	YbPO ₄ Reaction with CMAS.....	212
4.1.5.	Conclusion.....	216
4.2.	Holistic Comparison of Environmental Barrier Coating Material Candidates through Design of a Figure of Merit	217
4.2.1.	Introduction	217
4.2.2.	Background	218
4.2.2.1.	Gas Turbine/Air Plasma Spray Conditions	218
4.2.3.	EBC Failure Modes	220
4.2.3.1.	Steam Resistance	221
4.2.3.2.	Oxidant Diffusion/Silicon Bond Coat Oxidation Resistance.....	223
4.2.3.3.	CMAS Resistance.....	224
4.2.3.4.	Thermal Stresses	226
4.2.3.5.	Mechanical Erosion and Foreign Object Damage.....	228
4.2.4.	Results	228
4.2.5.	Discussion	234
4.2.6.	Conclusion.....	236
4.3.	Summary.....	238
5.	Final Remarks	240
6.	Future Work.....	243

6.1. Objective 1.....	243
6.2. Objective 2.....	244
6.3. Objective 3.....	246
7. Resulting Presentations, Publications, Patents, and Awards from this Work.....	247
7.1. Presentations:.....	247
7.2. Publications:	247
7.3. Patents:.....	249
7.4. Awards:.....	249
8. Appendices.....	250
8.1. Profilometry Mapping and Linescan Analysis of Al ₂ O ₃ (0001) Exposures to Steam.....	250
8.2. Crystal Data for δ-Y ₂ Si ₂ O ₇ from single crystal X-ray Diffraction	254
8.3. EDS Characterization of Multi-component Rare Earth Monosilicates	263
8.4. EDS Characterization of Multi-component Rare Earth Disilicates	268
8.5. Dilatometry Data for Silicate Materials.....	270
8.6. Figure of Merit Data Manipulation	273
9. Bibliography	277

List of Figures

Figure 1-1. Calculated SiO₂ recession depths as a function of time, with recession rates determined from Eq. 2-2.6

Figure 2-1. High velocity steamjet experimental setup [23]. 14

Figure 2-2. Sample view of high velocity steamjet experimental setup [23]. 15

Figure 2-3. ANSYS Computational Fluid Dynamics Model for steam velocity distribution across the sample face at 1400 °C. 16

Figure 2-4. BSE image of BSAS after SPS processing, box furnace annealing, and fine polishing, and an area EDS spectrum of the starting BSAS material. 17

Figure 2-5. XRD plots for BSAS coupons before and after steam exposure for 72h at 1200 °C, 1300 °C, and 1400 °C. 18

Figure 2-6. BSE plan view imaging of BSAS samples exposed to steam for 72h with gas velocities between 145-175 m/s at a) 1200 °C, b) 1300 °C, and c) 1400 °C. 19

Figure 2-7. BSE image of BSAS exposed to water vapor at 1200 °C for 72 hours with local gas velocity of 145-175 m/s, and EDS spectra of the black square region that estimates the product phase average concentration to be Ba_{0.55}Sr_{0.45}Al₂SiO₇. 19

Figure 2-8. Optical profilometry of the BSAS surface after steam exposure for 72 hours at a. 1200 °C, b. 1300 °C, and c. 1400 °C. Each depth profile is displayed with a unique scale bar where material recession is represented as a negative value.20

Figure 2-9. Line scan across the profilometer map of the BSAS sample exposed to water vapor at 1400 °C for 72h to display the total recession depths as a function of sample location.21

Figure 2-10. a. Specific mass loss (mg/cm^2) and b. maximum recession (μm) data plotted against water vapor exposure time (h) for 1200 °C, 1300 °C, and 1400 °C with reaction rates (kl) for each temperature.....22

Figure 2-11. Comparison of the recession data from profilometry line scan of BSAS exposed to 1400 °C for 72h (black) compared to the computed gas velocity line scan for the same sample position (blue).23

Figure 2-12. Gas velocity dependence on the linear reaction rate for BSAS after steam exposure for 72h at 1400 °C.....23

Figure 2-13. Temperature dependence of the maximum recession rates for the BSAS reaction with water vapor.....25

Figure 2-14. Equilibrium partial pressure dependences for BSAS constituent oxides, assuming ideal activities, reacting with water vapor for 1200 °C, 1300 °C, and 1400 °C.27

Figure 2-15. Temperature dependence for the summation of the equilibrium partial pressures of the product hydroxide gas species. Partial pressures were calculated with FactSage assuming an ideal solution from steam reaction for the constituent oxides (BaO , SrO , Al_2O_3 , SiO_2) and can be seen in Figure 2-14.31

Figure 2-16. a. Tetragonal HfSiO_4 [37] and b. monoclinic HfO_2 [38] crystal structures.....34

Figure 2-17. Backscattered electron image of bulk HfSiO_4 with white particulate HfO_2 inclusions.36

Figure 2-18. Normalized HfSiO_4 unit cell parameters from XRD data.38

Figure 2-19. CTE calculations from hot stage XRD unit cell refinement for HfSiO_438

Figure 2-20. XRD of HfSiO_4 samples after 60 hours of steam exposure.39

Figure 2-21. Representative backscatter SEM plan view images of HfSiO_4 samples after steam exposures of 60, 125, and 250 hours at 1400 °C with local gas velocity of 90-120 m/s. The area

fraction of porosity is given on each image. Images show the porous HfO₂ product from the steam interaction with HfSiO₄.....40

Figure 2-22. SEM of HfSiO₄ after steam exposure for 250 hours at 1300 °C in the stagnant gas velocity region under the platinum foil sample holder.40

Figure 2-23. Representative cross-section SEM images of HfSiO₄ after 125-hour steamjet exposures (velocity 125 -150 m/s) for a. 1200 °C, b. 1300 °C, and c. 1400 °C.41

Figure 2-24. Steam impingement site of HfSiO₄ exposed to steam for 250 hours (v=150-250 m/s) at a. 1200 °C and b. 1400 °C.....42

Figure 2-25. Stitched cross-section SEM images showing the silica depletion layer below 190 m/s and the large amounts of mechanical erosion at the impingement site where steam velocities exceed 190 m/s. The erosion depth at the impingement site averaged 105 μm after 250 hours at 1200 °C (100 μm scale bar) and 537 μm after 250 hours at 1400 °C (500 μm scale bar).42

Figure 2-26. HfSiO₄ specific mass loss (mg/cm²) plotted against square root of time.43

Figure 2-27. Average SiO₂ depletion depth for HfSiO₄ for intermediate velocity regions of 90-180 m/s plotted against square root of time.44

Figure 2-28. Log of the parabolic depletion rates and mass change rate divided by gas phase diffusion temperature dependence is plotted against inverse temperature to show the exponential temperature dependence of the HfSiO₄ reaction with water vapor to form HfO₂.....45

Figure 2-29. Backscatter SEM images of Yb₂Si₂O₇ coupons prior to steam testing, with Yb₂SiO₅ minor phase (light gray).53

Figure 2-30. XRD results for Yb₂Si₂O₇ after 250-hour water vapor exposures at temperatures between 1200 °C-1400 °C. Results are compared to initial XRD pattern of bulk Yb₂Si₂O₇. The boxed region highlights formation of Yb₂SiO₅ on the sample surface for all temperatures.54

Figure 2-31. Representative SEM images of the Yb_2SiO_5 product layer after 250-hour exposures of $\text{Yb}_2\text{Si}_2\text{O}_7$ in water vapor with predicted steam velocities of 80-110 m/s at a. 1200 °C, b. 1300 °C, and c. 1400 °C.55

Figure 2-32. $\text{Yb}_2\text{Si}_2\text{O}_7$ reaction product variation across a sample after exposure to water vapor at 1400 °C for 250 h. A strong gas stream velocity dependence is seen for the reaction to form Yb_2SiO_5 (image a) and for Yb_2SiO_5 to form Yb_2O_3 (image d). Approximate steam velocities are: a) 80 m/s, b) 145 m/s, c) 170 m/s, and d) 210 m/s.56

Figure 2-33. Representative $\text{Yb}_2\text{Si}_2\text{O}_7$ SEM cross-sections for varied exposure times and temperatures in a velocity region 80-100 m/s. The $\text{Yb}_2\text{Si}_2\text{O}_7$ samples exposed to 1200 °C show a scale bar of 5 μm57

Figure 2-34. Cross sections of $\text{Yb}_2\text{Si}_2\text{O}_7$ after 250 hours of steam exposure with gas velocities ~190-210 m/s. a) 1200 °C, b) 1300 °C, and c) 1400 °C. The $\text{Yb}_2\text{Si}_2\text{O}_7$ sample exposed to 1200 °C shows a scale bar of 10 μm58

Figure 2-35. Energy Dispersive Spectroscopy (EDS) of $\text{Yb}_2\text{Si}_2\text{O}_7$ products after water vapor exposure at 1400 °C for 250 hours with a local steam velocity of ~200-220 m/s. The silicon map shows distinct layering of Yb_2O_3 and Yb_2SiO_5 on top of the $\text{Yb}_2\text{Si}_2\text{O}_7$. The carbon map shows epoxy infiltration under vacuum halted by the dense intermediate Yb_2SiO_5 layer.....59

Figure 2-36. Stitched cross-section images of $\text{Yb}_2\text{Si}_2\text{O}_7$ after water vapor exposure for 250h at 1200 °C and 1300 °C, centered at the impingement site.....59

Figure 2-37. Stitched cross-section images of $\text{Yb}_2\text{Si}_2\text{O}_7$ after exposure to water vapor at 1400 °C for 250 hours. Images are from a. intermediate velocities (80-200 m/s) through b. the highest velocity (200-250 m/s) impingement site.60

Figure 2-38. a. Near stagnant velocity edge of $\text{Yb}_2\text{Si}_2\text{O}_7$ sample exposed to water vapor at 1300 °C for 60 hours showing initial Yb_2SiO_5 nucleation at grain boundaries, b. Low velocity (<50 m/s) region outside of the primary gas stream where alumina or impurities have reacted with the $\text{Yb}_2\text{Si}_2\text{O}_7$ surface.61

Figure 2-39. Average reaction depth plotted against the square root of time for a. Yb_2SiO_5 formation from $\text{Yb}_2\text{Si}_2\text{O}_7$ at velocities of 80-115 m/s and b. Yb_2O_3 formation from Yb_2SiO_5 on the same specimens at all velocities greater than ~140 m/s. Parabolic rate constants, k_p ($\mu\text{m}^2/\text{h}$), are shown for each temperature.62

Figure 2-40. Growth of the dense Yb_2SiO_5 layer after $\text{Yb}_2\text{Si}_2\text{O}_7$ steam exposures at 1300 °C and 1400 °C. An example of the measured dense layer is presented with red arrows for a $\text{Yb}_2\text{Si}_2\text{O}_7$ sample exposed to steam for 250h at 1400 °C ($v \sim 210$ m/s).....63

Figure 2-41. Specific mass loss of exposed $\text{Yb}_2\text{Si}_2\text{O}_7$ samples plotted against the square root of time. Parabolic rate constants, k_p $\text{mg}^2/\text{cm}^4\text{h}$, are shown for each temperature.64

Figure 2-42. Arrhenius dependence of measured reaction depths for bulk $\text{Yb}_2\text{Si}_2\text{O}_7$ EBC sample and the dense intermediate Yb_2SiO_5 reaction layer.65

Figure 2-43. $\text{Al}(\text{OH})_3$ (g) partial pressures, calculated with FactSage SGPS database for 1 atm H_2O (g).73

Figure 2-44. Profilometry maps for Al_2O_3 (0001) after steam exposure for 24h at 1300 °C, 1400 °C, and 1450 °C.....73

Figure 2-45. Surface topography of Al_2O_3 (0001) exposed to steam at 1300 °C for 24h. Recession depths along the arrow are plotted against position and compared to the calculated ANSYS steam velocity distribution through the impingement site.....74

Figure 2-46. Maximum recession depth plotted against time (hours) for (0001) Al₂O₃ reactions with high-velocity steam.75

Figure 2-47. Specific mass loss plotted against time (hours) for (0001) Al₂O₃ reactions with high-velocity steam.....75

Figure 2-48. Temperature dependences for specific mass loss and maximum recession data for Al₂O₃ in steam, compared to FactSage SGPS calculations.....77

Figure 2-49. Pseudobinary phase diagrams for the Y₂O₃-Al₂O₃ [60] and Y₂O₃-SiO₂ [61] systems..81

Figure 2-50. The calculated crystal structure of δ-Y₂Si₂O₇ viewed from the a, b, and c orthogonal axes. Red atoms are oxygen, blue atoms are silicon, and teal atoms are yttrium.82

Figure 2-51. Single crystal δ-Y₂Si₂O₇ before and after exposure to high-velocity steam at 1200 °C for 60 hours.84

Figure 2-52. Low magnification SEM of the Y₂Si₂O₇ impingement site region after steam exposure at 1200 °C for 60h, with higher magnification of specific regions: a. Y₂SiO₅ formation at the impingement site, b. Y₂SiO₅ and Y_{9.33}□_{0.67}Si₆O₂₆ formation two-phase region, c. upstream formation of silica-depleted Y-Si-Al-O phases, and d. Stagnant gas velocity regions of unreacted δ-Y₂Si₂O₇.....85

Figure 2-53. Single crystal X2 phase Y₂SiO₅ before and after exposure to high-velocity steam at 1200 °C for 60 hours.86

Figure 2-54. a. Low magnification SEM of the Y₂SiO₅ impingement site region after steam exposure at 1200 °C for 60h, and b. higher magnification SEM image of the Y₂O₃ formation around the impingement site.86

Figure 2-55. Single crystal YAG before and after exposure to high-velocity steam at 1200 °C for 60 hours.87

Figure 2-56. Low magnification SEM of the YAG impingement site region after steam exposure at 1200 °C for 60h, with higher magnification of specific regions: a. Y_2O_3 formation surrounding the impingement site, b. $Y_4Al_2O_9$ formation outside of the Y_2O_3 region, c. $Y_4Al_2O_9$ faceting on unreacted $Y_3Al_5O_{12}$ (YAG).....88

Figure 2-57. Steam reaction depths plotted against time for $Yb_2Si_2O_7$, $HfSiO_4$, and BSAS at 1200 °C, 1300 °C, and 1400 °C.93

Figure 3-1. Starting microstructures for a. Yb_2SiO_5 and b. Sc_2SiO_5 . Sc_2SiO_5 displayed $Sc_2Si_2O_7$ (dark grey) and trace amounts of Sc_2O_3 (light grey) phases from the starting powder.....99

Figure 3-2. XRD before and after steam exposure at 1400 °C for 125h for a. Yb_2SiO_5 and b. Sc_2SiO_599

Figure 3-3. Backscattered electron SEM images of Yb_2SiO_5 and Sc_2SiO_5 samples after steam exposure, displaying a. high-velocity steam impingement site, b. higher magnification SEM where the local steam velocity was 150-180 m/s, and c. high magnification SEM where the local steam velocity was 100-125 m/s..... 100

Figure 3-4. SEM Cross sections of Yb_2SiO_5 and Sc_2SiO_5 after steam exposure for a. intermediate steam velocities, 100-125 m/s and b. high steam velocities, 150-180 m/s. $Yb_2Si_2O_7$, $Sc_2Si_2O_7$, and Sc_2O_3 initial impurities are pointed out in a)..... 101

Figure 3-5. Structure and bonding of X1 and X2 phase RE_2SiO_5 [77]. 104

Figure 3-6. a. Thermal spray powders of as-received Sc_2SiO_5 , b. as-received Yb_2SiO_5 , and c. $(Yb,Sc)_2SiO_5$ powder after ball milling for 24 hours. Large particulate in image a. and in image c. were $Sc_2Si_2O_7$ from the starting Sc_2SiO_5 powder. 105

Figure 3-7. X-ray diffraction of single cation monosilicates and a multi-component RE_2SiO_5 , $RE=Sc, Y, Dy, Er,$ and Yb . All materials are of the same space group, although the small cation size and atomic radius of Sc_2SiO_5 result in noticeable peak shifting relative to the other RE_2SiO_5 108

Figure 3-8. Representative scanning electron micrographs of rare earth monosilicates after polishing and 1500 °C anneal for 30 minutes to show grain boundaries. a. Y_2SiO_5 , b. $(Dy,Er)_2SiO_5$, c. $(Yb,Sc)_2SiO_5$, d. Five-component RE_2SiO_5 ($RE=Sc, Y, Dy, Er, Yb$)..... 109

Figure 3-9. Energy dispersive spectroscopy maps for the five-component RE_2SiO_5 ($RE=Sc, Y, Dy, Er, Yb$)..... 109

Figure 3-10. Contrast-enhanced selected area electron diffraction map showing the [121] zone axis of the five-component RE_2SiO_5 ($RE=Sc, Y, Dy, Er, Yb$) and a simulated hkl plot with parameters derived from XRD refinement. 110

Figure 3-11. Five-component RE_2SiO_5 ($RE=Sc, Y, Dy, Er, Yb$) normalized unit cell parameters from hot stage XRD refinements. 111

Figure 3-12. X1 structure Nd_2SiO_5 unit cell expansion from hot stage XRD refinements..... 112

Figure 3-13. X2 structure RE_2SiO_5 unit cell a. perspective and b. viewed from the b-axis. Only oxygen atoms that are not bonded to the Si-O tetrahedra are shown. 113

Figure 3-14. Linear CTE of single cation RE_2SiO_5 from 100 °C to 1200 °C. 113

Figure 3-15. Axial CTEs for each single cation RE_2SiO_5 . a. a-axis, b. b-axis, c. c-axis, and d. beta angle. 115

Figure 3-16. Axial and linear CTE values for binary equimolar mixtures $(RE,RE)_2SiO_5$ compared to ROM values calculated from constituent RE_2SiO_5 : a. $(Dy,Sc)_2SiO_5$, b. $(Yb,Sc)_2SiO_5$, c. $(Dy,Er)_2SiO_5$ and d. $(Yb,Er)_2SiO_5$ 116

Figure 3-17. Axial and Linear CTE values for five-component RE_2SiO_5 , (RE=Sc, Y, Dy, Er, Yb) compared to ROM values..... 117

Figure 3-18. Room temperature thermal conductivity values of RE_2SiO_5 measured by Hot Disk method, with values corrected for apparent density. The five-component RE_2SiO_5 (RE=Sc, Y, Dy, Er, Yb) and SiO_2 are measured up to 300 °C..... 118

Figure 3-19. Linear CTE comparison to ionic radii, including all systems in this study along with other literature single cation RE_2SiO_5 , where RE= Y(X1), Sm, Gd, Tb, Ho, Tm, and Lu. 121

Figure 3-20. a. Linear CTE ratio and b. C-axis CTE ratio, compared to the standard deviation of rare earth cation mass for RE_2SiO_5 mixtures. 122

Figure 3-21. Room temperature thermal conductivity measurements compared to average linear CTE (100 °C-1200 °C)..... 123

Figure 3-22. Ratio of thermal conductivity to its ROM value plotted against the a. standard deviation of rare earth cation mass and b. standard deviation of rare earth ionic radius for each RE_2SiO_5 mixture. 124

Figure 3-23. Phase stability of $RE_2Si_2O_7$ relative to rare earth ionic radius [105]..... 128

Figure 3-24. Pseudobinary phase diagrams of the Yb_2O_3 - SiO_2 [110], Sc_2O_3 - SiO_2 [111], and Nd_2O_3 - SiO_2 systems [61]. 129

Figure 3-25. Starting microstructures of $RE_2Si_2O_7$, a. $Sc_2Si_2O_7$, b. $Nd_2Si_2O_7$, c. $Er_2Si_2O_7$, d. $Yb_2Si_2O_7$, and e. $Lu_2Si_2O_7$ 134

Figure 3-26. Baseline and post steam exposure XRD of $RE_2Si_2O_7$, RE = Er, Yb, and Lu..... 136

Figure 3-27. Representative backscattered electron SEM images of $RE_2Si_2O_7$ (RE = Er, Yb, Lu) after 125 hour steam exposures at 1400 °C for a. stagnant steam velocity region showing the initial formation of RE_2SiO_5 (brighter phase), b. intermediate steam velocity region where porous RE_2SiO_5

is the stable product phase (80-115 m/s), and c. high velocity steam region where RE_2O_3 is the stable product phase (165-185 m/s). 137

Figure 3-28. Cross-section SEM images of $RE_2Si_2O_7$ (RE = Er, Yb, Lu) after 125 hour steam exposures at 1400 °C for steam velocity regions of a. 80-115 m/s, b. 120-140 m/s, and c. 165-185 m/s. 138

Figure 3-29. XRD of $Sc_2Si_2O_7$ baseline and after steam exposure at 1400 °C for 125 hours. 139

Figure 3-30. Plan view SEM images of $Sc_2Si_2O_7$ after steam exposure for 125 hours at 1400 °C, displaying a. material mechanical erosion at the highest velocity impingement site (200-235 m/s), b. Sc_2O_3 formation in the stagnant gas velocity region, and c. Sc_2O_3 reaction product in the high steam velocity region (165-185 m/s). 140

Figure 3-31. Cross-section SEM images of $Sc_2Si_2O_7$ after steam exposure for 125 hours at 1400 °C. a. Sc_2O_3 reaction product thickness at steam velocities 80-180 m/s, b. $Sc_2Si_2O_7$ - Sc_2O_3 reaction interface, and c. EDS linescan across the reaction interface (yellow bar). 141

Figure 3-32. XRD of $Nd_2Si_2O_7$ baseline and after steam exposure at 1400 °C for 124 hours. 142

Figure 3-33. Plan view SEM images of $Nd_2Si_2O_7$ after steam exposure at 1400 °C for 124 hours, a. material mechanical erosion at the highest velocity impingement site (200-240m/s), b. dense hexagonal $Nd_{9.33}\square_{0.67}Si_6O_{26}$ formation in the stagnant gas velocity region, and c./d. $Nd_{9.33}\square_{0.67}Si_6O_{26}$ reaction product in the high steam velocity region (165-185 m/s). 143

Figure 3-34. Cross-section SEM images of $Nd_2Si_2O_7$ after steam exposure at 1400 °C for 124 hours, a. $Nd_{9.33}\square_{0.67}Si_6O_{26}$ reaction product thickness at steam velocities 80-130 m/s, b. $Nd_{9.33}\square_{0.67}Si_6O_{26}$ reaction product thickness at steam velocities 165-185 m/s, and c. EDS of the reaction product zone marked by the red box in Figure 3-34b. 143

Figure 3-35. Unit cell and extended crystal structure of $\text{Nd}_{9.33}\square_{0.67}\text{Si}_6\text{O}_{26}$, with the (100) hkl plane in black, where the (100) plane was preferentially formed on the surface of $\text{Nd}_2\text{Si}_2\text{O}_7$ after steam exposure at 1400 °C for 124 hours..... 150

Figure 3-36. Homologous temperatures for each $\text{RE}_2\text{Si}_2\text{O}_7$ steam product phase. Reaction products that exhibited densification of the product layer are shown in red. 151

Figure 3-37. Average steam reaction depths compared to EBC homologous temperature for steam exposures at 1400 °C..... 152

Figure 3-38. Thermal expansion of $\text{RE}_2\text{Si}_2\text{O}_7$ polymorphs compared to that of SiC (yellow bar) [105]. 155

Figure 3-39. Starting microstructures of multi-component $\text{RE}_2\text{Si}_2\text{O}_7$, for RE = a. $\text{Sc}_{0.33}\text{Yb}_{0.67}$, b. ScYYb , c. ErYbLu , d. YErYbLu , e. $\text{Sc}_{0.15}\text{Y}_{0.4}\text{Er}_{0.5}\text{Yb}_{0.5}\text{Lu}_{0.45}$, and f. ScNdErYbLu 159

Figure 3-40. XRD of $(\text{ScNdErYbLu})_2\text{Si}_2\text{O}_7$ sample after 1300 °C anneal for 24 hours, displaying the presence of β - and G- $\text{RE}_2\text{Si}_2\text{O}_7$ phases. 160

Figure 3-41. Pre- and post-steam test XRD patterns for $(\text{ScYYb})_2\text{Si}_2\text{O}_7$, $(\text{ErYbLu})_2\text{Si}_2\text{O}_7$, $(\text{YErYbLu})_2\text{Si}_2\text{O}_7$, and $(\text{ScNdErYbLu})_2\text{Si}_2\text{O}_7$ after steam exposure for 125 hours at 1400 °C..... 164

Figure 3-42. Macro image and low magnification SEM image of $(\text{Y,Er,Yb,Lu})_2\text{Si}_2\text{O}_7$ after steam exposure at 1400 °C for 125h..... 165

Figure 3-43. Plan view backscattered electron images of multi-component $\text{RE}_2\text{Si}_2\text{O}_7$ exposed to steam for 125 hours at 1400 °C, a. high velocity steam region where RE_2O_3 is the stable product phase (165-185 m/s), b intermediate steam velocity region where porous RE_2SiO_5 is the stable product phase (80-115 m/s), and c. stagnant steam velocity region showing the initial formation of RE_2SiO_5 (brighter phase). 166

Figure 3-44. Cross section SEM and EDS of $(YErYbLu)_2Si_2O_7$ after steam exposure for 125 hours at 1400 °C and steam velocity of 90-110 m/s. 167

Figure 3-45. Cross-section SEM images of multi-component $RE_2Si_2O_7$ after steam exposure at 1400 °C for 125 hours for steam velocity regions of a. 80-115 m/s, b. 120-140 m/s, and c. 165-185 m/s. Respective images for c. are displayed at a higher magnification for visibility of the multi-layer reaction product. 168

Figure 3-46. Plan view of $(Sc,Nd,Er,Yb,Lu)_2Si_2O_7$ after steam exposure for 125 hours at 1400 °C, where local steam velocities were: a. 180-200 m/s, b. 100-120 m/s, and c. 60-80 m/s. 169

Figure 3-47. EDS mapping of $(Sc,Nd,Er,Yb,Lu)_2Si_2O_7$ cross-section after steam exposure for 125 hours at 1400 °C and steam velocity 80-100 m/s, where the steam reaction product (RE_2SiO_5) formed as a solid solution of all rare earth cations. 169

Figure 3-48. Cross-section SEM images of multi-phase $(Sc,Nd,Er,Yb,Lu)_2Si_2O_7$ after steam exposure for 125 hours at 1400 °C, where local steam velocities were: a. 80-120 m/s, b. 150-180 m/s, and c. 200-240 m/s. 170

Figure 3-49. Ratio of rule of mixtures thermal conductivity values to the measured values for multi-component $RE_2Si_2O_7$, plotted against the standard deviation of rare earth ionic radius and the standard deviation of rare earth cation mass. 172

Figure 3-50. Thermal expansion and Young's Modulus ratios of measured values to rule of mixtures for multi-component $RE_2Si_2O_7$ 173

Figure 3-51. Young's Modulus (GPa) versus rare earth ionic radius for single and multi-component $RE_2Si_2O_7$ samples. 174

Figure 3-52. Equimolar $(\text{NdYb})_2\text{Si}_2\text{O}_7$ recovered from sample melt during SPS processing and annealed at 1430 °C for 8 hours. EDS point identification of the marked phases were 1.

$(\text{Nd}_{0.58}\text{Yb}_{0.42})_2\text{Si}_2\text{O}_7$, 2. $(\text{Nd}_{0.22}\text{Yb}_{0.78})_2\text{Si}_2\text{O}_7$, 3. SiO_2 with trace Nd and Yb signal. 176

Figure 3-53. EBC homologous temperature compared to average steam reaction depths after 125 hours of steam exposure at 1400 °C. Green triangles represent the four multi-component $\text{RE}_2\text{Si}_2\text{O}_7$ samples tested in this study. Blue dashed lines represent homologous temperatures for $\text{RE}_2\text{Si}_2\text{O}_7$ (RE = La, Gd, Dy, and Eu). 177

Figure 3-54. Linear thermal expansion of high-temperature silicates as a function of Pauling bond strength. 180

Figure 3-55. Linear thermal expansion of high-temperature silicates as a function of metal cation ionic radius, Å. 181

Figure 4-1. X-ray diffraction of initial YbPO_4 powder with hkl planes from ICDD pattern # 04-007-7022. 195

Figure 4-2. a. Backscattered SEM image of starting YbPO_4 powder and b. EDS spectra of YbPO_4 powder. 196

Figure 4-3. Backscattered electron SEM images a. of the sintered YbPO_4 after open air annealing at 1400 °C for 24 hours, and b. showing <1 at. % Yb_2O_3 inclusions (white). 196

Figure 4-4. a. Normalized unit cell parameters for tetragonal YbPO_4 powder from XRD scans at 25-1200 °C and b. thermal expansion measurements for the linear CTE, a=b axis, and c-axis from 100-1200 °C. 198

Figure 4-5. SEM of YbPO_4 after 1400°C steam exposure for 60 hours, a. stagnant steam velocity region underneath the platinum sample holder away from the impingement site (10 μm scale bar), b.

intermediate velocity regime where alumina contamination uptake occurs (~80 m/s), and c. high velocity region where Yb_2O_3 forms as the only stable reaction product (120-150 m/s)..... 199

Figure 4-6. Logarithmic XRD patterns of the sample surfaces after steam exposure for 60, 125, and 250 hours at 1400 °C..... 200

Figure 4-7. Zygo optical profilometry of the YbPO_4 surface after exposure to steam for 60 hours at 1400 °C..... 201

Figure 4-8. a. Plan view and b. Cross-section view of YbPO_4 after 250 hours at 1400 °C in the lower steam velocity range (~80 m/s) where Al_2O_3 and minor SiO_2 contamination react with Yb_2O_3 .
..... 201

Figure 4-9. YbPO_4 cross-sections displaying the Yb_2O_3 reaction layer for a. 60h, b. 125h, and c. 250h at 1400 °C in the 80-200 m/s steam velocity regime. 202

Figure 4-10. Average reaction depth and impingement erosion depths versus the square root of time for YbPO_4 in this study and $\text{Yb}_2\text{Si}_2\text{O}_7$ (previous study) at 1400 °C [29] and Chapter 2.3. 204

Figure 4-11. Macro images of YbPO_4 samples after CMAS exposure for 4, 24, and 96 hours at 1300 °C..... 204

Figure 4-12. Plot of XRD patterns for the starting YbPO_4 material and after CMAS exposure for 4, 24, and 96 hours at 1300 °C. 205

Figure 4-13. Stitched backscattered SEM images showing cross-sections of YbPO_4 after CMAS exposure for 4, 24, and 96 hours at 1300 °C in stagnant air. 206

Figure 4-14. Higher magnification SEM images acquired with backscattered electrons of the YbPO_4 -CMAS tri-layer reaction product for a. 4h, b. 24h, and c. 96 hours of exposure at 1300 °C.
..... 207

Figure 4-15. Energy Dispersive Spectroscopy of the YbPO₄ tri-layer reaction product after CMAS exposure for 96 hours at 1300 °C. Numbered areas in the image correspond to EDS results in Table 4-2.....207

Figure 4-16. Energy Dispersive Spectroscopy linescan of the tri-layer reaction product after exposure to 1300 °C for 96 hours. The linescan starts with 0 μm at the residual CMAS glass and ends with 51 μm at the continuous reaction layer near the YbPO₄ substrate.....209

Figure 4-17. Tri-layer reaction product average thickness plotted against the square root of time for the rare earth phosphate – CMAS reaction at 1300 °C.210

Figure 4-18. Rolls-Royce Inc. Turbofan [164] and general industrial gas turbine environmental conditions.219

Figure 4-19. APS Yb₂Si₂O₇ topcoat with silicon bond coat on a SiC CMC substrate after annealing for 2h at 1200 °C in air [166].220

Figure 4-20. EBC failure modes and their respective causations.221

Figure 4-21. Backscattered electron SEM cross section of bulk Yb₂Si₂O₇ after a 1400 °C exposure to 1 atm H₂O(g) at 190-210 m/s for 250 hours, adapted from [29].....223

Figure 4-22. Mixed phase Yb₂Si₂O₇ with 20 volume % Yb₂SiO₅ “splat” like microstructure after exposure to ~40 mg/cm² of 33CaO-9MgO-13AlO_{1.5}-45SiO₂ composition CMAS for 96 hours at 1300 °C, adapted from [185].....226

Figure 4-23. Phase-pure YbPO₄ after exposure to ~40 mg/cm² of 33CaO-9MgO-13AlO_{1.5}-45SiO₂ composition CMAS for 96 hours at 1300 °C, adapted from [181].226

Figure 4-24. Phase stability of RE₂Si₂O₇ relative to rare earth ionic radius [105].....227

Figure 4-25. Backscattered electron SEM cross section of bulk HfSiO₄ after a 1400 °C exposure to 1 atm H₂O(g) for 250 hours. Excessive stress cracking and mechanical erosion of ~625 μm was measured at the impingement site (200-240 m/s water vapor velocity). Adapted from [167].....228

Figure 4-26. Figure of merit visualization for EBC material candidates. Smaller encompassed area on the figure indicates increased overall stability as an EBC material.234

List of Tables

Table 2-1. Oxide activities for the 75 mol. % BAS + 25 mol. % SAS solution using FTOxide and SGPS databases in FactSage.26

Table 2-2. Comparison of BSAS reaction rates in steam with literature results. Recession rates from this study were first converted to TGA conditions in the literature study, and then converted to mass loss rates (mg/cm²h) from recession rates (μm/h). A gas velocity dependence of n=0.6 using Eq. 2 and water vapor partial pressure dependence of m=1.6 were used for the conversions.29

Table 2-3. Parabolic rates and calculated activation energies for HfSiO₄ reaction with steam.44

Table 2-4. Chemical reactions and reaction enthalpies for the two primary silicon hydroxide gaseous species formed during silicate reaction with water vapor. Data calculated from FactSage databases SGPS and HfSiO₄ data [47], liquids suppressed.48

Table 2-5. CMC and EBC CTE, melt temperature, and density.51

Table 2-6. Oxide reaction enthalpies for formation of metal hydroxide gas species upon steam reaction.71

Table 2-7. Linear reaction rates for Al₂O₃ (0001) after high velocity steam exposures.76

Table 2-8. Slopes and reaction enthalpies for the temperature dependences plotted in Figure 2-48 for the reactions of Al₂O₃ with steam.77

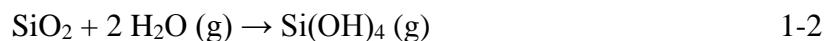
Table 2-9. Reaction enthalpies for the steam reaction with Al_2O_3 to form $\text{Al}(\text{OH})_3$ (g).	78
Table 2-10. Reaction enthalpies, steam reactions, and melting temperatures for P_2O_5 , Al_2O_3 , and AlPO_4 , from [13].	79
Table 2-11. Peak positions and hkl values for reaction products of $\text{Y}_2\text{Si}_2\text{O}_7$ after steam exposure at 1200 °C for 60h.	84
Table 2-12. Peak positions and hkl values for reaction products of YAG after steam exposure at 1200 °C for 60h.	87
Table 3-1. RE_2SiO_5 compositions and material densities from this work.	106
Table 3-2. Thermal expansion coefficients for powder and sintered Yb_2SiO_5	111
Table 3-3. Average linear CTE for single rare earth cation monosilicates from this study compared with literature values measured. *Refers to non-ambient XRD measurements.	114
Table 3-4. Room temperature thermal conductivity measured values for RE_2SiO_5 and values corrected for density.	118
Table 3-5. Dual phase field silica activities for RE_2O_3 - SiO_2 systems.	127
Table 3-6. Melting temperatures of line compounds on the Toropov RE_2O_3 - SiO_2 pseudobinary phase diagrams.	130
Table 3-7. Steam testing of $\text{RE}_2\text{Si}_2\text{O}_7$ in the literature.	131
Table 3-8. Stable phase, porosity area fraction, secondary phase area fraction, and densities for the processed $\text{RE}_2\text{Si}_2\text{O}_7$	135
Table 3-9. Summary of measured mass loss, reaction depths, and area fractions of porosity produced for $\text{RE}_2\text{Si}_2\text{O}_7$ (RE = Sc, Nd, Er, Yb, and Lu) after high velocity steam exposure at 1400 °C for 125 hours. * $\text{Sc}_2\text{Si}_2\text{O}_7$ reaction depth and produced porosity amount are averages value over the entire 80-200 m/s steam velocity range.	145

Table 3-10. Starting mixtures, stable phases, SEM area fractions, and densities for multi-component RE ₂ Si ₂ O ₇ samples.....	158
Table 3-11. Room temperature thermal conductivity (κ) for single and multi-component RE ₂ Si ₂ O ₇	161
Table 3-12. Linear CTE for single and multi-component RE ₂ Si ₂ O ₇	162
Table 3-13. Room temperature Young's Modulus for single and multi-component RE ₂ Si ₂ O ₇ . *Values are calculated.....	163
Table 3-14. Specific mass loss and reaction depths for multi-component RE ₂ Si ₂ O ₇ after steam exposure for 125h at 1400 °C.....	171
Table 3-15. Melting temperatures of yttrium-erbium silicate compounds in solution [128]......	175
Table 4-1. Steam chemical reaction to form hydroxide gaseous species for silica, yttria, and aluminum phosphate [13]......	190
Table 4-2. Energy Dispersive Spectroscopy area phase identification of the positions labelled in Figure 4-15.	208
Table 4-3. Partial pressures of metal hydroxide species (atm) at 1200 °C with P(H ₂ O)=1. * Estimated metal hydroxide partial pressures.....	222
Table 4-4. Thermo-chemical and thermo-mechanical properties of selected high-temperature EBC materials. Conditional binary values are denoted with *. Footnotes a-m are provided in Appendix 8.6.....	231
Table 4-5. Figure of Merit score for each material, determined from summation of Table 4-4 after normalization of each sub category with values from 0 to 1. Smaller FoM scores represent the most desirable EBC material candidate.	233

1. Motivation

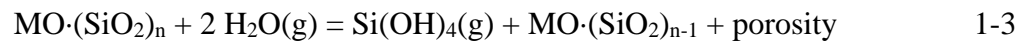
Ceramic matrix composites (CMCs), made of SiC fibers with a SiC matrix (SiC/SiC), entered commercial operation as hot section gas turbine engine components in 2016 [2]. SiC/SiC CMCs are lightweight alternatives to superalloys for power and propulsion gas turbine components, and show promise for 100 °C – 200 °C increases in turbine operating temperatures due to their high-temperature stability and high decomposition temperature of 2545 °C [3]. Introduction of CMCs for turbine components, such as shrouds, combustor liners, and nozzles, can result in decreased reliance on cooling air which consequently can either lead to increased engine efficiency or a decrease in turbine NO_x and CO_x emissions. In 2008, the U.S. spent an estimated \$73B in fuel for commercial and DoD flights [4]. Even a 5% efficiency increase could result in billions of dollars in savings per year for commercial and government organizations. While introduction of multiple CMC components into turbine hot sections show promise for improvements greater than a 5% efficiency increase, the reliance on environmental barrier coatings (EBCs) as long-term protective topcoats remains a critical research topic to enable CMC technology. Microstructural evolution of EBCs, chemical reactions with high-velocity water vapor or ingested debris, and behavior of EBCs in cyclic temperature exposures all represent knowledge gaps and available avenues for scientific research.

SiC exhibits chemical resistance to high-temperature environments through formation of a protective SiO₂ thermally grown oxide (TGO) when in contact with oxygen (Equation 1-1). However, SiO₂ reacts with water vapor, a product of the gas combustion process, to form the volatile hydroxide species Si(OH)₄ (g) as shown in Equation 1-2 [5]–[7].



The reaction with water vapor degrades the protective SiO₂ scale and results in detrimental rates of recession for the SiC-base CMC. Oxidation and volatilization kinetics of SiC in reaction with H₂O (g) are controlled by a gas phase diffusion process, where diffusion of a silicon hydroxide product species outward through a gaseous boundary layer represents the rate limiting step for the steam reaction [8]. Environmental barrier coatings (EBCs) are thus required to mitigate SiO₂ volatilization, although the long-term stability for a variety of EBC candidates in high temperature water vapor is not thoroughly understood.

EBCs are most often silicate ceramics due to excellent chemical compatibility with SiC, the silicon bond coat, and the SiO₂ thermally grown oxide at the bond coat interfaces. Silicate EBCs show fractional silica activities compared to pure silica, and therefore react with water vapor but at a reduced rate compared to pure SiO₂. Silica-depleted reaction products have lower molar volumes and thus form associated porosity from the steam reaction. Water vapor reacts with silica-based materials through the generalized reaction shown in Equation 1-3, where MO represents a metal oxide component as part of a metal silicate compound. The silica-depleted and porous product layer can provide fast pathways for gas diffusion to the underlying silicate, promoting further degradation.



The thermochemical stability of EBCs is not limited to high-velocity water vapor interaction. EBCs must be resistant to molten calcium magnesium aluminosilicate (CMAS) exposure, which occurs by turbine ingestion of siliceous debris such as dirt, sand, or volcanic ash [9], [10]. A low EBC oxidant diffusivity is desired to limit oxidation of the underlying silicon bond coat or CMC. EBCs must exhibit good thermomechanical stability with the underlying material(s), obtained by a matching coefficient of thermal expansion (CTE) and minimal thermal expansion

anisotropy to minimize interfacial and internal stress buildup. The linear CTEs of SiC and the silicon bond coat are $4.5\text{-}5.5 \times 10^{-6} / ^\circ\text{C}$ [3] and $3.5\text{-}4.5 \times 10^{-6} / ^\circ\text{C}$ [11], respectively. Candidates should also have high melting temperatures, limited phase changes at relevant temperatures, and thermal shock resistance.

1.1. History of EBC materials

The earliest generation EBC systems consisted of a silicon bond coat, a mullite ($3\text{Al}_2\text{O}_3 \cdot 2\text{SiO}_2$) intermediate layer, and an outer layer composed of yttria-stabilized zirconia (YSZ) [12]. Mullite was chosen due to its CTE match with SiC and its exceptional thermal shock resistance, although the high silica activity of mullite (0.4) allowed for large amounts of material recession after steam ingress through the YSZ layer [12]. An additional early EBC system included a silicon bond coat, a mullite/BSAS ($\text{Ba}_{0.75}\text{Sr}_{0.25}\text{Al}_2\text{Si}_2\text{O}_8$) intermediate layer, and a BSAS topcoat. BSAS was applied as an outer EBC layer to provide protection for both SiC and mullite from water vapor reaction because it was thought to have a low silica activity of <0.1 [12] or 0.01 [13]. BSAS also exhibited a low CTE and low moduli which limited crack formation upon thermal cycling. BSAS is no longer considered a suitable EBC candidate due to a low melting eutectic (1311°C) that forms when in contact with silicon or a SiO_2 TGO [12]. However, the relative stability of the coating constituents and fundamental microstructural evolution were not well studied. In laboratory conditions where free SiO_2 can be avoided, the thermochemical stability of BSAS can be studied to support the understanding of water vapor reaction mechanisms for silicate ceramic materials.

Rare earth silicate systems are state-of-the-art EBC candidates and consist primarily of rare earth (RE) disilicates, $\text{RE}_2\text{Si}_2\text{O}_7$, with a rare earth monosilicate, RE_2SiO_5 , secondary phase. Both $\text{RE}_2\text{Si}_2\text{O}_7$ and RE_2SiO_5 show tradeoffs in terms of their EBC stability. RE_2SiO_5 display enhanced high-temperature chemical stability compared to $\text{RE}_2\text{Si}_2\text{O}_7$. Yet, The RE_2SiO_5 materials have poor

linear CTE match with SiC CMCs and also possess a high degree of CTE anisotropy which leads to thermal stress cracking upon engine cycling. Many rare earth disilicates exhibit a thermal expansion match with the silicon bond coat and SiC substrate with minimal CTE anisotropy [14].

Rare earth silicates still react with steam to form $\text{Si}(\text{OH})_4$ (g), although at a reduced rate due to a decreased silica activity compared to SiO_2 . The steam reactivity of rare earth silicates is still an active area for research due to the complexity of experimental facilities to best model gas turbine environments. A fundamental understanding of the microstructure evolution of rare earth silicates in high-temperature high-velocity steam and their reaction mechanisms are lacking and must be addressed to further CMC/EBC technology and lifetime prediction. Material property trends with individual silicate compounds should then be compared to properties of multi-component and high entropy silicate mixtures to determine the ability to optimize silicate EBCs. Given the reactive nature of SiO_2 with high-temperature H_2O (g), non-silicate EBC materials should also be identified and explored to increase the scope of EBC research.

1.2. Volatilization Kinetics for SiO_2

The volatilization kinetics for oxides such as SiO_2 in steam are rate-limited by hydroxide gas phase diffusion through a boundary layer [8], such that reaction rates can be analytically calculated for oxides in steam environments through mass transfer in the gas phase. Assuming laminar flow conditions and a flat plate geometry, the flux of metal hydroxide leaving the sample surface, J_l , can be defined as Equation 1-4:

$$J_l = 0.664(Re)^{\frac{1}{2}}(Sc)^{\frac{1}{3}}\frac{D_{AB}\rho'}{L} \quad 1-4$$

where Re is the Reynolds number, Sc is the Schmidt number, D_{AB} is the gas interdiffusion coefficient for the metal hydroxide and water vapor, ρ' is the equilibrium concentration of metal hydroxide at the sample reaction interface, and L is the sample length [15].

The Reynolds and Schmidt numbers can be expanded such that Equation 1-4 can be rewritten as:

$$J_l = 0.664 \left(\frac{\rho v L}{\mu} \right)^{\frac{1}{2}} \left(\frac{\mu}{\rho D_{AB}} \right)^{\frac{1}{3}} \frac{D_{AB} \rho'}{L} \quad 1-5$$

where ρ is the concentration of water vapor in the boundary layer, v is the water vapor velocity, and μ is the gas viscosity [15]. Through the given variables, the volatilization rate can be calculated with clear dependences on steam velocity, partial pressures of water vapor and the metal hydroxide reaction product, total pressure, and temperature. Equation 1-5 was solved for the SiO_2 reaction at 1200 °C, 1300 °C, and 1400 °C with 125 m/s gas velocity and 1 atm total pressure for a 10 x 10 mm SiO_2 coupon. Recession rates were calculated from the flux solutions and are presented in Figure 1-1. The expected recession rates for SiO_2 exposed to 125 m/s steam would result in millimeters of material recession even before reaching 1,000 hours, further emphasizing the requirement of environmental barrier coatings for SiC/SiC CMC usage for gas turbine components.

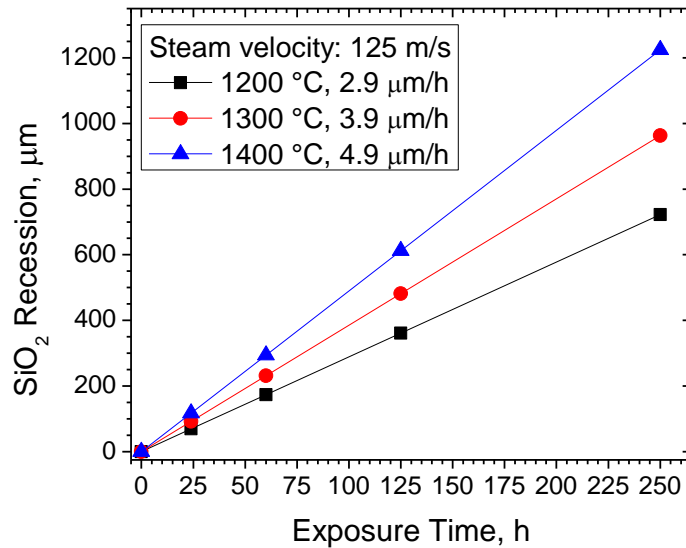


Figure 1-1. Calculated SiO_2 recession depths as a function of time, with recession rates determined from Eq. 2-2.

Calculated reaction rates through Equation 1-5 do not account for microstructural evolution of materials that react with steam to form a porous silica-depleted product phase, as described in Equation 1-3. The porous network produced from the EBC-steam reaction and subsequent changes in microstructure such as coarsening, densification, and secondary steam reactions need to be fully understood before an analytical or numerical model can be applied to EBC material systems.

1.3. Thermochemical Stability of Phase Pure Silicates in Steam

Gas turbine environments contain approximately 10% H_2O (g) as well as unreacted oxygen under high pressures [7], where the high total pressures of gas turbines translates to water vapor partial pressures near 1 atm. Historically, high-temperature water vapor studies have been limited to low total pressures of water vapor or low velocity steam due to complexities in high velocity steam testing setups. Testing EBC reactivities with steam in stagnant air [16], [17] and at velocities below 50 m/s [18], [19] does provide information on product phases, but can also mischaracterize both the degree of degradation and the degradation mechanism. Low velocity steam can result in

contamination from the test environment, such as deposition of $\text{Al}(\text{OH})_3$ (g) impurities from an alumina furnace environment [20] or limited sample reactivity by artificially decreasing the silica reactivity from use of fused quartz components [7]. The inlet gas velocity for a Model 501-K turbine (Rolls-Royce, Indianapolis, IN) field test at vane mid-span has been measured at ~ 160 m/s, and the gas stream is further accelerated to ~ 575 m/s at the vane exit [21]. High velocities are hence vital to steam testing for accurate understanding of thermochemical and thermomechanical stability of EBCs.

1.4. Knowledge Gaps

Near-stagnant steam velocity testing of silicate EBCs is commonly described in the literature, although the thermochemical stability of EBC candidates in high-velocity water vapor has not been adequately examined. It is unknown if microstructural evolution of the steam reaction products would provide additional steam resistance for EBCs with increasing exposure time and temperature. Additionally, thermodynamic data for EBC materials are not yet fully determined, which limits the ability to predict material stability in steam. EBC materials are also not fully characterized in terms of general material properties, such as thermal expansion anisotropy, Young's Modulus, and thermal conductivity. Without a general understanding of material properties and steam behavior, optimization and comparison of EBC stabilities in combustion environments cannot be adequately performed.

Linear reaction kinetics were expected to occur for materials exposed to steam when the gas phase diffusion distance was not changing. Simple oxides such as SiO_2 and Al_2O_3 should display linear steam reaction kinetics as the reacted sample surface is volatilized with no production of a protective reaction product. Parabolic reaction kinetics were expected for EBCs exposed to high-velocity steam when the gas diffusion distance increases with increasing time. This behavior was

predicted to occur for HfSiO_4 and $\text{Yb}_2\text{Si}_2\text{O}_7$, where respective components HfO_2 and Yb_2O_3 are known to be relatively stable in steam. Thus, HfO_2 and Yb_2O_3 should remain on the sample surfaces as steam reaction products that grow with increasing exposure time and temperature. The steam reaction kinetics for BSAS were unknown due to conflicting studies in the literature. The temperature dependence of silicate EBCs were hypothesized to reflect the formation of $\text{Si}(\text{OH})_4$ (g) with a reaction enthalpy comparable to that of pure SiO_2 exposed to water vapor at 56 kJ/mol [22].

An assumption of this work was that all RE_2SiO_5 and $\text{RE}_2\text{Si}_2\text{O}_7$ (RE = Sc, Y, La-Lu) should display similar steam reaction products and reaction rates as neighboring RE silicates with similar crystal structures. Material properties such as thermal expansion and Young's Modulus were expected to be dependent on the crystal structure and rare earth cation size, such that mixing of multiple cations in solution should result in rule of mixtures values for these properties. Thermal conductivity was anticipated to be an exception to this trend, as mixing of multiple cations in solution along a crystal lattice should result in dispersion of phonons such that thermal conductivity is decreased compared to a simple rule of mixtures.

The EBC community has focused material testing on primary EBC failure modes, including reaction with water vapor, steam oxidation of the silicon bond coat, thermomechanical fatigue, corrosion by ingested debris, erosion, and foreign object damage [1]. All failure modes are connected through the microstructural evolution of the EBC. Research focus has been placed on select rare earth silicate EBC candidates, such as $\text{Yb}_2\text{Si}_2\text{O}_7$. Yet, to date, no clear comparison of EBCs against all known failure modes has been presented. Without a holistic comparison of known EBC materials, novel multi-component silicate and non-silicate EBCs cannot be confirmed as viable avenues of research for next-generation materials development.

This dissertation attempts to better understand EBC-water vapor degradation mechanisms, long term phase stability, thermochemical stability, and criteria for development of next generation EBC candidates through the following objectives:

1. Uncover fundamental mechanisms for high-velocity steam degradation and microstructural evolution of silicate EBC candidates such as barium strontium aluminosilicate (BSAS, $\text{Ba}_{0.75}\text{Sr}_{0.25}\text{Al}_2\text{Si}_2\text{O}_8$), hafnon (HfSiO_4), and ytterbium disilicate (Yb_2SiO_7)
2. Determine fundamental relationships between rare earth elements and rare earth silicate material properties to tailor improved properties such as thermal expansion, phase stability, steam resistance, thermal conductivity, and Young's Modulus
3. Develop the first figure of merit for holistic comparison of EBC materials, for identification and exploration of novel EBC candidates such as ytterbium phosphate (YbPO_4), and for advancement of next-generation EBCs

2. Objective 1. Microstructural Evolution and Quantitative Analysis of Silicates in High-Velocity Steam

Steam degradation of silicate materials can be best understood with high gas velocities and water vapor partial pressures that are achieved with a steamjet testing method, described later. The goal of Objective 1 is to uncover fundamental mechanisms for high-velocity steam degradation and microstructural evolution of silicate EBC candidates. Steam testing will first be described, followed by steamjet characterization of barium strontium aluminosilicate (BSAS, $\text{Ba}_{0.75}\text{Sr}_{0.25}\text{Al}_2\text{Si}_2\text{O}_8$), hafnion (HfSiO_4), and ytterbium disilicate (Yb_2SiO_7).

Parabolic reaction kinetics are desired for EBCs to decrease the steam reaction depth over time, although the reaction rates for these materials in high velocity steam have not yet been determined. The gaseous species formed from reaction of pure SiO_2 in steam is $\text{Si}(\text{OH})_4$ (g) [22], although this hydroxide species has not been verified for complex silicate compounds exposed to steam. Quantitative analysis of the steam reaction process will be discussed for each material to attempt addressing both the time-dependent reaction kinetics and the temperature-dependent thermodynamic reaction enthalpy, which should be related to the gaseous product species. The quantitative nature of the steamjet will be analyzed through determination of time and temperature dependences for the volatilization behavior of (0001) plane sapphire coupons.

The formation of reaction product phases can be predicted based on available phase diagrams and literature steam testing, although the reaction product stability in high-temperature high-velocity steam remains an important question. Porosity networks and microstructural evolution of the steam reaction products will be addressed for each material to support future development of lifetime prediction models of EBCs. Preliminary results regarding preferred orientation for growth

of steam reaction products for single crystal compounds $Y_2Si_2O_7$, Y_2SiO_5 , and $Y_3Al_5O_{12}$ will also be described.

2.1. High-Temperature Water-Vapor Reaction Mechanism of Barium Strontium Aluminosilicate (BSAS)

2.1.1. Introduction

A BSAS outer layer on a mullite inner layer was an early EBC system described earlier. BSAS was thought to have a low silica activity of <0.1 [12] or 0.01 [13]. Strontium-containing BAS was chosen to stabilize the monoclinic celsian phase at high temperatures. The celsian phase limits the CTE mismatch between BSAS ($4.5 \times 10^{-6} / ^\circ\text{C}$) [14], mullite ($4.5\text{-}5.5 \times 10^{-6} / ^\circ\text{C}$) [23], and SiC ($4.5\text{-}5.5 \times 10^{-6} / ^\circ\text{C}$) [14]. However, BSAS has a eutectic around 1311°C with SiO_2 , the thermally grown oxide formed at the silicon bond coat, which results in a detrimental glass formation that can lead to spallation of the EBC [12].

While the low melting eutectic present between BSAS and SiO_2 prevents the use of BSAS as an EBC at temperatures greater than 1300°C , the thermochemical stability of BSAS in steam has not been fully investigated. Lee, Fox, and Bansal reported linear steam reaction kinetics for BSAS through thermogravimetric mass loss measurements in a 50% H_2O /50% O_2 environment at a 4.4 cm/s flow rate, 1500°C , and 1 atm total pressure [14]. No product phase was reported for BSAS after steam exposure by x-ray diffraction. Alternatively, a BSAS-coated combustor liner was exposed in a gas-burner rig for 500h at 1200°C with 1.5 atm H_2O (g) and 10 atm total pressure. After exposure, a strontium-rich product phase ($\text{Sr}_2\text{Al}_2\text{SiO}_7$) was seen on the surface as nonprotective nodules [24]. Determination of the BSAS reaction mechanism in steam environments can allow for understanding as to why a strontium-enriched product phase has been observed under certain conditions, yet no product phase was detected for other experimental conditions.

While the silicate EBC-water vapor reactions are known to occur, the rate-controlling mechanisms for the reactions are not fully understood. This work studies the steam reaction process for barium strontium aluminosilicate (BSAS, $\text{Ba}_{0.75}\text{Sr}_{0.25}\text{Al}_2\text{Si}_2\text{O}_8$), an early EBC material candidate. The time and temperature dependences of the BSAS-water vapor reaction are experimentally determined, and the steam reaction mechanism for BSAS is hypothesized.

2.1.2. Methods

2.1.2.1. Processing

Pre-reacted thermal spray powders of BSAS ($\text{Ba}_{0.75}\text{Sr}_{0.25}\text{Al}_2\text{Si}_2\text{O}_8$) were utilized to make test samples. The purity of the starting powder (Praxair: Danbury, CT) was verified with a Panalytical Empyrean X-ray diffractometer (XRD: Westborough, MA) and characterized with X'Pert High Score Plus software to detect phases present. Powders were dry ball milled for 24 hours with yttria stabilized zirconia milling beads. Milled powders were then loaded into a 20 mm diameter graphite die and consolidated by spark plasma sintering (SPS) using a Thermal Technologies DCS 25-10 SPS (Santa Rosa, CA) in argon. The SPS process for the given silicate materials involved 30-minute holds at maximum temperatures and pressures of 1250 °C and 65 MPa. After SPS, samples were annealed for 24 hours at 1300 °C in a stagnant air box furnace (CM Rapid Furnace, Bloomfield NJ) to remove residual carbon and restore oxygen stoichiometry. Resulting pucks were sectioned into test coupons with dimensions ~10 x 10 x 1 mm. BSAS specimens were exposed to high-velocity water vapor at temperatures of 1200 °C, 1300 °C, and 1400 °C for exposure times of 24, 48, and 72h.

2.1.2.2. Steamjet Experimental Setup and ANSYS Steam Velocity Distribution Model

A modified horizontal tube furnace (Model 1730-12 HTF, CM Furnace Inc., Bloomfield,

NJ), termed a steamjet, was used in this research to model turbine environments. The steamjet simulates a 10 atm turbine environment containing 10% H₂O (g) by maintaining 1 atm steam. The experimental design, shown in Figure 2-1, originated from Dos Santos et al. [25] with further modifications by Golden, Parker, and Opila [26], [27]. Deionized water was pumped into a 1 mm diameter Pt-Rh capillary passing through a 900 °C preheater and into the tube furnace hot zone. Argon flowed in the tube furnace at 30 sccm around the outer surface of the platinum capillary to limit oxidation of the capillary. The water in the capillary was vaporized in the preheater section, which accelerated steam flow into the tube furnace.

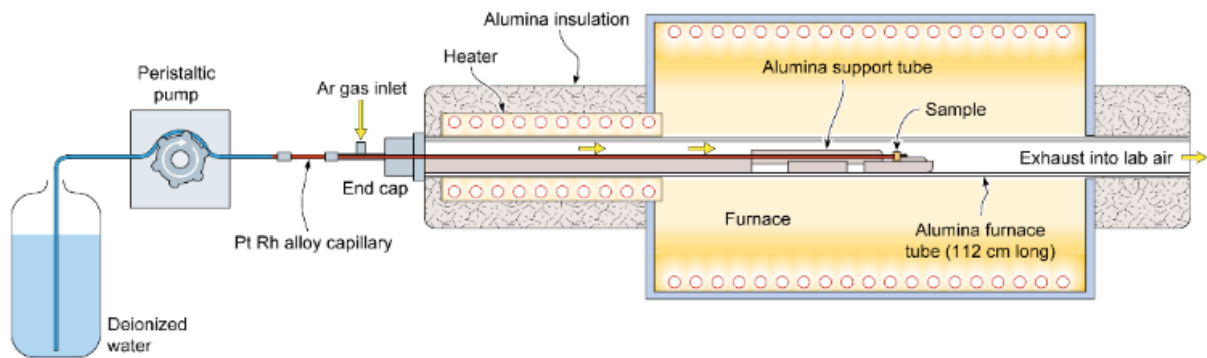


Figure 2-1. High velocity steamjet experimental setup [23].

The sample was held in place on an Al₂O₃ holder with platinum wire at a 45-degree angle relative to the capillary outlet, as shown in Figure 2-2. Platinum foil was used between the sample and Al₂O₃ holder to limit direct contact contamination. The test specimen was placed 1 mm away from the capillary exit in the furnace hot zone, where the proximity of the sample to the capillary outlet allowed for high-velocity steam to impinge upon sample surface with a water vapor partial pressure of 1 atm, thus preventing tube furnace impurities from reacting with most of the coupon

face. Samples were loaded and removed from the furnace at temperature at a rate of approximately 75 °C/min. Specimen exposures in water vapor can be performed up to 1500 °C.

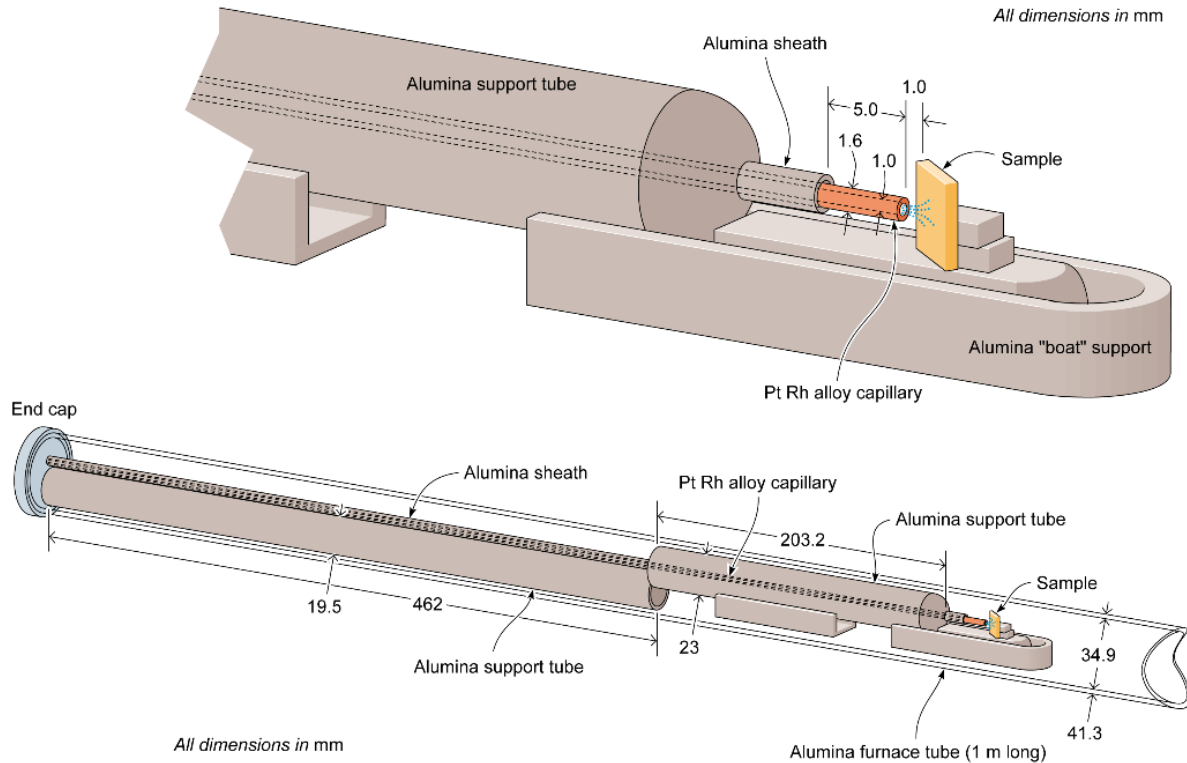


Figure 2-2. Sample view of high velocity steamjet experimental setup [23].

Gas velocities were experimentally controlled through input of the liquid water flow rate (1.8-2.1 g/min) and experimental setup geometry. ANSYS (Canonsburg, PA) computational fluid dynamics software was used to model the water vapor velocity distribution across the surface of the sample. A maximum velocity of ~240 m/s at 1400 °C was calculated for a 2 ml/min liquid water flow rate, as shown in Figure 2-3. ANSYS velocity maps were used to correlate local recession depths and microstructural features to a water vapor velocity. The *average* water vapor velocity across the entire 10x10 mm coupon with a 2 ml/min flow rate was 37 m/s, 44 m/s, and 47 m/s for 1200 °C, 1300 °C, and 1400 °C, respectively.

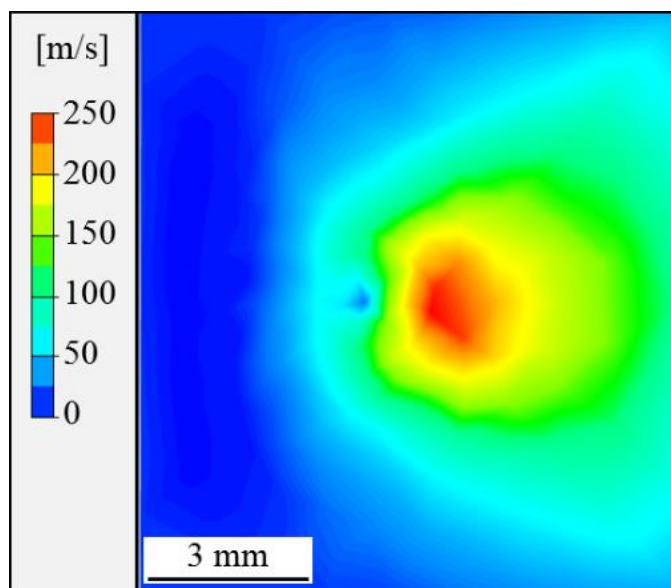


Figure 2-3. ANSYS Computational Fluid Dynamics Model for steam velocity distribution across the sample face at 1400 °C.

2.1.2.3. Characterization

Sample mass was recorded before and after steam exposure to an accuracy of 0.05 mg (MS105DU, Mettler-Toledo, Columbus, OH) as a secondary metric for measuring the volatilization reaction. The uncertainty for the mass loss data includes error in mass measurement before and after testing as well as a general uncertainty of ± 0.5 mm for sample dimension measurement. Optical profilometry (Zygo NewView 7300: Middlefield, CT) was used to depth profile the surfaces after steam exposure and to provide quantitative data on material recession. Maximum recession data, discussed later in this work, do not inherently contain uncertainty, as they are singular data points from the profilometry linescans. An uncertainty of ± 5 microns was placed on all maximum recession datapoints to encompass any unknown experimental test error or profilometer error.

X-ray diffraction, scanning electron microscopy (SEM: FEI Quanta 650, Hillsboro, OR), and energy dispersive spectroscopy (EDS: XMax 150, Oxford Instruments, Abingdon, UK) were used to characterize the initial sample chemistry and surface microstructure, as well as reaction products and microstructure changes after steam exposure. Backscattered electron (BSE) SEM in

Figure 2-4 displays as-prepared BSAS microstructure with a corresponding EDS spectrum of the starting material. The lighter phase corresponds to Yb_2O_3 impurities from the starting BSAS powder, which reacted to form $\text{Yb}_3\text{Al}_5\text{O}_{12}$ impurities upon sample annealing. The BSAS samples contained ~6% $\text{Yb}_3\text{Al}_5\text{O}_{12}$ and ~6% porosity by image area fraction analysis with ImageJ analysis suite (National Institutes of Health, Bethesda, Maryland). Samples were mounted in epoxy and polished to 1 μm with diamond suspension prior to SEM imaging.

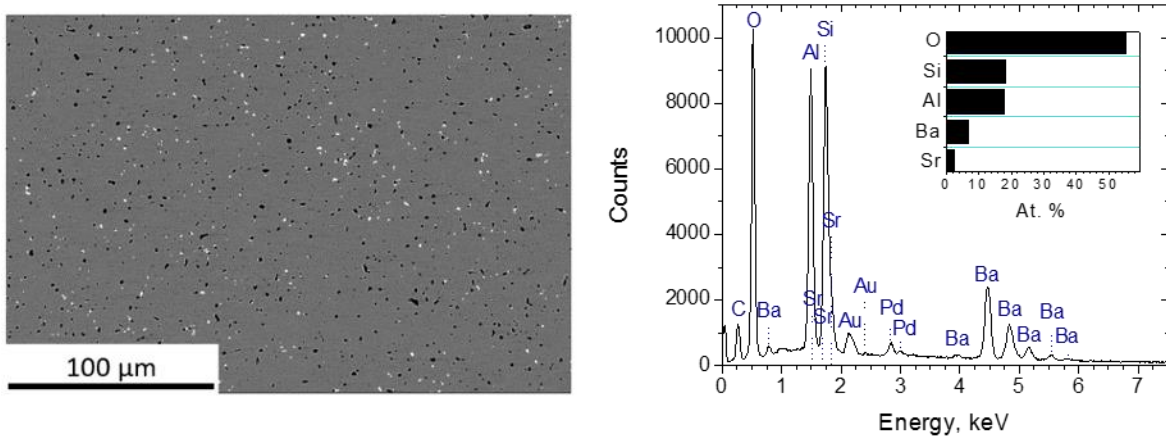


Figure 2-4. BSE image of BSAS after SPS processing, box furnace annealing, and fine polishing, and an area EDS spectrum of the starting BSAS material.

2.1.2.4. Thermodynamic Assessment of BSAS

Complete thermodynamic data are not available for the BSAS system in the literature. Initial estimations of BSAS thermodynamic data are made in the FactSage thermodynamic database using the compounds SAS ($\text{SrAl}_2\text{Si}_2\text{O}_8$) and BAS ($\text{BaAl}_2\text{Si}_2\text{O}_8$) as well as an ideal BSAS system from individual constituent oxides: BaO , SrO , Al_2O_3 , and SiO_2 [28]. Equilibrium vapor species and solid oxide activities were calculated with FTOxide and SGPS databases, with liquid phases suppressed. The FTOxide database provided data on the SAS and BAS compounds as well as their constituent solid oxides, and SGPS provided thermodynamic data on the hydroxide gaseous species formed

upon reaction with water vapor. Presented data on Al_2O_3 and SiO_2 are for the alpha corundum and high cristobalite phases, respectively.

2.1.3. Results

XRD plots of an as-prepared BSAS coupon and of BSAS samples exposed to steam for 72 hours at 1200 °C, 1300 °C, and 1400 °C are shown in Figure 2-5. $\text{Yb}_3\text{Al}_5\text{O}_{12}$, a minor impurity phase from the starting powder, was the only detectable phase other than BSAS. Three minor peaks are present after exposure at 1200 °C and could not be identified.

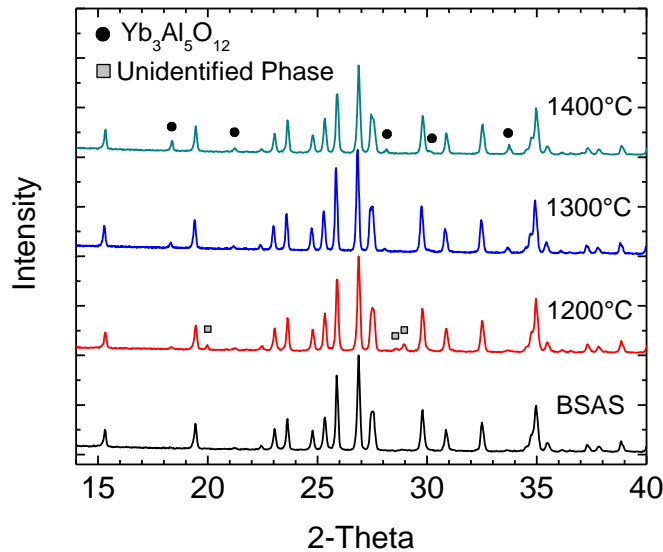


Figure 2-5. XRD plots for BSAS coupons before and after steam exposure for 72h at 1200 °C, 1300 °C, and 1400 °C.

Figure 2-6 shows BSE images of BSAS samples exposed to steam for 72 hours at each temperature. Each image was taken in a sample region where local gas velocities are predicted to be 145-175 m/s. For all BSAS samples exposed to steam at 1200 °C, a silica-depleted and strontium-rich product phase was seen on the surface as isolated nodules. With increasing temperature, the total concentration of the Sr-rich nodules on the surface decreases. The minor impurity phase Yb_2O_3 (white) remains present at 1400 °C which indicates the stability of Yb_2O_3 in high-temperature steam

[27], [29]. All specimens subjected to steam exposures at 1400 °C are absent of any reaction product on the surface, suggesting volatilization of all BSAS constituents: BaO, SrO, Al₂O₃, and SiO₂. Minor coarsening was seen for BSAS with increasing exposure time and temperature. The results described experimentally were consistent with the volatility of individual constituents in steam, as described in the discussion section.

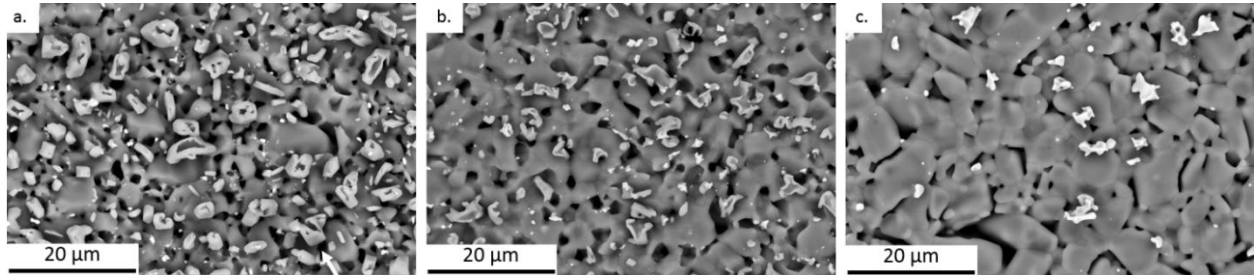


Figure 2-6. BSE plan view imaging of BSAS samples exposed to steam for 72h with gas velocities between 145-175 m/s at a) 1200 °C, b) 1300 °C, and c) 1400 °C.

Figure 2-7 shows a higher magnification image of a BSAS sample exposed to water vapor at 1200 °C for 72h, along with EDS spectra showing the elemental makeup of the framed area on the BSE image. Qualitative EDS shows a composition close to Ba_{0.55}Sr_{0.45}Al₂SiO₇. The product phase appeared to be both depleted in silica and enriched in strontium oxide when compared to the EDS spectra of the starting BSAS material in Figure 2-4.

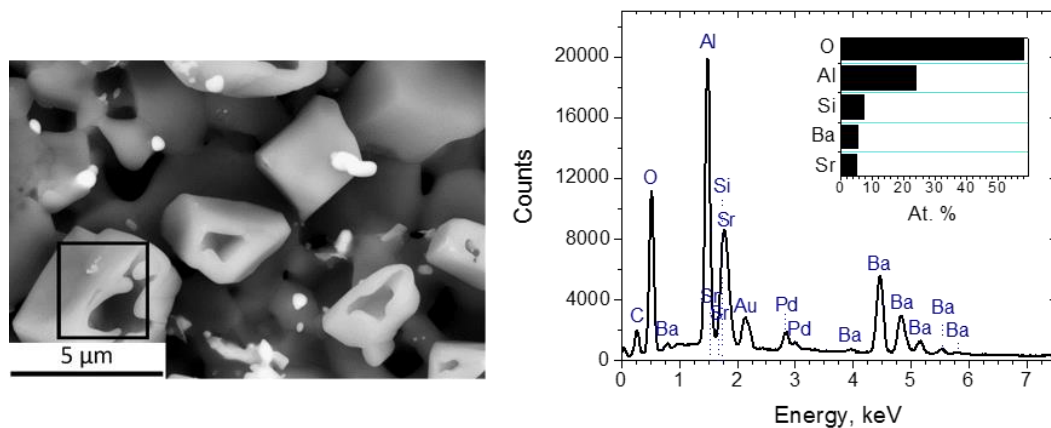


Figure 2-7. BSE image of BSAS exposed to water vapor at 1200 °C for 72 hours with local gas velocity of 145-175 m/s, and EDS spectra of the black square region that estimates the product phase average concentration to be Ba_{0.55}Sr_{0.45}Al₂SiO₇.

Depth profiling of the surface provided information on total reaction depths, since a protective product layer was not present after steam testing. Optical profilometry was used to determine maximum recession points for each sample, as is shown in Figure 2-8 for BSAS samples exposed to steam for 72 hours at exposure temperatures of 1200 °C, 1300 °C, and 1400 °C. A velocity dependence for the reaction rate can be qualitatively seen through visual comparison of the profilometry maps in Figure 2-8 and the ANSYS velocity map in Figure 2-3, indicating that gas-phase diffusion limits the reaction rather than a solid-state transport mechanism.

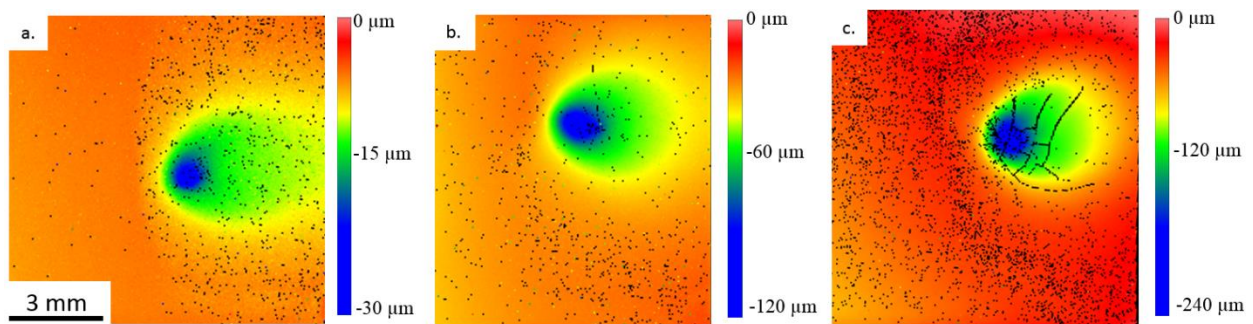


Figure 2-8. Optical profilometry of the BSAS surface after steam exposure for 72 hours at a. 1200 °C, b. 1300 °C, and c. 1400 °C. Each depth profile is displayed with a unique scale bar where material recession is represented as a negative value.

2.1.4. Analysis

2.1.4.1. Time Dependence

The reaction depths can be determined by taking line scans across the profilometry maps. Figure 2-9 displays a line scan across Figure 2-8c, showing the reaction depth for the sample exposed to steam at 1400 °C for 72h. The first 4 mm of the line scan correspond to the region left of the highest velocity impingement site, where minimal changes in surface height were observed. A maximum recession depth of 209 microns was seen at the impingement site. The maximum recession depths at the impingement sites of each sample were used for analysis of the time and temperature dependences of the steam reaction with BSAS.

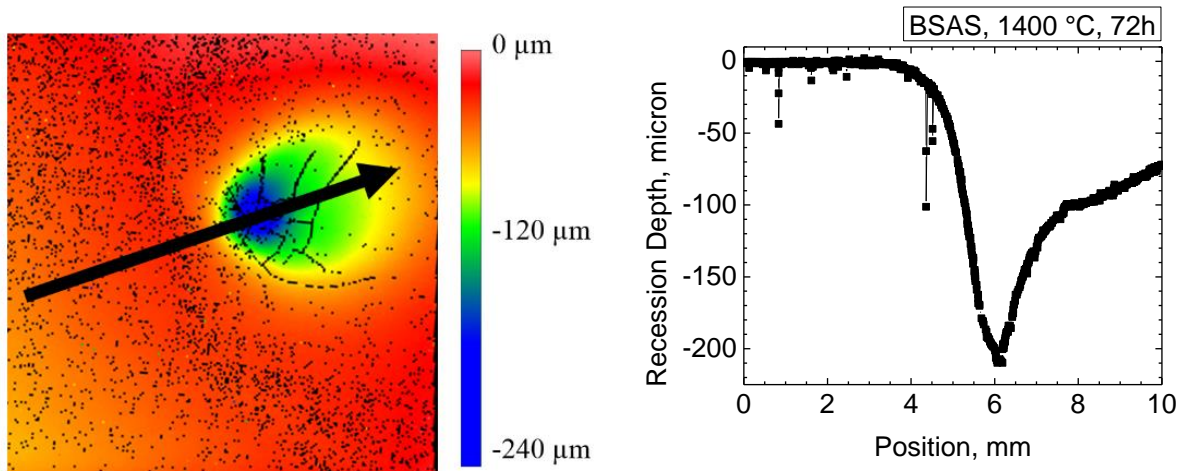


Figure 2-9. Line scan across the profilometer map of the BSAS sample exposed to water vapor at 1400 °C for 72h to display the total recession depths as a function of sample location.

The specific mass loss and maximum recession points are plotted against water vapor exposure time for each sample in Figure 2-10a and Figure 2-10b, respectively. An *average* velocity for the full sample coupons has been estimated to be 37 m/s, 44 m/s, and 47 m/s for 1200 °C, 1300 °C, and 1400 °C, respectively, to correspond to the specific mass loss for each sample. Maximum recession data are presented in Figure 2-10b for gas velocities of 209 m/s, 230 m/s, and 239 m/s for 1200 °C, 1300 °C, and 1400 °C, respectively. A linear fit was observed for both the specific mass change and maximum recession data versus steam exposure time with lines passing through the origin. The linear reaction rates (k_i) are given on the plots for each exposure temperature.

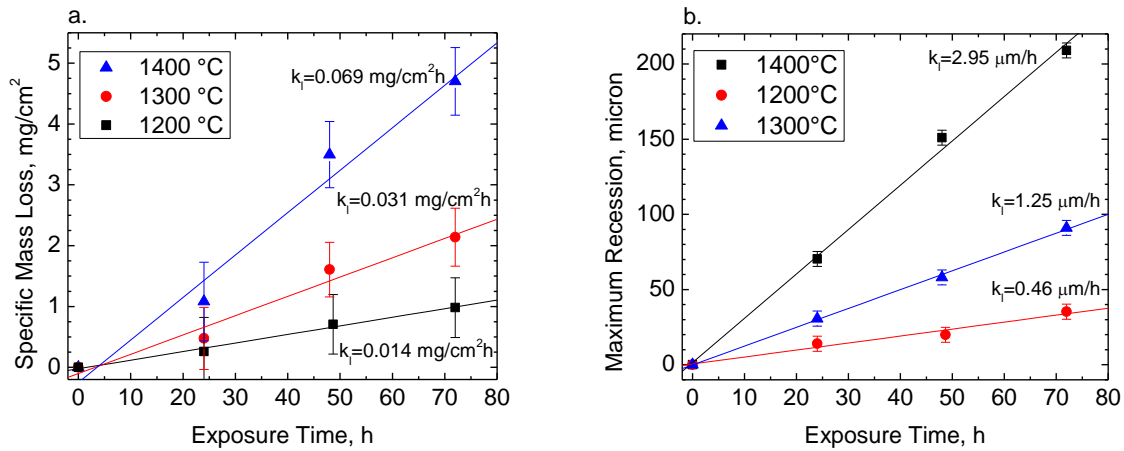


Figure 2-10. a. Specific mass loss (mg/cm²) and b. maximum recession (μm) data plotted against water vapor exposure time (h) for 1200 °C, 1300 °C, and 1400 °C with reaction rates (k_l) for each temperature.

2.1.4.2. Velocity Dependence

A gas stream velocity dependence was observed through qualitative comparison of the profilometry results and the ANSYS velocity map. The velocity dependence for the recession rate was a result of the gas flux through a boundary layer produced at the BSAS-gas interface. Equation 2-1 displays the known relationship, derived from gas boundary layer theory:

$$k_l \propto \frac{v^n P_{H_2O}^m}{P_{Total}^{\frac{1}{2}}} \quad 2-1$$

where k_l is the linear recession rate, v is the gas velocity, n is the gas velocity exponent, P_{H_2O} is the water vapor partial pressure, m is the water vapor exponent, and P_{Total} is the total pressure [30]. The water vapor exponent was set to $m=1.6$ in accordance with the final chemical reaction proposed later in this work (Eq. 2-9). Figure 2-11 displays the line scan from a BSAS sample exposed to steam at 1400 °C for 72h compared to a calculated steam velocity line scan from the ANSYS model. Material recession was seen to increase as gas velocity increases. The recession rate was compared to the gas velocity to measure the gas velocity exponent term, n , shown earlier in Equation 2-3. From the velocity dependence for mass transfer, laminar flow is seen when $n=0.5$ and

turbulent flow is seen when $n=0.8$ [15]. Figure 2-12 plots the log of the recession rates against the log of gas velocities for various points on the line scan in Figure 2-9a. The slope of the log-log plot represents a gas velocity exponent of $n=0.60 \pm 0.03$ for a gas velocity range of 33 m/s to 240 m/s. The water vapor impinging upon the samples in the steamjet was determined to be primarily consistent with laminar gas flow.

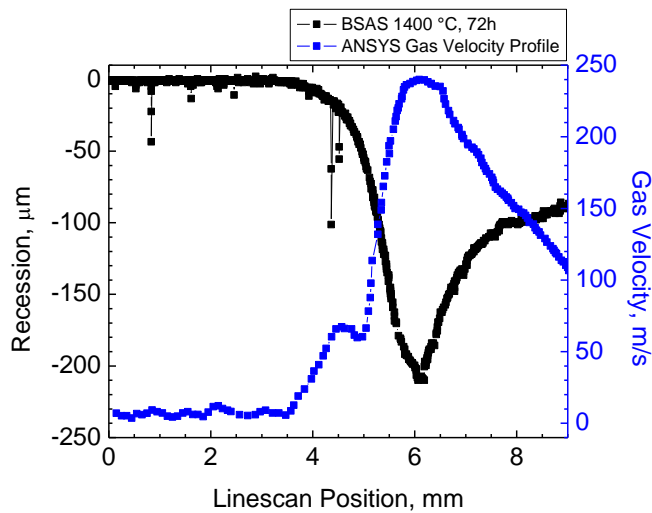


Figure 2-11. Comparison of the recession data from profilometry line scan of BSAS exposed to 1400 °C for 72h (black) compared to the computed gas velocity line scan for the same sample position (blue).

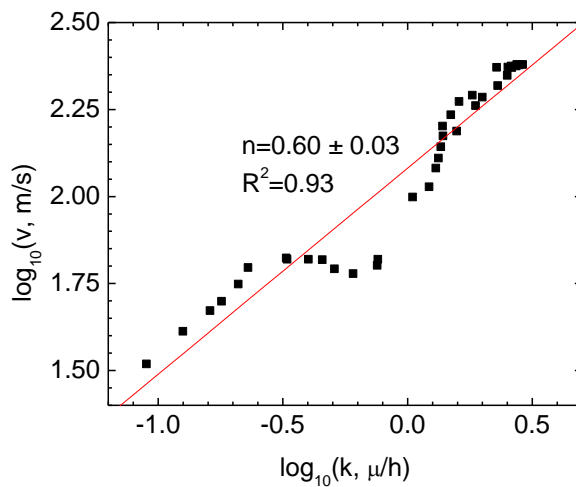


Figure 2-12. Gas velocity dependence on the linear reaction rate for BSAS after steam exposure for 72h at 1400 °C.

2.1.4.3. Temperature Dependence

While the linear reaction kinetics shown earlier are consistent with a surface reaction-controlled process, the presence of a gas velocity dependence on the reaction rate instead suggests a gas diffusion-controlled process. Gas-phase diffusion processes display linear reaction kinetics when the gas boundary layer diffusion distance maintains a constant thickness with time. An excess of H₂O (g) in the system implies that the diffusion of gaseous product species out of the boundary layer is rate-limiting rather than H₂O (g) diffusion inward to the sample interface. The reaction rate should therefore reflect both the temperature dependence from gas phase interdiffusion as well as an Arrhenius temperature dependence for formation of equilibrium partial pressures of metal hydroxide gaseous species.

A general relationship between the linear recession rates (k_l) and temperature (T) is shown in Equation 2-2. A $T^{3/2}$ dependence arises from gas phase molecular interdiffusion, and an Arrhenius temperature dependence is present from the chemical reaction process, where ΔH_{rxn} is the reaction enthalpy to form the product gas species and R is the universal gas constant. Thermodynamic equilibrium is assumed to be established at the high temperatures in this study, such that the reaction enthalpy term should not include an energy barrier for the reaction process.

$$k_l \propto \left[D_{1,2} \times \exp\left(-\frac{\Delta H_{rxn}}{RT}\right) \right] \propto T^{3/2} \exp\left(-\frac{\Delta H_{rxn}}{RT}\right) \quad 2-2$$

Temperature dependences are reported for the maximum recession rate data, as shown earlier in the time dependence of the BSAS-steam reaction. The reaction enthalpy can be calculated from the slope of the plot in Figure 2-13, where the y-axis is $\log(k_l/T^{3/2})$ and the x-axis is inverse temperature. The reaction enthalpy for BSAS recession in water vapor was 170 ± 13 kJ/mol. The temperature dependence determined from specific mass loss data was 143 ± 41 kJ/mol, although these data are not shown due to the high uncertainty from mass loss measurements.

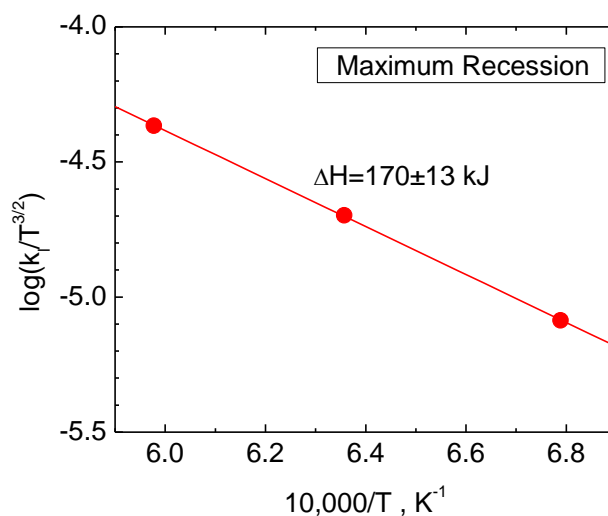


Figure 2-13. Temperature dependence of the maximum recession rates for the BSAS reaction with water vapor.

2.1.4.4. FactSage Calculations for the BaO-SrO-Al₂O₃-SiO₂ system

Oxide activities were computed from the FactSage SGPS and FTOxide thermodynamic databases for a solution of 75 mol. % BAS + 25 mol. % SAS. Given that both BAS and SAS are celsian structures in the temperature range of interest, it is assumed that changing the Ba/Sr ratio in BSAS should not induce major changes in the bond strengths beyond a linear approximation. Oxide activities calculated from a 75 mol. % BAS + 25 mol. % SAS solution are presented in Table 2-1. The predicted stable phases for the FactSage calculations at 1200 °C, 1300 °C, and 1400 °C were BaAl₂Si₂O₈ (BAS), SrAl₂Si₂O₈ (SAS), Al₂O₃, and SrAl₁₂O₁₉, although it was known through this work that the non-silicate SrAl₁₂O₁₉ compound was not expected to form as an equilibrium phase.

BSAS silica activity, $a(\text{SiO}_2)$, have been estimated previously to be <0.1 [12] and 0.01 [13]. FactSage data calculated in this work suggests that the $a(\text{SiO}_2) = 0.11$ at 1200 °C, which is slightly higher than values reported in the literature. For comparison, the $a(\text{SiO}_2)$ for the individual solutions of BAS and SAS at 1200 °C in equilibrium with Al₂O₃ were calculated to be 0.035 and 0.22, respectively. Activities of other constituent oxides in BSAS have not been previously reported in

the literature, although the volatility of Al₂O₃, BaO, and SrO as gaseous hydroxide species are shown to occur in this work. The BSAS mixture displayed equilibrium with Al₂O₃. BSAS should then behave similarly to pure alumina in combustion environments, which was proven by clear volatilization of Al₂O₃ in amounts comparable to that of SiO₂. The low activities for BaO and SrO reflect what was seen experimentally, where any product phase present on the surface was enriched in Ba and Sr and depleted in Al and Si.

Table 2-1. Oxide activities for the 75 mol. % BAS + 25 mol. % SAS solution using FTOxide and SGPS databases in FactSage.

75 mol. % BAS + 25 mol. % SAS = BSAS				
Temperature, °C	a(Al ₂ O ₃)	a(SiO ₂)	a(BaO)	a(SrO)
1200	1	0.11	6.7x10 ⁻⁸	3.7x10 ⁻⁶
1300	1	0.13	1.5x10 ⁻⁷	6.4x10 ⁻⁶
1400	1	0.15	2.9x10 ⁻⁷	1.0x10 ⁻⁵

The FactSage thermodynamic database was used to calculate the equilibrium partial pressures for hydroxide species formed from steam reaction with an ideal BSAS solution from the constituent oxides: BaO, SrO, Al₂O₃, SiO₂. Each oxide constituent undergoes the following reactions with high-temperature steam to produce a primary hydroxide species.

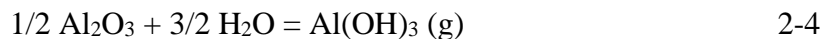


Figure 2-14 displays the equilibrium partial pressures for each primary metal hydroxide gas species produced from the BSAS oxide constituents. Molar concentrations of oxide species and water used for calculations were determined from Equations 2-3, 2-4, 2-5, and 2-6. All BSAS constituents volatilize as hydroxide species when in contact with high-temperature water vapor. The

temperature dependences for Ba(OH)_2 , Sr(OH)_2 , and Al(OH)_3 (g) are all shown to be greater than that of Si(OH)_4 (g).

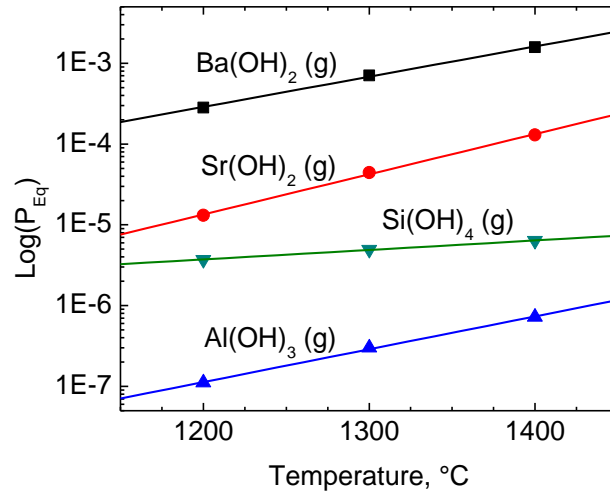
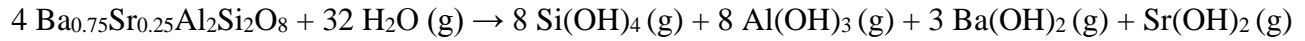


Figure 2-14. Equilibrium partial pressure dependences for BSAS constituent oxides, assuming ideal activities, reacting with water vapor for 1200 °C, 1300 °C, and 1400 °C.

2.1.5. Discussion

BSAS showed sample regions both with and without product phases after exposure to high velocity steam, which agrees with the literature [14], [24]. The product phase, when present, is strontium enriched and silica depleted in composition, which is similar to observations by More et al. [24]. The product phase is present as nonprotective nodules. It is likely that this product phase is related to the unmatched peaks present on the BSAS samples after water vapor exposures at 1200 °C. At higher temperatures and velocities, the product phase is not present, indicating full volatilization of all BSAS constituent oxides, consistent with results of Lee, Fox, and Bansal [14]. Based on the results of this study, a stoichiometric chemical reaction between BSAS and water vapor that assumes the activities of all oxide constituents are ideal is proposed as Equation 2-7.



2-7

Each metal hydroxide species formed, yet they have differing thermodynamic stabilities. Thus, there should be reactive environments where a product phase was enriched in the least volatile species. The 1200 °C steam test environment in this study and the 1200 °C steam test environment from More et al. [24] both show a strontium-rich product phase, suggesting that SrO is the least volatile oxide out of the BSAS constituents at this temperature, in agreement with the low $a(\text{SrO})$ calculated in Table 2-1.

A linear time dependence for the BSAS reaction in water vapor was seen for both the specific mass change and for the maximum recession points from profilometry data. Given that the time dependence for the reaction was also linear at 1200 °C where the product phase nodules are present, it was concluded that the nodules are not protective and do not contribute to changes in time or temperature dependences with temperature. An expected velocity dependence was displayed in Figure 2-10 and Figure 2-12, which validated that gas phase diffusion plays an important role as the rate-limiting mechanism for the water vapor reaction with BSAS.

Lee, Fox, and Bansal performed the earliest kinetic study on BSAS using thermogravimetric analysis (TGA) experiments [12]. The TGA mass loss rates for BSAS in low velocity steam are presented in Table 2-2 along with a conversion of data from this study to the TGA conditions for comparison. Equation 2-1 was used to convert the BSAS recession rates measured in this study to the gas velocity, water vapor pressure, and total pressure of the TGA environment by Lee et al. The gas velocity exponent $n=0.60 \pm 0.03$ and water vapor partial pressure exponent of $m=1.6$ were used for Equation 2-1. The exponent of 1.6 for the water vapor partial pressure arises from Equation 2-7, where 32 moles of water are required to create 20 moles of metal hydroxide species. The calculated

recession rates ($\mu\text{m/h}$) for the new environment were then converted to mass loss rates ($\text{mg/cm}^2\text{h}$) using the theoretical density of BSAS and the relative density for the starting material. Converted values from this study were only 2.5 times larger than those measured by TGA, which was deemed in fair agreement. Using the 1300 °C and 1400 °C TGA reaction rates from Lee. et al., a reaction enthalpy of 169 kJ/mol was calculated as part of this work. Lee et al. also performed TGA experiments on BSAS at 1500 °C, although the reaction rate at 1500 °C did not follow a linear fit with the results from 1300 °C and 1400 °C and therefore was not used in the comparison for this work. The change in temperature dependence at 1500 °C in their work may represent a change in the reaction products at higher temperatures where other hydroxide species become important for consideration, such as $\text{SiO}(\text{OH})_2$ (g). While this value was only derived from two temperatures, it is in agreement with the reaction enthalpy value measured in this study for 1200 °C-1400 °C temperature range (170 ± 13 kJ/mol, Figure 2-13).

Table 2-2. Comparison of BSAS reaction rates in steam with literature results. Recession rates from this study were first converted to TGA conditions in the literature study, and then converted to mass loss rates ($\text{mg/cm}^2\text{h}$) from recession rates ($\mu\text{m/h}$). A gas velocity dependence of $n=0.6$ using Eq. 2 and water vapor partial pressure dependence of $m=1.6$ were used for the conversions.

	TGA Conditions [12]		This study, Steamjet Conditions	
Temperature, °C	1300	1400	1300	1400
Gas Velocity, m/s	4.40×10^{-2}	4.40×10^{-2}	230	239
P(H_2O), atm	0.5	0.5	1	1
P total, atm	1	1	1	1
	TGA BSAS Reaction Rates [12]		This study, Steamjet BSAS Maximum Recession Rates Converted to Mass Loss Rates for the TGA Conditions	
Mass loss rates, $\text{mg/cm}^2\text{h}$	2.4×10^{-4}	5.7×10^{-4}	6.11×10^{-4}	1.4×10^{-3}

The gaseous phases produced from the BSAS-steam reaction process were continuously flushed out of the system. Therefore, a concentration gradient of gaseous product species was

established for each steam exposure. The sum of the equilibrium partial pressures of gaseous product species should then be proportional to the linear rate constant, as shown in Equation 2-8.

$$\Sigma P_{eq} \propto \frac{k_l}{T^2} \quad 2-8$$

The log of the summation of the equilibrium partial pressures of the species is plotted in Figure 2-15 to represent the temperature dependence of an ideal BSAS solution from steam reaction with the constituent oxides (BaO, SrO, Al₂O₃, SiO₂). In a similar manner as Figure 2-13, the slope of this plot represents the reaction enthalpy for the ideal solution. The experimentally determined reaction enthalpy from this work (170±13 kJ/mol) is in agreement with the reaction enthalpy calculated from an ideal BSAS solution in FactSage (175 kJ/mol) and with the value determined from work by Lee et al. at 1300 °C and 1400 °C (169 kJ/mol). Experimental agreement with both literature and FactSage calculations suggest that the rate-limiting mechanism for the reaction of BSAS with water vapor is consistent with the volatilization of all constituent oxides as metal hydroxide gas species given by Equation 2-9. This is in agreement with the lack of product phase seen on the BSAS surfaces after steam exposure.

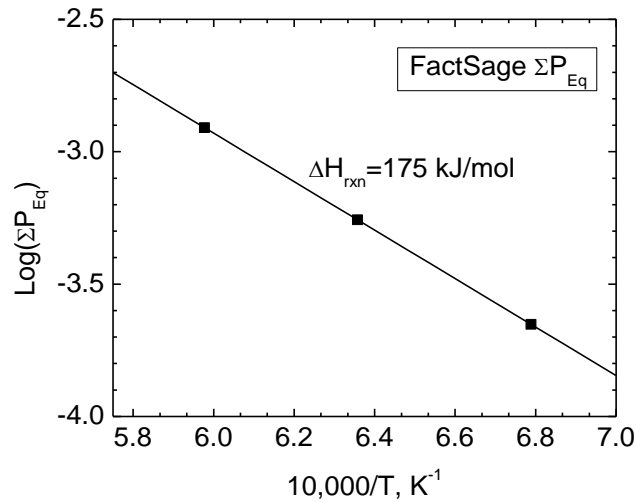


Figure 2-15. Temperature dependence for the summation of the equilibrium partial pressures of the product hydroxide gas species. Partial pressures were calculated with FactSage assuming an ideal solution from steam reaction for the constituent oxides (BaO, SrO, Al₂O₃, SiO₂) and can be seen in Figure 2-14.

2.1.6. Conclusions

A high velocity steamjet furnace was utilized to assess microstructural evolution and the rate limiting mechanism for steam degradation of BSAS. After steam exposures at 1200 °C, a silica-depleted and strontium enriched product phase was seen on the surface as nonprotective nodules. The product phase decreases in concentration with increasing temperature, resulting in volatilization of all BSAS constituent oxides. Linear steam reaction kinetics were reported for the temperature range of 1200 °C-1400 °C. A reaction enthalpy of 170 ± 13 kJ/mol was determined for the maximum recession data. While a fully assessed thermodynamic database was not available for BSAS, the FactSage thermodynamic database was used to estimate oxide activities from a 75 mol. % BAS + 25 mol. % SAS solution. Hydroxide partial pressures calculated from an ideal solution of the constituent oxides (BaO, SrO, Al₂O₃, and SiO₂) were shown to validate the experimental portion of this work. The mechanism for BSAS volatility in steam was proposed to be through volatilization of all constituent oxides (BaO, SrO, Al₂O₃, and SiO₂) as metal hydroxide gas species: Ba(OH)₂,

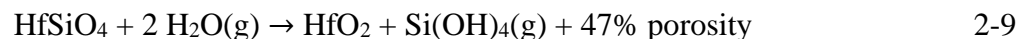
$\text{Sr}(\text{OH})_2$, $\text{Al}(\text{OH})_3$, and $\text{Si}(\text{OH})_4$. EBC systems should thus contain at least one constituent oxide that is not volatile in combustion environments to provide additional environmental protection and increase coating lifetime.

2.2. Thermomechanical and Thermochemical Stability of HfSiO₄ for Environmental Barrier Coating Applications

2.2.1. Introduction

HfSiO₄ is a proposed EBC candidate due to its relatively high decomposition temperature of 1750 °C and low oxygen diffusivity [31]. HfSiO₄ displays a CTE match with SiC and the silicon bond coat (4.5-5.5 x10⁻⁶ / °C for SiC [3], and 3.5-4.5x10⁻⁶ / °C for silicon [32]). The low CTE of hafnium has been measured in prior studies via dilatometry to be 3.6x10⁻⁶ / °C [33] or 4.17 x10⁻⁶ / °C [34], which provides an average CTE value without information on anisotropy. The importance of CTE anisotropy is demonstrated specifically for rare earth monosilicate EBC candidates, where large degrees of CTE anisotropy result in internal stress buildup with cracking and material spallation during thermal cycling [35]. The CTE anisotropy of HfSiO₄ has not yet been investigated in the literature.

HfSiO₄ represents the only line compound on the HfO₂-SiO₂ phase diagram, which simplifies the number of possible products that can form within a steam environment [36]. Equation 2-9 displays the predicted reaction between HfSiO₄ and water vapor to form the HfO₂ and a silicon hydroxide gas species. The crystal structures of the reactant phase, HfSiO₄ (tetragonal), and product phase, HfO₂ (monoclinic), are shown in Figure 2-16.



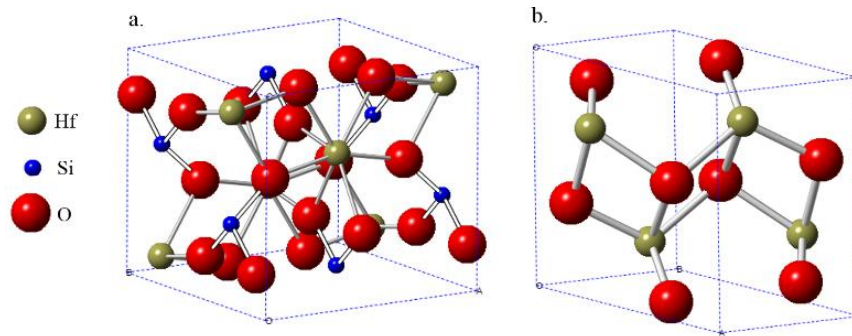


Figure 2-16. a. Tetragonal HfSiO₄ [37] and b. monoclinic HfO₂ [38] crystal structures.

Similarities in properties and chemical behavior of ZrSiO₄ and HfSiO₄ allow for qualitative comparison between the two systems. Burner rig testing on multi-phase ZrSiO₄ (73 wt.% ZrSiO₄, 25 wt.% ZrO₂, 2 wt.% SiO₂) and single phase ZrO₂ samples was performed from 1300-1500 °C for 130-300 hours under 100 m/s gas stream velocity [39]. ZrSiO₄ showed linear reaction kinetics from mass changes upon steam exposures, representative of either a gas diffusion-controlled process by a constant diffusion distance as was seen for BSAS, or of a surface reaction-controlled process. Burner rig testing of bulk ZrO₂ showed no reaction process and no measurable weight change after testing [39], suggesting porous ZrO₂ should remain present on the surface after steam exposures. Extensive cracking from a monoclinic to tetragonal phase transition of ZrO₂ at 1170 °C prevents ZrSiO₄ from being a reliable EBC candidate [40]. The same phase transformation for HfO₂ occurs around 1750 °C, which is above the use temperatures of interest [41]. HfSiO₄ is therefore considered a more viable EBC candidate than ZrSiO₄.

Researchers tested bulk Zr_{0.4}Hf_{0.6}SiO₄ in a stagnant steam environment of P(H₂O)= 0.47 atm at 1300 °C for 100 hours [33]. It was stated that minimal reaction occurred during testing and that a -0.07% weight change was measured after testing. During steam testing, the density of the samples increased and the porosity decreased, suggesting that sintering occurred during testing, which may have impacted the results. Ueno et al. tested HfSiO₄ in a stagnant environment with 30 wt. % steam for 50-100 hours at 1500 °C and found a linear weight loss rate of 7.08 x10⁻⁶ g/cm² h, where silica

was being depleted from the system [42]. From their results, bulk HfSiO₄ showed greater steam resistance than the state-of-the-art EBC Yb₂Si₂O₇ (7.5 x10⁻⁶ g/cm² h). Additionally, Ueno tested Si₃N₄ coated with various EBC candidates under similar conditions as their bulk silicate testing previously mentioned and found that Si₃N₄ coated with HfSiO₄ showed weight gain rates less than half of Si₃N₄ samples coated with Yb₂Si₂O₇. The weight gain of the coated Si₃N₄ coupons comes from oxidation of the Si₃N₄ substrate to form a SiO₂ scale [17]. The results point to HfSiO₄ being a more effective oxygen barrier than rare earth silicates such as Yb₂Si₂O₇, which further drives the need to confirm the chemical stability of HfSiO₄ in a fully saturated steam environment where velocities more closely resemble turbine operation.

This work explored the value of hafnon as an EBC candidate in hot section turbine applications. The degree of CTE anisotropy of HfSiO₄ was measured up to 1200 °C via *in situ* X-ray diffraction. Additionally, the microstructural stability of HfSiO₄ in high velocity water vapor was characterized after exposure at 1200 °C, 1300 °C, and 1400 °C for 60, 125, and 250 hours.

2.2.2. Methods

2.2.2.1. Processing and Characterization

The purity of the starting HfSiO₄ powder (Praxair: Danbury, CT) was verified with a Panalytical Empyrean X-ray diffractometer (Westborough, MA) and characterized with X'Pert High Score Plus software to find unit cell parameters and phases present. Starting HfSiO₄ powder showed 6-8% HfO₂ content with no additional phases detected by XRD or energy dispersive spectroscopy (EDS).

The powder was dry ball milled for 24 hours with yttria stabilized zirconia milling beads. Fine powders were loaded into a 20 mm diameter graphite die and consolidated in argon by spark

plasma sintering (SPS) using a Thermal Technologies DCS 25-10 SPS (Santa Rosa, CA). The SPS process utilized a 20-minute hold at a maximum temperature and pressure of 1600 °C and 65 MPa. After SPS, samples were annealed for 24 hours at 1200 °C in air to remove residual carbon and restore oxygen stoichiometry. Resulting pucks were sectioned into test coupons with dimensions ~10x10x1mm. Figure 2-17 shows the final microstructure after processing. The backscattered electron (BSE) image shows atomic number contrast between HfSiO₄ (dark grey) and HfO₂ particulate (white).

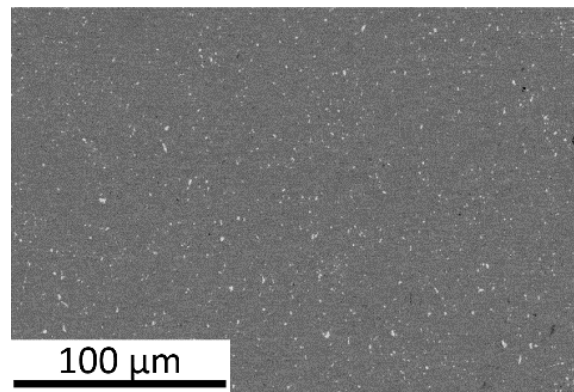


Figure 2-17. Backscattered electron image of bulk HfSiO₄ with white particulate HfO₂ inclusions.

2.2.2.2. High-temperature XRD

CTE was measured from the unit cell expansion by high-temperature XRD with an Anton Paar HTK 1200N non-ambient stage (Graz, Austria). Measurements were made in air at 100 °C increments upon heating from room temperature up to 1200 °C with a 60 °C/min heating rate. Rietveld refinements were used in HighScore Plus software to determine the unit cell parameter changes with temperature so that the CTE of each unit cell axis could be calculated.

2.2.2.3. High Velocity Steamjet

The steamjet setup was described in Chapter 2.1.2.2. Specific mass change was determined for each specimen to correlate with average silica depletion as a function of exposure time.

Uncertainty in reported specific mass change includes ± 0.05 mg in mass measurement (MS105DU, Mettler-Toledo, Columbus, OH), as well as ± 0.5 mm for sample dimension measurement. XRD and SEM were used to characterize reaction products and microstructure changes. Following surface imaging, samples were mounted in epoxy, polished to 1 micron with diamond suspension, and cross-sectioned for SEM imaging to measure the silica depletion depths into the samples. The silica depletion depth (HfO_2 thickness) was measured and averaged across the sample cross-sections using ImageJ analysis suite to relate depletion depths to exposure times, temperatures, and steam velocities. The 1200 °C test sample data utilized average statistics of ~ 35 measurements per sample with ~ 65 microns spacing in measurements. For all 1300 °C and 1400 °C samples, average statistics of ~ 75 measurements per sample with ~ 85 micron spacing between measurements were used.

2.2.3. Results

2.2.3.1. Thermal Expansion and Thermal Expansion Anisotropy

Figure 2-18 shows the results of refinements of the XRD data for each temperature. The normalized unit cell dimensions show that the unit cell is expanding uniformly over the entire temperature range. The HfSiO_4 crystal structure is tetragonal where the a-axis is equal to the b-axis. The CTE of each unit cell axis was calculated with a reference temperature of 25 °C. Linear CTE is calculated from Equation 2-10 where ΔV is the unit cell volume change, V is the initial unit cell volume, and ΔT is the temperature change. Equation 2-10 represents the average CTE over directions a, b, and c.

$$CTE = \frac{1}{3} \frac{\Delta V}{V \Delta T} \quad 2-10$$

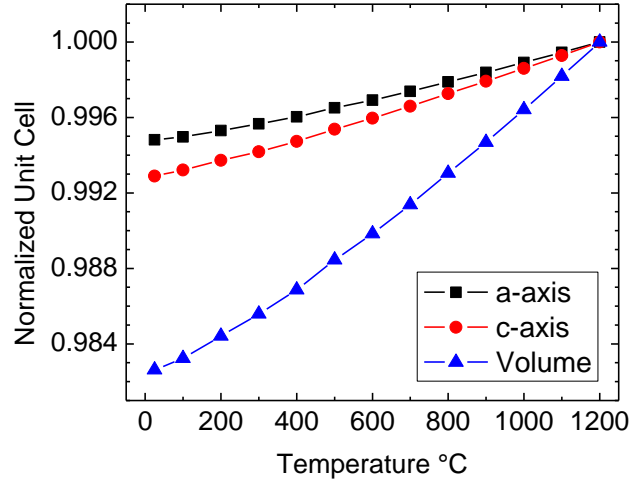


Figure 2-18. Normalized $HfSiO_4$ unit cell parameters from XRD data.

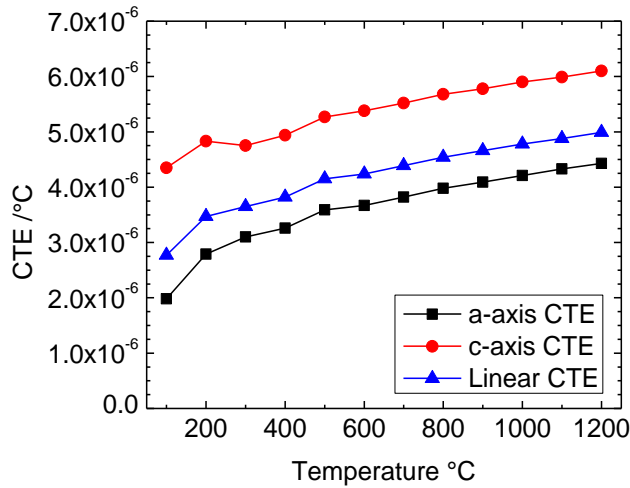


Figure 2-19. CTE calculations from hot stage XRD unit cell refinement for $HfSiO_4$.

The CTE of the a- and c-axes, as well as the linear CTE, are shown in Figure 2-19. The average linear CTE of $HfSiO_4$ from 100-1200 °C is $4.19 \times 10^{-6} / ^\circ C$, which is in agreement with literature values [33]. A difference of $\sim 2 \times 10^{-6} / ^\circ C$ is seen between the a- and c-axis CTEs. Both axes generally show limited CTE mismatch with SiC and a silicon bond coat, which should not result in major stress buildup upon thermal cycling. The limited CTE mismatch and CTE anisotropy support the idea that $HfSiO_4$ is a viable EBC candidate from a thermomechanical standpoint.

2.2.3.2. X-ray Diffraction of Steam Reaction Layer

Representative ambient XRD data from the sample face after steam exposure are shown in Figure 2-20. Each XRD pattern represents a sample exposed for 60 hours at either 1200, 1300, or 1400 °C. HfSiO_4 readily forms HfO_2 at 1200 °C for 60 hours of exposure to high-velocity steam. The HfSiO_4 peaks are almost entirely hidden at temperatures above 1200 °C which demonstrates the rapid reaction of HfSiO_4 with water vapor to form HfO_2 . XRD and SEM/EDS analysis show that no other product phases form during experiments.

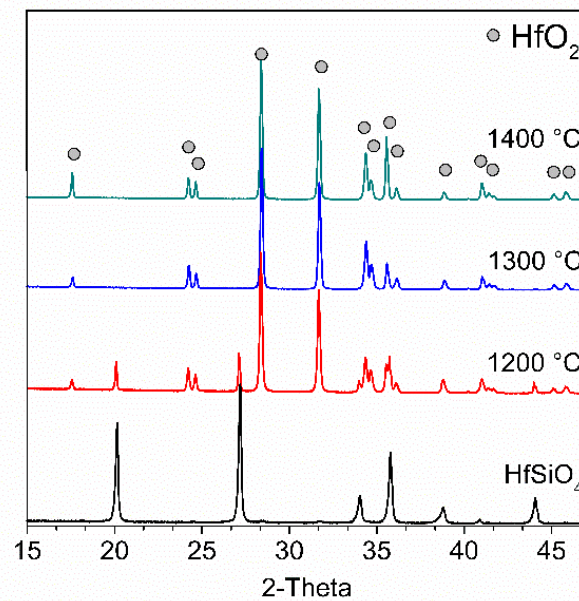


Figure 2-20. XRD of HfSiO_4 samples after 60 hours of steam exposure.

2.2.3.3. Plan View SEM of Steam Reaction Layer

Figure 2-21 shows representative surface microstructures of samples exposed at 1400 °C for 60, 125, and 250 hours. Shown images correlate to a position 3-4 mm downstream from the impingement site with the ANSYS model predicting a velocity of 90 – 120 m/s at this location on the samples. The porous HfO_2 product layer shows ~30% porosity by area fraction, which is lower than the predicted 47% volume change in Equation 2-9. Slight coarsening of the HfO_2 grains can be

seen with an increase in time and temperature, but due to the high melting temperature of HfO_2 , the microstructure is stable and generally consistent across all samples.

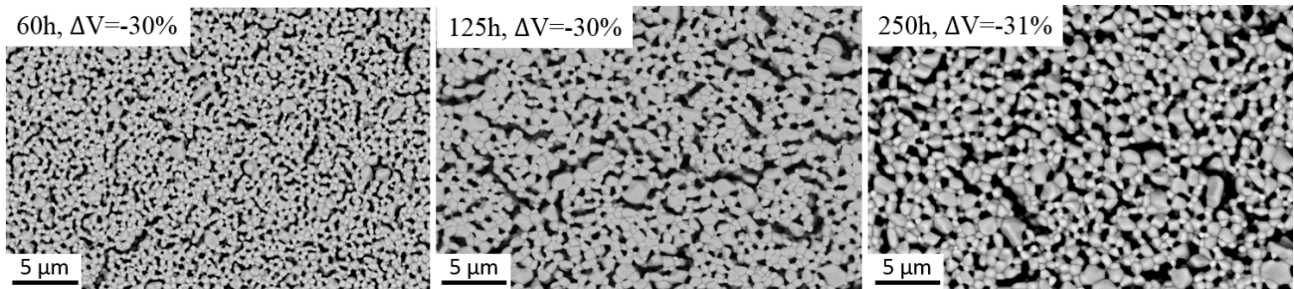


Figure 2-21. Representative backscatter SEM plan view images of HfSiO_4 samples after steam exposures of 60, 125, and 250 hours at 1400 °C with local gas velocity of 90-120 m/s. The area fraction of porosity is given on each image. Images show the porous HfO_2 product from the steam interaction with HfSiO_4 .

A unique morphology was observed for the HfO_2 reaction product at sample edges where the gas velocity was near stagnant. Figure 2-22 displays the HfSiO_4 surface under the platinum foil sample holder after exposure to steam for 250 hours at 1300 °C. The HfO_2 reaction product under the given conditions was present as dense clusters surrounded by fine porosity, where the grain size of HfO_2 was much larger than that of the original HfSiO_4 material. The unique reaction microstructure at low gas velocities implied that a different reaction mechanism may be occurring at near stagnant gas velocities compared to high-velocity regions of interest.

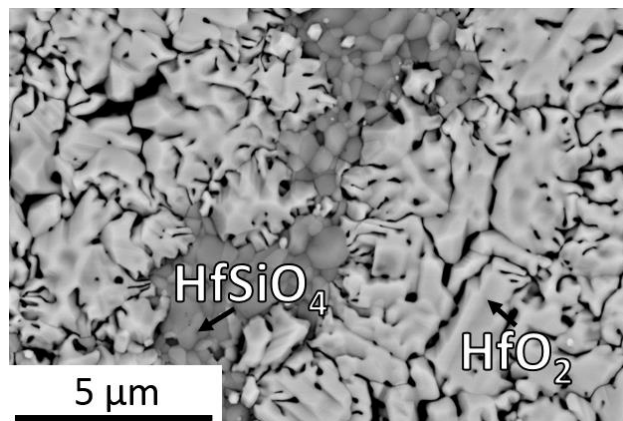


Figure 2-22. SEM of HfSiO_4 after steam exposure for 250 hours at 1300 °C in the stagnant gas velocity region under the platinum foil sample holder.

2.2.3.4. Cross-section SEM of Steam Reaction Layer

Cross-section images of samples exposed for 125-hours at each temperature in Figure 2-23 show the silica depleted HfO_2 layer on the surface of the exposed samples. A minor dependence of the SiO_2 depletion depth on gas velocity was seen across the sample cross-sections and was only prominent in regions of the sample where velocities were below 80 m/s. For all exposed samples, the depletion depth increased with increasing time and temperature. Minor coarsening was the only microstructural change seen from the reaction front at the HfSiO_4 - HfO_2 interface to the HfO_2 -gas surface, best seen in Figure 2-23c.

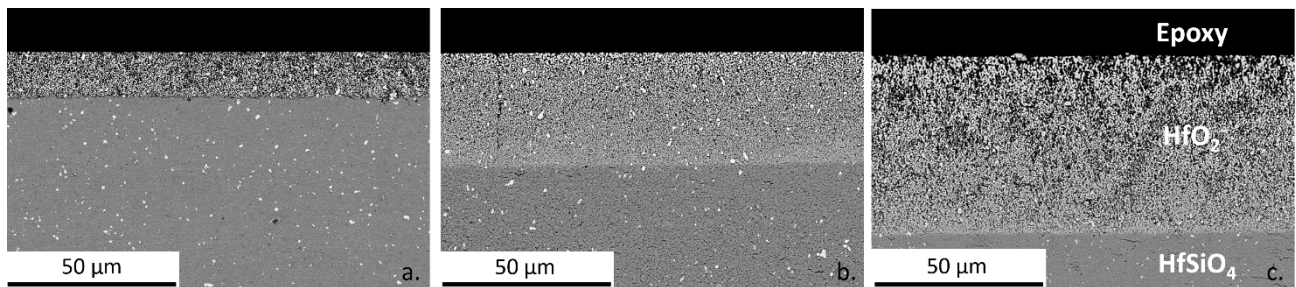


Figure 2-23. Representative cross-section SEM images of HfSiO_4 after 125-hour steamjet exposures (velocity 125 -150 m/s) for a. 1200 °C, b. 1300 °C, and c. 1400 °C.

2.2.3.5. Specimen Extended Cross-section

Figure 2-24 shows the low magnification plan view SEM of the high-velocity steam impingement site for HfSiO_4 samples exposed at 1200 °C and 1400 °C for 250 hours. Excessive cracking near the highest velocity impingement site (~190-250 m/s) of the sample exposed at 1400 °C led to surface charging under the electron beam. Clear material loss was seen for all samples in this region. Figure 2-25 shows extended SEM images of the same samples in cross section through the highest velocity impingement site. The HfO_2 layer did not show dramatic microstructural changes or further reaction with changes in gas stream velocity, until near the impingement site (>190 m/s) where a large amount of material loss is seen. This material loss is attributed to mechanical erosion by high velocity steam and occasional residual liquid water droplets. Average

mechanical erosion depths of 105 μm and 537 μm were measured at the impingement sites for HfSiO_4 samples after steam exposure for 250 hours at 1200 $^\circ\text{C}$ and 1400 $^\circ\text{C}$, respectively. Material loss was prevalent from the high pore concentration in the HfO_2 product layer and minimal sintering, allowing for mechanical erosion at these high steam velocities. HfO_2 product formed along cracks that occurred during testing, while cracks without any reaction product were assumed to occur upon sample removal from the tube furnace.

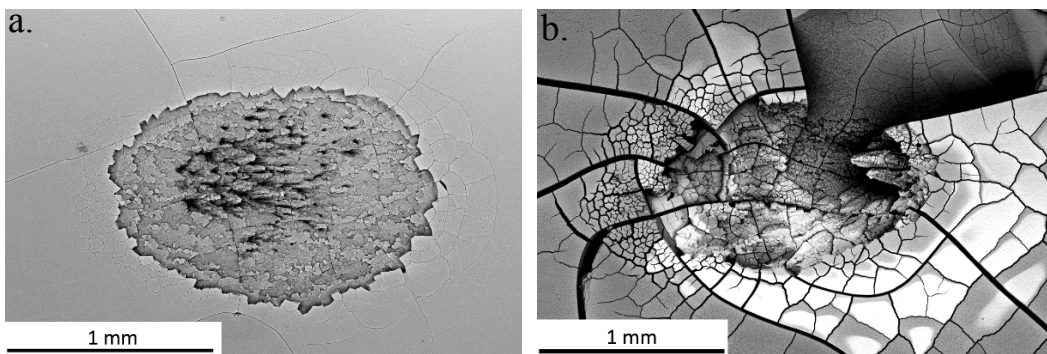


Figure 2-24. Steam impingement site of HfSiO_4 exposed to steam for 250 hours ($v=150\text{-}250$ m/s) at a. 1200 $^\circ\text{C}$ and b. 1400 $^\circ\text{C}$.

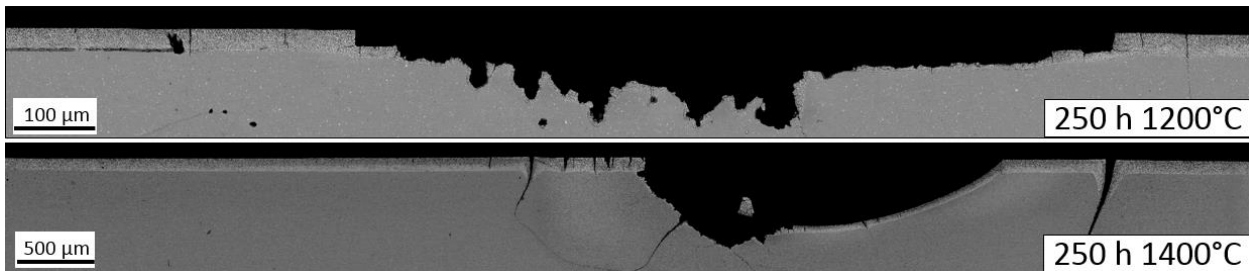


Figure 2-25. Stitched cross-section SEM images showing the silica depletion layer below 190 m/s and the large amounts of mechanical erosion at the impingement site where steam velocities exceed 190 m/s. The erosion depth at the impingement site averaged 105 μm after 250 hours at 1200 $^\circ\text{C}$ (100 μm scale bar) and 537 μm after 250 hours at 1400 $^\circ\text{C}$ (500 μm scale bar).

2.2.3.6. Time and Temperature Dependences

Mass change data for calculating average reaction kinetics in high velocity steam were considered semi-quantitative due to varied water vapor velocity across the sample face, impurity uptake on sample edges, and mechanical erosion at the impingement site that all also contribute to mass changes with time and temperature. Mass change data for the exposed samples are shown for

each temperature in Figure 2-26. The linear slope fit to specific mass loss versus the square root of time demonstrates parabolic kinetics, indicative of a diffusion-controlled process. Extrapolation of the best fit lines for each temperature intersects the x-axis at times between 4-12 hours.

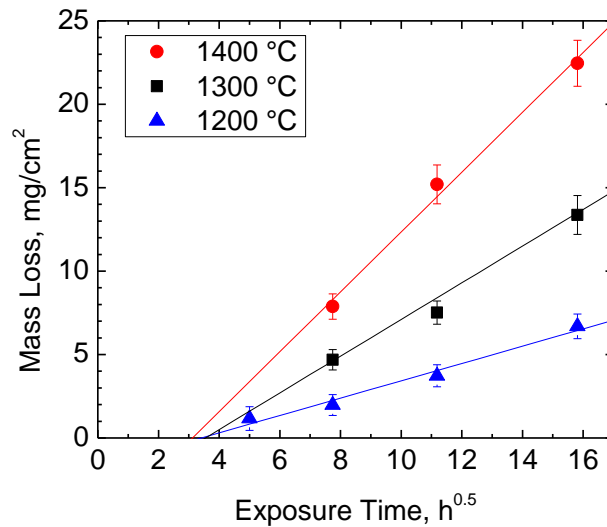


Figure 2-26. $HfSiO_4$ specific mass loss (mg/cm^2) plotted against square root of time.

Figure 2-27 shows parabolic kinetics of the measured average silica depletion depth, or HfO_2 oxide layer thickness, for intermediate velocity regions of 90-180 m/s. The extrapolated best fit lines for 1200 °C and 1400 °C data intercept the x axis around 4-16 hours for both the specific mass loss and average silica depletion plots. This time range represents an incubation period for parabolic kinetics to control the reaction process and may be related to nucleation of the HfO_2 product phase across the entire sample coupon. Parabolic rate constants representing both mass change and the silica depletion rates were calculated from the square of the best fit lines for each testing temperature and are shown in Table 2-3.

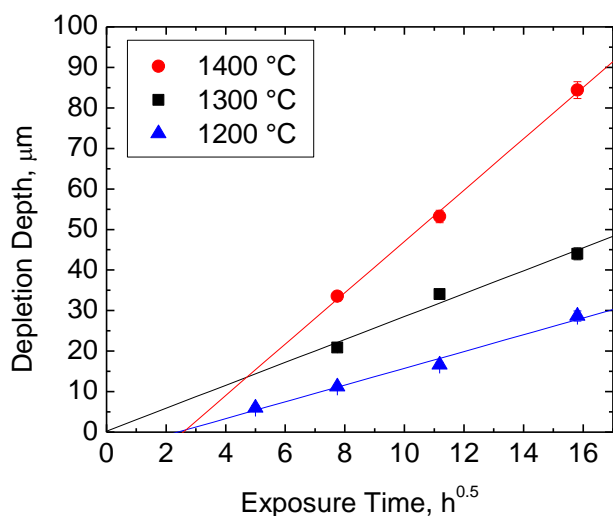


Figure 2-27. Average SiO₂ depletion depth for HfSiO₄ for intermediate velocity regions of 90-180 m/s plotted against square root of time.

Table 2-3. Parabolic rates and calculated activation energies for HfSiO₄ reaction with steam.

Temperature (°C)	Mass Change k _p (mg ² /cm ⁴ h)	Reaction	Depletion Depth k _p (μm ² /h)	Reaction
		Enthalpy (kJ/mol)		Enthalpy (kJ/mol)
1200	2.70 ± 0.03 x10 ⁻¹	235 ± 15	4.3 ± 0.9	207 ± 39
1300	1.15 ± 0.01		8.0 ± 0.2	
1400	3.22 ± 0.02		40.1 ± 0.3	

A velocity dependence for the reaction rate was seen, especially at velocities below 80 m/s, indicating gas phase diffusion limits the reaction rather than solid-state transport. Gas transport can occur by two steps in the reaction process: 1. water vapor transport to the HfO₂/HfSiO₄ interface and 2. product gas species (i.e. Si(OH)₄) diffusing outward through the porous HfO₂. Saturation of the system with water vapor implies that outward diffusion of a product gas species such as Si(OH)₄ (g) is more likely rate-limiting.

Outward diffusion of product gas species will show a $T^{3/2}$ temperature dependence from gas phase interdiffusion through the boundary layer [43], [44] as well as an Arrhenius temperature dependence from the equilibrium chemical reaction process. A general relationship between the parabolic reaction rates and temperature is shown in Equation 2-11, where k_p is the parabolic rate constant for thickening of the porous HfO_2 layer, $D_{1,2}$ is gas interdiffusion of $\text{Si}(\text{OH})_4$ (g) and H_2O (g), ΔH_{Rxn} is the reaction enthalpy, R is the universal gas constant, and T is temperature.

$$k_p \propto \left[D_{1,2} \times \exp\left(-\frac{\Delta H_{\text{rxn}}}{RT}\right) \right] \propto T^{\frac{3}{2}} \exp\left(-\frac{\Delta H_{\text{rxn}}}{RT}\right) \quad 2-11$$

By dividing the parabolic rate by the temperature dependence from gas phase diffusion, any exponential dependence can be revealed. Figure 2-28 shows the log of the depletion rate divided by $T^{3/2}$, plotted against inverse temperature.

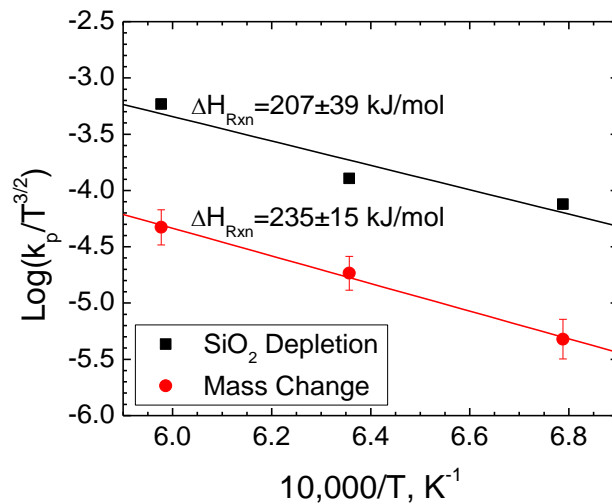


Figure 2-28. Log of the parabolic depletion rates and mass change rate divided by gas phase diffusion temperature dependence is plotted against inverse temperature to show the exponential temperature dependence of the HfSiO_4 reaction with water vapor to form HfO_2 .

The slopes were used to determine a reaction enthalpy of 207 ± 39 kJ/mol for the silica depletion of HfSiO_4 exposed to high-velocity steam, based on the chemical reaction provided in Equation 2-9. It was assumed that thermodynamic equilibrium was established for the system at

these high temperatures. The reaction enthalpy from mass loss was deemed less reliable due to the varied gas velocities across the sample face, impurity uptake on sample edges outside of the water vapor stream, and mechanical erosion at the highest velocity regions.

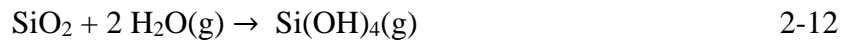
2.2.4. Discussion

The high-temperature XRD of bulk HfSiO_4 from room temperature to 1200 °C showed a low linear CTE that agreed well with literature dilatometer measurements. Hot stage XRD allowed for verification of minimal CTE anisotropy between the a=b and c axes. The thermomechanical results suggest HfSiO_4 is an acceptable EBC candidate due to its lack of CTE anisotropy and limited CTE mismatch with structural CMCs, a silicon bond coat, and SiO_2 thermally grown oxide.

Thermochemical interaction of HfSiO_4 with steam (Equation 2-9) predicted a theoretical 47% volume reduction from the HfSiO_4 and HfO_2 crystal structures. Through SEM imaging of the samples after exposure, only ~30% porosity formation was observed. It was unclear as to why the experimental porosity formation was not as high as that predicted from the unit cell molar volumes. Due to the high melting temperature of HfO_2 at 2758 °C [36], the product layer did not sinter or undergo substantial grain growth even at 1400 °C for 250 hours steam exposure. Above 1400 °C, there remains a possibility that microstructural changes in the HfO_2 product layer, such as sintering and densification, could further enhance the protective nature of HfSiO_4 . The porous product layer provided only a small amount of protection to HfSiO_4 by increasing the diffusion distance of gaseous species to and from the sample interface, as seen by the parabolic mass loss and depletion depths for all exposure temperatures. Figure 2-27 showed that 1400 °C steam testing resulted in large depletion depths, with the 250-hour water vapor exposure showing an average depletion depth near 85 μm . Typical environmental barrier coating thicknesses are on the order of 100-400 μm , which suggest that HfSiO_4 would not be a protective coating for extended periods of time. At the

highest velocities, >190 m/s, HfSiO₄ experienced mechanical erosion from high-velocity steam impingement upon the sample. HfSiO₄ exposed for 250 hours at 1400 °C displayed a mechanical erosion depth of 537 μm, greater than typical EBC coating thicknesses. Both high-velocity erosion of the porous HfO₂ product layer and high-temperature steam interaction suggest that HfSiO₄ is not a suitable EBC candidate for long term hot section turbine coating applications.

The depletion rates were used to approximate a reaction enthalpy of 207 ± 39 kJ/mol for the reaction shown in Eq. 2-9. Calculated enthalpies for the reaction of pure SiO₂ with water vapor, shown in Eq. 2-12,



range from 40 kJ/mol [45] to 75 kJ/mol [7], which are significantly lower values than reaction enthalpies determined from this work. FactSage calculations have been made using the SGPS database and thermodynamic data in the literature to estimate a reaction enthalpy of 56 kJ/mol for the SiO₂ reaction with water vapor to form Si(OH)₄ (g) [22]. Using thermodynamic data available for zircon, ZrSiO₄, the temperature dependence for the ZrSiO₄/H₂O(g) reaction was calculated to be 85 kJ/mol for Si(OH)₄ (g) formation and 342 kJ/mol for SiO(OH)₂ (g) formation [46]. Data from O'Neil et al. [47] were input into FactSage thermodynamic reaction module to calculate the temperature dependence for HfSiO₄/H₂O(g) reaction to be 56 kJ/mol for Si(OH)₄ (g) formation and 314 kJ/mol for SiO(OH)₂ (g) formation. The chemical reactions and reaction enthalpies are listed in Table 2-4. Jacobson et al. found that SiO(OH)₂ (g) becomes an important secondary reaction product in SiO₂/H₂O transpiration studies above 1300°C [45], yet SiO(OH)₂ (g) formation was predicted by FactSage calculations to be at least an order of magnitude lower in concentration compared to Si(OH)₄ (g) at 1300 °C.

Table 2-4. Chemical reactions and reaction enthalpies for the two primary silicon hydroxide gaseous species formed during silicate reaction with water vapor. Data calculated from FactSage databases SGPS and HfSiO₄ data [47], liquids suppressed.

Chemical Reaction		Reaction Enthalpy, kJ/mol
1	$\text{HfSiO}_4 + 2\text{H}_2\text{O}(\text{g}) = \text{HfO}_2 + \text{Si}(\text{OH})_4(\text{g})$	56
2	$\text{HfSiO}_4 + \text{H}_2\text{O}(\text{g}) = \text{HfO}_2 + \text{SiO}(\text{OH})_2(\text{g})$	314

The combined impact of multiple hydroxide gaseous species may be contributing to the high reaction enthalpy determined through high-velocity steam testing in this work, although this hypothesis could not be validated with the limited available thermodynamic data. While the gas product composition could not be verified, the kinetic trends did show that the rate-controlling mechanism was best explained by product gas species diffusing outward from the reaction interface upon steam reaction. The presence of a highly porous HfO₂ layer on HfSiO₄ may contribute to the difference in reaction enthalpies from those of pure SiO₂ that undergo complete volatilization with no product phase. Future work will attempt to further elucidate the rate controlling mechanism for SiO₂ depletion for silicate EBCs to provide new insight towards life prediction and development of coatings for SiC/SiC CMCs with improved protection.

2.2.5. Conclusions

High-temperature thermomechanical and thermochemical properties were evaluated for EBC candidate HfSiO₄. Hot stage XRD verified the minimal CTE mismatch of HfSiO₄ with SiC and a silicon bond coat for CMCs. Minor CTE anisotropy was displayed up to 1200 °C, suggesting limited internal stress buildup during thermal cycling. Chemical stability of HfSiO₄ was determined through high-temperature high-velocity water vapor exposures in a fully saturated steam environment. The samples formed porous HfO₂ as a stable product for testing from 1200 to 1400 °C and exposure times up to 250 hours. The time dependence of the reaction

is parabolic in nature, indicative of a diffusion-controlled reaction process. An observed velocity dependence and exponential temperature dependence for the reaction suggests formation of silicon hydroxide gas with outward diffusion through the porous product layer best explains the rate-limiting step in the reaction process. High-temperature high-velocity steam testing shows excessive reaction rates at gas velocities of 90-180 m/s and mechanical erosion of the product layer at velocities exceeding 190 m/s, which prevent HfSiO_4 from being a suitable EBC candidate for turbine applications.

2.3. Thermochemical Stability and Microstructural Evolution of $\text{Yb}_2\text{Si}_2\text{O}_7$ in High-Velocity High-Temperature Water Vapor

2.3.1. Introduction

Ytterbium disilicate, the state-of-the-art EBC material, reacts with high-temperature water vapor to form $\text{Si}(\text{OH})_4$ (g) by Reactions 2-13 and 2-14 [17], [20], [48].



Porosity formation was estimated in these equations from changes in the unit cell volumes for each crystal structure. The stability of $\text{Yb}_2\text{Si}_2\text{O}_7$ in high-velocity water vapor is addressed with steamjet furnace exposures in order to determine rate-limiting steps for the reactions listed above. This work also characterizes microstructural evolution of bulk $\text{Yb}_2\text{Si}_2\text{O}_7$ as a function of time, temperature, and steam velocity.

2.3.2. Background

Rare earth silicates are current EBC candidates for CMC protection in turbine environments. EBC design focuses on the following criteria: thermochemical stability with combustion gases and ingested debris, thermomechanical stability between EBC/CMC layers, and low oxygen diffusivity of the EBC to limit oxidation of the underlying bond coat and SiC CMC. To limit coating spallation, the thermal expansion coefficient (CTE) of the EBC should be compatible with all layers of the CMC-EBC system. Table 2-5 shows the linear CTE and melting temperatures of all compounds of the $\text{Yb}_2\text{O}_3 - \text{SiO}_2$ system compared to SiC and the silicon bond coat. $\text{Yb}_2\text{Si}_2\text{O}_7$ shows minimal CTE mismatch with SiC and the silicon bond coat. The CTE for each axis of the unit cells are also shown for $\text{Yb}_2\text{Si}_2\text{O}_7$ and Yb_2SiO_5 , where large degrees of

anisotropy are present in the Yb_2SiO_5 that can lead to stress-induced cracking upon thermal cycling. While CTE anisotropy is not prevalent for $\text{Yb}_2\text{Si}_2\text{O}_7$, the monosilicate phase is the predicted reaction product when in contact with high-temperature steam, and therefore CTE anisotropy should be considered during EBC design.

Table 2-5. CMC and EBC CTE, melt temperature, and density.

	CTE $\times 10^6 / ^\circ\text{C}$	Melt Temperature $^\circ\text{C}$	Density g/cm^3
Yb_2O_3	6.8-8.4 [49]	2250	9.17
Yb_2SiO_5	100-1200 $^\circ\text{C}$ [35] Linear: 7.25 a-axis: 2.2 b-axis: 6.6 c-axis: 10.3	1950	7.28
$\text{Yb}_2\text{Si}_2\text{O}_7$	800-1800 $^\circ\text{C}$ [50] Linear: 4.2 a-axis: 5.7 b-axis: 3.7 c-axis: 3.2	1850	6.18
Silicon	3.5-4.5 [11]	1414	2.32
SiC	4.5-5.5 [3]	2545 (decomposition)	3.21

The silica activity of rare earth silicates correlates with the reactivity of the material with water vapor. Uncoated SiC reacts in air and water vapor to form SiO_2 , a thermally grown oxide with a silica activity of 1. The silica activity of the $\text{Yb}_2\text{Si}_2\text{O}_7 + \text{Yb}_2\text{SiO}_5$ two-phase region of the phase diagram was determined to be 0.194 at 1600 K, while the silica activity for the $\text{Yb}_2\text{SiO}_5 + \text{Yb}_2\text{O}_3$ phase field was 0.00298 [51]. Yb_2SiO_5 should show superior steam resistance compared to $\text{Yb}_2\text{Si}_2\text{O}_7$ due to a lower silica activity.

High-temperature water vapor studies have been limited to low partial pressures of water vapor or low velocity steam due to difficulty in obtaining high velocity steam. Maier showed that

$\text{Yb}_2\text{Si}_2\text{O}_7$ can form garnet and apatite phases from reaction with surrounding Al_2O_3 furnace equipment during steam testing at 1500 °C with 30% steam atmosphere and near stagnant flow rate [20]. Thermogravimetric analysis at 1500 °C in a 50% H_2O (g)/50% O_2 (g) atmosphere showed linear mass loss kinetics for $\text{Yb}_2\text{Si}_2\text{O}_7$ after 100 hours as well as no measurable weight change for Yb_2SiO_5 [14]. Ueno et al. also tested $\text{Yb}_2\text{Si}_2\text{O}_7$ in stagnant velocity steam with 30% steam and found small linear mass loss kinetics after 100 hours at 1500 °C [17].

The formation of a porous Yb_2SiO_5 product layer, shown by the chemical reaction in Equation 2-13, implies that the reaction interface will continually advance into the sample. Growth of a porous oxide layer would then increase the gas phase diffusion distance to the reaction interface, where parabolic growth rate kinetics should be observed. Klemm reported parabolic kinetics for $\text{Yb}_2\text{Si}_2\text{O}_7$ under conditions of 1450 °C, 100 m/s gas flow rate, and 0.28 atm of water vapor pressure [48]. The contradictory kinetics of the EBC reactions between testing methods described in the literature may arise from the low-velocity steam testing and low steam partial pressures of the experimental rigs. An understanding of time, temperature, and velocity dependences for rare earth silicate reactions with high-velocity steam is necessary to compare testing between laboratories and to develop lifetime prediction models for EBCs in service.

2.3.3. Methods

Pre-reacted $\text{Yb}_2\text{Si}_2\text{O}_7$ powders (Praxair Inc., Danbury, CT) were initially ball milled with yttria stabilized zirconia ball mill media to reduce particulate size. Powders were loaded into a 20 mm diameter graphite die and consolidated by spark plasma sintering (SPS) using a Thermal Technologies DCS 25-10 SPS (Santa Rosa, CA). Samples were sintered in an argon environment using a 15 minute hold at a maximum temperature and pressure of 1550 °C and 65 MPa. Following the SPS process, samples were annealed for 24 hours at 1500 °C in air to remove

residual carbon and restore oxygen stoichiometry. Resulting $\text{Yb}_2\text{Si}_2\text{O}_7$ pucks were sectioned into $\sim 10 \text{ mm} \times 10 \text{ mm} \times 1.25 \text{ mm}$ coupons and polished to $1 \mu\text{m}$ with diamond suspension prior to steam testing, as shown in Figure 2-29. The relative density obtained from XRD and SEM was 96% with less than 3% Yb_2SiO_5 in the starting samples.

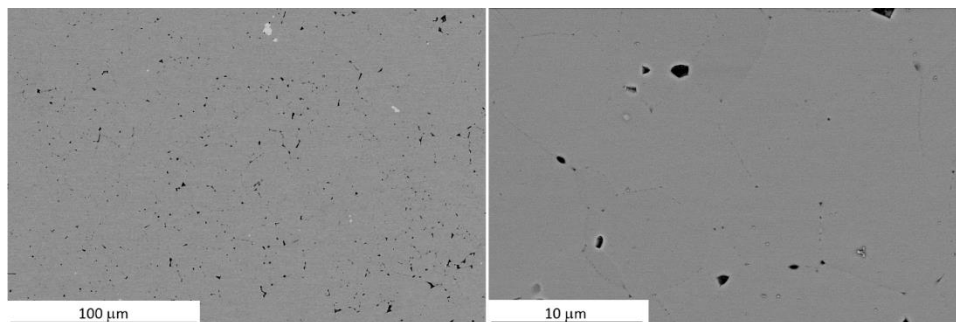


Figure 2-29. Backscatter SEM images of $\text{Yb}_2\text{Si}_2\text{O}_7$ coupons prior to steam testing, with Yb_2SiO_5 minor phase (light gray).

Sample mass was recorded before and after steam exposures to an accuracy of $\pm 0.05 \text{ mg}$ with a microbalance (MS105DU, Mettler-Toledo, Columbus, OH). Post-test characterization included XRD (Panalytical Empyrean X-ray diffractometer, Westborough, MA) and SEM (FEI Quanta 650 SEM, Hillsboro, OR) of the sample surface in plan view. Cross-section SEM imaging was used to measure reaction depths in the samples. Cross-sectioned samples are mounted in epoxy under vacuum to ensure filling of connected voids in the product layer. Reaction depths reported here represent the average cross section reaction layer thickness for 50-60 measurements across the sample, where each measurement is spaced $\sim 80 \mu\text{m}$ apart. Specimen exposures in water vapor were made at 1200, 1300, and 1400 °C for times of 60, 125, and 250 hours.

2.3.4. Results

2.3.4.1. X-ray diffraction

Figure 2-30 shows XRD of the $\text{Yb}_2\text{Si}_2\text{O}_7$ (ICDD # 04-007-4857) sample surfaces after 250 hours of steam exposure at temperatures of 1200-1400 °C. Yb_2SiO_5 readily formed at all temperatures and exposure times. Yb_2O_3 peaks were also present at all temperatures for longer exposure times, and were most prominent for 1300 °C and 1400 °C exposures. The presence of Yb_2SiO_5 (ICDD # 00-040-0386) and Yb_2O_3 (ICDD # 04-003-4990) products show that Reactions 2-13 and 2-14 were occurring simultaneously during testing. Additional peaks corresponded to $\text{Yb}_3\text{Al}_5\text{O}_{12}$ (ICDD # 01-073-1369) formation from the Al_2O_3 tube furnace environment. It will be shown later that impurities were limited to edges and sides of the coupons, and that sample contamination was negligible in the high-velocity regions of interest.

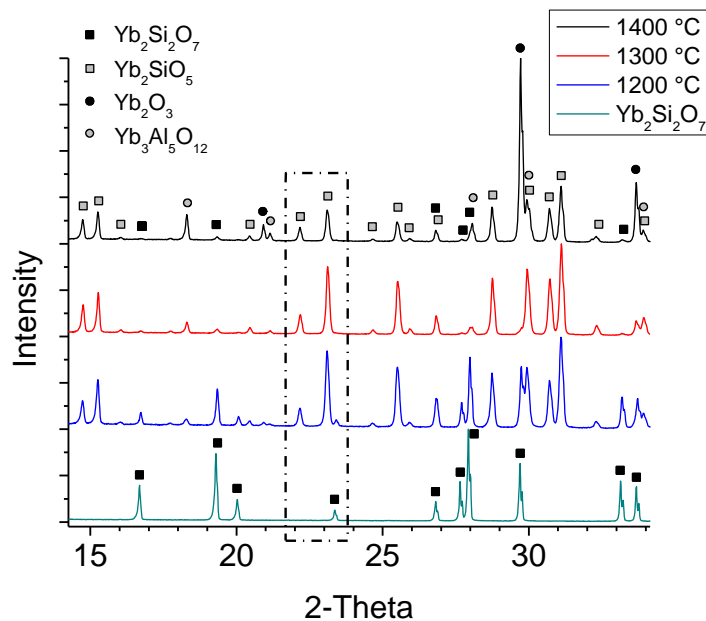


Figure 2-30. XRD results for $\text{Yb}_2\text{Si}_2\text{O}_7$ after 250-hour water vapor exposures at temperatures between 1200 °C-1400 °C. Results are compared to initial XRD pattern of bulk $\text{Yb}_2\text{Si}_2\text{O}_7$. The boxed region highlights formation of Yb_2SiO_5 on the sample surface for all temperatures.

2.3.4.2. Plan View SEM

Reaction products and surface morphologies at various regions across the samples were correlated to local qualitative steam velocities utilizing the ANSYS velocity contour maps. Figure 2-31 shows porous Yb_2SiO_5 formation on the 250-hour exposure samples at a position of ~3-4 mm downstream from the high velocity impingement site. Steam exposures at 1200 °C resulted in a unique Yb_2SiO_5 morphology. The Yb_2SiO_5 product layer at 1300 °C and 1400 °C exposures consistently showed spherical morphology with interconnected porosity. Grain sizes of the product phase increase with both exposure time and temperature.

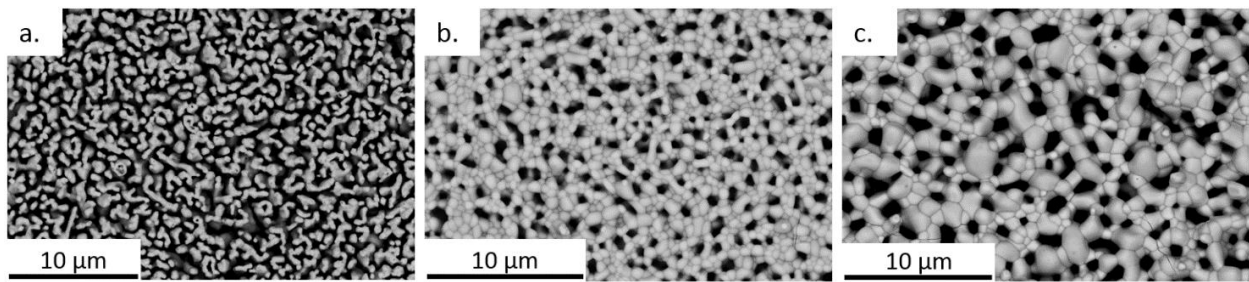


Figure 2-31. Representative SEM images of the Yb_2SiO_5 product layer after 250-hour exposures of $\text{Yb}_2\text{Si}_2\text{O}_7$ in water vapor with predicted steam velocities of 80-110 m/s at a. 1200 °C, b. 1300 °C, and c. 1400 °C.

XRD of reacted samples showed that multiple reaction products formed across each sample face. Figure 2-32 shows backscatter SEM images at regions across a single $\text{Yb}_2\text{Si}_2\text{O}_7$ sample exposed to water vapor at 1400 °C for 250 hours. All images are from downstream of the impingement site and are arranged with increasing velocity from left to right. A transition velocity was seen at ~140 m/s (Figure 2-32b) where Yb_2O_3 was initially observed. A stable and highly porous Yb_2O_3 layer was present on the surface at the highest gas velocities, shown in Figure 2-32d.

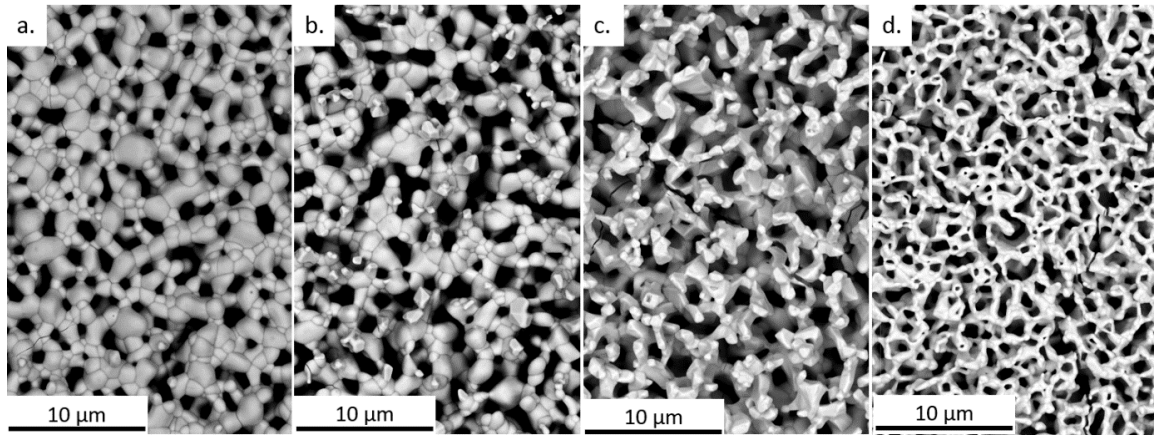


Figure 2-32. $\text{Yb}_2\text{Si}_2\text{O}_7$ reaction product variation across a sample after exposure to water vapor at 1400 °C for 250 h. A strong gas stream velocity dependence is seen for the reaction to form Yb_2SiO_5 (image a) and for Yb_2SiO_5 to form Yb_2O_3 (image d). Approximate steam velocities are: a) 80 m/s, b) 145 m/s, c) 170 m/s, and d) 210 m/s.

2.3.4.3. Cross-section SEM

Figure 2-33 shows a matrix of representative images for $\text{Yb}_2\text{Si}_2\text{O}_7$ after each exposure time and temperature (60, 125, and 250 hours at 1200 °C, 1300 °C, or 1400 °C). Cross-sections shown here were taken from sample regions that experience a predicted velocity of 80-100 m/s where $\text{Yb}_2\text{Si}_2\text{O}_7$ reacts to form porous Yb_2SiO_5 (Reaction 2-13). A thin dense layer of Yb_2SiO_5 formed on the $\text{Yb}_2\text{Si}_2\text{O}_7$ surface at these intermediate velocities only for 1200 °C exposures. Cross-section and plan view images suggest that the samples exposed to steam at 1200 °C had a different rate-limiting mechanism for the reaction process compared to 1300 °C and 1400 °C exposures.

The 1300°C and 1400 °C exposures of $\text{Yb}_2\text{Si}_2\text{O}_7$ resulted in a porous silica-depleted zone of Yb_2SiO_5 that increased in thickness with increasing time and temperature. From the reaction interface upwards, pore size increased and formed a columnar type structure. The orientation of pores relative to the surface suggests a preferred gas phase diffusion pathway through the reaction product to and from the $\text{Yb}_2\text{SiO}_5/\text{Yb}_2\text{Si}_2\text{O}_7$ reaction interface.

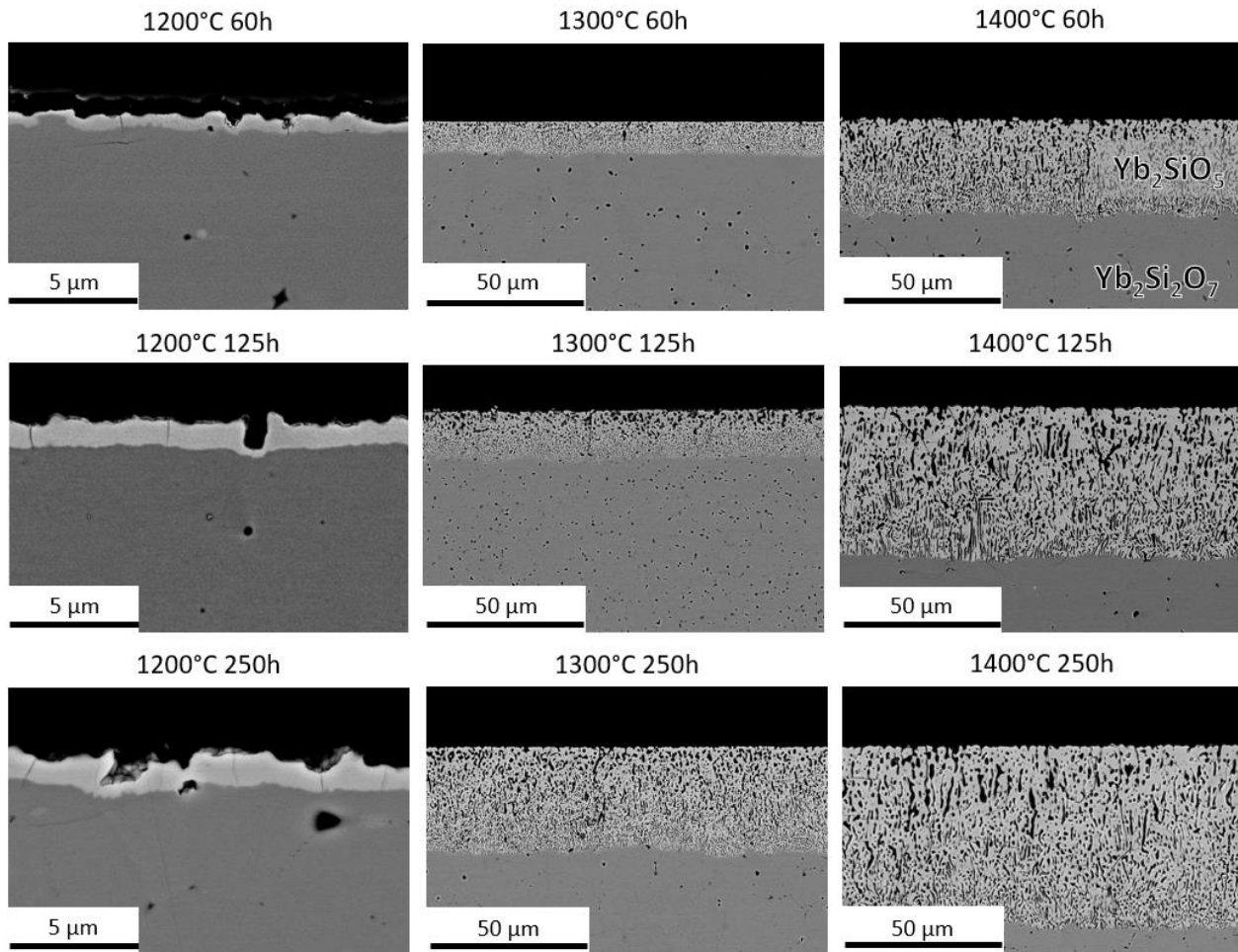


Figure 2-33. Representative $\text{Yb}_2\text{Si}_2\text{O}_7$ SEM cross-sections for varied exposure times and temperatures in a velocity region 80-100 m/s. The $\text{Yb}_2\text{Si}_2\text{O}_7$ samples exposed to 1200 °C show a scale bar of 5 μm .

The highest velocity (>190 m/s) sample regions showed formation of both Yb_2SiO_5 and Yb_2O_3 (Reactions 2-13 and 2-14). Figure 2-34 displays cross-sections of $\text{Yb}_2\text{Si}_2\text{O}_7$ after 250-hour steam exposure at 1200-1400 °C. The 1200 °C steam exposure samples showed a columnar structure that was unique compared to higher temperatures. The product layer for the 1200 °C sample separated at the reaction interface during the epoxy mounting and polishing process. A dense Yb_2SiO_5 layer was seen at the reaction front of the 1200 °C samples, consistent with the thin dense layer seen at the lower velocities in Figure 2-33.

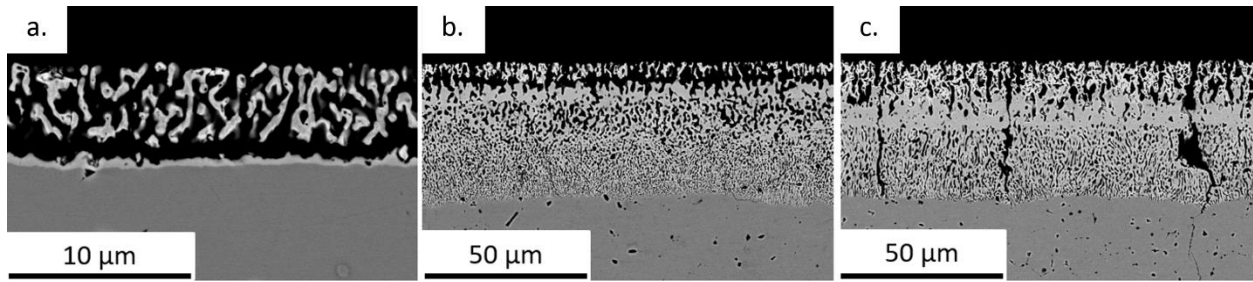


Figure 2-34. Cross sections of $\text{Yb}_2\text{Si}_2\text{O}_7$ after 250 hours of steam exposure with gas velocities $\sim 190\text{-}210$ m/s. a) 1200 °C, b) 1300 °C, and c) 1400 °C. The $\text{Yb}_2\text{Si}_2\text{O}_7$ sample exposed to 1200 °C shows a scale bar of 10 μm .

$\text{Yb}_2\text{Si}_2\text{O}_7$ exposed to steam at 1300 °C and 1400 °C in the 190-210 m/s region showed a distinct 3-layer reaction product: a porous Yb_2SiO_5 layer, a dense intermediate Yb_2SiO_5 layer, and a highly porous Yb_2O_3 top layer. The densified intermediate Yb_2SiO_5 layer was most prominent at 1400 °C and restricted growth of the total silica depletion zone in the high-velocity regions of the samples. As a result, the total reaction depths for Figure 2-34b and Figure 2-34c were similar, despite there being a 100 °C difference in exposure temperature.

Figure 2-35 shows energy dispersive spectroscopy (EDS) maps of the tri-layer reaction product formed after $\text{Yb}_2\text{Si}_2\text{O}_7$ steam exposure for 1400 °C and 250 hours. The BSE image and silicon map allowed for a clear distinction between reaction layers Yb_2O_3 , Yb_2SiO_5 , and the $\text{Yb}_2\text{Si}_2\text{O}_7$ substrate. No impurities were observed by EDS. The carbon EDS map shows the epoxy depth obtained during sample infiltration. When the densified Yb_2SiO_5 layer was present, epoxy infiltration was halted. This supports the hypothesis that Yb_2O_3 was only produced when H_2O (g) transport to $\text{Yb}_2\text{Si}_2\text{O}_7$ or $\text{Si}(\text{OH})_4$ (g) outward transport was limited through closing of interconnected porosity.

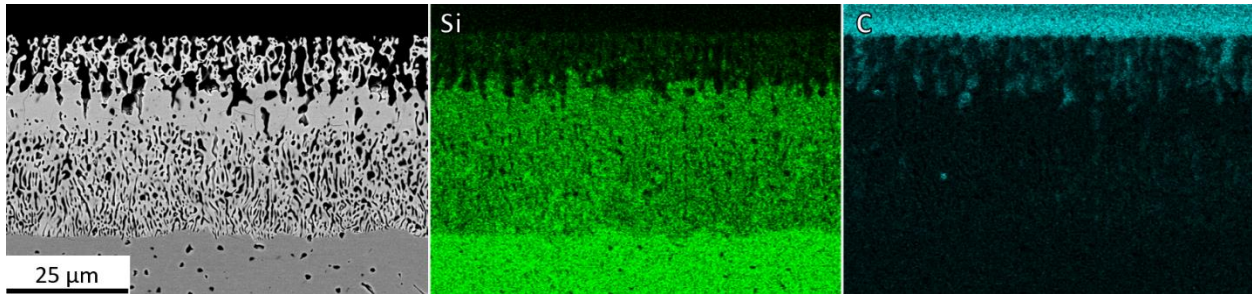


Figure 2-35. Energy Dispersive Spectroscopy (EDS) of $\text{Yb}_2\text{Si}_2\text{O}_7$ products after water vapor exposure at 1400 °C for 250 hours with a local steam velocity of ~200-220 m/s. The silicon map shows distinct layering of Yb_2O_3 and Yb_2SiO_5 on top of the $\text{Yb}_2\text{Si}_2\text{O}_7$. The carbon map shows epoxy infiltration under vacuum halted by the dense intermediate Yb_2SiO_5 layer.

2.3.4.4. Extended SEM Cross-sections

Extended BSE images of the sample surface provided comparison and quantification of reaction depths and product layer morphologies related to velocity, time, and temperature changes. Figure 2-36 shows stitched cross-section images centered on the highest velocity regions for $\text{Yb}_2\text{Si}_2\text{O}_7$ exposed in steam at 1200 °C and 1300 °C for 250 hours. Both impingement sites were void of product phase material due to mechanical erosion from the high-velocity water vapor or occasional liquid water impingement.

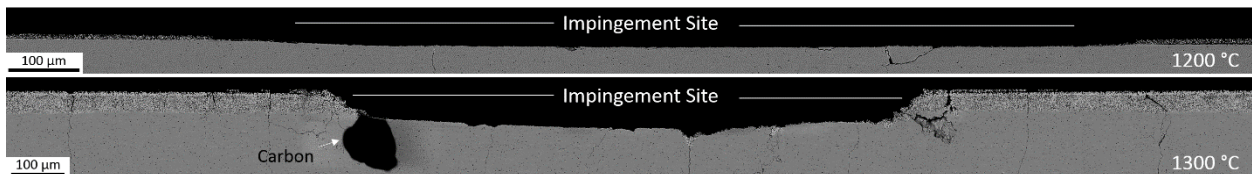


Figure 2-36. Stitched cross-section images of $\text{Yb}_2\text{Si}_2\text{O}_7$ after water vapor exposure for 250h at 1200 °C and 1300 °C, centered at the impingement site.

Figure 2-37 shows an extended stitching, split into two images, of a single $\text{Yb}_2\text{Si}_2\text{O}_7$ sample after steam exposure at 1400 °C for 250 hours. The top image in Figure 2-37 shows an intermediate velocity regime (80-200 m/s) and the bottom image shows the highest velocity (200-250 m/s) impingement site. Velocity increases from left to right as the stitched images approach the impingement site. At the lowest velocity regions (80-115 m/s), a uniform and porous Yb_2SiO_5 layer was present with a large reaction zone thickness. As the top of the Yb_2SiO_5 layer started to densify, the overall reaction zone thickness concurrently decreased.

Once pore connectivity from the $\text{Yb}_2\text{Si}_2\text{O}_7$ reaction interface to the sample surface was limited, H_2O (g) reacted with the densified Yb_2SiO_5 to form the porous columnar Yb_2O_3 outer layer. The impingement sites for all $\text{Yb}_2\text{Si}_2\text{O}_7$ 1400 °C exposure times showed minimal material loss compared to lower temperatures, suggesting increased structural integrity of the product phase.

Cracking was prominent in the product layer for $\text{Yb}_2\text{Si}_2\text{O}_7$ tested at all temperatures, especially at the highest velocities (200-250 m/s). Reaction products penetrating deeper into the $\text{Yb}_2\text{Si}_2\text{O}_7$ sample near cracks suggests these cracks formed during testing. When cracks showed no impact on local reaction zone depth, they were attributed to stress cracking upon removal of the sample from the furnace after testing, occurring from the high CTE anisotropy of Yb_2SiO_5 .

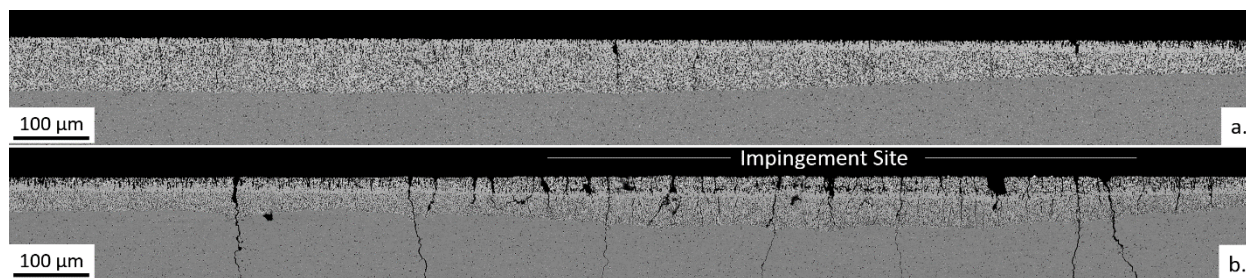


Figure 2-37. Stitched cross-section images of $\text{Yb}_2\text{Si}_2\text{O}_7$ after exposure to water vapor at 1400 °C for 250 hours. Images are from a. intermediate velocities (80-200 m/s) through b. the highest velocity (200-250 m/s) impingement site.

2.3.4.5. Low Gas Velocity Regions

The region of the $\text{Yb}_2\text{Si}_2\text{O}_7$ sample under the platinum foil showed limited reaction due to almost stagnant gas velocities at this location. Figure 2-38a shows a BSE image of one region of the $\text{Yb}_2\text{Si}_2\text{O}_7$ sample after stagnant steam exposure for 60 hours at 1300 °C. Clusters of Yb_2SiO_5 are seen forming on the $\text{Yb}_2\text{Si}_2\text{O}_7$ grain boundaries. Initial nucleation of the reaction process was thus expected to occur by Yb_2SiO_5 nuclei forming along grain boundaries and then spreading into the $\text{Yb}_2\text{Si}_2\text{O}_7$ grains.

$\text{Yb}_2\text{Si}_2\text{O}_7$ specimen regions upstream of the impingement site, with gas velocities less than ~50 m/s, showed Al-containing phases attributed to the tube furnace environment. $\text{Al}(\text{OH})_3$

(g) species from the tube furnace were not swept away fast enough to prevent reaction with the sample. Figure 2-38b shows the alumina contamination in these regions that correspond to the $\text{Yb}_3\text{Al}_5\text{O}_{12}$ pattern from XRD analysis. Both $\text{Yb}_2\text{Si}_2\text{O}_7$ and Yb_2SiO_5 displayed interactions with the $\text{Al}(\text{OH})_3$ gas species in these sections of the sample, and therefore these regions were ignored during analysis.

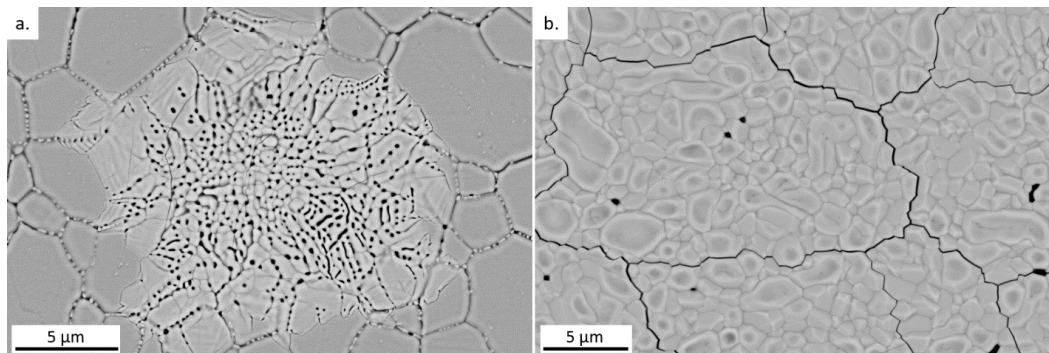


Figure 2-38. a. Near stagnant velocity edge of $\text{Yb}_2\text{Si}_2\text{O}_7$ sample exposed to water vapor at 1300 °C for 60 hours showing initial Yb_2SiO_5 nucleation at grain boundaries, b. Low velocity (<50 m/s) region outside of the primary gas stream where alumina or impurities have reacted with the $\text{Yb}_2\text{Si}_2\text{O}_7$ surface.

2.3.5. Analysis

The time and temperature dependences of $\text{Yb}_2\text{Si}_2\text{O}_7$ reaction to form Yb_2SiO_5 by Reaction 2-13 can be determined from specific mass changes and measured silica depletion thickness from cross-section SEM imaging. Analysis was conducted for two sample regions. The first region corresponded to cross-section BSE images taken in regions exposed to gas velocities between 80-115 m/s where only the porous Yb_2SiO_5 product phase forms, such that the kinetics of Reaction 2-13 can be isolated. The second region, where Yb_2O_3 formed at the highest velocities (>140 m/s), was analyzed to estimate the kinetics of Reaction 2-14. Figure 2-39a shows a plot of the average porous Yb_2SiO_5 reaction zone depth for each exposure time and temperature. The linear relationship between reaction depth and the square root of time shows that the Reaction 2-13 has a parabolic time dependence, indicative of a diffusion-controlled

process. Best fit lines are squared to provide parabolic rate constants for each test temperature. Additionally, it is seen that the best fit lines cross the x-axis between 1-15 hours, representing a possible incubation period for the parabolic kinetics to begin controlling the reaction, similar to what was seen for the HfSiO_4 -steam reaction in Chapter 2.2. The Yb_2O_3 reaction depth was also plotted against the square root of time in Figure 2-39b to show that Reaction 2-14 also occurred by a diffusion-controlled process. Measurements of the Yb_2O_3 thickness corresponded to average values of Yb_2O_3 layer thicknesses at all velocities above ~ 140 m/s. Due to the unique morphology of $\text{Yb}_2\text{Si}_2\text{O}_7$ samples exposed to steam at 1200°C at the velocities 115-210 m/s, the Yb_2O_3 thickness could not be differentiated from Yb_2SiO_5 for analysis. The kinetics of Reaction 2-14 to form Yb_2O_3 are shown to be much slower than Reaction 2-13 to form Yb_2SiO_5 , where the reaction rates at 1400°C are $0.3 \pm 0.2 \mu\text{m}^2/\text{h}$ and $21 \pm 2 \mu\text{m}^2/\text{h}$, respectively. The reduced reaction rate of Yb_2O_3 formation was consistent with the reduced silica activity of Yb_2SiO_5 relative to $\text{Yb}_2\text{Si}_2\text{O}_7$.

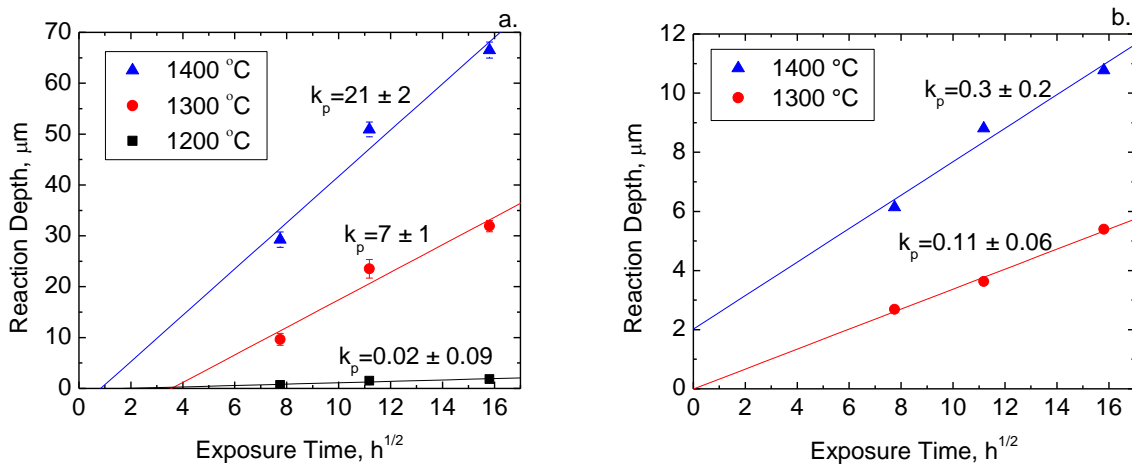


Figure 2-39. Average reaction depth plotted against the square root of time for a. Yb_2SiO_5 formation from $\text{Yb}_2\text{Si}_2\text{O}_7$ at velocities of 80-115 m/s and b. Yb_2O_3 formation from Yb_2SiO_5 on the same specimens at all velocities greater than ~ 140 m/s. Parabolic rate constants, k_p ($\mu\text{m}^2/\text{h}$), are shown for each temperature.

The thicknesses of the dense intermediate Yb_2SiO_5 reaction product were recorded and averaged for 1300 °C and 1400 °C steam exposures. The 1300 °C data was collected over 1-2.5 mm length scales of the sample cross-sections in the high-velocity regions where densification occurred. The 1400 °C data was collected over 4-5 mm of the sample cross-sections, as the densified regions were more prevalent at 1400 °C than at 1300 °C. The parabolic growth of the dense layer with time is shown in Figure 2-40 along with a micrograph annotating the measured Yb_2SiO_5 dense intermediate layer of interest after a 1400 °C steam exposure for 250h.

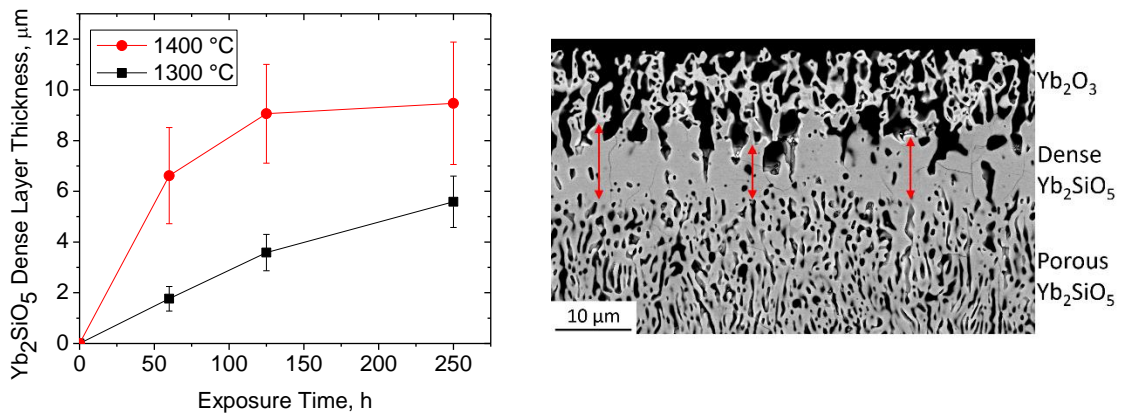


Figure 2-40. Growth of the dense Yb_2SiO_5 layer after $\text{Yb}_2\text{Si}_2\text{O}_7$ steam exposures at 1300 °C and 1400 °C. An example of the measured dense layer is presented with red arrows for a $\text{Yb}_2\text{Si}_2\text{O}_7$ sample exposed to steam for 250h at 1400 °C ($v \sim 210$ m/s).

Specific mass changes were also calculated for each $\text{Yb}_2\text{Si}_2\text{O}_7$ sample, shown in Figure 2-41, which also displayed parabolic kinetics. The mass changes did incorporate significant uncertainty due to mass gain from furnace impurities at the sample edges and mass loss from mechanical erosion at the highest velocity impingement site. The mass loss data were only used as a qualitative representation of the parabolic reaction kinetics.

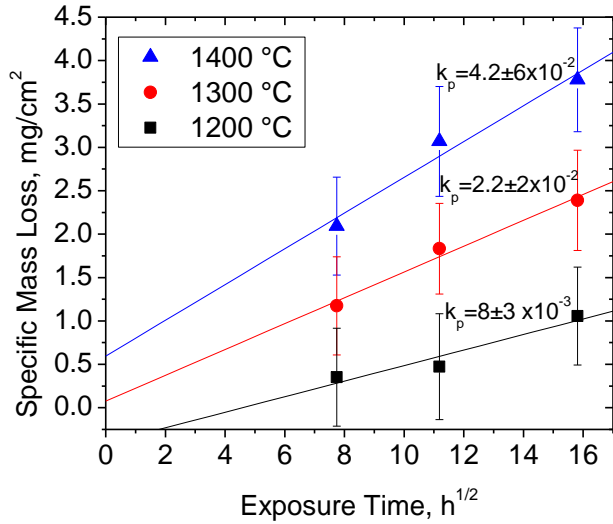


Figure 2-41. Specific mass loss of exposed $\text{Yb}_2\text{Si}_2\text{O}_7$ samples plotted against the square root of time. Parabolic rate constants, k_p , $\text{mg}^2/\text{cm}^4\text{h}$, are shown for each temperature.

The reaction enthalpies for Equations 2-13 and 2-14 can be determined from the temperature dependence of the reaction rates, assuming equilibrium at the reaction interfaces. A velocity dependence on the reaction rate was most clearly shown in Figure 2-37 and suggests that the rate-limiting mechanism involves diffusion through the gas phase. For the given system, gas diffusion processes include H_2O (g) diffusion to the $\text{Yb}_2\text{Si}_2\text{O}_7$ reaction interface or product $\text{Si}(\text{OH})_4$ (g) diffusing outward. Since there is an excess of H_2O (g) in this system, it is assumed that outward diffusion of $\text{Si}(\text{OH})_4$ (g) product species is rate limiting. Therefore, the reaction rate should reflect the temperature dependence from both gas phase interdiffusion as well as an Arrhenius temperature dependence for formation of the equilibrium partial pressure of $\text{Si}(\text{OH})_4$ (g). A general relationship for the temperature dependences is shown in Equation 2-15 where $D_{1,2}$ is gas-phase interdiffusion, ΔH_{rxn} is the reaction enthalpy, R is the universal gas constant, and T is temperature.

$$k_p \propto \left[D_{1,2} \times \exp\left(-\frac{\Delta H_{rxn}}{RT}\right) \right] \propto T^{\frac{3}{2}} \exp\left(-\frac{\Delta H_{rxn}}{RT}\right) \quad 2-15$$

Figure 2-42 shows a plot of the log of the parabolic rates divided by $T^{3/2}$ on the y-axis against inverse temperature on the x-axis to allow for determination of ΔH_{rxn} . As expected from previously shown SEM images, a dramatic change in the temperature dependence for 1200 °C sample exposures was seen. The temperature dependence and reaction morphologies for $\text{Yb}_2\text{Si}_2\text{O}_7$ steam exposures at 1200 °C imply that a different mechanism is controlling the reaction rate at lower temperatures, and therefore 1200 °C test results are not accounted for in the calculation of the reaction enthalpy. Bulk $\text{Yb}_2\text{Si}_2\text{O}_7$ and the dense intermediate Yb_2SiO_5 layer show similar temperature dependences for their respective reactions with water vapor at 1300 °C and 1400 °C.

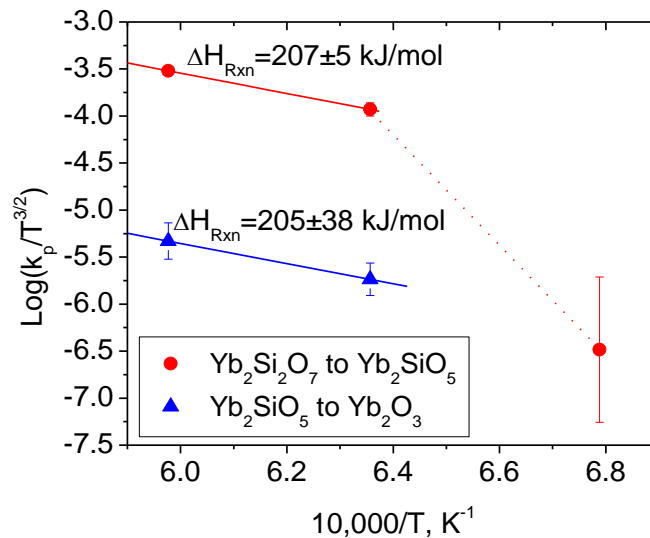


Figure 2-42. Arrhenius dependence of measured reaction depths for bulk $\text{Yb}_2\text{Si}_2\text{O}_7$ EBC sample and the dense intermediate Yb_2SiO_5 reaction layer.

2.3.6. Discussion

$\text{Yb}_2\text{Si}_2\text{O}_7$ exposed to steam at 1200 °C showed a reaction to form thin dense Yb_2SiO_5 layer at velocities below 115 m/s. At velocities greater than 115 m/s, columnar Yb_2SiO_5 was present on top of a dense interfacial Yb_2SiO_5 layer. Yb_2O_3 then formed around the columnar

Yb_2SiO_5 on exposed surfaces. Golden et al. exposed $\text{Y}_2\text{Si}_2\text{O}_7$ to water vapor at 1200 °C under comparable experimental conditions [60-250h steam exposures, $P(\text{H}_2\text{O})=1$ atm, $v=158-174$ m/s] [52]. The Y_2SiO_5 product phase had a porous microstructure comparable to $\text{Yb}_2\text{Si}_2\text{O}_7$ samples exposures at 1300 and 1400 °C shown in Figure 2-33, yet neither the thin film monosilicate (Figure 2-33, 1200 °C) or a columnar monosilicate (Figure 2-34a) product phase formed during the yttrium silicate steam exposures at 1200 °C. Yttrium and ytterbium silicates are assumed to have similar thermochemical stability in steam due to similar silica activities in both systems [51], [53]. The conflicting reaction product morphologies forming at 1200 °C in high-velocity steam are expected to greatly impact the overall magnitude of the reaction rate, and therefore deserve additional study to understand the reaction mechanism under this condition.

$\text{Yb}_2\text{Si}_2\text{O}_7$ exposed at 1300 °C and 1400 °C with water vapor velocities greater than 115 m/s showed formation of a dense intermediate Yb_2SiO_5 layer that was extremely beneficial for $\text{Yb}_2\text{Si}_2\text{O}_7$ water vapor resistance by limiting gas transport to the $\text{Yb}_2\text{Si}_2\text{O}_7$ reaction interface. Reducing pore connectivity in the Yb_2SiO_5 layer decreased the total reaction depth compared to intermediate velocity regimes with no dense layer present. The mechanism for formation of an intermediate dense Yb_2SiO_5 layer remains unknown. $\text{Yb}_2\text{Si}_2\text{O}_7$ steam exposures at 1300 °C and 1400 °C were at 71% and 75% of the Yb_2SiO_5 homologous melting temperature, respectively, suggesting that sintering could reasonably occur during testing. It has also been shown that Yb_2O_3 reacts readily with trace amounts of silicon hydroxide gas to form Yb_2SiO_5 [27]. A silicon hydroxide gas species diffusing outward from the reaction interface might react with Yb_2O_3 that has already formed at the sample surface. Such a reaction, the reverse of Reaction 2-14, results in a 32% volume expansion which may limit pore connectivity in the reaction product. Either individually or in tandem, the combination of high-temperature sintering capability of Yb_2SiO_5

with possible volume expansion by Yb_2O_3 uptake of $\text{Si}(\text{OH})_4$ (g) could explain the formation of the intermediate dense Yb_2SiO_5 layer. Future work will attempt to uncover the mechanism for densification in the product Yb_2SiO_5 phase at temperatures ≥ 1300 °C.

The microstructural evolution of ytterbium silicates in environments representative of service conditions is essential to understanding the thermochemical stability and hence the life cycle for an EBC. The industry standard lifetime for gas turbine components is 25,000 hours [54], with typical EBCs being 100-400 μm in total thickness. Extrapolation of the 80-115 m/s velocity results for bulk $\text{Yb}_2\text{Si}_2\text{O}_7$ predict reaction thicknesses of 22 μm for 1200 °C, 428 μm at 1300 °C, and 720 μm for 1400 °C. Similarly, extrapolation of the Yb_2SiO_5 intermediate layer reaction to form Yb_2O_3 suggests that a bulk Yb_2SiO_5 EBC would show reaction depths of only 53 μm and 89 μm at 1300 °C and 1400 °C, respectively. While $\text{Yb}_2\text{Si}_2\text{O}_7$ is predicted to display high reaction thicknesses at 25,000 hours compared to a realistic EBC thickness in service applications, the desired lifetime includes extended time periods where the engine is not at maximum temperature. Additionally, all applied coatings usually contain concentrations of Yb_2SiO_5 which would likely decrease the overall reaction rate. The long-term thermochemical stability of EBCs in high-temperature high-velocity steam may be increased further through changes in relative concentrations of rare earth disilicate and monosilicate phases in the EBC, as well as promotion of beneficial microstructure changes such as densification of the product phase, as is shown in this work. The decrease in the amount of material loss from mechanical erosion at the impingement site for the 1400 °C steam exposures suggests that the Yb_2SiO_5 product phase displays increased structural integrity at higher temperatures.

The calculated reaction enthalpies for $\text{Yb}_2\text{Si}_2\text{O}_7$ and Yb_2SiO_5 reactions with water vapor at 1300 °C and 1400 °C were comparable values of 207 ± 5 kJ/mol and 205 ± 38 kJ/mol,

respectively. The predicted hydroxide species in both Reactions 2-13 and 2-14 is Si(OH)_4 (g). The reaction enthalpy for SiO_2 to react with water vapor and form Si(OH)_4 (g) is 56 kJ/mol [22]. The discrepancy in reaction enthalpies determined in this work and that of pure SiO_2 in water vapor is significant, however, reliable thermodynamic data for both $\text{Yb}_2\text{Si}_2\text{O}_7$ and Yb_2SiO_5 are unavailable.

Both reaction enthalpies presented in this work were calculated from only two temperatures. The reported uncertainty only reflected error in the two data points, and was expected to change once results at additional temperatures are obtained. Due to the small sampling size where Yb_2O_3 formed and the complexity of measuring Yb_2O_3 thickness on an initially rough surface, the Yb_2O_3 thickness results were considered semi-quantitative. Future work must involve high-velocity testing of bulk Yb_2SiO_5 coupons to reduce uncertainty in measurements. Similar temperature dependences across $\text{Yb}_2\text{Si}_2\text{O}_7$, Yb_2SiO_5 , and HfSiO_4 (Figure 2-28) suggested that a single reaction mechanism may be prevalent for all complex silicate EBC materials forming a porous product phase when in contact with water vapor.

2.3.7. Conclusions

A high-temperature high-velocity steamjet rig was used to study thermochemical stability and microstructural evolution of $\text{Yb}_2\text{Si}_2\text{O}_7$ in a 1 atmosphere steam environment. $\text{Yb}_2\text{Si}_2\text{O}_7$ exposed to steam at 1200 °C formed a dense thin film of Yb_2SiO_5 , which implied that $\text{Yb}_2\text{Si}_2\text{O}_7$ is highly stable in operating temperatures ≤ 1200 °C. $\text{Yb}_2\text{Si}_2\text{O}_7$ underwent a reaction with H_2O (g) to form a porous Yb_2SiO_5 layer for steam exposures at 1300 °C and 1400 °C and local velocities of 80-115 m/s. At steam velocities above ~ 115 m/s, the porous Yb_2SiO_5 densified to form an intermediate Yb_2SiO_5 layer, where densification decreased the total reaction depth compared to the lower velocity regions. A secondary reaction to form Yb_2O_3 occurred on top of

the dense Yb_2SiO_5 layer at velocities greater than ~ 140 m/s. The slower reaction rates of the Yb_2SiO_5 layer than that of the bulk $\text{Yb}_2\text{Si}_2\text{O}_7$ demonstrated the superior thermochemical stability of rare earth monosilicates compared to their disilicate counterparts.

Diffusion-controlled kinetics were seen for silica depletion of both $\text{Yb}_2\text{Si}_2\text{O}_7$ and Yb_2SiO_5 . Similar reaction enthalpies were seen for both Reactions 2-13 and 2-14 at 1300 °C and 1400 °C which may be explained as a single rate-controlling mechanism for steam volatility of silicate-base materials that react with steam to form a porous reaction product. The rate-controlling mechanism involved formation and outward diffusion of $\text{Si}(\text{OH})_4$ (g) from the reaction interfaces. Microstructure evolution of ytterbium silicates shows promise for additional thermochemical resistance under high-velocity steam conditions.

2.4. Sapphire (0001) Volatility in High-Velocity Steam

2.4.1. Introduction

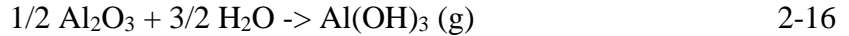
Chapters 2.1, 2.2, and 2.3 studied complex silicate compounds after exposure to high-velocity steam, where reaction enthalpies were calculated from mass loss and recession data to determine temperature dependences for the steam reactions occurring. It was believed that select volatilization of SiO_2 from HfSiO_4 and $\text{Yb}_2\text{Si}_2\text{O}_7$ would result in a reaction enthalpy similar to that of pure SiO_2 , yet experimental values were much higher than predicted. The quantitative nature of the steamjet experimental setup had not yet been verified for simple oxides, whose thermodynamic and kinetic properties are well studied compared to complex compounds.

Table 2-6 displays the steam reactions for various materials, along with material melting temperatures and estimated reaction enthalpies from Meschter et al. [13]. Each material was categorized by the dominant metal (M) hydroxide product phase, $\text{M}(\text{OH})_x$ (g). The temperature dependences for the presented oxides range from 150 – 300 kJ/mol, with the exception of SiO_2 . P_2O_5 displays a melting temperature far too low for the interest of this work. The presence of alumina furnace ware has prevented quantitative analysis of most oxides in the steamjet, where alumina deposition or reaction to form aluminate compounds rapidly occur. Exposure of amorphous SiO_2 in the steamjet has been attempted, yet material shearing prevented accurate baseline measurements from being determined. Additionally, crystalline SiO_2 has multiple polymorph transitions and associated volume changes up to the temperature ranges of interest which would result in material cracking upon entry and removal of samples from the furnace. Thus, steam exposures of Al_2O_3 represent the clearest route for analysis of the temperature dependence of simple oxide volatilization in the steamjet.

Table 2-6. Oxide reaction enthalpies for formation of metal hydroxide gas species upon steam reaction.

Oxide	Reaction Enthalpy, kJ/mole	Steam Reaction	Oxide Melting Temperature, °C
P ₂ O ₅	172.56	0.5P ₂ O ₅ +0.5 H ₂ O = PO ₂ (OH)(g)	340
MgO	270.7	MgO + H ₂ O = Mg(OH) ₂	2852
CaO	266.15	CaO+H ₂ O = Ca(OH) ₂	2572
SrO	238.06	SrO+H ₂ O = Sr(OH) ₂	2531
BaO	163.37	BaO+H ₂ O = Ba(OH) ₂	1923
Y ₂ O ₃	290.24	0.5Y ₂ O ₃ +1.5H ₂ O=Y(OH) ₃	2425
Al ₂ O ₃	184.61	0.5Al ₂ O ₃ +1.5H ₂ O=Al(OH) ₃	2072
ZrO ₂	209.95	ZrO ₂ +2H ₂ O=Zr(OH) ₄	2715
SiO ₂	53.67	SiO ₂ +2H ₂ O=Si(OH) ₄	1710

High-velocity steam exposures were performed on basal plane (0001) sapphire to determine the reaction kinetics for the following:



Alumina furnace ware reacts with water vapor to also form the Al(OH)₃ (g) species, such that low velocity regions of the samples were expected to have suppressed steam reactions due to saturation of hydroxide species in the gas boundary layer. At the high velocities of interest, a water vapor partial pressure of 1 atm promoted the steam volatilization of sapphire.

Material recession depths and mass loss data were utilized to calculate the temperature dependence for Al(OH)₃ (g) formation from 1200 °C – 1450 °C as a comparison to data from FactSage thermodynamic database and from the literature. Calculated reaction enthalpies of oxides and complex compounds in the steamjet will be discussed.

2.4.2. Methods

C-plane Al₂O₃ (0001) samples were received from MTI Corporation (Richmond, Ca.) as 10 x 10 x 1 mm coupons with both faces polished to less than 5 Å average roughness. Sample exposures were performed at 1200 °C, 1300 °C, 1400 °C, and 1450 °C with a water inlet flow rate of 1.65 ml/min and a sample loading/unloading rate of ~100 °C/min. To prevent sample cracking, samples were loaded into the furnace with the steam already flowing to ensure water volatilization in the steamjet capillary was at equilibrium. Sample mass loss was recorded for each specimen (MS105DU, Mettler-Toledo, Columbus, OH) before and after steam exposures. Samples were then sputter coated with a reflective Au/Pd film to produce surface topography maps via white light profilometry (Zygo: NewView 7300: Middlefield, CT). Recession linescans were created with Mountain Maps software (Digital Surf, France) to determine the maximum recession depths for each sample, with the unreactive sample regions as references to the initial sample heights. Steam velocities were calculated with ANSYS (Canonsburg, PA) computational fluid dynamics module for each temperature at the given water flow rate. The maximum sample recession corresponds to the maximum steam velocity and was used for analysis of the Al₂O₃ (0001) steam reaction alongside specific mass loss data.

2.4.3. Results

The FactSage SGPS database was used to calculate the equilibrium partial pressure of Al(OH)₃ (g) for Reaction 2-16 from 1000 °C – 1500 °C, as shown in Figure 2-43. Al(OH)₃ (g) is the dominant hydroxide species expected to form. The next most stable aluminum hydroxide species was Al(OH)₂ (g) with a partial pressure of 1.1x10⁻¹⁰ atm at 1500 °C. Formation of all Al(OH)_x (g) species besides Al(OH)₃ (g) were considered negligible and were not accounted for in future analysis.

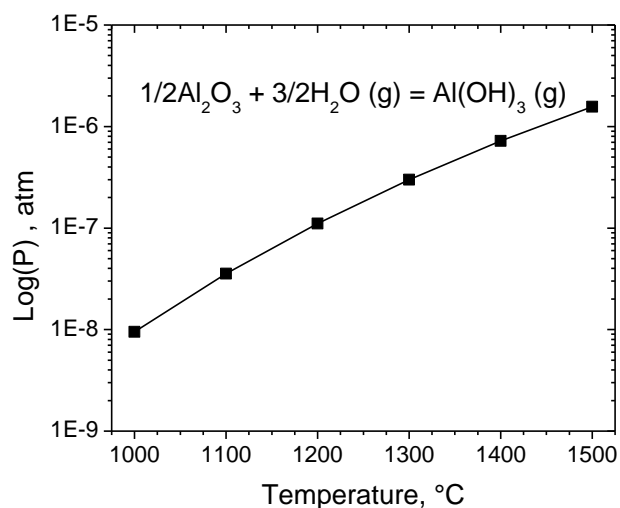


Figure 2-43. Al(OH)_3 (g) partial pressures, calculated with FactSage SGPS database for 1 atm H_2O (g).

Profilometer maps for three Al_2O_3 (0001) samples after steam exposure for 24 hours are presented in Figure 2-44, where each profile has the same color scale corresponding to the surface depth. The 1 mm circular impingement site on each sample decreases in relative depth with increasing temperature, corresponding to increased Al_2O_3 volatilization at the highest steam velocities. The left side of each sample is upstream of the gas flow direction. Negligible steam reactivity occurred in the upstream regions, which provided references for the maximum recession depth at the impingement site.

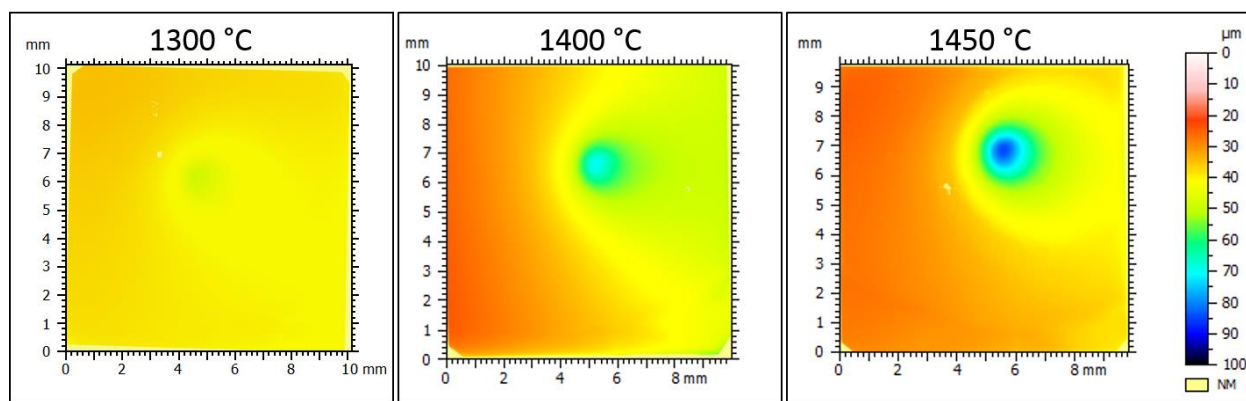


Figure 2-44. Profilometry maps for Al_2O_3 (0001) after steam exposure for 24h at 1300 °C, 1400 °C, and 1450 °C.

Figure 2-45 displays the profilometry map and recession linescan for Al_2O_3 (0001) exposed to steam at 1300 °C for 24 hours, where the recession depth color scale has been adapted to better display the volatilization behavior across the sample. A linescan was taken across the arrow on the profilometry map and is compared to the ANSYS steam velocity. Material recession is plotted inversely to provide a direct comparison to calculated steam velocities. The impingement site displayed a maximum recession of 14.3 μm at a gas velocity of 184 m/s. Profilometer data and subsequent recession linescans for all test samples are presented in Appendix 8.1.

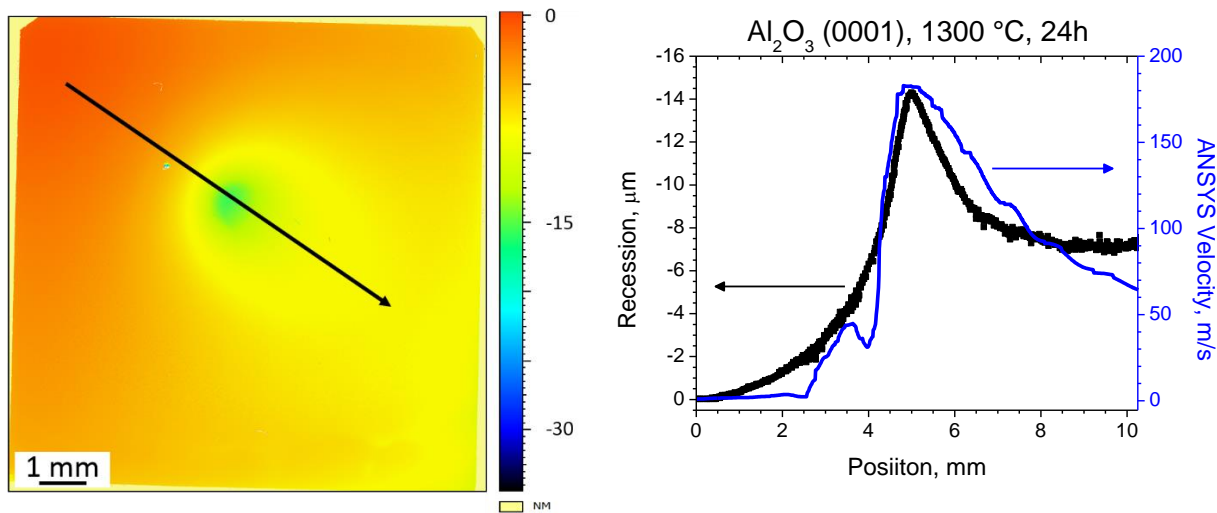


Figure 2-45. Surface topography of Al_2O_3 (0001) exposed to steam at 1300 °C for 24h. Recession depths along the arrow are plotted against position and compared to the calculated ANSYS steam velocity distribution through the impingement site.

Maximum recession and specific mass loss data for each sample are presented in Figure 2-46 and Figure 2-47, respectively. Mass loss data were considered accurate due to the minimal sample cracking and lack of additional sample reactions with furnace ware. Linear reaction rates for both mass loss and maximum recession data are presented in Table 2-7. The calculated velocities for each temperature are also presented, as maximum steam velocities varied between 173 – 202 m/s for the 1200 °C – 1450 °C temperature range.

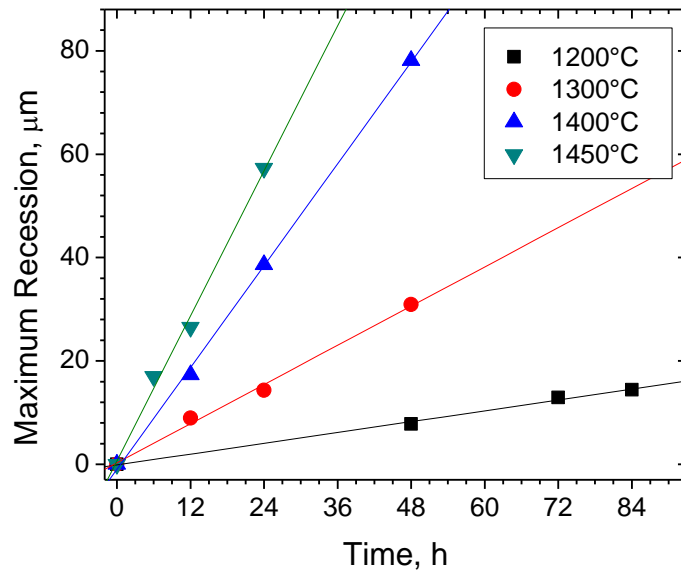


Figure 2-46. Maximum recession depth plotted against time (hours) for (0001) Al_2O_3 reactions with high-velocity steam.

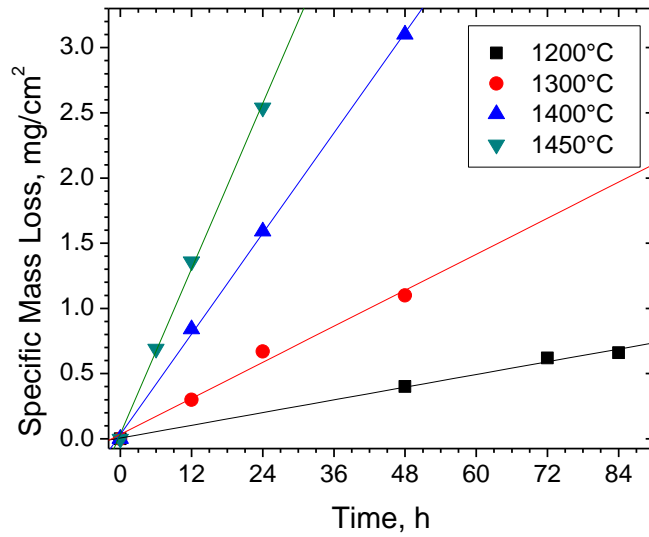


Figure 2-47. Specific mass loss plotted against time (hours) for (0001) Al_2O_3 reactions with high-velocity steam.

Table 2-7. Linear reaction rates for Al₂O₃ (0001) after high velocity steam exposures.

Temperature	Linear Reaction Rates		Maximum Velocity
°C	mg/cm ² h	μm/h	m/s
1200	8.1 ± 0.2 × 10 ⁻³	0.18 ± 0.01	173
1300	2.3 ± 0.2 × 10 ⁻²	0.63 ± 0.03	184
1400	6.4 ± 0.1 × 10 ⁻²	1.64 ± 0.04	196
1450	1.05 ± 0.03 × 10 ⁻¹	2.3 ± 0.1	202

2.4.4. Analysis

FactSage equilibrium partial pressures from Figure 2-43 were used to calculate a theoretical temperature dependence for Reaction 2-16 through the following relationship:

$$P_{Eq} \propto T^{\frac{3}{2}} \exp\left(-\frac{\Delta H_{rxn}}{RT}\right) \quad 2-17$$

where P_{Eq} is the equilibrium partial pressure of Al(OH)₃ (g), T is temperature, R is the universal gas constant, and H is the reaction enthalpy. A reaction enthalpy of 192 kJ/mol was calculated from Eq. 2-17 for the FactSage SGPS thermodynamic data.

The temperature dependences for the mass loss and maximum recession data were also dependent on gas phase interdiffusion through a boundary layer created by the steam flow, and thus require an additional T^{3/2} temperature dependence, as shown in Equation 2-18.

$$k_l \propto \left[D_{1,2} \times \exp\left(-\frac{\Delta H_{rxn}}{RT}\right) \right] \propto T^{\frac{3}{2}} \exp\left(-\frac{\Delta H_{rxn}}{RT}\right) \quad 2-18$$

Temperature dependences and calculated reaction enthalpies for (0001) plane Al₂O₃ exposed to high-velocity steam and FactSage SGPS calculations are presented in Figure 2-48 with slope analysis in Table 2-8. Mass loss and maximum recession data displayed reaction enthalpies of 197 ± 5 kJ/mol and 200 ± 10 kJ/mol, respectively, in good agreement with each other. Both values were slightly higher than the reaction enthalpy determined from FactSage,

which may have been due to the slightly increasing steam velocity with increasing furnace temperature.

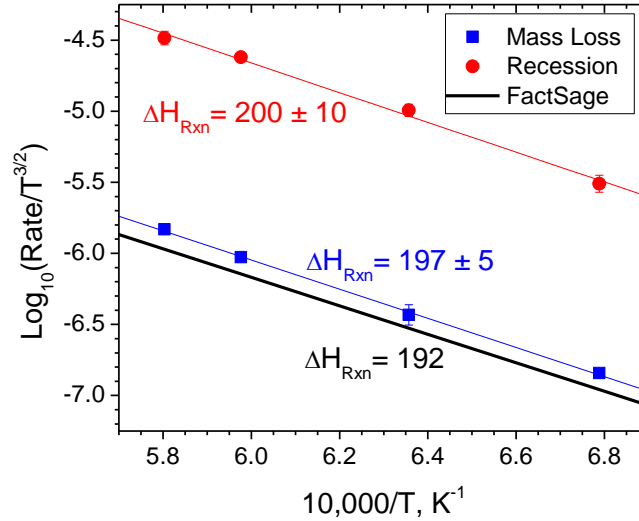


Figure 2-48. Temperature dependences for specific mass loss and maximum recession data for Al_2O_3 in steam, compared to FactSage SGPS calculations.

Table 2-8. Slopes and reaction enthalpies for the temperature dependences plotted in Figure 2-48 for the reactions of Al_2O_3 with steam.

	Temperature Dependence		
	mg/cm ² h	um/h	FactSage
Slope	-1.03 ± 0.03	-1.05 ± 0.05	-1.00135
ΔH_{Rxn} , kJ/mol	197 ± 5	200 ± 10	192

2.4.5. Discussion

Rapid testing of (0001) plane Al_2O_3 in high-velocity steam was performed to calculate the reaction enthalpy for the temperature dependence of the reaction with steam. Experimental and calculated reaction enthalpies for $\text{Al}(\text{OH})_3$ (g) formation are presented in Table 2-9. An average value was determined from the literature to be 203 ± 15 kJ/mol. Mass loss and recession data from this work resulted in reaction enthalpies of 197 ± 5 kJ/mol and 200 ± 10 kJ/mol,

respectively, which were both in agreement with the reaction enthalpies determined from FactSage and the literature.

Table 2-9. Reaction enthalpies for the steam reaction with Al_2O_3 to form $Al(OH)_3$ (g).

ΔH_{Rxn} , kJ/mol	Notes
229	Ab Initio [55]
210 ± 20	Thermogravimetric analysis (0001) plane Al_2O_3 [56]
210 ± 9	Transpiration measurements of $CaAl_4O_7$ [57]
192	FactSage SGPS
191	Calculated [58]
185	Calculated [13]
Average	
203 ± 15	

The results of this work confirm that formation of $Al(OH)_3$ (g) is the rate-limiting step for the Al_2O_3 volatilization reaction in steam. For complex oxides, such as $HfSiO_4$ and $Yb_2Si_2O_7$ studied in Chapters 2.2 and 2.3, $Si(OH)_4$ (g) was the predicted rate limiting step due to the selective removal of SiO_2 to produce porous HfO_2 and Yb_2O_3 -rich reaction products. The stability of the reaction product layer implied negligible volatilization of HfO_2 and Yb_2O_3 for sample cross-sections. Calculated reaction enthalpies for $HfSiO_4$ and $Yb_2Si_2O_7$ were 207 ± 39 kJ/mol and 207 ± 5 kJ/mol, respectively, while the calculated reaction enthalpy for SiO_2 was near 56 kJ/mol [22]. The temperature dependences for the $HfSiO_4$ and $Yb_2Si_2O_7$ reactions must then be linked to one of the following: 1. The transport of gas species through a porous reaction product layer grown on complex silicates after steam exposure, or 2. The volatilization reaction of SiO_2 from the complex silicates. Gas transport has been traditionally represented with very low temperature dependences, $T^{3/2}$, consistent with the kinetic theory of gases. It is hypothesized here that the temperature dependence, and thus the reaction enthalpy, of SiO_2 volatilization for

complex silicates is being measured correctly with the steamjet experimental setup. The reaction enthalpies for complex silicate compounds would then be unique values compared to that of pure SiO₂.

The steam reaction for CaAl₄O₇ was utilized to accurately determine reaction enthalpies comparable to formation of Al(OH)₃ (g) through indirect transpiration measurements, as presented earlier [57]. Such testing of complex compounds such as CaAl₄O₇ implies that compounds should display similar reaction enthalpies as their constituent volatile oxide species, such as was seen with analysis of BSAS in high-velocity steam in Chapter 2.1. Though, CaAl₄O₇ displayed both volatilization of CaO and Al₂O₃, suggesting a porous reaction product was not present on the surface after steam measurements. Contrarily, Table 2-10 presents estimated reaction enthalpies for P₂O₅, Al₂O₃, and AlPO₄ (0.5 Al₂O₃·0.5 P₂O₅) provided by Meschter et al. [13]. The reaction enthalpies for P₂O₅ and Al₂O₃ are similar, despite their unique gas product species upon steam reaction and widely different melting temperatures.

Table 2-10. Reaction enthalpies, steam reactions, and melting temperatures for P₂O₅, Al₂O₃, and AlPO₄, from [13].

Oxide	Reaction Enthalpy, kJ/mole	Reaction	Oxide Melting Temperature, °C
P ₂ O ₅	173	0.5P ₂ O ₅ +0.5 H ₂ O = PO ₂ (OH)(g)	340
Al ₂ O ₃	185	0.5Al ₂ O ₃ +1.5H ₂ O=Al(OH) ₃	2072
AlPO ₄	303	AlPO ₄ (c) + 0.5H ₂ O(g) = 0.5Al ₂ O ₃ + PO ₂ (OH)(g)	1800

Selective volatilization of P₂O₅ from AlPO₄ has been determined experimentally [59], where a porous Al₂O₃ product layer is present after steam exposures. Yet, the estimated reaction enthalpy for AlPO₄ does not agree with that of pure P₂O₅ and is not represented by any form of rule of mixtures between P₂O₅ and Al₂O₃. While the reaction enthalpies presented are not experimentally determined, the volatilization behavior of P₂O₅ agrees with the current theory that

complex compounds that react with steam to form a porous product layer may not display similar reaction enthalpies as their individual volatile components.

2.4.6. Conclusion

Rapid high-velocity steam testing was performed for (0001) plane Al_2O_3 from 1200 °C – 1450 °C. Linear reaction kinetics were measured for formation of $\text{Al}(\text{OH})_3$ (g). The temperature dependences for specific mass loss and maximum recession data resulted in reaction enthalpies of 197 ± 5 kJ/mol and 200 ± 10 kJ/mol, respectively. Reaction enthalpies in this work were in agreement with thermodynamic calculations and literature values, which support the quantitative nature of the steamjet experimental setup and verifies formation of $\text{Al}(\text{OH})_3$ (g) as the rate-limiting step for Al_2O_3 exposed to water vapor. The results of this work suggest that complex compounds, such as HfSiO_4 and $\text{Yb}_2\text{Si}_2\text{O}_7$, show temperature dependences related to production of $\text{Si}(\text{OH})_x$ (g) species. Reaction enthalpies for complex compounds may be unique values compared to that of the pure oxides exposed to water vapor, depending on the production of a porous product layer, although future work is needed to verify this hypothesis.

2.5. Preferred Orientations for Steam Reaction Products of $Y_2Si_2O_7$, Y_2SiO_5 , and $Y_3Al_5O_{12}$ Single Crystals

2.5.1. Introduction

Preliminary steam testing was performed on single crystal compounds, received from Dr. Peter Mechnich (German Aerospace Center (DLR), Köln) of δ - $Y_2Si_2O_7$ (Pna21), X2 phase Y_2SiO_5 (C2/c), and $Y_3Al_5O_{12}$ (YAG, garnet) to determine orientation effects for the respective steam reactions. Figure 2-49 displays the Y_2O_3 - Al_2O_3 and Y_2O_3 - SiO_2 pseudobinary phase diagrams relevant for these material systems. Due to the excellent stability of Y_2O_3 in high-velocity steam [27], all compounds are expected to produce yttria-rich compounds upon reaction with steam. Based on the phase diagrams, YAG should react with steam to produce any of the following Al_2O_3 -depleted phases: $YAlO_3$ (YAP), $Y_2Al_4O_9$ (YAM), and Y_2O_3 . $Y_2Si_2O_7$ and Y_2SiO_5 were expected to form Y_2SiO_5 and Y_2O_3 steam reaction products, respectively.

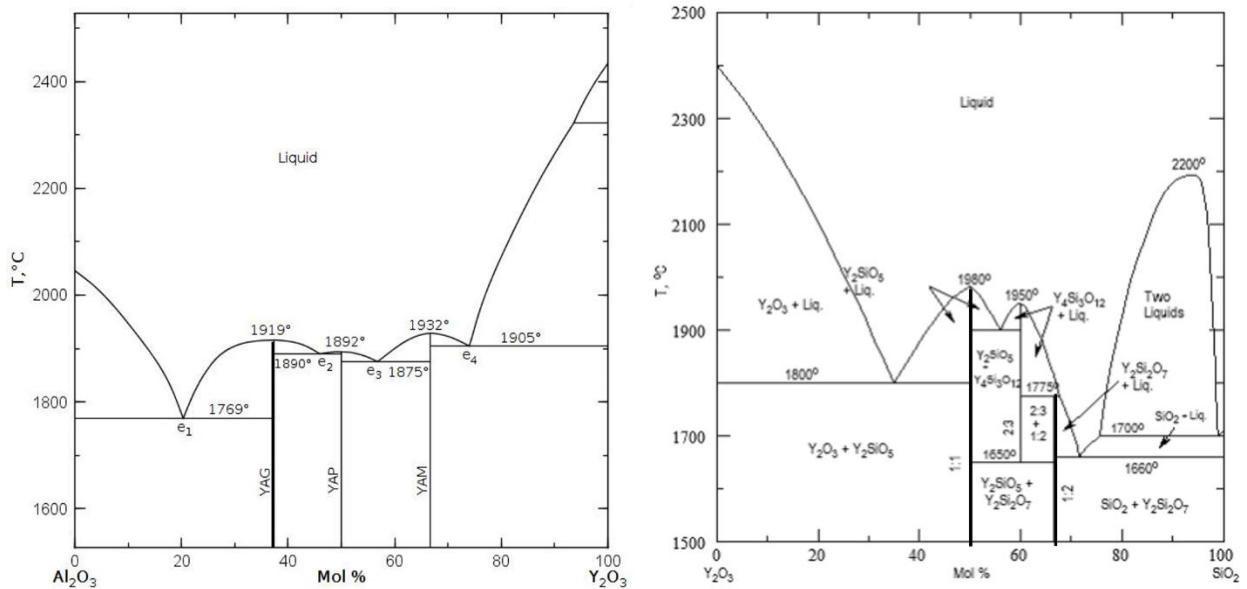


Figure 2-49. Pseudobinary phase diagrams for the Y_2O_3 - Al_2O_3 [60] and Y_2O_3 - SiO_2 [61] systems.

2.5.2. Methods

The $\text{Y}_2\text{Si}_2\text{O}_7$ single crystal was received without knowledge of the polymorph. Structure and crystal data for $\text{Y}_2\text{Si}_2\text{O}_7$ were obtained with a Bruker Kappa APEXII Duo Diffractometer equipped with a fine-focus sealed tube ($\text{Mo K}\alpha$, $\lambda = 0.71073 \text{ \AA}$) and a graphite monochromator. Data integration resulted in 3493 total reflections up to a maximum theta angle of 28.28° with 0.75 \AA resolution. The $\text{Y}_2\text{Si}_2\text{O}_7$ structure was solved and refined using the Bruker SHELXTL Software Package [62] within APEX3 [63] and OLEX2 [64] to be an orthorhombic crystal structure with space group Pnma and $Z=4$. A final structure model is presented in Figure 2-50 where red atoms are oxygen, blue atoms are silicon, and teal atoms are yttrium. Orthorhombic $\text{Y}_2\text{Si}_2\text{O}_7$ is often termed the δ -phase in the rare earth orthosilicate literature, and will be referred to as such throughout this work. The cell constants of $\delta\text{-Y}_2\text{Si}_2\text{O}_7$ were $a = 13.6788(15) \text{ \AA}$, $b = 8.1574(9) \text{ \AA}$, $c = 5.0243(5) \text{ \AA}$, and volume = $560.63(10) \text{ \AA}^3$. The calculated density was 4.099 g/cm^3 . Additional information, such as atomic coordinates, bond lengths, and bond angles can be found in Appendix 8.2.

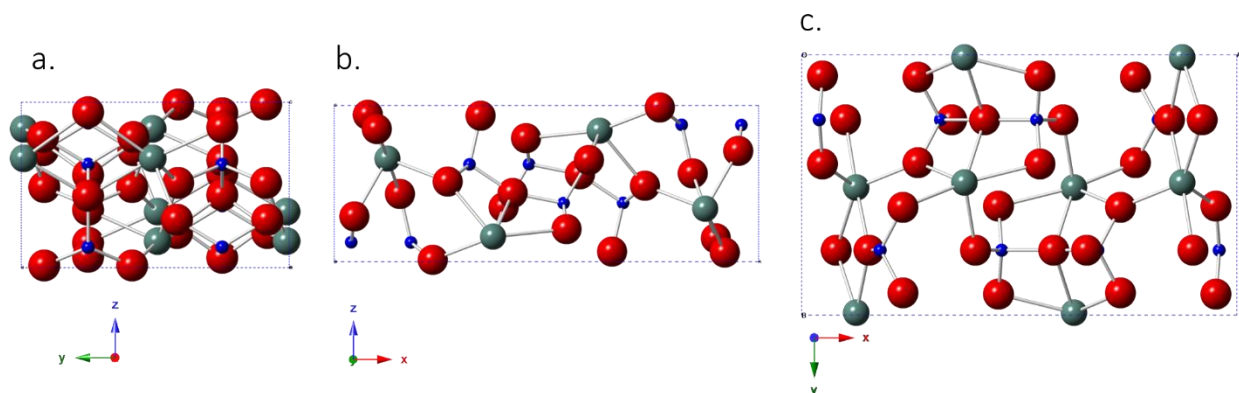


Figure 2-50. The calculated crystal structure of $\delta\text{-Y}_2\text{Si}_2\text{O}_7$ viewed from the a , b , and c orthogonal axes. Red atoms are oxygen, blue atoms are silicon, and teal atoms are yttrium.

Single crystals Y_2SiO_5 and YAG were received with knowledge of crystal structure and composition but no orientation information. Powder XRD was used to determine which hkl plane

was in plan view prior to testing. Single steamjet exposures for each single crystal were performed at 1200 °C for 60 hours. The steamjet setup was been described in Chapter 2.1. For each single crystal, the impingement site experienced excessive mechanical erosion and thermal shock cracking from loading and unloading the samples from the furnace, which prevented quantitative analysis on specific mass loss and depletion depths. Therefore, plan view analysis of the material surfaces after steam exposures was performed with XRD and SEM/EDS.

2.5.3. Results

2.5.3.1. Single Crystal δ - $Y_2Si_2O_7$ Steamjet Exposure

Figure 2-51 displays XRD of the single crystal δ - $Y_2Si_2O_7$ before and after 1200 °C steam exposure for 60 hours. The (301) hkl plane was present for δ - $Y_2Si_2O_7$ prior to testing, corresponding to the plane in plan view for the single crystal. After steam exposure, two silica-depleted product phases were observed: $Y_{9.33}\square_{0.67}Si_6O_{26}$ and Y_2SiO_5 . The $Y_{9.33}\square_{0.67}Si_6O_{26}$ is a hexagonal apatite phase, and Y_2SiO_5 is monoclinic C2/c, corresponding to the X2 phase for rare earth monosilicates. Due to peak overlap, many peaks could not be differentiated between the two product phases. The peak positions and matched hkl planes for the reaction products are presented in Table 2-11, representing clear preferential orientation for the steam reaction. The intensity of the $Y_{9.33}\square_{0.67}Si_6O_{26}$ hkl peaks (200) and (211) relative to Y_2SiO_5 implies that $Y_{9.33}\square_{0.67}Si_6O_{26}$ may be the dominant surface reaction product.

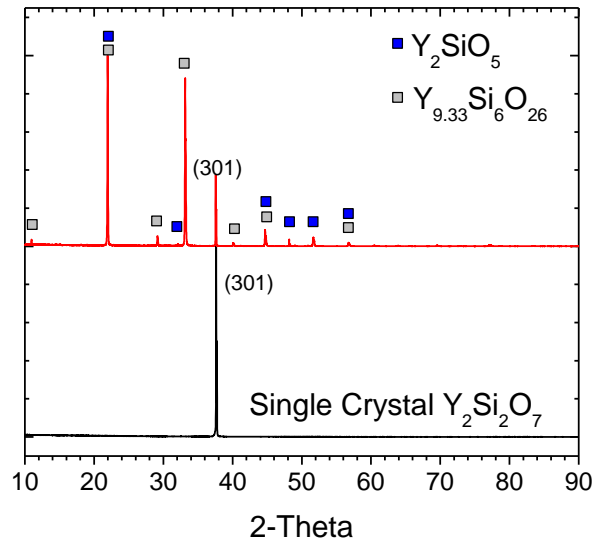


Figure 2-51. Single crystal δ - $Y_2Si_2O_7$ before and after exposure to high-velocity steam at 1200 °C for 60 hours.

Table 2-11. Peak positions and hkl values for reaction products of $Y_2Si_2O_7$ after steam exposure at 1200 °C for 60h.

$Y_{9.33}\square_{0.67}Si_6O_{26}$, 01-086-5065		Y_2SiO_5 , 01-074-2011	
$^{\circ}2\theta$	(hkl)	$^{\circ}2\theta$	(hkl)
10.942	100	21.873	-211
21.985	200	31.934	220
29.221	210	44.612	006 / 132
33.221	211	48.176	413
40.026	122	51.696	-521 / 233
44.836	400	56.841	042
56.797	322		

Figure 2-52 displays the surface morphology around the steam impingement site, where the impingement site was lost due to mechanical erosion. From EDS analysis, the impingement site region (Figure 2-52a) consisted of Y_2SiO_5 , and a lower gas velocity region 1 mm below the impingement site (Figure 2-52b) consisted of $Y_2Si_2O_7$ and $Y_{9.33}\square_{0.67}Si_6O_{26}$. EDS results matched with the expected phase identification from XRD analysis. Upstream regions of the sample (Figure 2-52c) consisted of multi-phase regions with varying Y-Si-Al-O concentrations with the

resultant Al concentration from reaction with alumina furnace ware. Figure 2-52d is representative of the near stagnant gas velocity regions where δ - $Y_2Si_2O_7$ was left unreacted on the sample surface.

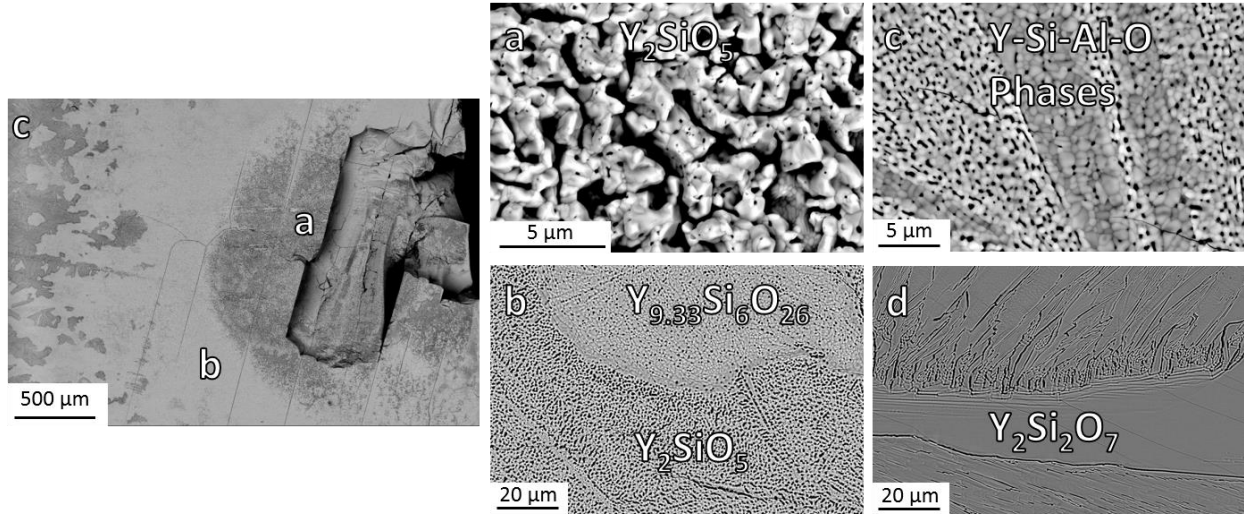


Figure 2-52. Low magnification SEM of the $Y_2Si_2O_7$ impingement site region after steam exposure at 1200 °C for 60h, with higher magnification of specific regions: a. Y_2SiO_5 formation at the impingement site, b. Y_2SiO_5 and $Y_{9.33}Si_6O_{26}$ formation two-phase region, c. upstream formation of silica-depleted Y-Si-Al-O phases, and d. Stagnant gas velocity regions of unreacted δ - $Y_2Si_2O_7$.

2.5.3.2. Single Crystal Y_2SiO_5 Steamjet Exposure

XRD for X2-phase Y_2SiO_5 before and after steam exposure shown on a logarithmic scale in Figure 2-53. The (842) hkl peak for the initial single crystal orientation remained dominant after steam exposure at 1200 °C for 60 hours, reflecting the increased stability of Y_2SiO_5 compared to $Y_2Si_2O_7$ in high-velocity steam. Seven peaks could be matched to a cubic Y_2O_3 (ICDD pattern #04-006-1998) reaction product phase. Other unmatched peaks may correspond to surface reaction with alumina impurities from the alumina tube and furnace ware.

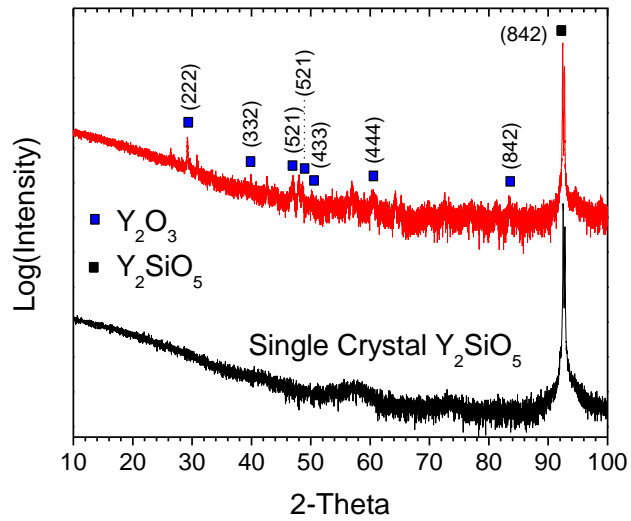


Figure 2-53. Single crystal X2 phase Y_2SiO_5 before and after exposure to high-velocity steam at 1200 °C for 60 hours.

Figure 2-54a displays the impingement region with excessive material loss by mechanical erosion at the impingement site. The steam impingement zone is marked by the white oval on the figure. Surrounding the impingement site, faceted Y_2O_3 formation was confirmed by EDS, corresponding to the matched XRD peaks for cubic Y_2O_3 .

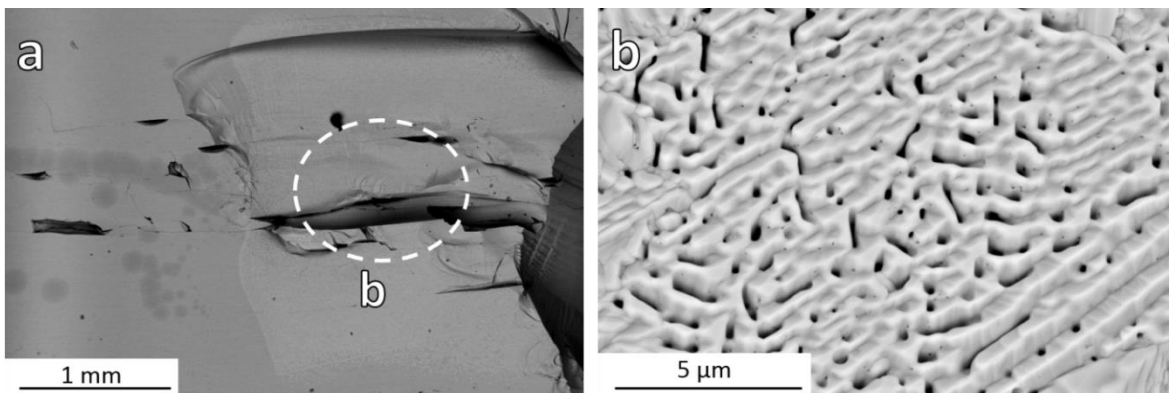


Figure 2-54. a. Low magnification SEM of the Y_2SiO_5 impingement site region after steam exposure at 1200 °C for 60h, and b. higher magnification SEM image of the Y_2O_3 formation around the impingement site.

2.5.3.3. Single Crystal $Y_3Al_5O_{12}$ Steamjet Exposure

Logarithmic scale XRD of YAG before and after steam exposure is shown in Figure 2-55. The initial YAG single crystal had a plan view orientation of the (444) plane, with a minor

(11 3 2) hkl plane and two peaks corresponding to initial $Y_4Al_2O_9$ impurities. After steam exposure, Y_2O_3 and $Y_4Al_2O_9$ peaks were present. The (11 3 2) peak for YAG was not present after steam exposure, which may be representative of preferred water vapor attack compared to the (444) plane. The Y_2O_3 and $Y_4Al_2O_9$ reaction products formed with preferred orientation on the YAG surface, as shown in Table 2-12.

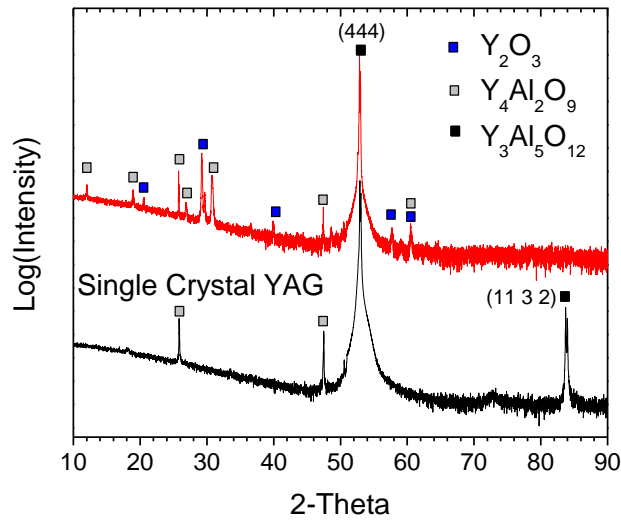


Figure 2-55. Single crystal YAG before and after exposure to high-velocity steam at 1200 °C for 60 hours.

Table 2-12. Peak positions and hkl values for reaction products of YAG after steam exposure at 1200 °C for 60h.

$Y_4Al_2O_9$, 01-084-6878		Y_2O_3 , 00-043-1036	
$^{\circ}2\theta$	(hkl)	$^{\circ}2\theta$	(hkl)
11.901	011	20.499	211
18.831	021 / 012	29.15	222
25.645	-122 / 112	39.838	332
26.876	031	57.614	622
30.689	220 / 032	60.433	444
47.482	143		
60.432	154		

Low magnification of the YAG impingement site is shown in Figure 2-56 where the impingement site is missing due to mechanical erosion from the high-velocity water vapor. Surrounding the impingement site (Figure 2-56a) Y_2O_3 formation was confirmed by EDS, representing full volatility of alumina from the system in the highest velocity regions. An alumina-depleted $Y_4Al_2O_9$ phase was present at intermediate steam velocities, shown in Figure 2-56b. Figure 2-56c displays heavily faceted $Y_4Al_2O_9$ on unreacted YAG at lower velocity sample regions and upstream regions. Upstream of the impingement site, alumina impurity concentrations from the experimental setup limit the volatilization of Al_2O_3 from the surface. It is therefore assumed that the $Y_4Al_2O_9$ present on the surface as shown in Figure 2-56c is representative of the initial $Y_4Al_2O_9$ in the YAG single crystal shown earlier with XRD.

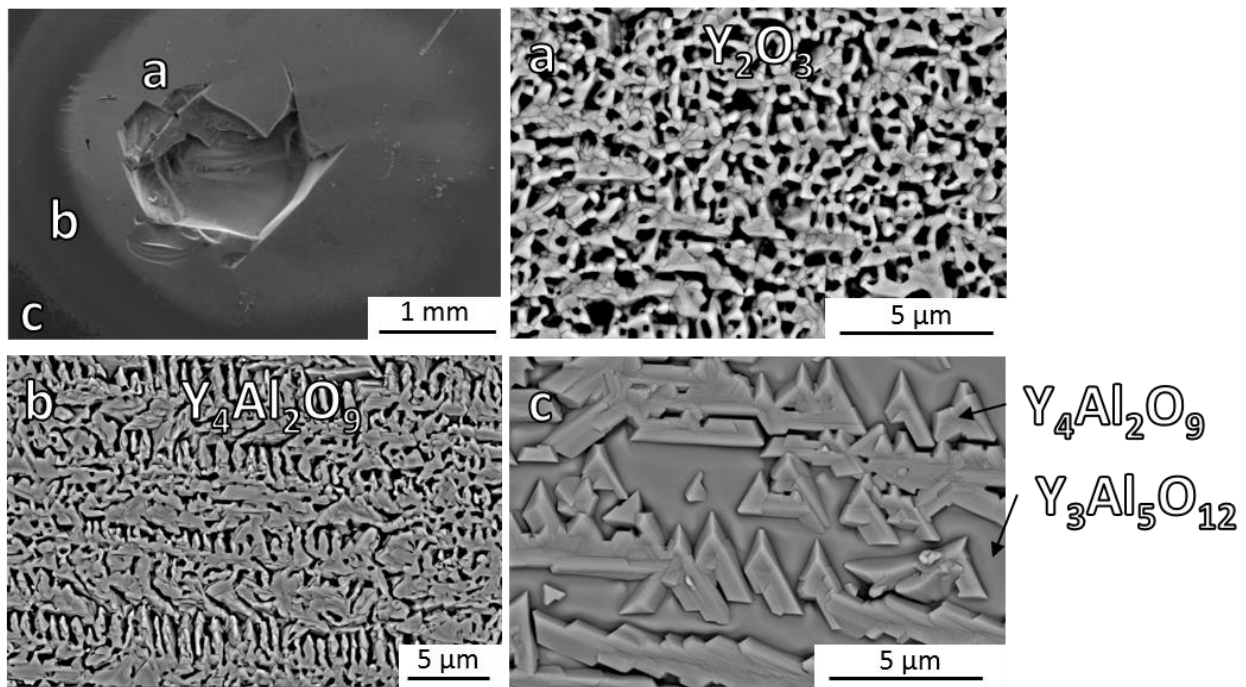


Figure 2-56. Low magnification SEM of the YAG impingement site region after steam exposure at 1200 °C for 60h, with higher magnification of specific regions: a. Y_2O_3 formation surrounding the impingement site, b. $Y_4Al_2O_9$ formation outside of the Y_2O_3 region, c. $Y_4Al_2O_9$ faceting on unreacted $Y_3Al_5O_{12}$ (YAG).

2.5.4. Discussion

The brittle nature of single crystal ceramics compared to polycrystalline materials resulted in excessive mechanical erosion at the highest velocity impingement site, which greatly limited the depth of this study. Still, a clear directional dependence for the growth of high-velocity steam reaction products was shown for single crystals δ - $\text{Y}_2\text{Si}_2\text{O}_7$, Y_2SiO_5 , and $\text{Y}_3\text{Al}_5\text{O}_{12}$ (YAG) exposed to water vapor at 1200 °C for 60 hours. The presence of Y_2O_3 and Y_2O_3 -rich reaction products in steam verified the findings in the literature that rare earth oxides show excellent stability in high-velocity steam relative to SiO_2 and Al_2O_3 [27], [29].

Both single crystal Y_2SiO_5 and YAG produced the expected steam reaction products based on the available phase diagrams. The δ - $\text{Y}_2\text{Si}_2\text{O}_7$ single crystal reacted with steam to form Y_2SiO_5 and $\text{Y}_{9.33}\square_{0.67}\text{Si}_6\text{O}_{26}$ product phases in the highest steam velocity regions where alumina contamination was minimal. The formation of the $\text{Y}_{9.33}\square_{0.67}\text{Si}_6\text{O}_{26}$ apatite phase was unexpected and was not been seen for polycrystalline β - $\text{Y}_2\text{Si}_2\text{O}_7$ under comparable furnace conditions [27]. According to the phase diagram, the apatite phase is not stable below 1650 °C [61]. Rare earth apatite formation may preferentially occur from $\text{RE}_2\text{Si}_2\text{O}_7$ with a dependence on the stable $\text{RE}_2\text{Si}_2\text{O}_7$ polymorph or with a dependence on the hkl plane undergoing the steam reaction process.

2.5.5. Conclusion

Preferential growth of steam reaction products was shown for single crystal δ - $\text{Y}_2\text{Si}_2\text{O}_7$, Y_2SiO_5 , and $\text{Y}_3\text{Al}_5\text{O}_{12}$ (YAG) exposed to water vapor at 1200 °C for 60 hours. While both Y_2SiO_5 and $\text{Y}_3\text{Al}_5\text{O}_{12}$ displayed reaction products predicted from their respective phase diagrams, δ - $\text{Y}_2\text{Si}_2\text{O}_7$ produced the $\text{Y}_{9.33}\square_{0.67}\text{Si}_6\text{O}_{26}$ apatite phase, which has not been a reported steam reaction product reported for polycrystalline $\text{Y}_2\text{Si}_2\text{O}_7$ steam exposures. Additional study

should include analysis of the requirements for formation of the rare earth apatite phases in steam environments, as well as the stability of the apatite phase in the 1000 °C-1500 °C temperature range.

2.6. Summary

The steamjet was used to model the high gas velocities of a combustion environment at 1 atm total pressure with 1 atm H₂O (g) surrounding the sample impingement site. EBC reaction products and microstructural evolution of reaction products were observed for the 1200 °C – 1400 °C temperature range. Qualitative information, such as reaction rates, gas velocity dependences, and reaction enthalpies were determined from sample analysis.

The formation of steam reaction products and the associated porosity networks varied greatly for each material studied. The steam reaction product for BSAS was unprotective at 1200 °C and 1300 °C, and not present for 1400 °C steam exposures, resulting in linear reaction kinetics. This work provides a better understanding for results in the literature, where lower temperature testing of BSAS produces a silica-depleted reaction product while higher temperature steam exposures display volatilization of all oxide components with no reaction product.

HfSiO₄ produced a highly porous HfO₂ steam reaction product with spherical sub-micron sized grains and a uniformly distributed pore network. The excellent stability of HfO₂ was related to its high melting temperature of 2758 °C [36] which prevented microstructural evolution and sintering with both time and temperature. The HfO₂ reaction layer was especially susceptible to mechanical erosion at regions of high steam velocities without microstructural evolution of HfO₂ or the associated pore network, which prevents HfSiO₄ from being an acceptable EBC candidate for turbine applications.

The steam reaction of Yb₂Si₂O₇ resulted in formation of a porous Yb₂SiO₅ reaction layer. The reaction layer displayed alignment of porosity channels normal to the interface, suggesting some degree of atomic mobility at each exposure temperature. Additional microstructural

changes were seen at the higher gas velocities, where the Yb_2SiO_5 surface densified and shut off water vapor transport to the underlying $\text{Yb}_2\text{Si}_2\text{O}_7$ substrate. This beneficial densification of the reaction product decreased the total reaction depths compared to lower velocity regions of the sample, and may also represent a reason for increased resistance to mechanical erosion compared to porous HfO_2 . The Yb_2SiO_5 densified intermediate layer underwent a secondary reaction to form Yb_2O_3 at a greatly reduced reaction rate compared to that of $\text{Yb}_2\text{Si}_2\text{O}_7$. The relationships between exposure temperature, water vapor velocity, water vapor partial pressure, and the densification of the steam reaction product are now presented as major questions for future research to better understand microstructural changes that EBCs may undergo in turbine environments.

The temperature dependences for HfSiO_4 and $\text{Yb}_2\text{Si}_2\text{O}_7$ were predicted to agree with the reaction enthalpy for pure SiO_2 , although much higher values were determined experimentally. The quantitative nature of the steamjet was verified through rapid testing of basal plane sapphire to determine the temperature dependence for the formation of $\text{Al}(\text{OH})_3$ (g). Reaction enthalpies calculated in this work for HfSiO_4 , $\text{Yb}_2\text{Si}_2\text{O}_7$, and Yb_2SiO_5 are thus reliable, and future work should be performed to verify the meaning of these values.

Quantitative analysis verified the expected linear reaction kinetics (k_l , $\mu\text{m}/\text{h}$) for BSAS and the parabolic reaction kinetics (k_p , $\mu\text{m}^2/\text{h}$) for HfSiO_4 and $\text{Yb}_2\text{Si}_2\text{O}_7$ materials in high velocity steam, summarized in Figure 2-57. $\text{Yb}_2\text{Si}_2\text{O}_7$ displayed the slowest degradation rates for each exposure temperature compared to HfSiO_4 and BSAS, even without considering the beneficial densification of Yb_2SiO_5 product layer observed at the higher steam velocities.

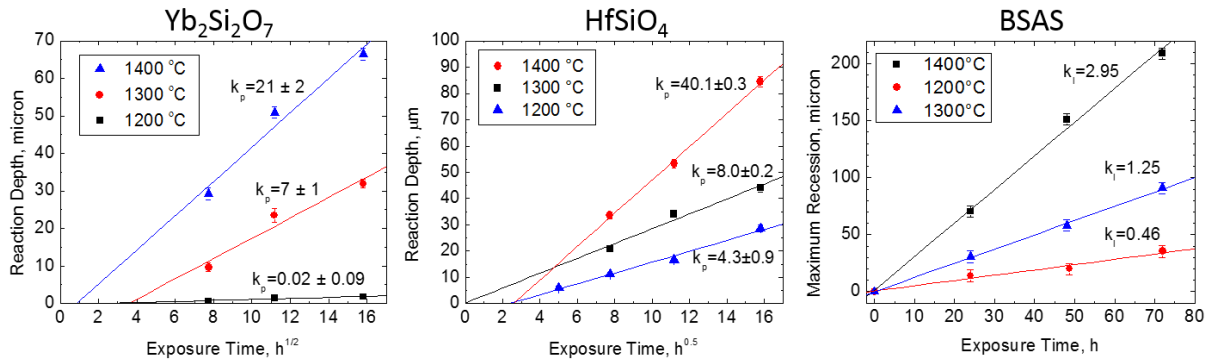


Figure 2-57. Steam reaction depths plotted against time for Yb₂Si₂O₇, HfSiO₄, and BSAS at 1200 °C, 1300 °C, and 1400 °C.

Environmental barrier coating candidates should display parabolic steam reaction kinetics through the formation of a semi-protective and porous product layer. Formation of a product phase requires one or more of the EBC oxide constituents to be chemically stable in high-temperature water vapor. Desirable EBCs should produce a porous product phase that has the ability to sinter at relevant turbine conditions to further enhance steam resistance and coating durability.

3. Objective 2: Tailoring Rare Earth Silicate Thermal, Mechanical, and Chemical Properties

It is clear that with increasing fuel burn temperatures of turbine engines, CMC technology could be limited by the melting temperature of the silicon bond coat at 1414 °C. One approach to mitigate the melting of silicon is a dual-purpose thermal/environmental barrier coating (T/EBC) system or a multi-layer T/EBC system to decrease operating temperatures of the bond coat while still increasing fuel burn temperatures. A multi-functional T/EBC would primarily require that EBCs to have low thermal conductivities, to limit heat transport to the bond coat and CMC substrate. This solution also requires backside or interior cooling. Additionally, fuel burn at higher temperatures leads to an even greater need for tailored EBC thermal properties and chemical stability.

Rare earth silicates can be represented as complex $A_xB_yO_z$ compounds, where sites A and B represent rare earth elements and silicon, respectively. It is hypothesized that combinations of rare earth cations in multi-component solid solutions (multiple rare earth elements on the ‘A’ site) can be a method for optimizing thermal and chemical properties. The second objective of this dissertation analyzed trends in thermal and chemical properties that could be tailored through cation mixing and rare earth silicate solid solutions.

The concept of utilizing entropy has revolutionized materials design in many alloy and ceramic systems [65]–[69], challenging state-of-the-art materials design. “High entropy,” as commonly used to describe materials systems, refers to mixing at least 5 elements in equimolar or near equimolar proportions on a single atomic lattice site, which results in increased configurational entropy [69]. At elevated temperatures, entropy can become a dominating factor

for minimizing Gibbs free energy through $\Delta G = \Delta H - T\Delta S$, where ΔG is Gibbs free energy, ΔH is enthalpy, T is temperature, and ΔS is entropy [70]. Minimization of Gibbs free energy can lead to improved material stability at elevated temperatures, where changes in bond strength and melting temperature are hypothesized to contribute material property changes. A possible example of unique high entropy material properties was noted by Ushakov et al., where a single phase (La,Sm,Dy,Er,Nd)₂O₃ solution displayed a measured melting temperature (2456 ± 12 °C) higher than all of the individual constituent oxides [71]. Rare earth silicate specimens containing two or more rare earth cations in solid solution will be referred to as multi-component rare earth silicates in this work. Properties of these multi-component silicate systems, including CTE, CTE anisotropy, phase stability, steam resistance, thermal conductivity, and Young's Modulus will be characterized to understand any trends dependent on the rare earth constituents and to develop an optimized multi-component silicate T/EBC.

It has been shown with DFT and experimental work that flexural strength, elastic modulus, and thermal shock resistance are all dependent on rare earth cation mass for RE₂SiO₅ with the C2/c monoclinic crystal structure, termed the X2 structure [72]. Thermal expansion research has been mostly limited to mean expansion values via dilatometry, where no internal anisotropy is measured. Thermal expansion and Young's Modulus of multi-component silicates are predicted to follow a rule of mixtures with additions of multiple rare earth cations, as expansion and compression of bonds should be dictated by bond strength and the cation size. Mixing of rare earth disilicates has been shown to produce a minimum in thermal conductivity at equimolar amounts through mass and bonding heterogeneity across the lattice [73], and is predicted to also occur for the monosilicate phase [74], [75].

The silica activity, a thermodynamic metric used for comparing steam reactivity of rare earth silicates, is believed to be relatively constant for individual rare earth silicates with the same crystal structure. The silica activities of β -RE₂Si₂O₇ + RE₂SiO₅ for yttrium and ytterbium rare earth elements are near 0.2-0.3 at 1600 K, while for RE₂SiO₅ + RE₂O₃ the activity of silica is closer to $2-3 \times 10^{-3}$ [51], [53]. High-velocity steam testing of individual and multi-component RE₂Si₂O₇ will be performed to compare the steam reactivity for various silicates to verify the hypothesis that silica activity is relatively constant within a given two-phase field with changing rare earth cations. For rare earth silicates with similar silica activities, the average steam reaction depths for each material should also be similar. In addition to the average reaction depth, microstructural evolution of the steam reaction products will be determined and compared to HfSiO₄ and Yb₂Si₂O₇ materials addressed in Chapter 2. The steam reaction depths and reaction product microstructural changes will be compared against the melting temperatures of each tested material and rule of mixtures melting temperatures of multi-component silicates.

Computationally, Han et al. hypothesize that rare earth cation mixing in monosilicates could lead to possible tailoring of water vapor resistance through adjustment of Si-O bond strengths [76]. The low silica activity of the RE₂SiO₅ + RE₂O₃ dual phase field highlights the need to identify methods for tailoring rare earth monosilicates for use in turbine applications, although the thermal expansion anisotropy of RE₂SiO₅ currently prevent their use as standalone EBC materials. Both RE₂SiO₅ and RE₂O₃ are the expected reaction products for RE₂Si₂O₇ after exposure to steam, and thus, analysis of RE₂SiO₅ steam behavior remains vital for prediction of microstructural evolution and development of EBC lifetime prediction models.

Initial analysis of Sc₂SiO₅ and Yb₂SiO₅ exposures to high-velocity steam will be presented, followed by trends in thermal conductivity, thermal expansion, and thermal expansion

anisotropy for single and multi-component RE_2SiO_5 . High-velocity steam exposures for single rare earth cation $\text{RE}_2\text{Si}_2\text{O}_7$ will then be analyzed, followed by research on the thermal expansion, Young's Modulus, and thermal conductivity of single and multi-component $\text{RE}_2\text{Si}_2\text{O}_7$. Utilizing measured thermal expansion data and values from the literature, an empirical model for predicting silicate thermal expansion will be presented.

3.1. High-velocity Steam Resistance of Yb_2SiO_5 and Sc_2SiO_5

3.1.1. Introduction

Two RE_2SiO_5 materials, Yb_2SiO_5 and Sc_2SiO_5 , were subjected to high-velocity steam exposure at 1400 °C for 125 hours to verify the stability of rare earth monosilicates in high-velocity steam. Yb_2SiO_5 was chosen to compare to $\text{Yb}_2\text{Si}_2\text{O}_7$ steamjet exposures presented in Objective 1, as the Yb_2SiO_5 reaction product underwent an additional steam reaction to form Yb_2O_3 . Sc_2SiO_5 was chosen due to the small ionic radius and atomic mass of scandium compared to other rare earth cations and the limited analysis of Sc_2SiO_5 exposed to steam in the literature. Klemm et al. found that Sc_2SiO_5 displayed similar steam reaction kinetics to $\text{Sc}_2\text{Si}_2\text{O}_7$, although no microstructure images were presented with the data [48]. No other RE_2SiO_5 has been reported to have similar steam reaction kinetics as its $\text{RE}_2\text{Si}_2\text{O}_7$ counterpart.

3.1.2. Methods

The steamjet setup has been described in Chapter 2.1.2.2. Powders were ball milled for 24 hours with Y-ZrO₂ ball mill media and consolidated via spark plasma sintering (DCS 25-10 SPS, Thermal Technologies, Santa Rosa, Ca.) for 30 minutes at 1550 °C and 65 MPa. Yb_2SiO_5 and Sc_2SiO_5 coupons of 10x10x1.25 mm dimensions were annealed at 1500 °C for 24 hours and polished to 1 μm. Starting microstructures are shown in Figure 3-1. Yb_2SiO_5 displayed a minor $\text{Yb}_2\text{Si}_2\text{O}_7$ secondary phase with extensive cracking that occurred during processing as a result of thermal expansion anisotropy, discussed later in Chapter 3.2. Sc_2SiO_5 contained $\text{Sc}_2\text{Si}_2\text{O}_7$ and trace Sc_2O_3 phases in the starting material.

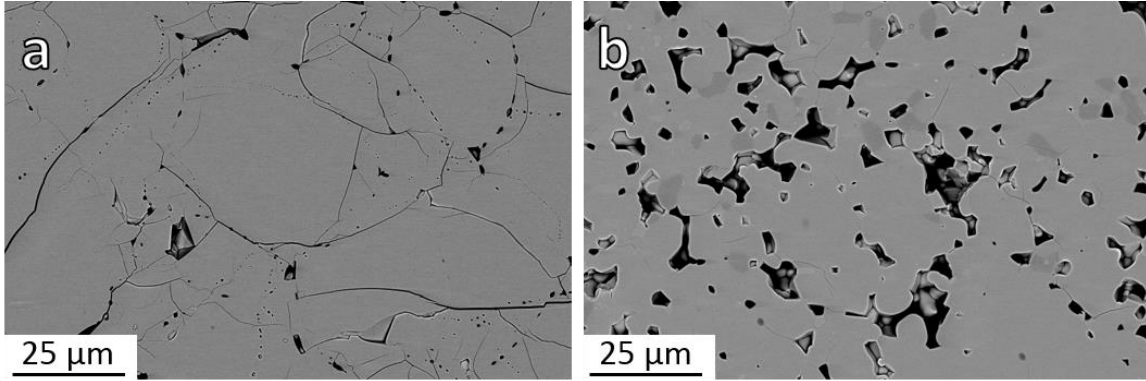


Figure 3-1. Starting microstructures for a. Yb_2SiO_5 and b. Sc_2SiO_5 . Sc_2SiO_5 displayed $\text{Sc}_2\text{Si}_2\text{O}_7$ (dark grey) and trace amounts of Sc_2O_3 (light grey) phases from the starting powder.

3.1.3. Results

X-ray diffraction data for each sample before and after exposure to high-velocity steam are presented in Figure 3-2. Both Yb_2SiO_5 and Sc_2SiO_5 displayed RE_2O_3 formation after steam exposure. Yb_2SiO_5 peaks were present after steam exposure for the Yb_2SiO_5 sample, indicating much of the surface did not react with steam. The Sc_2SiO_5 coupon displayed exclusively Sc_2O_3 peaks after exposure. No alternate phases were observed through XRD analysis.

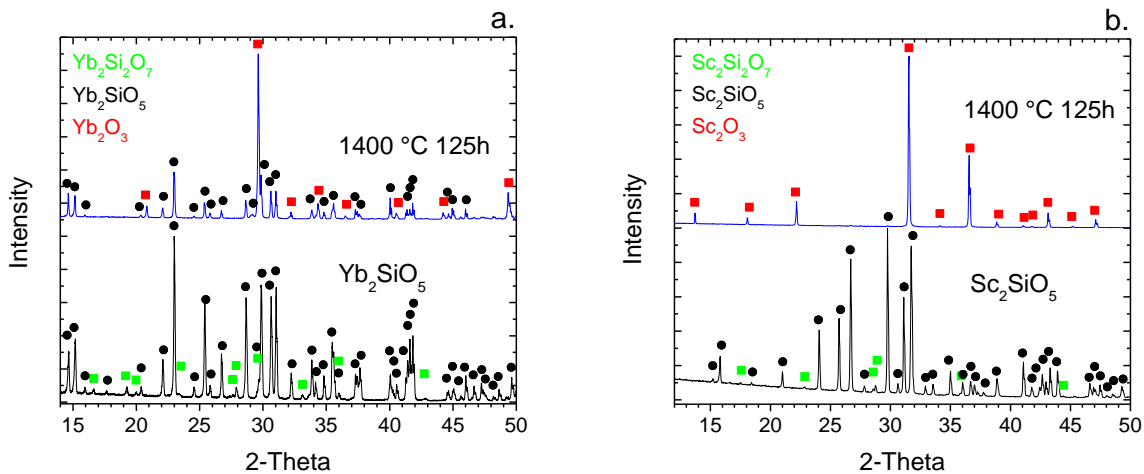


Figure 3-2. XRD before and after steam exposure at 1400 °C for 125h for a. Yb_2SiO_5 and b. Sc_2SiO_5 .

Low magnification plan view SEM imaging of the impingement site and high magnification plan view SEM for regions with high (150-180 m/s) and intermediate (100-125

m/s) steam velocities are shown in Figure 3-3. At the highest steam velocities, both materials reacted with steam to form rare earth oxides. Further from the impingement site at intermediate gas velocities (100-125 m/s), the Yb_2SiO_5 surface remained unreacted while Sc_2SiO_5 continued displaying a Sc_2O_3 reaction product on the surface. The grain size of the Sc_2O_3 product phase increased as the gas velocity decreased across the sample.

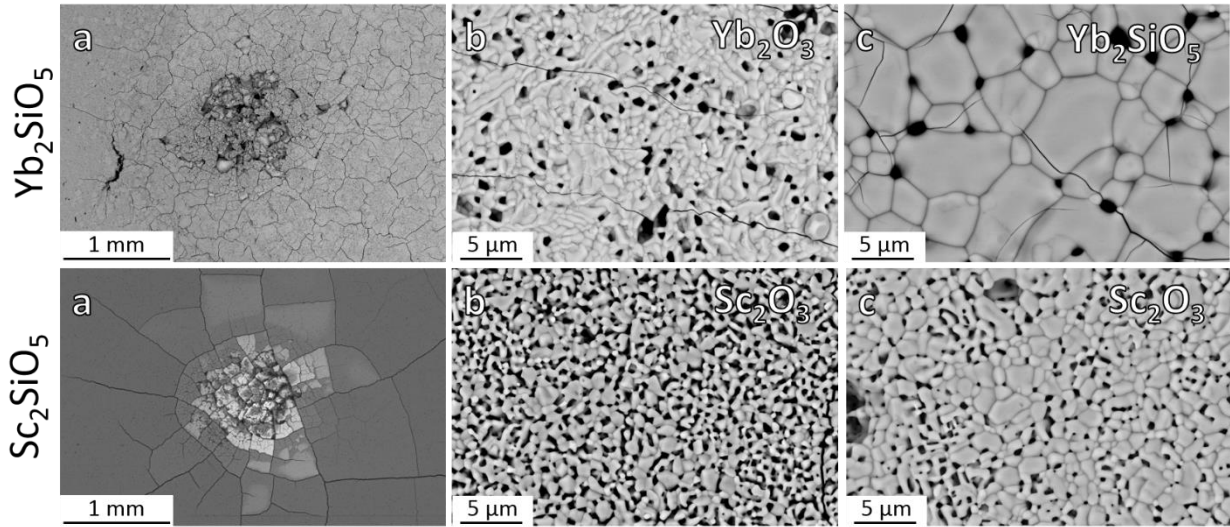


Figure 3-3. Backscattered electron SEM images of Yb_2SiO_5 and Sc_2SiO_5 samples after steam exposure, displaying a. high-velocity steam impingement site, b. higher magnification SEM where the local steam velocity was 150-180 m/s, and c. high magnification SEM where the local steam velocity was 100-125 m/s.

Similar behavior was seen in cross-section for both materials. Figure 3-4 displays the intermediate and high velocity regimes for Yb_2SiO_5 and Sc_2SiO_5 . Again, the Yb_2SiO_5 surface was nonreactive within the 100-125 m/s steam velocity range, while Sc_2SiO_5 reacted to form Sc_2O_3 . In the velocity range of 150-180 m/s, Sc_2O_3 formation occurred at a greater rate than Yb_2O_3 formation, even while the Yb_2SiO_5 starting material displayed extensive cracking that should have allowed steam infiltration further into the material. The pore network within the Sc_2O_3 reaction product coarsened at the intermediate steam velocities compared to the high velocity region. ImageJ analysis suite was utilized to measure the reaction depth across the sample cross-sections. Yb_2SiO_5 displayed a Yb_2O_3 thickness of $9 \pm 5 \mu\text{m}$ in the 130-200 m/s

velocity regime, which was comparable to the Yb_2O_3 thickness measured on $\text{Yb}_2\text{Si}_2\text{O}_7$ at gas velocities greater than 140 m/s ($9 \pm 6 \mu\text{m}$, Chapter 2.3, Figure 2-39). Sc_2SiO_5 displayed a Sc_2O_3 thickness of $33 \pm 2 \mu\text{m}$ in the 100-200 m/s velocity regime.

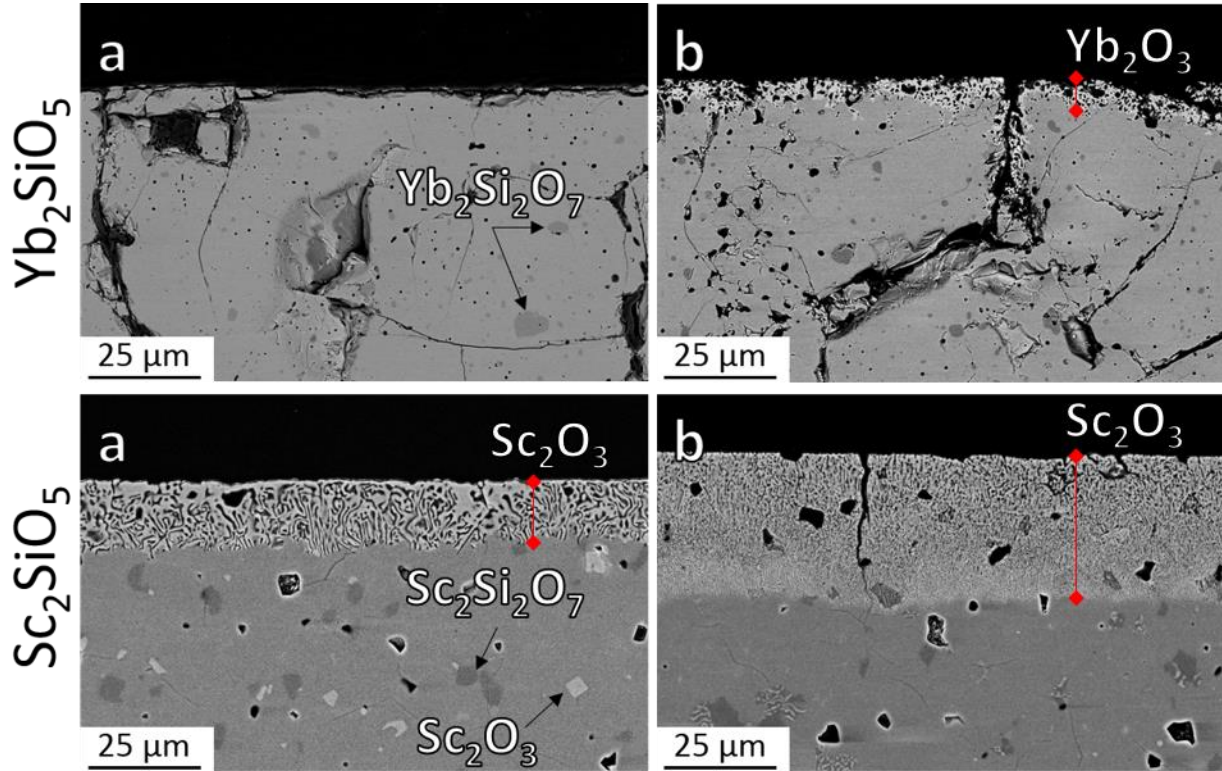


Figure 3-4. SEM Cross sections of Yb_2SiO_5 and Sc_2SiO_5 after steam exposure for a. intermediate steam velocities, 100-125 m/s and b. high steam velocities, 150-180 m/s. $\text{Yb}_2\text{Si}_2\text{O}_7$, $\text{Sc}_2\text{Si}_2\text{O}_7$, and Sc_2O_3 initial impurities are pointed out in a).

3.1.4. Conclusion

Initial findings on rare earth monosilicate stability in steam showed RE_2O_3 formation from RE_2SiO_5 (RE = Yb, Sc) samples occurred at unique rates for the two materials studied. Sc_2SiO_5 reacted with steam to form Sc_2O_3 at much lower gas velocities than Yb_2SiO_5 to form Yb_2O_3 . The stability of rare earth monosilicates in steam environments may not be comparable, as previously stated in the literature [16]. It is unknown if the increased steam reactivity of Sc_2SiO_5 was representative of other RE_2SiO_5 or if it was only related to the scandium rare earth cation. The steam reactivity of bulk Yb_2SiO_5 in this study was comparable to the steam reactivity

of the dense Yb_2SiO_5 product phase on bulk $\text{Yb}_2\text{Si}_2\text{O}_7$, implying high-velocity steam testing of $\text{RE}_2\text{Si}_2\text{O}_7$ can be utilized to study the reaction rates for both RE_2SiO_5 and RE_2O_3 formation simultaneously. Future work should investigate the changes in steam reactivity for an equimolar $(\text{Sc},\text{Yb})_2\text{SiO}_5$ to determine trends in steam reactivity and to optimize rare earth monosilicate stability for use in combustion environments.

3.2. Tailoring Thermal Properties of Multi-component Rare Earth

Monosilicates

3.2.1. Introduction

State-of-the-art EBCs are primarily rare earth disilicates due to chemical compatibility and CTE match to both the silicon bond coat and CMC. Rare earth monosilicates exhibit superior chemical stability, lower thermal conductivity, limited number of polymorphs, and higher melting temperatures compared to their disilicate counterparts. Monosilicates are T/EBC candidates either within a monosilicate/disilicate mixture or as a top coat [74]. De-bonding and spallation from CTE mismatch and microcracking from elastic anisotropy currently prevent rare earth monosilicate usage as a single EBC layer for extended lifetimes.

The goal of this research is to explore possibilities in tailoring thermal expansion and thermal conductivity of rare earth monosilicates by mixing rare earth cations. Results of binary equimolar mixtures of X2 monosilicates, $(RE,RE)_2SiO_5$ of (Dy,Er), (Dy,Sc), (Yb,Sc), and (Yb,Er), and a 5-cation equimolar mixture, RE_2SiO_5 (RE=Sc, Y, Dy, Er, and Yb), are explored alongside each single cation system. Multi-component rare earth cation systems are compared to their rule of mixtures values to elucidate how changes in average ionic radius and cation mass affect thermal expansion, CTE anisotropy, and thermal conductivity.

3.2.1.1. Structure

All RE_2SiO_5 are monoclinic and stable as either space group $P2_1/c$ or $C2/c$, which are generally termed the X1 and X2 structure, respectively. Both structures are displayed in Figure 3-5. X1 is the stable structure for larger rare earth cations La-Tb, while X2 is the stable structure for smaller cations Tb-Lu. For rare earth monosilicates showing both structures as polymorphs,

such as Y_2SiO_5 and Tb_2SiO_5 , X1 is stable at low temperatures while X2 appears at elevated temperatures. Each structure contains rigid silicon-oxygen tetrahedron and soft rare earth-oxygen polyhedron, where one oxygen atom position in each system is not a part of a Si-O tetrahedron and instead is loosely bound to rare earth atoms. Nd_2SiO_5 is the only X1 structure material discussed in this work. All other rare earth monosilicates (RE=Sc, Y, Dy, Er, or Yb) in this work appeared stable as the X2.

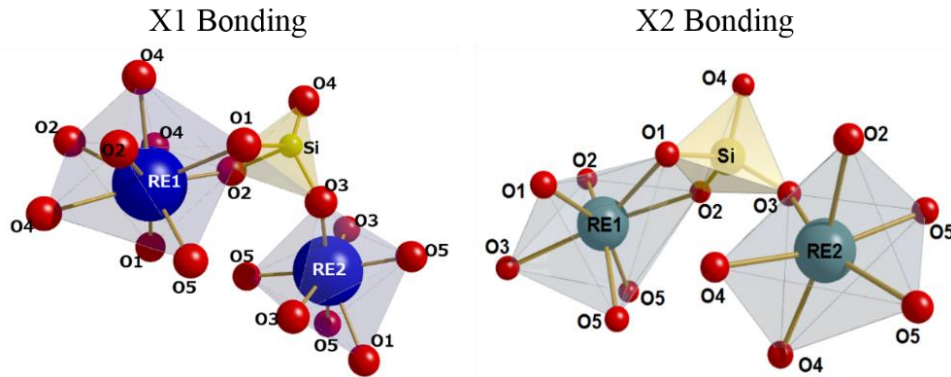


Figure 3-5. Structure and bonding of X1 and X2 phase RE_2SiO_5 [77].

3.2.2. Methods

3.2.2.1. Sample Preparation

Mixed RE_2SiO_5 were made by mixing equimolar ratios of pre-reacted single cation monosilicates (Praxair, United States). Starting Nd_2SiO_5 powder had an average diameter of 0.8 μm . All other initial powders were obtained as spray granules composed of 1 μm to sub-micron particles as shown in Figure 3-6. Fine powders were desired to promote solid solution formation upon processing.

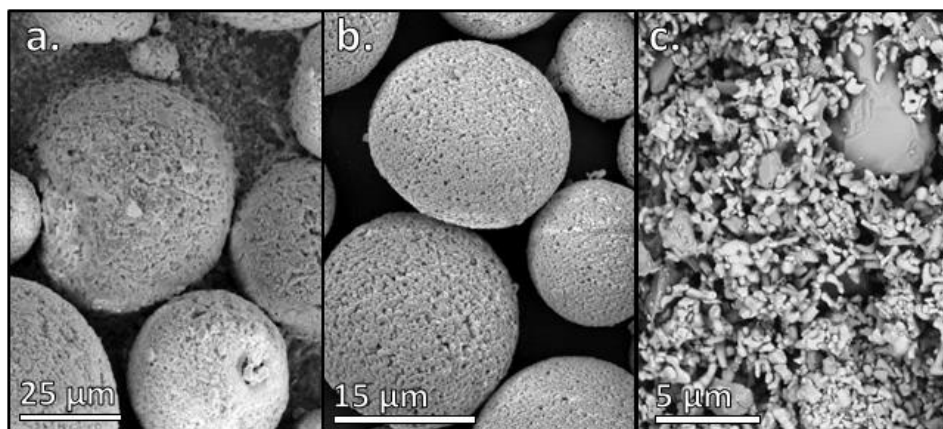


Figure 3-6. a. Thermal spray powders of as-received Sc_2SiO_5 , b. as-received Yb_2SiO_5 , and c. $(\text{Yb},\text{Sc})_2\text{SiO}_5$ powder after ball milling for 24 hours. Large particulate in image a. and in image c. were $\text{Sc}_2\text{Si}_2\text{O}_7$ from the starting Sc_2SiO_5 powder.

The purity of each starting powder was verified with a Panalytical Empyrean X-ray diffractometer (United Kingdom). Starting powders and sintered products were characterized with X'Pert High Score Plus software to find unit cell parameters and phases present. RE_2SiO_5 (RE = Sc, Dy, Er, Yb) displayed minor amounts of $\text{RE}_2\text{Si}_2\text{O}_7$ or RE_2O_3 in the starting powder. In RE_2SiO_5 (RE=Y, Nd) no additional phases were detected by XRD or energy dispersive spectroscopy (EDS) techniques.

Powders were weighed to an accuracy of +/- 0.5 mg and mixed in equimolar ratios by dry ball milling for 24 hours with stabilized zirconia ball mill media. Uniformly mixed powders were then loaded into a 20 mm diameter graphite die and consolidated by spark plasma sintering (SPS) using a Thermal Technologies DCS 25-10 SPS (Santa Rosa, CA). The SPS process was performed in argon, with a 10 to 20 minute hold at a maximum temperature and pressure of 1550-1700 °C and 65-70 MPa, respectively. After the SPS process, samples were annealed for 24 hours at 1500 °C in air to remove residual carbon and restore oxygen stoichiometry. Sample cracking was present for all tested materials due to the anisotropic nature of RE_2SiO_5 .

The sample compositions and material densities are presented in Table 3-1. Densities were calculated by ASTM standard (B962 – 15) Archimedes method with oil infiltration under

vacuum to account for the impact of sample porosity on thermal conductivity measurements [78]. Single cation monosilicates showed densities of 92.5-98.8% relative density, binary solutions showed 90.2-96.2%, and the five-cation solution showed 86.8% relative density. For mixed rare earth cation monosilicates, crystal density was calculated via Rietveld refinement.

Table 3-1. RE_2SiO_5 compositions and material densities from this work.

RE_2SiO_5	Relative Density, %	Theoretical Density, g/cm^3	RE_2SiO_5	Relative Density, %	Theoretical Density, XRD, g/cm^3
Sc	92.5	3.51 [79]	(Yb _{0.5} Y _{0.5})	90.2	7.11
Y	96.7	4.44 [80]	(Dy _{0.5} Sc _{0.5})	95.2	6.80
Nd	98.8	6.00 [79]	(Dy _{0.5} Er _{0.5})	96.2	5.08
Dy	94.1	6.65 [79]	(Yb _{0.5} Er _{0.5})	95.0	5.79
Er	93.9	6.94 [79]	(Sc _{0.2} Y _{0.2} Dy _{0.2} Er _{0.2} Yb _{0.2})	87.7	5.76
Yb	95.0	7.28 [79]			

Samples were polished to 1 μm using diamond suspension, then thermally treated at 1500 °C for 30 minutes in air to show grain boundaries. The microstructures were characterized with FEI Quanta LV200 scanning electron microscope (SEM) with energy dispersive spectroscopy (EDS). Transmission electron microscopy (TEM) was conducted with a Themis Z (Thermo Fisher Scientific: Waltham, MA). TEM sample preparation for the five-component RE_2SiO_5 included fine polishing with 0.05 μm colloidal silica.

3.2.2.2. Thermal Expansion and Thermal Conductivity

Coefficients of thermal expansion (CTE) were measured by hot stage XRD with an Anton Parr (Ashland, VA) HTK 1200N non-ambient stage. Measurements were made in air at 100 °C increments upon heating from room temperature up to 1200 °C with 60 °C/min heating rate. Upon reaching each temperature increment, three XRD scans from 13-60° were acquired

consecutively and combined by HighScore Plus software after measurement. Thermal conductivity was measured with Hot Disk, a transient plane source method where a sensor heats a sample through short current pulses and then measures thermal transport by time dependent resistivity changes [81]–[83]. Thermal transport is measured by fine control of electronic transport through the sensor, which is geometry dependent. Using this method, both thermal conductivity and thermal diffusivity are measured. The Hot Disk measurements were calibrated over a temperature range from room temperature up to 300 °C by a SiO₂ reference sample, and were found to agree well with literature values [84]. Room temperature values for each sample were measured along with temperature dependence for the five RE cation mixture RE₂SiO₅ (RE=Sc, Y, Dy, Er, and Yb) up to 300 °C.

3.2.3. Results

3.2.3.1. Phase Stability

X-ray diffraction of the single cation monosilicate components and the five rare earth cation monosilicate are shown in Figure 3-7. Phase purity was characterized with the ICDD XRD patterns in HighScore Plus software. The Sc₂SiO₅ and Yb₂SiO₅ ICDD stick patterns are presented on the figure as a guide to the peaks associated with the monosilicate phases. RE₂SiO₅ (RE = Y, Dy, Er, and Yb) display similar peak positions with minor shifts from changes in rare earth cation size. Sc₂SiO₅ displays unique peak positions from its small cation mass and atomic radius compared to the other RE₂SiO₅ in this study. Minor peaks corresponding to either a disilicate phase RE₂Si₂O₇ or a rare earth oxide phase RE₂O₃ are present from impurities in starting powder material. It can be seen that peaks for the five rare earth cation mixture are consolidated, representing a single phase mixed rare earth silicate material.

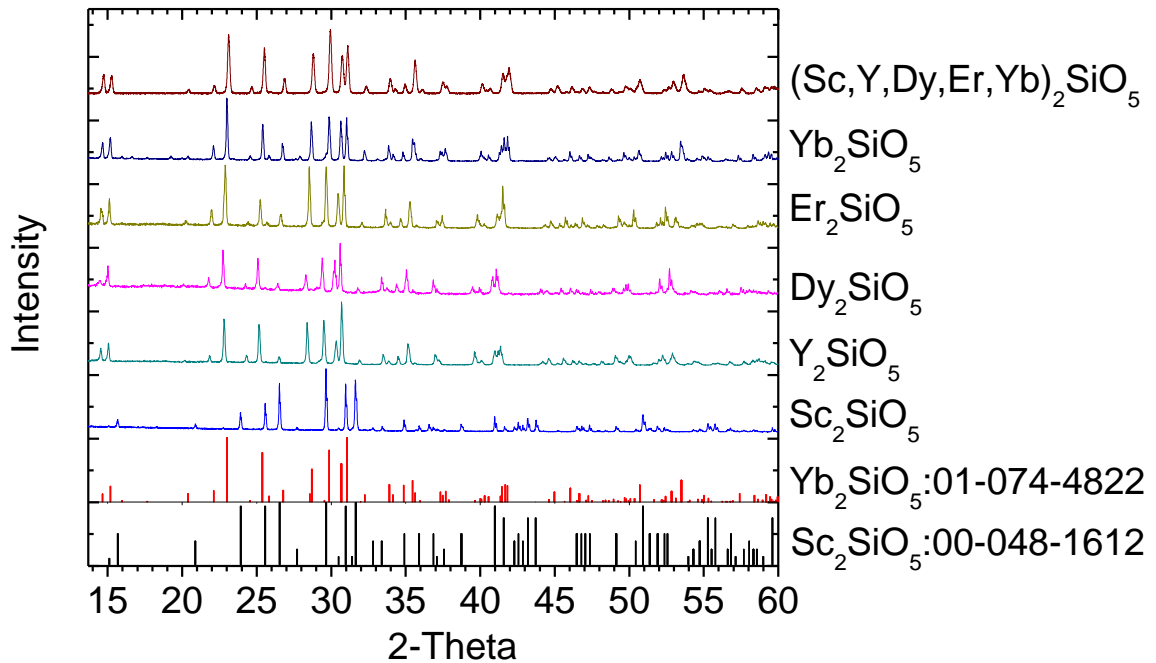


Figure 3-7. X-ray diffraction of single cation monosilicates and a multi-component RE_2SiO_5 , $RE=Sc, Y, Dy, Er, \text{ and } Yb$. All materials are of the same space group, although the small cation size and atomic radius of Sc_2SiO_5 result in noticeable peak shifting relative to the other RE_2SiO_5 .

Figure 3-8 shows representative microstructures of single cation and mixed rare earth cation systems. EDS maps of each mixed cation sample, found in Appendix 8.3, showed solid solution mixing, with occasional 1-10 μm clustering of single cations. The size of rare earth cation clustering corresponds to the size of rare earth oxide RE_2O_3 and/or disilicate $RE_2Si_2O_7$ impurities within the starting powders before and after ball milling. This implies that there is no phase separation of the RE_2SiO_5 mixed cation samples after the SPS processing and annealing procedure on the micron length scale. As the number of rare earth element additions in each specimen increased, the bulk density was seen to decrease. It is possible that the decrease in

density represents a resistance to sintering for multi-component rare earth silicates.

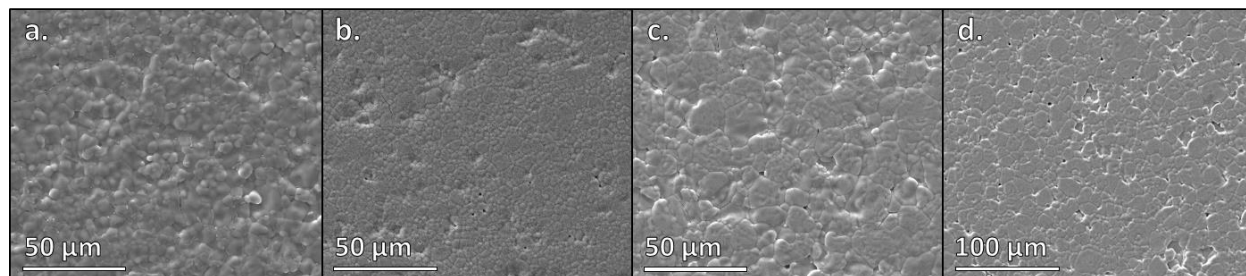


Figure 3-8. Representative scanning electron micrographs of rare earth monosilicates after polishing and 1500 °C anneal for 30 minutes to show grain boundaries. a. Y_2SiO_5 , b. $(Dy,Er)_2SiO_5$, c. $(Yb,Sc)_2SiO_5$, d. Five-component RE_2SiO_5 ($RE=Sc, Y, Dy, Er, Yb$).

Energy dispersive spectroscopy (EDS) of the five-rare earth cation monosilicate system is shown in Figure 3-9. Minor clustering of cation intensity on the maps correspond to starting impurities in the powders. Impurities such as the rare earth clustering in Figure 3-9 were not noticeable in the XRD pattern due to X-ray peak overlap.

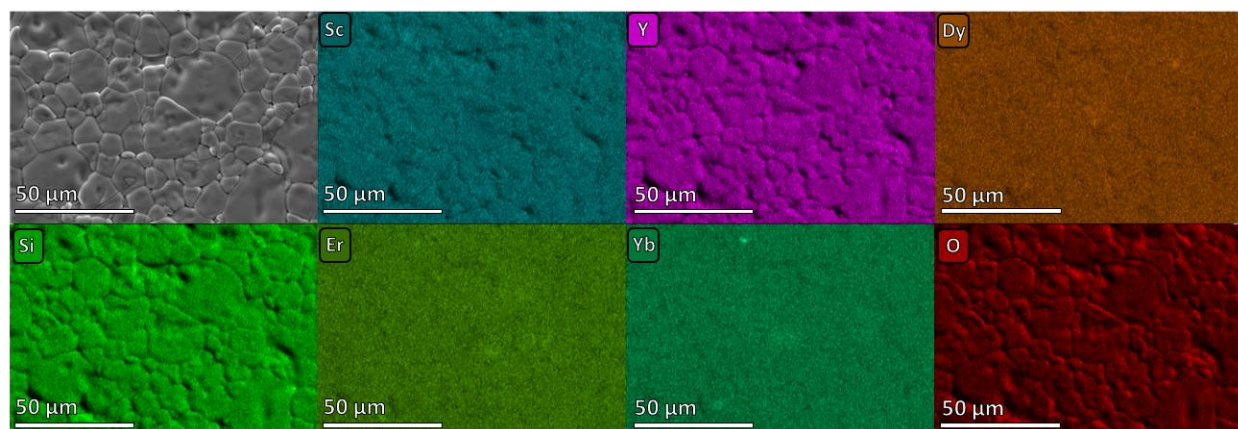


Figure 3-9. Energy dispersive spectroscopy maps for the five-component RE_2SiO_5 ($RE=Sc, Y, Dy, Er, Yb$).

Selected area electron diffraction (SAED) was also performed in order to resolve local segregation on the nanometer scale. Figure 3-10 shows the SAED pattern of the [121] zone axis for the five-component RE_2SiO_5 as well as a simulated pattern of the [121] zone axis derived from XRD crystal data. A single monoclinic crystalline pattern is presented with no visible distortions or satellite peaks. TEM EDS is provided as supplementary information in Appendix 8.3.

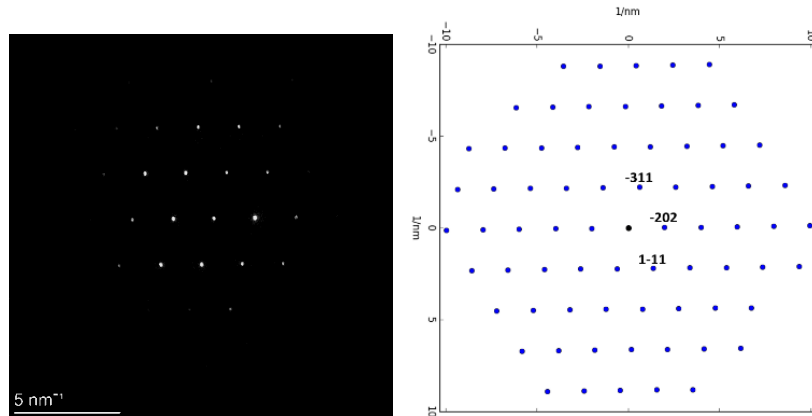


Figure 3-10. Contrast-enhanced selected area electron diffraction map showing the $[121]$ zone axis of the five-component RE_2SiO_5 ($RE=Sc, Y, Dy, Er, Yb$) and a simulated hkl plot with parameters derived from XRD refinement.

3.2.3.2. Thermal Expansion and Thermal Expansion Anisotropy

Unit cell dimensions for each sample were calculated from the X-ray data for each corresponding temperature. The differences in room temperature unit cell volume parameters were below 0.3% between measured and ICDD database values [79], [85]–[87]. Results for the five-component RE_2SiO_5 are shown in Figure 3-11 as a representative of the temperature dependent unit cell growth, where a , b , c , beta angle, and unit cell volume are normalized to 1 for comparison. It can be seen that as the unit cell expands, X2 monosilicates show a decrease in the beta angle as the unit cell moves towards a more orthorhombic-type structure.

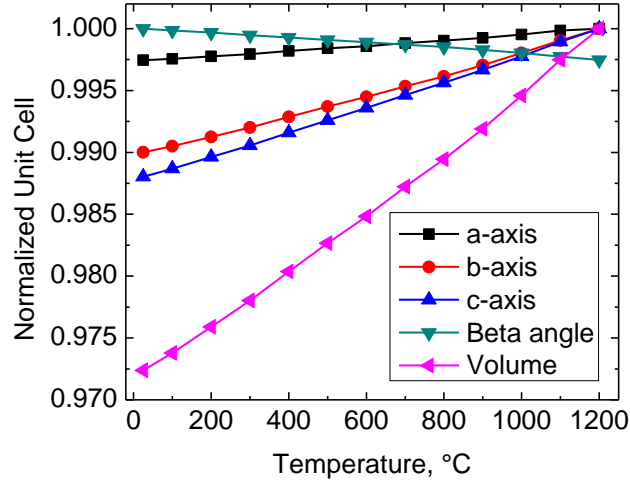


Figure 3-11. Five-component RE_2SiO_5 ($RE=Sc, Y, Dy, Er, Yb$) normalized unit cell parameters from hot stage XRD refinements.

A comparison of average axial CTE from 100-1200 °C of Yb_2SiO_5 powder and sintered sample is shown in Table 3-2 in order to validate the provided X-ray diffraction data. Average axial CTE and volumetric CTE results between powder and sintered Yb_2SiO_5 samples agree well, which verifies that residual stresses in sintered samples do not significantly impact CTE results.

Table 3-2. Thermal expansion coefficients for powder and sintered Yb_2SiO_5 .

CTE $\times 10^6 / ^\circ C, 100 ^\circ C-1200 ^\circ C$					
Yb_2SiO_5	a-axis	b-axis	c-axis	beta angle	Linear
Powder	2.65	6.59	10.5	-1.59	7.33
Sintered	2.73	6.57	10.3	-1.49	7.25

Unlike all X2 structure materials, X1 Nd_2SiO_5 stands out as the only material to show non-linear variation in unit cell parameters as temperature is increased up to 1200 °C, as seen in Figure 3-12. Implications of this for CTE calculations of Nd_2SiO_5 are discussed later.

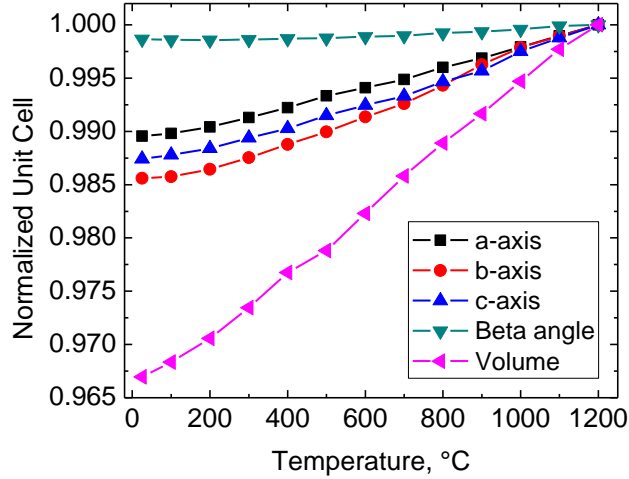


Figure 3-12. X1 structure Nd_2SiO_5 unit cell expansion from hot stage XRD refinements.

Linear CTE was calculated from the volume expansion divided by 3 to represent the average CTE in arbitrary directions x, y, and z, by the relationship $CTE = \frac{1}{3} \frac{\Delta V}{V \Delta T}$. These arbitrary directions do not necessarily correspond to a, b, and c axes due to the beta angle being unequal to 90° . The CTE of the unit cell axes and beta angle were calculated similarly, with the reference temperature being 20°C . Each a, b, and c direction and beta angle for which axial CTE is calculated are defined in Figure 3-13a. The smaller blue atoms represent silicon, red atoms represent oxygen, and teal atoms represent a rare earth. Figure 3-13b shows Si-O tetrahedra displayed in blue, with only oxygen atoms that are not bonded from the Si-O tetrahedra shown in red. Rare earth cations and the oxygen unbonded to Si form directional chains alongside Si-O tetrahedra parallel to the c-axis direction.

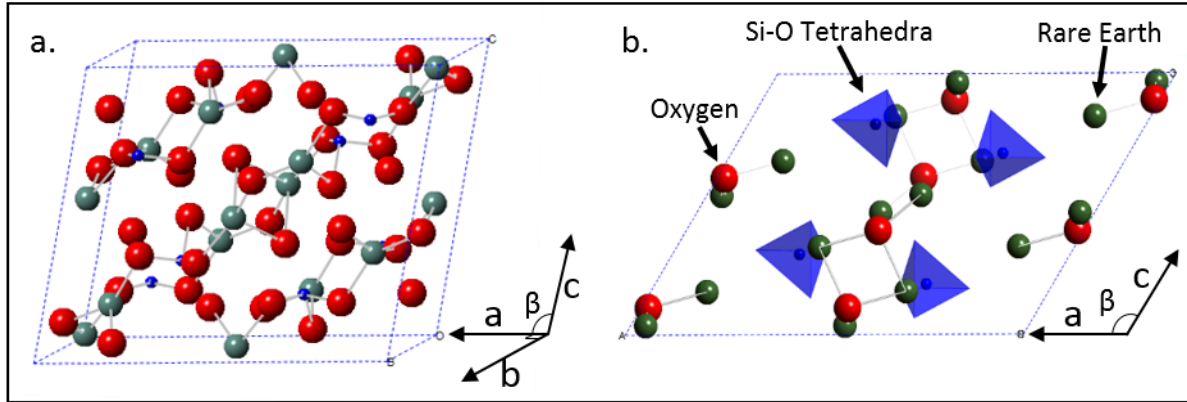


Figure 3-13. X2 structure RE_2SiO_5 unit cell a. perspective and b. viewed from the b-axis. Only oxygen atoms that are not bonded to the Si-O tetrahedra are shown.

Figure 3-14 displays linear CTE for each single cation rare earth monosilicate from 100-1200 °C. The averages of the linear CTE for this temperature range are presented in Table 3-3 to compare with literature values. Literature comparisons of Yb_2SiO_5 and Y_2SiO_5 are also from hot stage XRD, while all other comparisons come from dilatometric techniques. X1 monosilicate Nd_2SiO_5 shows a higher linear CTE than all X2 RE_2SiO_5 in this study. Sc_2SiO_5 shows the lowest linear CTE, and has the closest CTE match to SiC [3], a silicon bond coat [11], and to low CTE rare earth disilicates EBC candidates [87].

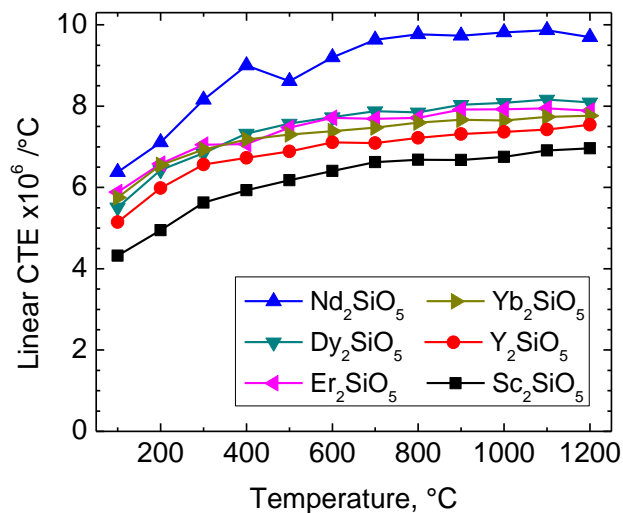


Figure 3-14. Linear CTE of single cation RE_2SiO_5 from 100 °C to 1200 °C.

Table 3-3. Average linear CTE for single rare earth cation monosilicates from this study compared with literature values measured. *Refers to non-ambient XRD measurements.

RE ₂ SiO ₅ RE Cation	Measured CTE (XRD) 100-1200 °C, x10 ⁶ /°C	Literature CTE x10 ⁶ /°C	Literature Temperature Range, °C
Sc	6.17	6.2 [88], 5-6 [14]	400-1400, 200-1400
Y	6.86	6.9 [89], *6.9 [90]	200-1350, 100-1200
Nd (X1)	8.91	9.9 [74]	400-1400
Dy	7.46	8 [88]	400-1400
Er	7.40	7.5 [91]	100-1300
Yb	7.25	7.2 [89], *6.3 [92]	200-1350, 200-1400

Figure 3-15 shows the directional axis CTE values for all single cation rare earth monosilicates. Initially it can be seen that X1 Nd₂SiO₅ shows unique CTE behavior for each direction of its unit cell. The thermal expansion of the Nd₂SiO₅ is highly temperature dependent up to 1000 °C, especially in the b-axis. X2 monosilicates (Sc, Y, Dy, Er, and Yb) show a low a-axis CTE below 3.64 x10⁻⁶ /°C. C-axis CTEs are close to an order of magnitude greater than the a-axis CTEs, with values of 9-10 x10⁻⁶ /°C. Sc₂SiO₅ shows the lowest linear CTE and least amount of CTE anisotropy of the X2 structure monosilicates. The axis CTE results from single cation monosilicates were used to determine if mixed rare earth cation monosilicates show an average CTE value, or if linear CTE could be tailored beyond a rule of mixtures. Specifically, Sc₂SiO₅ additions were evaluated as a means to lower the overall degree of internal anisotropy.

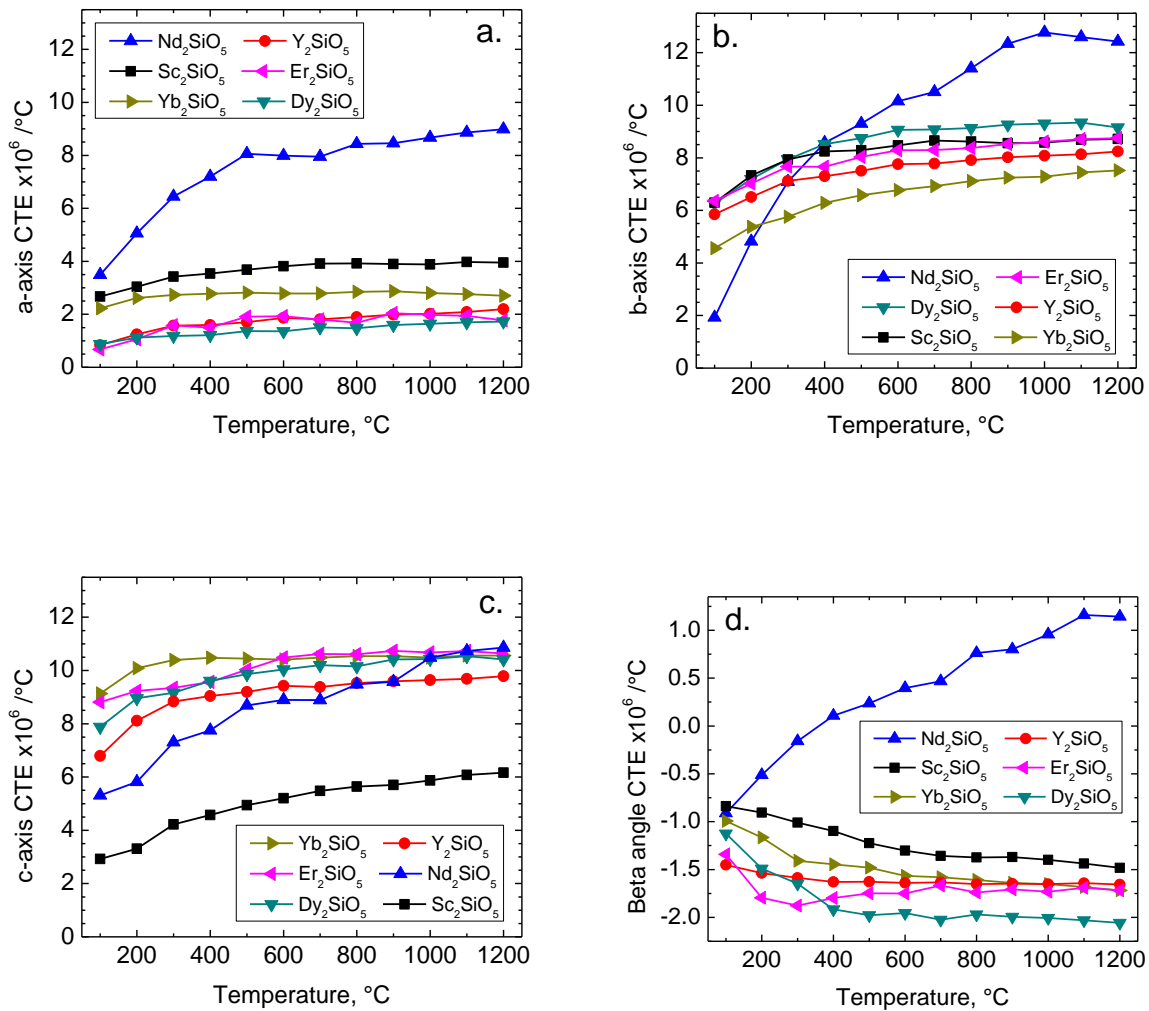


Figure 3-15. Axial CTEs for each single cation RE_2SiO_5 . a. a-axis, b. b-axis, c. c-axis, and d. beta angle.

$(RE,RE)_2SiO_5$ of (Dy,Er), (Dy,Sc), (Yb,Sc), and (Yb,Er) axis CTEs are displayed against their rule of mixtures (ROM) average in Figure 3-16. Each axis CTE is labelled on the graph and is associated with both colored and grey data points. The colored data points represent measured CTE values for the given axis. Solid gray data points represent ROM determined by single rare earth cation measurements, shown previously in Figure 3-15. Measured linear CTE and the rule of mixtures linear CTE are shown as lines in color and in gray, respectively. (Yb,Er) and (Dy,Er) mixtures represent combinations of two rare earth cations of similar mass and ionic radii, while

(Yb,Sc) and (Dy,Sc) show results of more widely varying mass and ionic radii. CTE results within $0.5 \times 10^{-6}/^{\circ}\text{C}$ are considered insignificant differences for comparison of results. All systems show linear CTE that are close to ROM, while larger deviations are present in terms of internal CTE anisotropy. The (Dy,Er) and (Yb,Er) mixtures both show slightly lower values than predicted ROM but differences are within $0.5 \times 10^{-6}/^{\circ}\text{C}$.

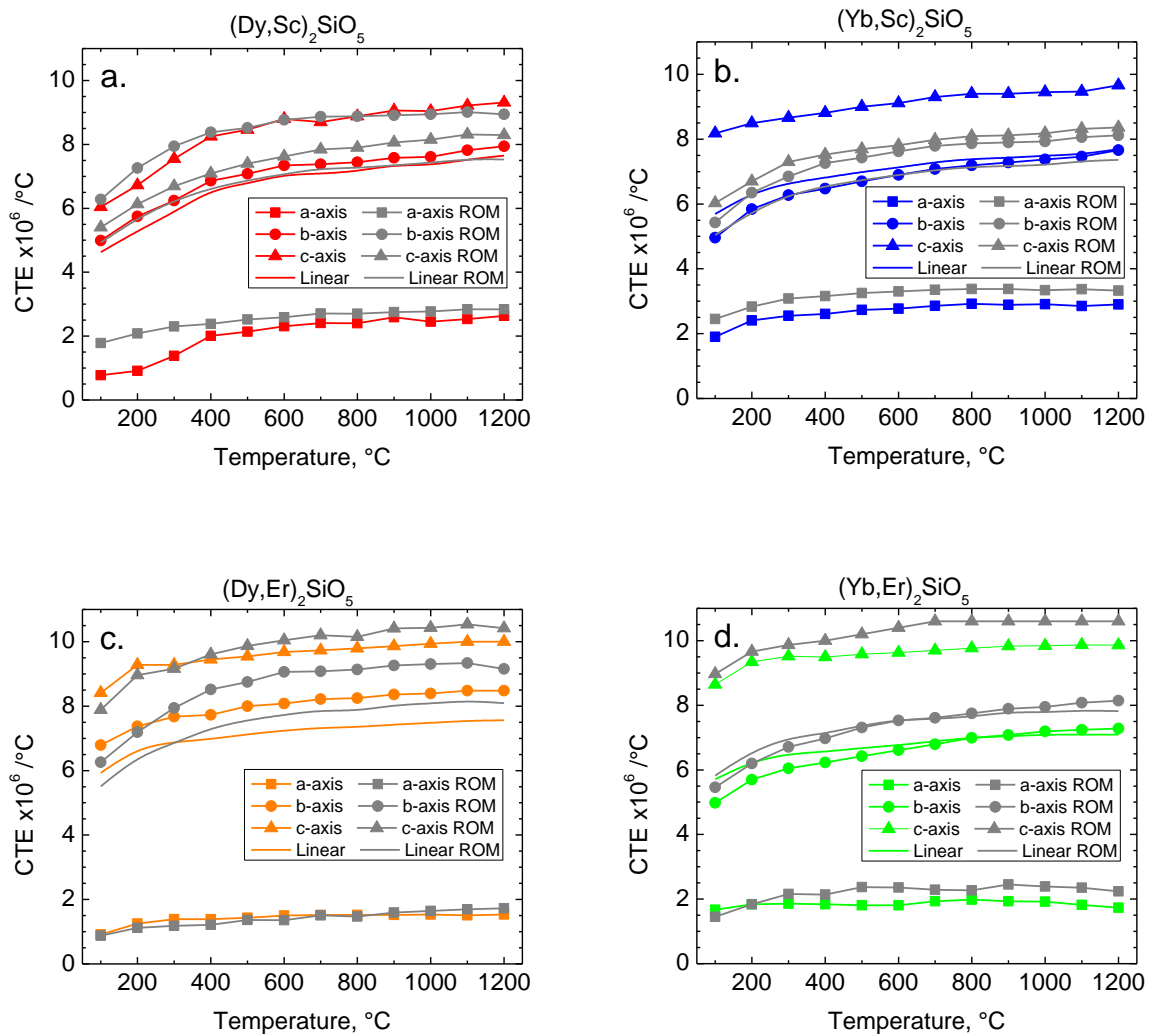


Figure 3-16. Axial and linear CTE values for binary equimolar mixtures $(RE,RE)_2\text{SiO}_5$ compared to ROM values calculated from constituent RE_2SiO_5 : a. $(\text{Dy,Sc})_2\text{SiO}_5$, b. $(\text{Yb,Sc})_2\text{SiO}_5$, c. $(\text{Dy,Er})_2\text{SiO}_5$ and d. $(\text{Yb,Er})_2\text{SiO}_5$.

Figure 3-17 shows the axis CTEs for the five-component RE_2SiO_5 in comparison with the predicted rule of mixtures values. From the graph, it is seen that linear CTE (solid line) does

generally follow a ROM. Still, the c-axis CTE, as well as the beta angle CTE not shown here, show larger differences. This c-axis deviation from ROM shows that scandium additions do not decrease CTE anisotropy for the five-component mixture as predicted by ROM, even while the linear CTE remains in bounds of a ROM prediction.

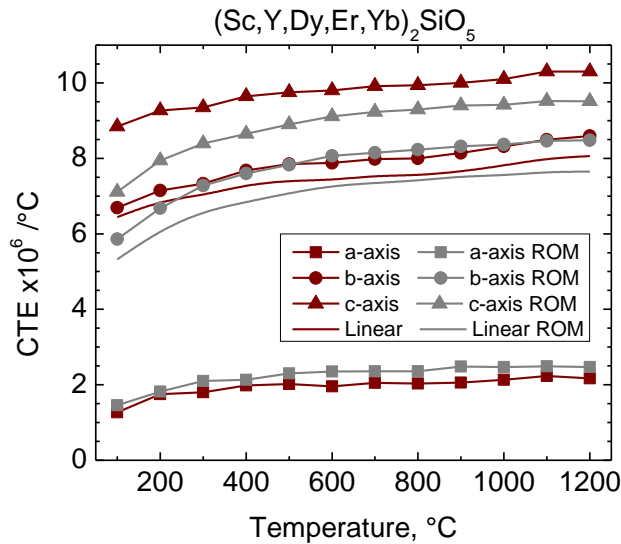


Figure 3-17. Axial and Linear CTE values for five-component RE_2SiO_5 , ($RE=Sc, Y, Dy, Er, Yb$) compared to ROM values.

3.2.3.3. Hot Disk Measurements of Thermal Conductivity

The Hot Disk technique allows for direct measurement of diffusivity (D) and thermal conductivity (κ) with specific heat (C_p) being approximated by Neumann-Kopp rule from the constituent oxides. The relationship is $\kappa = DC_p\rho$, where ρ represents the theoretical compound density. Values are corrected for effect of porosity and cracking by the Maxwell-Gernett model [93]:

$$\kappa_{Solid} = \frac{\kappa_{Porous}}{\left(\frac{1-\phi}{1+\phi}\right)} \quad 3-1$$

where ϕ represents the relative porosity percentage of each sample. A summary of measured thermal conductivity values, as well as values corrected for porosity are shown tabulated in Table 3-4 and graphically in Figure 3-18. An uncertainty of 3% was assigned to the

density measurements, which was incorporated into the hot disk measurement uncertainty.

Values presented in Table 3-4 are still impacted by other bulk features such as impurity phases or grain boundaries.

Table 3-4. Room temperature thermal conductivity measured values for RE_2SiO_5 and values corrected for density.

Rare Earth Cations	Measured $W(m K)^{-1}$	Density Corrected $W(m K)^{-1}$	Five cation RE_2SiO_5 Temperature $^{\circ}C$	Measured $W(m K)^{-1}$	Density Corrected $W(m K)^{-1}$
Sc	2.41 ± 0.05	2.80 ± 0.10	20	0.93 ± 0.02	1.06 ± 0.04
Y	1.95 ± 0.05	2.08 ± 0.08	50	0.90 ± 0.04	1.02 ± 0.06
Nd	2.26 ± 0.16	2.31 ± 0.18	100	0.88 ± 0.04	1.00 ± 0.05
Dy	1.02 ± 0.02	1.15 ± 0.04	150	0.87 ± 0.03	0.98 ± 0.05
Er	1.30 ± 0.03	1.47 ± 0.06	200	0.85 ± 0.03	0.96 ± 0.04
Yb	1.23 ± 0.04	1.36 ± 0.06	250	0.84 ± 0.03	0.95 ± 0.04
(Yb,Y)	1.24 ± 0.05	1.37 ± 0.07	300	0.76 ± 0.03	0.86 ± 0.04
(Dy,Sc)	1.01 ± 0.03	1.09 ± 0.05			
(Dy,Er)	1.24 ± 0.19	1.34 ± 0.21			
(Yb,Er)	1.08 ± 0.03	1.32 ± 0.05			

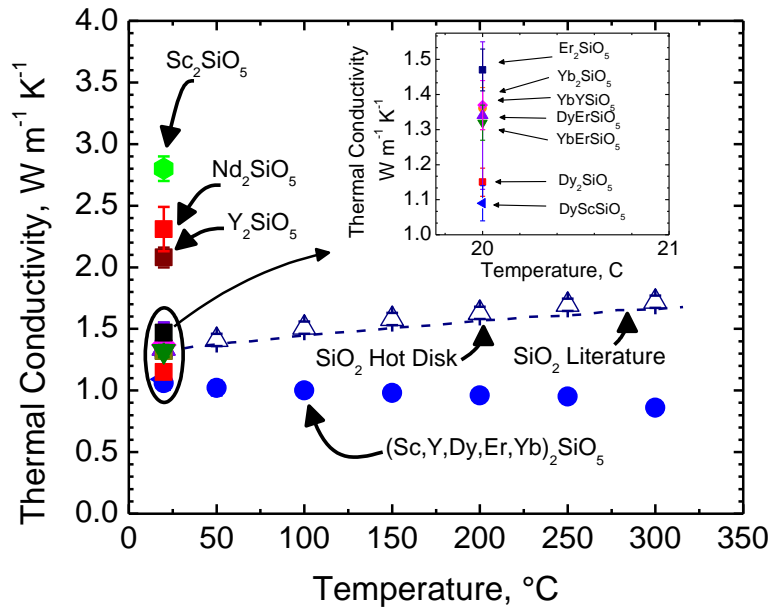


Figure 3-18. Room temperature thermal conductivity values of RE_2SiO_5 measured by Hot Disk method, with values corrected for apparent density. The five-component RE_2SiO_5 (RE=Sc, Y, Dy, Er, Yb) and SiO_2 are measured up to 300 $^{\circ}C$.

Y_2SiO_5 thermal conductivity was experimentally measured by Sun et al. who reported a value of 1.86 W/mK at room temperature [94], which is similar to the value measured in this study. Literature values of measured room temperature thermal conductivity values are as follows: $\text{Dy}_2\text{SiO}_5 \sim 1.9$ W/mK, $\text{Yb}_2\text{SiO}_5 \sim 2.2$ W/mK, $\text{Er}_2\text{SiO}_5 \sim 2.7$ W/mK, and $\text{Y}_2\text{SiO}_5 \sim 3.5$ W/mK [72]. The samples reported on in this work have slightly lower thermal conductivities, which could be due to microstructural differences such as grain size variations. The ranking of thermal conductivity values in this study remains comparable to both experimental and computational results by Tian et al. [72]. Ranking from lowest to highest thermal conductivity: Dy_2SiO_5 , Yb_2SiO_5 , Er_2SiO_5 , and Y_2SiO_5 . Additionally, a measured thermal conductivity for hot pressed Nd_2SiO_5 of ~ 2.8 W/mK at room temperature was reported in the literature [88], which is comparable to the value of 2.31 ± 0.18 W/mK presented in this study. The five-component rare earth silicate shows a low room temperature thermal conductivity of 1.06 ± 0.04 W/mK. In addition to possessing a thermal conductivity lower than each of the individual or binary cation monosilicates, the five-component RE_2SiO_5 (RE=Sc, Y, Dy, Er, Yb) shows a relatively flat trend over the temperature range tested in this study. While thermal conductivity was not tested up to relevant operating temperatures for EBC materials, previous literature has shown that the thermal conductivity of RE monosilicates is relatively flat above 300 °C [95], [96]. This suggests that the thermal conductivity of ~ 0.9 W/mK at 300 °C serves as a conservative upper bound for the thermal conductivity at elevated temperatures. A similar reduction in thermal conductivity at room temperature, compared to the constituent materials, of high entropy ceramics has recently been shown for similar multi-cation high entropy borides and silicides, and entropy stabilized oxides [65], [66], [97].

3.2.4. Discussion

3.2.4.1. *Thermal Expansion and Thermal Expansion Anisotropy*

Figure 3-12 shows a unique thermal expansion feature of Nd_2SiO_5 , the representative X1 structure in this study. While both X1 and X2 monosilicates show a decreasing beta angle at low temperatures, the X1 structure beta angle starts increasing near 300 °C, producing non-linear results in both linear and axial CTE. It is uncertain if this trend holds true for other RE_2SiO_5 with the X1 structure.

Linear CTE for each sample can be compared to average ionic radii for the two rare earth cation sites within the unit cell, as shown in Figure 3-19. Single cation monosilicates from this study and from literature are presented alongside equimolar rare earth cation mixtures, displaying a positive correlation between ionic radii and linear CTE. Points on this graph with ionic radii above 0.95 Å are X1, while all points below are X2 structure monosilicates. Other rare earth cations in RE_2SiO_5 from literature are as follows: Y(X1 structure) [90], Sm [98], Gd [99], Tb [72], Ho [100], Tm [72], and Lu [99]. The thermal expansion was seen to increase with increasing cation ionic radius due to a decrease in bond strength associated with the larger rare earth cations. The relations between bond strength, ionic radius, and thermal expansion will be addressed in Chapter 3.5.

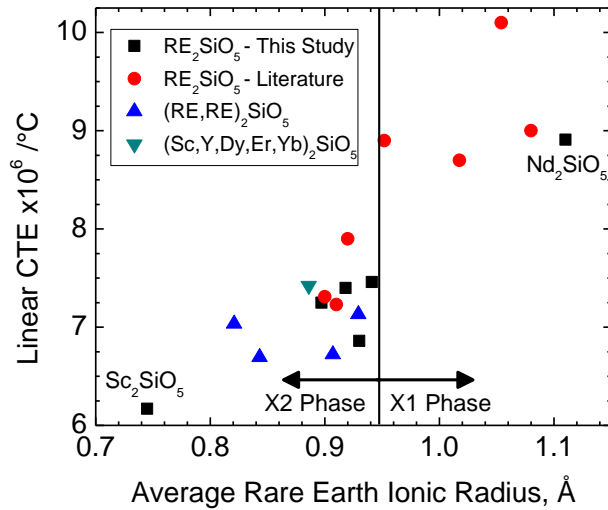


Figure 3-19. Linear CTE comparison to ionic radii, including all systems in this study along with other literature single cation RE₂SiO₅, where RE= Y(X1), Sm, Gd, Tb, Ho, Tm, and Lu.

The standard deviation of rare earth cation mass was calculated for each sample to represent the spread of rare earth cation mass for each material relative to an average rare earth cation mass. This method for comparison was chosen to display how mixing of rare earth cations with similar cation masses (small standard deviation) could produce differing thermal properties than from mixing rare earth cations with widely varying cation masses (large standard deviation). Figure 3-20a shows that there is negligible effect of cation mass differences in mixed cation rare earth monosilicates on linear CTE. X2 structure single cation and multi-rare earth cation monosilicates show linear CTE values between 6 and 7.5x10⁻⁶ /°C. Ren et al. state that a multi-component RE₂SiO₅ (RE=Y, Ho, Er, and Yb) showed CTE that deviated from a ROM [96], which is contradictory to the results of this work. It was hypothesized in their work that increased lattice distortion from the multiple components led to an increase in elastic stiffness. Therefore, CTE decreased by -11.3% and Young's Modulus was increased 7.4% relative to the ROM values. Dong et al. report the CTE of an equiatomic 5 cation RE₂Si₂O₇ (RE=Sc, Y, Gd, Yb, Lu) to be between 3.7 and 5.7x10⁻⁶ /°C in the temperature range of 300 °C to 1350 °C [101].

While the ROM value is not discussed by the authors, a ROM value can be estimated from data provided by Turcer et al., which displayed the average CTE of the rare earth disilicates [74]. The ROM value for the five cation $RE_2Si_2O_7$ (RE=Sc, Y, Gd, Yb, Lu) is around $4.9 \times 10^{-6} / ^\circ C$, which agrees well with the results presented in this work that the linear CTE of multiple cation rare earth silicates can be approximated by a ROM value.

Differences in anisotropy between mixed and single rare earth cation monosilicates are also minimal. Figure 3-20b displays the minor trend of c-axis CTE ratio to the ROM value, where the c-axis CTE increases with increasing cation mass standard deviation. This shows that additions of lightweight scandium cation in solution does not decrease internal anisotropy as predicted by the rule of mixtures. It is hypothesized that the scandium, the smallest cation in this study, interacts less with the rigid Si-O tetrahedron in the structure.

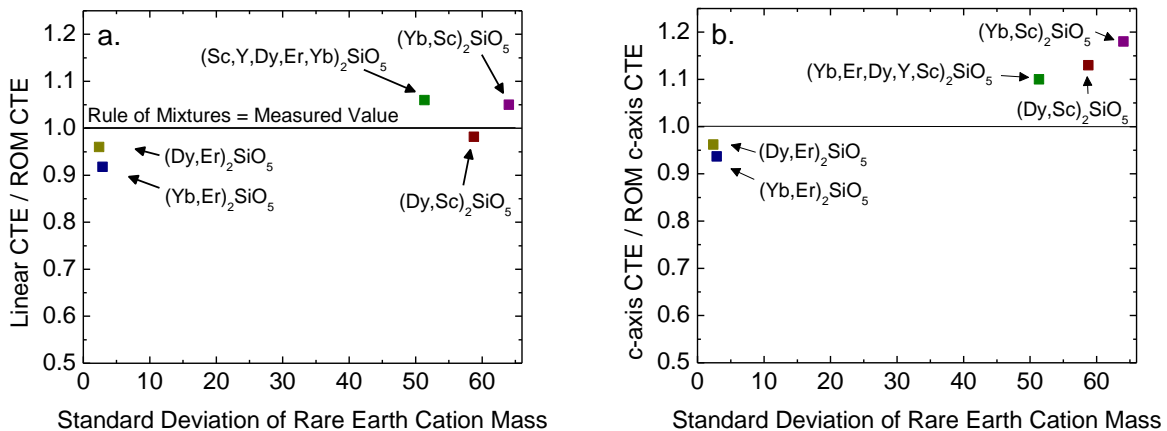


Figure 3-20. a. Linear CTE ratio and b. C-axis CTE ratio, compared to the standard deviation of rare earth cation mass for RE_2SiO_5 mixtures.

Felsch characterized the rare earth silicates as containing strong covalently bonded Si-O tetrahedron and comparatively soft ionically bonded RE-O polyhedra [102]. Further, the Si-O bonding in many silicates has been shown to have near zero thermal expansion, which points to the thermal expansion being governed by rare earth oxygen bonds [103]. Viewing the X2 unit

cell along the b-axis helps to explain the anisotropy of X2 monosilicates, as shown in Figure 3-13b. The c-axis shows the greatest CTE because this direction has planes where no Si-O tetrahedra inhibit expansion of the rare earth polyhedra. Similarly, the a-axis direction has the highest density of rigid Si-O tetrahedron, which explains the low a-axis CTE of $1 - 3 \times 10^{-6} / ^\circ\text{C}$. Nd_2SiO_5 , being X1 structure monosilicate with different bonding characteristics, displayed higher CTE values, but overall a decreased amount of CTE anisotropy.

3.2.4.2. Thermal Conductivity

An inverse correlation between linear CTE and thermal conductivity for single rare earth cation X2 monosilicates is seen in Figure 3-21, where the fit line is used to guide the eye. For example, Dy_2SiO_5 has the largest linear CTE of the single cation monosilicates measured, and also shows the lowest thermal conductivity at room temperature. The X1 Nd_2SiO_5 does not fit the trend due to significantly different expansion trends. Mixed cation X2 systems have lower thermal conductivities, presumably due to increased phonon scattering with mixed mass and ionic sizes.

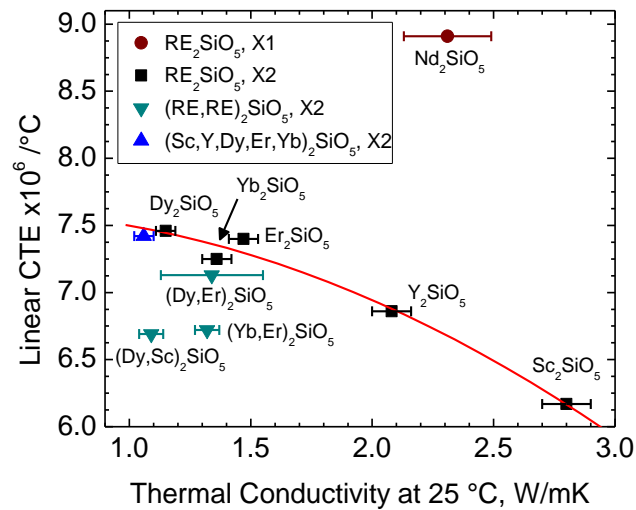


Figure 3-21. Room temperature thermal conductivity measurements compared to average linear CTE (100 °C-1200 °C).

A general trend with multi-component RE_2SiO_5 systems is that mixing decreases thermal conductivity more with each additional cation added in mixing. $(\text{Dy,Er})_2\text{SiO}_5$ appears as the only exception in this study, which could arise from differences in bulk defects such as grain size or alternate phases. Figure 3-22 shows the ratio of measured and ROM thermal conductivity values plotted against the standard deviation of the rare earth cation mass and the ionic radius for each mixture. These results demonstrate that thermal conductivity can be most effectively tailored below the ROM value through further increasing the lattice heterogeneity. This trend has been validated in previous studies where deviations from a ROM thermal conductivity are attributed to phonon scattering from increased lattice disorder [72], [73], [75]. In this case, disorder arises from rare earth cation mass and bonding heterogeneity. The curvature of each plot in Figure 3-22 implies that introduction of ionic radii heterogeneity more effectively reduces thermal conductivity than increasing cation mass heterogeneity for multicomponent RE_2SiO_5 .

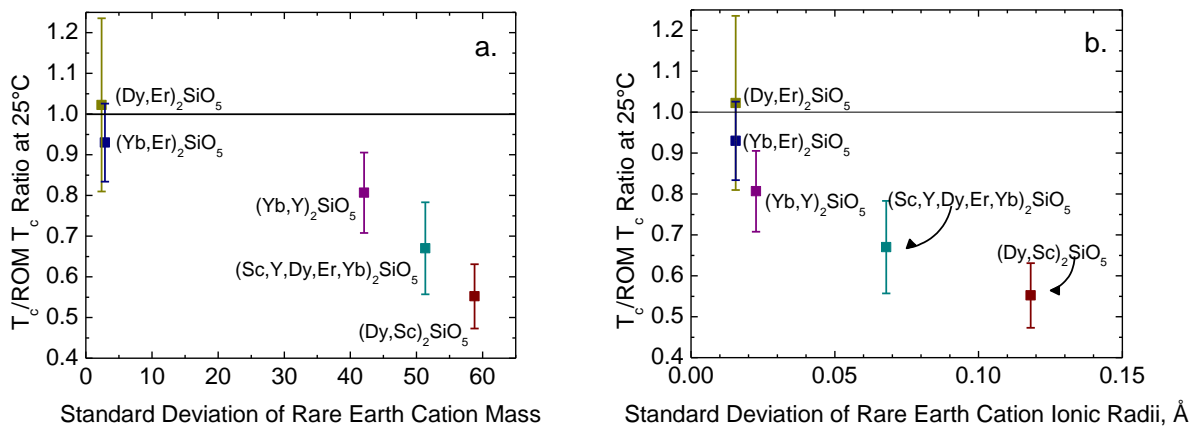


Figure 3-22. Ratio of thermal conductivity to its ROM value plotted against the a. standard deviation of rare earth cation mass and b. standard deviation of rare earth ionic radius for each RE_2SiO_5 mixture.

Further studies looking at three and four component mixtures may shed more light on the structure-property relationships between the rare earth cations and relevant thermal properties for EBCs. Using the observations for the various binary systems as well as the five-component

system, future rare earth compositions could be tailored to further decrease thermal conductivity by increasing heterogeneity in the crystal lattice. Additionally, the high-temperature thermal conductivity of multi-component rare earth silicates should be addressed for optimized mixtures that may represent novel EBC material candidates.

3.2.5. Conclusions

The degree of CTE anisotropy in X2 structure rare earth monosilicates was quantified by high-temperature XRD. The results show that scandium monosilicate has a significantly lower degree of CTE anisotropy than other X2 materials. Mixed rare earth cation monosilicates followed a rule of mixtures for tailoring CTE, while a weak dependence of c-axis CTE anisotropy on cation mass is seen. The high and anisotropic CTEs are not appropriate for a single layer EBC material on SiC-based CMCs. Both the high linear CTE and significant CTE anisotropy should be taken into account when considering rare earth monosilicates for designing rare earth silicate EBCs.

Thermal conductivity of mixed rare earth cation monosilicates follows a rule of mixtures when rare earth cations of similar ionic radii and mass were combined. Thermal conductivity can be reduced by increasing heterogeneity in both cation mass and ionic radii, where large differences in ionic radii more readily decreased the thermal conductivity compared to cation mass heterogeneity. The (Dy,Sc)₂SiO₅ mixture contained the largest difference in rare earth cations mass for the RE lattice sites and also showed the greatest decrease in room temperature thermal conductivity from a ROM. A five-component RE₂SiO₅ provided the lowest thermal conductivity value, with a room temperature value of 1.06 W/mK that further decreases upon heating to 300°C. The five-component rare earth monosilicate also showed a relatively high CTE of $7.42 \times 10^{-6} / ^\circ\text{C}$ which agrees with an inverse correlation between CTE and thermal conductivity

observed for single cation X₂ structure rare earth monosilicates. The ability to lower thermal conductivity to near 1 W/mK at room temperature has been shown for mixed rare earth cation monosilicates, and allows for potential to tailor thermal properties of T/EBC systems for future increases in turbine operating temperatures.

3.3. High-velocity Steam Resistance of RE₂Si₂O₇ (RE = Sc, Nd, Er, Yb, and Lu) at 1400 °C

3.3.1. Introduction

It is assumed that all RE₂Si₂O₇ behave similarly in steam environments through production of a Si(OH)₄ (g) species, as shown in Equation 3-2.



The dual phase field silica activities for all currently available RE₂O₃-SiO₂ systems have been listed in Table 3-5. Silica activities are not yet determined for most rare earth silicate systems. Rare earth disilicates are assumed to have similar a(SiO₂), although changes in crystal structure and bonding for various RE_xSi_yO_z polymorphs may result in noticeable changes in silica activity. The clearest representation of how silica activities might be varied among various rare earth systems can be seen with the La₂SiO₅ - La₂O₃ phase field, where the a(SiO₂) is roughly an order of magnitude greater than respective Yb and Y systems. The silica activities here suggest that X1 phase La₂SiO₅ would display greater steam reaction rates than X2 phase RE₂SiO₅ (Y, Yb).

Table 3-5. Dual phase field silica activities for RE₂O₃-SiO₂ systems.

Rare Earth	SiO ₂ - RE ₂ Si ₂ O ₇	RE ₂ Si ₂ O ₇ - RE ₂ SiO ₅	RE ₂ SiO ₅ - RE ₂ O ₃	Notes
Y	1	0.28	0.002	1923 K, mass spectrometry [53]
Y	1	0.08	0.0001	1473 K, Thermo-calc [104]
Yb	1	0.194	0.003	1600 K, mass spectrometry [51]
La	1	0.317	0.0127	1473 K, Thermo-calc [104]

3.3.1.1. High-temperature Stability and Structures of $RE_2Si_2O_7$

Rare earth disilicates are found in 7 polymorphs, as described by Felsche [102]. Figure 3-23 shows temperature regions for phase stability of each polymorph as a function of rare earth (RE) ionic radius. $RE_2Si_2O_7$ with smaller ionic radii, such as RE = Sc, Er, Yb, and Lu disilicates, all are monoclinic $C2/m$, termed β -phase disilicates, at the temperatures of interest in this work. This phase is the desired phase for EBC candidates due to the associated low thermal expansion in the range of $3.9 - 5.4 \times 10^{-6} / ^\circ C$ [103]. $Nd_2Si_2O_7$ is tetragonal P41 space group, often termed A-phase, and has a much higher linear thermal expansion of $10.5 \times 10^{-6} / ^\circ C$ [105]. Due to the thermal expansion mismatch, $Nd_2Si_2O_7$ is therefore not a desirable standalone EBC coating material on SiC, which has a CTE of $4.5-5.5 \times 10^{-6} / ^\circ C$ [3]. Both RE = Er and Nd also have a polymorph transition in the temperature range of turbine applications, which would make them unsuitable as EBC candidates without stabilizing a single phase up to 1600 °C.

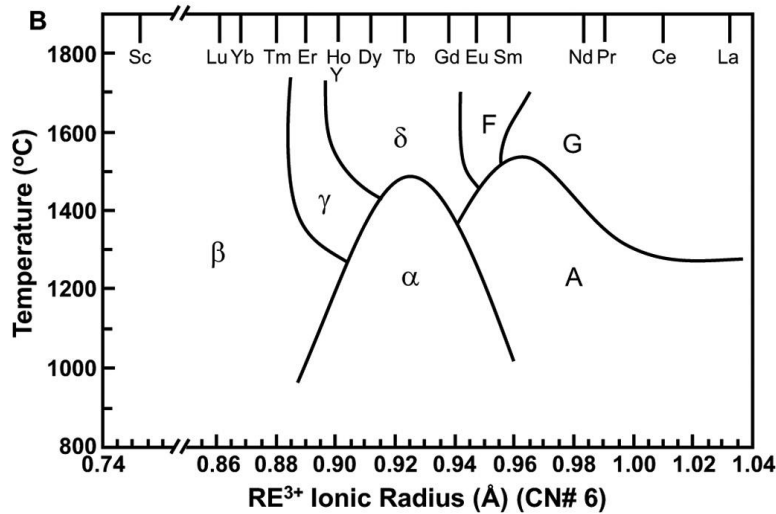


Figure 3-23. Phase stability of $RE_2Si_2O_7$ relative to rare earth ionic radius [105].

The $Yb_2O_3-SiO_2$, $Sc_2O_3-SiO_2$, and $Nd_2O_3-SiO_2$ pseudo-binary phase diagrams are shown in Figure 3-24. The $Yb_2O_3-SiO_2$ diagram is representative of RE = Sc, Er, and Lu phase diagrams in terms of line compounds. Stable line compounds include SiO_2 , $RE_2Si_2O_7$,

$\text{RE}_4\text{Si}_3\text{O}_{12}$, RE_2SiO_5 , and RE_2O_3 . For RE = Er, Yb, and Lu systems, the intermediate apatite phase ($\text{RE}_4\text{Si}_3\text{O}_{12}$) is only stable at high temperatures outside the range of interest so that the disilicate and monosilicate line compounds are the only stable phases. The intermediate apatite line compound ($\text{Sc}_4\text{Si}_3\text{O}_{12}$) is not present for the Sc_2O_3 - SiO_2 system. The Nd_2O_3 - SiO_2 system shows greater stability of the apatite phase, with variability in the stable temperature region and composition reported in the literature. The Nd_2O_3 - SiO_2 phase diagram by Toropov displays the $\text{Nd}_4\text{Si}_3\text{O}_{12}$ apatite line compound with predicted stability to 1500 °C [61]. Toropov and Kougiya later showed how the $\text{Nd}_4\text{Si}_3\text{O}_{12}$ apatite phase displayed Nd_2O_3 solubility near 7 mol % at 1400 °C [106]. The apatite phase composition has also been represented experimentally as $\text{Nd}_{9.33}\square_{0.67}\text{Si}_6\text{O}_{26}$, a cation deficient apatite structure [107]. More recent computational modelling has also predicted that the apatite phase is better represented by $\text{Nd}_{9.33}\square_{0.67}\text{Si}_6\text{O}_{26}$ [108], [109] rather than $\text{Nd}_4\text{Si}_3\text{O}_{12}$. The melting temperatures for the line compounds are presented in Table 3-6 for reference.

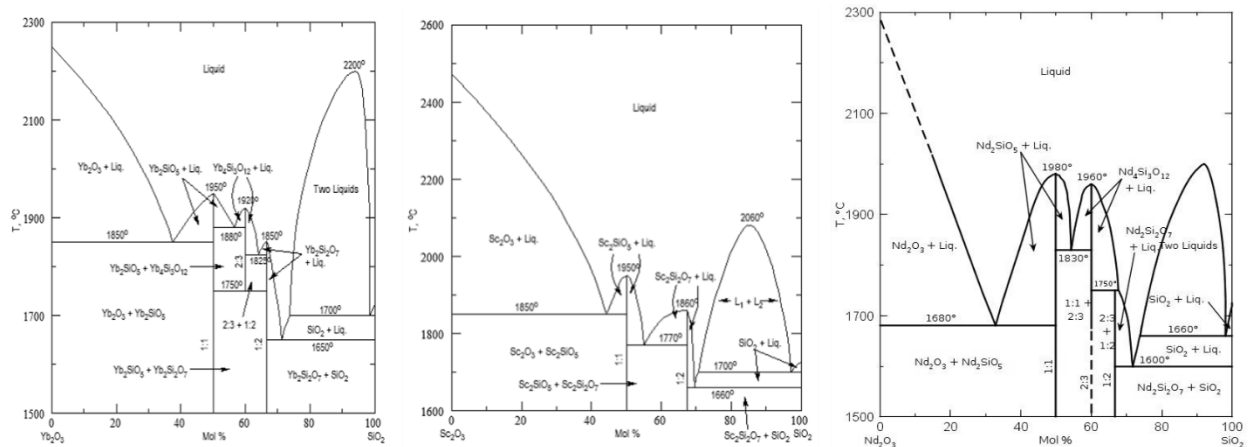


Figure 3-24. Pseudobinary phase diagrams of the Yb_2O_3 - SiO_2 [110], Sc_2O_3 - SiO_2 [111], and Nd_2O_3 - SiO_2 systems [61].

Table 3-6. Melting temperatures of line compounds on the Toropov RE_2O_3 - SiO_2 pseudobinary phase diagrams.

Melting Temperatures, °C				
Rare Earth	RE_2O_3	RE_2SiO_5	$RE_{9.33}\square_{0.67}Si_6O_{26}$	$RE_2Si_2O_7$
Sc [111]	2472	1950	n/a	1860
Nd [61]	2284	1980	1960	1750
Er [110]	2282	1980	1900	1800
Yb [112]	2250	1950	1920	1850
Lu [113]	2510	2000	1869	1860

3.3.1.2. Steam Reactivity of $RE_2Si_2O_7$

Steam reactivity of silicate EBC materials occurs through silica depletion via production of $Si(OH)_4$ (g). Steam testing described in the literature has often been limited to experimental setups with low steam velocities or low water vapor partial pressures, which do not approach the extreme environment of a gas turbine. As shown in Table 3-7 for steam testing described in the literature, near stagnant gas flow steam testing has often resulted in linear reaction kinetics, whereas high velocity testing results in parabolic reaction kinetics.

Table 3-7. Steam testing of $RE_2Si_2O_7$ in the literature.

Material	Temperature, °C	Exposure Time, h	H ₂ O velocity, m/s	P _{H₂O} , atm	P _{Total} , atm	Reaction Products	Reaction Kinetics	Notes
Yb ₂ Si ₂ O ₇	1500	100	0.044	0.1	1	Al ₅ Yb ₃ O ₁₂	Linear	Thermogravimetric Analysis, excess Yb ₂ SiO ₅ in starting material [14]
	1316	2000	0.044	0.9	1	Yb ₂ SiO ₅	n/a	Steam cycling furnace, Air Plasma Sprayed Yb ₂ Si ₂ O ₇ on Si+SiC [114]
	1450	100 - 700	100	0.27	1	Yb ₂ SiO ₅	Parabolic	Burner Rig [48]
	1200, 1300, 1400	60,125,250	240	1	1	Yb ₂ SiO ₅ , Yb ₂ O ₃	Parabolic	Steam jet [29]
Lu ₂ Si ₂ O ₇	1300 and 1500	100	50	-	-	Lu ₂ SiO ₅ , Lu ₂ Si ₂ O ₇	n/a	Excess SiO ₂ in starting material [17]
	1500	310	0.13	0.3	1	Al ₅ Lu ₃ O ₁₂	Not linear	Al(OH) ₃ and Si(OH) ₄ (g) saturation from furnace-ware [20]
Sc ₂ Si ₂ O ₇	1500	100	0.044	0.1	1	None	Linear	Thermogravimetric Analysis, excess SiO ₂ in starting material [14]
	1450	100-700	100	0.27	1	Sc ₂ SiO ₅	Linear	Burner Rig [48]

Yb₂Si₂O₇ is one of the more extensively studied RE₂Si₂O₇ due to its optimum thermal expansion match with SiC and acceptable high-temperature mechanical and chemical stability. Most prior studies have found that Yb₂Si₂O₇ reacts with steam to form porous Yb₂SiO₅ [17], [29], [48]. For high velocity testing above 1200 °C, parabolic reaction kinetics have been reported which imply diffusion-controlled kinetics. Low steam velocity experimental setups often result in linear reaction kinetics and impurity uptake from furnace ware. The Yb₂Si₂O₇ data from our laboratory was presented earlier in this work (Chapter 2.3) and has been described in detail elsewhere [29]. Ueno et al. have also extensively studied the Lu₂Si₂O₇ reaction in both low and high velocity steam. While SiO₂ at the starting grain boundaries limited steam reaction,

Lu_2SiO_5 and trace Lu_2O_3 were observed after steam exposure [115]. It is assumed that $\text{Lu}_2\text{Si}_2\text{O}_7$ behaves similarly to $\text{Yb}_2\text{Si}_2\text{O}_7$ in terms of its steam resistance and steam reaction mechanism.

Steam resistance of $\text{Sc}_2\text{Si}_2\text{O}_7$ has been reported only twice in the literature.

Thermogravimetric analysis (TGA) at near stagnant gas velocities showed nonlinear mass loss with no reaction products, where mass loss can be attributed to excess SiO_2 volatility in steam [14]. Klemm et al. have also reported burner rig testing of bulk $\text{Sc}_2\text{Si}_2\text{O}_7$ and Sc_2SiO_5 samples [48]. Their results indicated that $\text{Sc}_2\text{Si}_2\text{O}_7$ decomposed to Sc_2SiO_5 upon steam reaction, and that bulk Sc_2SiO_5 samples decomposed to form Sc_2O_3 on the surfaces. RE_2SiO_5 in their work were shown to be highly resistant to steam reaction.

Steam resistance of rare earth disilicates with a stable apatite compound in the temperature regions of EBC application, such as $\text{Nd}_2\text{Si}_2\text{O}_7$ or $\text{Er}_2\text{Si}_2\text{O}_7$, have not yet been reported in the literature. It is therefore unknown if the apatite phase will remain a stable product phase after steam reaction. Both the high-velocity steam reactivity and steam reaction products are not yet fully understood for all rare earth silicate materials. This work compares $\text{RE}_2\text{Si}_2\text{O}_7$ (RE = Sc, Nd, Er, Yb, Lu) to verify steam stabilities and compare microstructural evolution of steam reaction products for 125 hour steam exposures at 1400 °C.

3.3.2. Methods

3.3.2.1. Processing

Samples were produced from high purity pre-reacted $\text{RE}_2\text{Si}_2\text{O}_7$ (Praxair: Danbury, CT). $\text{RE}_2\text{Si}_2\text{O}_7$ (RE = Sc, Er, Yb, Lu) granules were annealed at 900 °C for 30 minutes to bake off organics supporting the granules to result in sub-micron powder sizes, following by ball milling with yttria stabilized zirconia milling media for 24 hours. Both $\text{Nd}_2\text{Si}_2\text{O}_7$ and $\text{Yb}_2\text{Si}_2\text{O}_7$ powders

were as-received with a particulate size of $\sim 1 \mu\text{m}$, and therefore were not heat treated or ball milled prior to processing. Powders were loaded into a 20 mm diameter graphite die and sintered in an argon atmosphere using spark plasma sintering (DCS 25-10 SPS, Thermal Technologies, Santa Rosa, Ca.) at 65 MPa with maximum temperatures of 1550 – 1600 °C for 30 minutes. Resulting pucks were then placed in an open-air box furnace (CM Rapid Furnace, Bloomsfield NJ) for 24 hours at 1400 °C – 1500 °C to restore oxygen stoichiometry. Material densities were determined by Archimedes method in deionized water, with 3-5 measurements per sample. Sample coupons were sectioned from the annealed pucks to produce 10x10x1 mm coupons and polished to 0.25 μm with diamond suspension prior to characterization and steam exposure.

3.3.2.2. *Steam Testing*

Each $\text{RE}_2\text{Si}_2\text{O}_7$ coupon was exposed to steam at 1400 °C for 125 hours. The steamjet setup has been described in Chapter 2.1.2.2. Sample mass was recorded before and after exposure (MS105DU, Mettler-Toledo, Columbus, OH). X-ray diffraction (XRD, Panalytical Empyrean X-ray diffractometer Westborough, MA) and scanning electron microscopy (SEM: FEI Quanta 650, Hillsboro, OR) with energy dispersive spectroscopy (EDS: Oxford Instruments, Abingdon, UK) were used for analysis in plan view to determine surface reaction products. Coupons were then mounted in cross-section and polished through the center of the highest velocity impingement site for further SEM/EDS analysis to measure reaction depths and morphology changes. Pore formation and cross-section SEM images were analyzed in ImageJ Analysis Suite. Reaction depth measurements were taken around 70-110 μm apart across 2-7 mm cross section distances, depending on the region of interest.

3.3.3. Results

3.3.3.1. Initial $RE_2Si_2O_7$ Characterization

The starting microstructures of each $RE_2Si_2O_7$ material are presented in Figure 3-25, with analysis of porosity and minor phases in Table 3-8. XRD of the starting material will be shown later. All samples displayed relatively high density after processing. $Sc_2Si_2O_7$ and $Yb_2Si_2O_7$ showed ZrO_2 and Yb_2SiO_5 secondary phases, respectively. ZrO_2 was introduced to the $Sc_2Si_2O_7$ through the ball milling process with zirconia milling media, and Yb_2SiO_5 was present in $Yb_2Si_2O_7$ as-received. Both $Er_2Si_2O_7$ and $Nd_2Si_2O_7$ displayed sample cracking from high-temperature phase transformations near 1325 °C and 1410 °C, respectively.

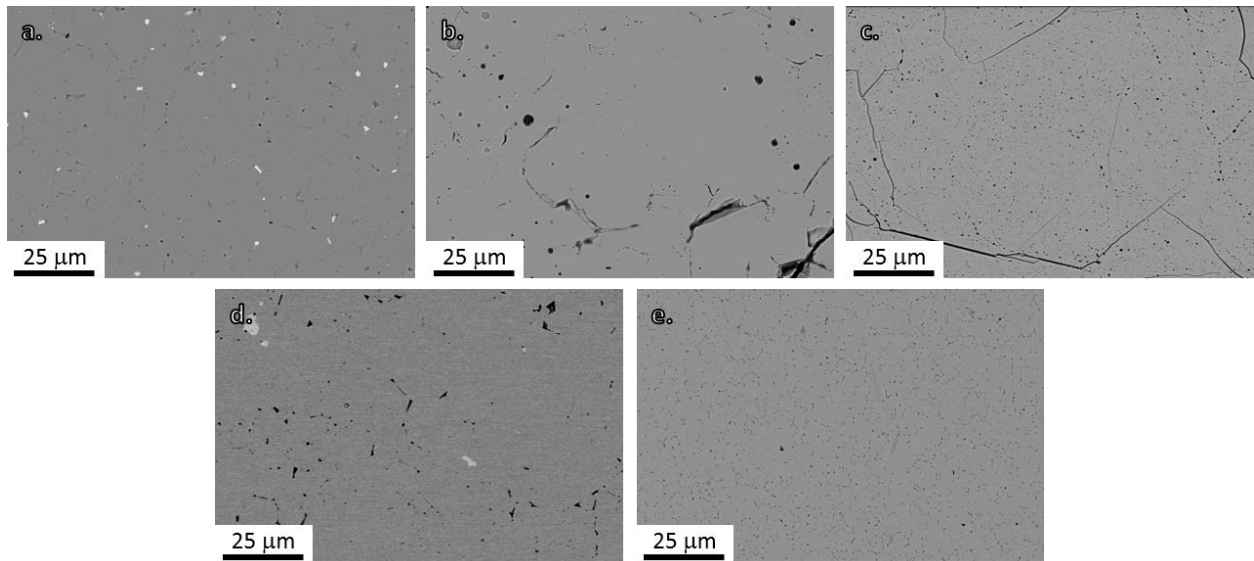


Figure 3-25. Starting microstructures of $RE_2Si_2O_7$, a. $Sc_2Si_2O_7$, b. $Nd_2Si_2O_7$, c. $Er_2Si_2O_7$, d. $Yb_2Si_2O_7$, and e. $Lu_2Si_2O_7$.

Table 3-8. Stable phase, porosity area fraction, secondary phase area fraction, and densities for the processed RE₂Si₂O₇.

Sample	Stable Phase	Porosity Area Fraction	Minor Phase Area Fraction	Measured Density, g/cm ³	Theoretical Density, g/cm ³	Relative Density
Sc ₂ Si ₂ O ₇	β, C2/m	2%	ZrO ₂ , 2%	3.33 ± 0.01	3.4	98%
Nd ₂ Si ₂ O ₇	A, P41	10%	n/a	5.02 ± 0.02	5.45	92%
Er ₂ Si ₂ O ₇	β, C2/m	6%	n/a	5.74 ± 0.03	5.91	97%
Yb ₂ Si ₂ O ₇	β, C2/m	4%	Yb ₂ SiO ₅ , 2%	6.03 ± 0.03	6.15	98%
Lu ₂ Si ₂ O ₇	β, C2/m	4%	n/a	6.08 ± 0.02	6.2	98%

3.3.3.2. Steam Exposure of RE₂Si₂O₇ (Re = Er, Yb, Lu)

Figure 3-26 displays XRD patterns for RE = Er, Yb, and Lu coupons before and after steam exposure at 1400 °C for 125h. For all three materials, the RE₂SiO₅ monosilicate phase is the predominant product species that forms upon steam reaction. Additionally, RE₂O₃ oxide patterns were matched to each scan, representing a secondary reaction product that is fully depleted of SiO₂. The Yb₂Si₂O₇ coupon additionally displayed Yb₃Al₅O₁₂ peaks that are representative of impurity deposition from Al(OH)₃ (g) resulting from reaction of the alumina furnace ware with H₂O (g). Alumina uptake was seen by SEM only at sample edges for all samples, yet XRD peaks for alumina uptake could not be identified on the RE = Er, Lu coupons. It will be shown that alumina impurities are not forming in the regions of interest for analysis.

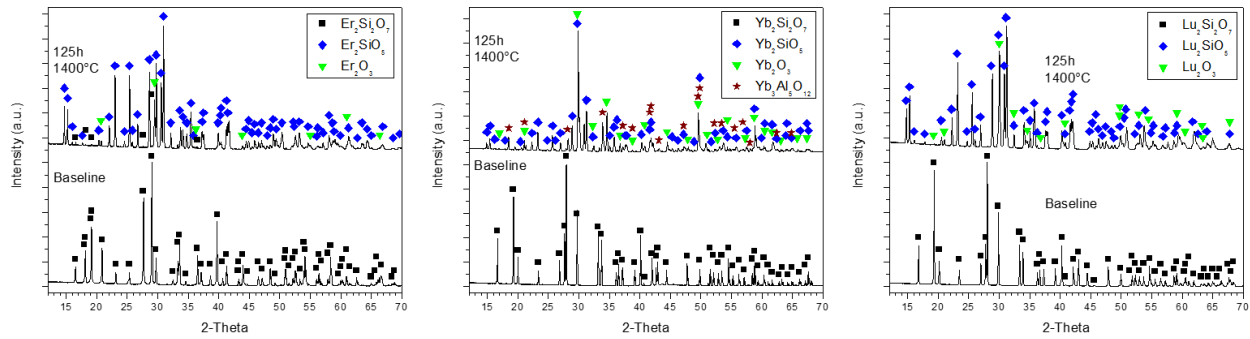


Figure 3-26. Baseline and post steam exposure XRD of $RE_2Si_2O_7$, RE = Er, Yb, and Lu.

Plan view backscattered SEM imaging of $RE_2Si_2O_7$ (RE = Er, Yb, Lu) allowed for visual analysis of various regions across the coupons where steam velocity varied greatly. Figure 3-27a displays the sample region underneath platinum foil sample holder, where gas velocities are near stagnant flow. Initial RE_2SiO_5 formation in this region (light grey) began along cracks and grain boundaries as a dense surface layer on the $RE_2Si_2O_7$ base material (dark grey). No RE_2O_3 formation was seen under the platinum foil. Figure 3-27b displays the RE_2SiO_5 product layer morphology at intermediate gas velocities of 80-115 m/s. RE = Er, Yb, and Lu coupons all displayed a fine porous structure where product grain size was independent of the starting coupon grain size. At the highest velocities, shown in Figure 3-27c, RE_2O_3 formation was dominant on the surface. Gas velocities in this region were calculated to be 150-200 m/s. The RE_2O_3 showed increased porosity formation compared to the RE_2SiO_5 product layer.

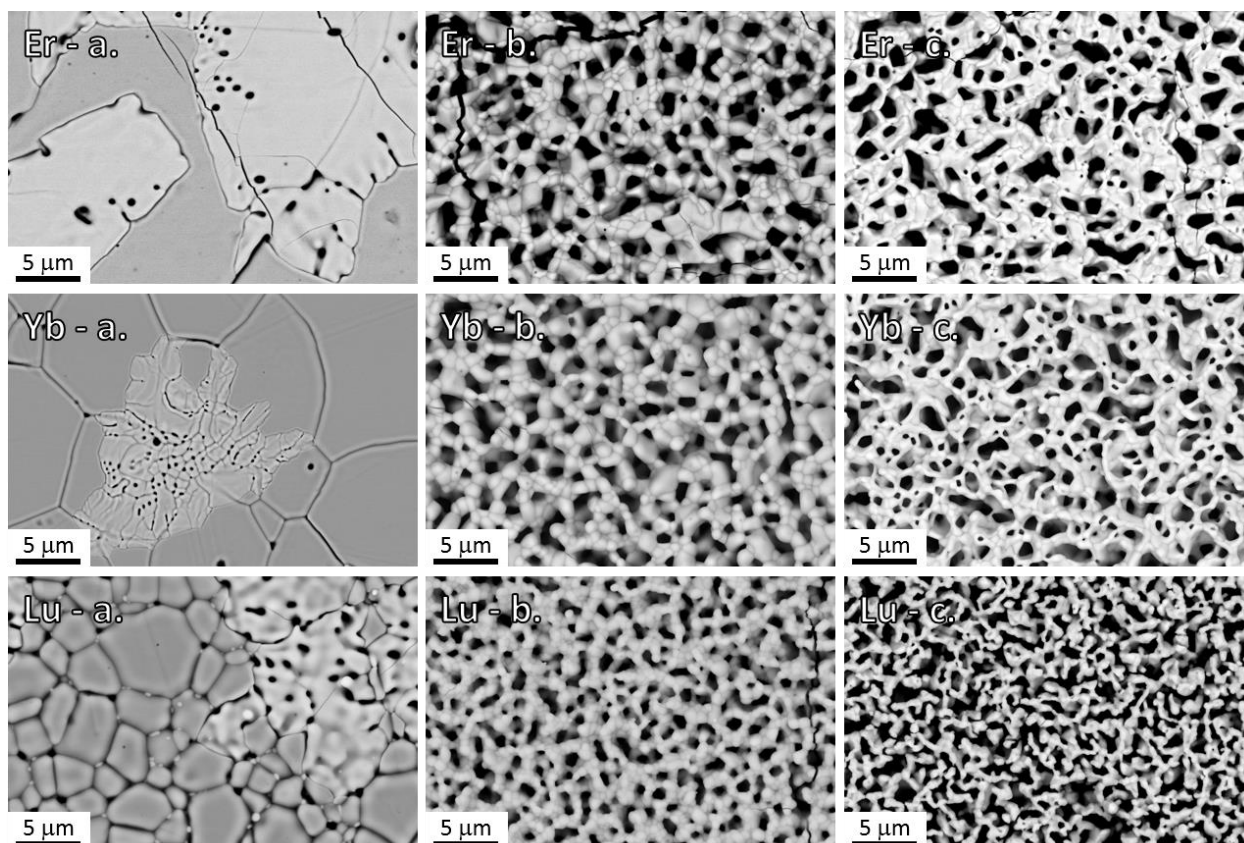


Figure 3-27. Representative backscattered electron SEM images of $RE_2Si_2O_7$ ($RE = Er, Yb, Lu$) after 125 hour steam exposures at 1400 °C for a. stagnant steam velocity region showing the initial formation of RE_2SiO_5 (brighter phase), b. intermediate steam velocity region where porous RE_2SiO_5 is the stable product phase (80-115 m/s), and c. high velocity steam region where RE_2O_3 is the stable product phase (165-185 m/s).

Figure 3-28 displays $RE = Er, Yb, Lu$ coupons mounted in cross section so that the reaction depth could be analyzed. All three materials displayed similar behavior in steam. Figure 3-28a is representative of the 80-115 m/s velocity range shown earlier in plan view. Here, porous RE_2SiO_5 formed on the coupons, with porosity oriented perpendicular to the reaction interface. Increasing in gas velocity to 115-150 m/s, Figure 3-28b shows densification of the outer layer of the RE_2SiO_5 product phase. Densification of the product layer limited gas ingress to the reaction layer so that the total reaction depth decreased compared to the intermediate gas velocity regime of 80-115 m/s. Finally, Figure 3-28c shows RE_2O_3 formation occurring on top of the densified RE_2SiO_5 layer with a continual decrease in total reaction thickness. RE_2O_3 formation implied that the dense RE_2SiO_5 layer was preventing steam reaction with the $RE_2Si_2O_7$ coupons.

Therefore, RE_2O_3 formation was occurring as a secondary reaction of the RE_2SiO_5 product phase.

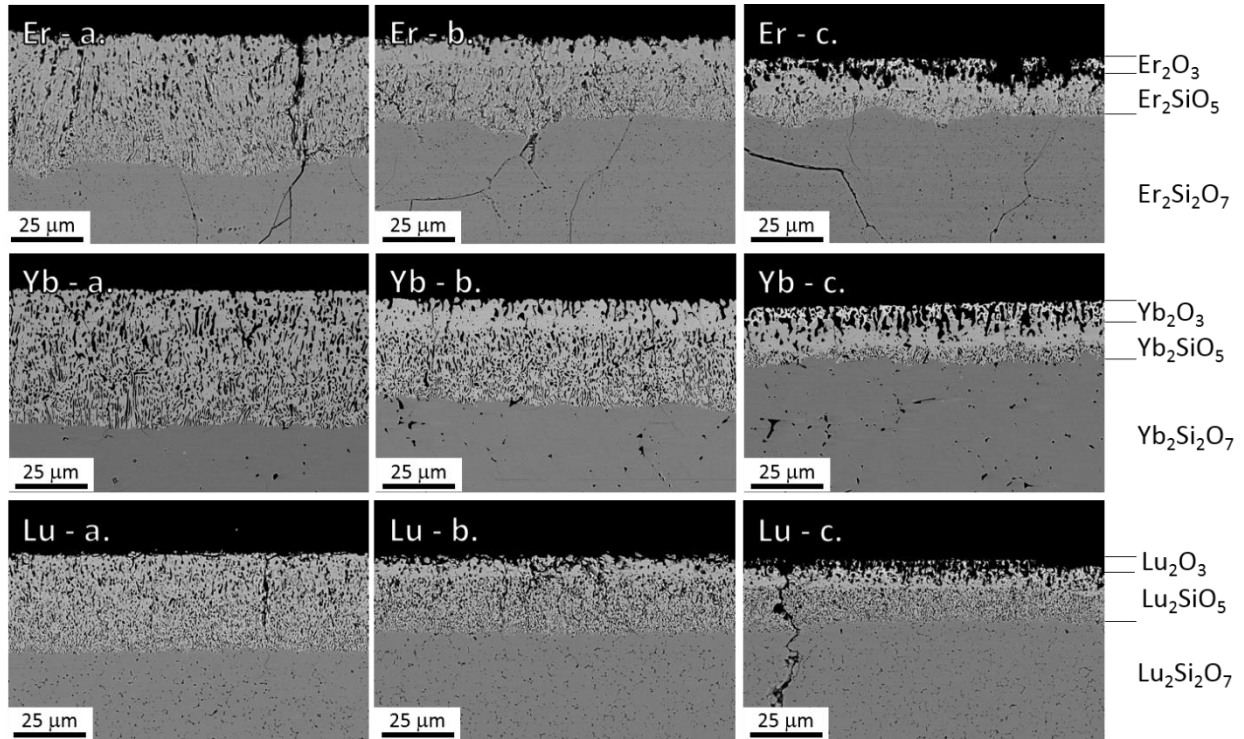


Figure 3-28. Cross-section SEM images of $\text{RE}_2\text{Si}_2\text{O}_7$ ($\text{RE} = \text{Er}, \text{Yb}, \text{Lu}$) after 125 hour steam exposures at $1400\text{ }^\circ\text{C}$ for steam velocity regions of a. 80-115 m/s, b. 120-140 m/s, and c. 165-185 m/s.

3.3.3.3. Steam Exposure of $\text{Sc}_2\text{Si}_2\text{O}_7$

$\text{Sc}_2\text{Si}_2\text{O}_7$ shows unique behavior compared to the previous $\text{RE}_2\text{Si}_2\text{O}_7$ ($\text{RE} = \text{Er}, \text{Yb}, \text{Lu}$) in that Sc_2O_3 was the only product detected after steam exposure. XRD of $\text{Sc}_2\text{Si}_2\text{O}_7$ before and after steam exposure is shown in Figure 3-29. All peaks were matched to either the baseline $\text{Sc}_2\text{Si}_2\text{O}_7$ pattern or Sc_2O_3 . The largest Sc_2O_3 peak (222 hkl plane) displayed a higher intensity compared to the predicted peak heights for Sc_2O_3 , representing some amount of preferential orientation of the oxide after the steam reaction.

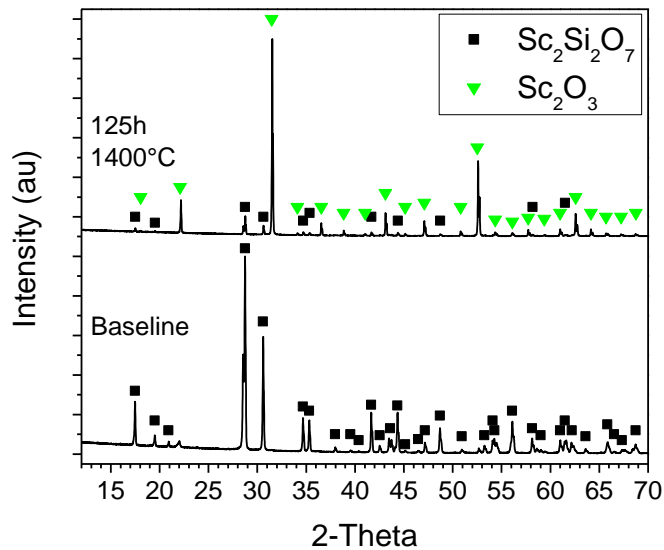


Figure 3-29. XRD of $\text{Sc}_2\text{Si}_2\text{O}_7$ baseline and after steam exposure at 1400 °C for 125 hours.

Plan view SEM images of $\text{Sc}_2\text{Si}_2\text{O}_7$ after steam exposure are shown in Figure 3-30.

Figure 3-30a displays the highest velocity impingement site, where excess material loss attributed to erosion was recorded. Under the platinum foil at near stagnant gas velocities (Figure 3-30b) Sc_2O_3 readily formed across the surface. Sc_2SiO_5 formation was not identified by SEM/EDS in this region even though the local environment was less extreme than at other regions across the sample face. Figure 3-30c is representative of the majority of the sample surface for all gas velocities 80-200 m/s. Here, sub-micron Sc_2O_3 grain formation was present across the sample face with a high amount of sample porosity.

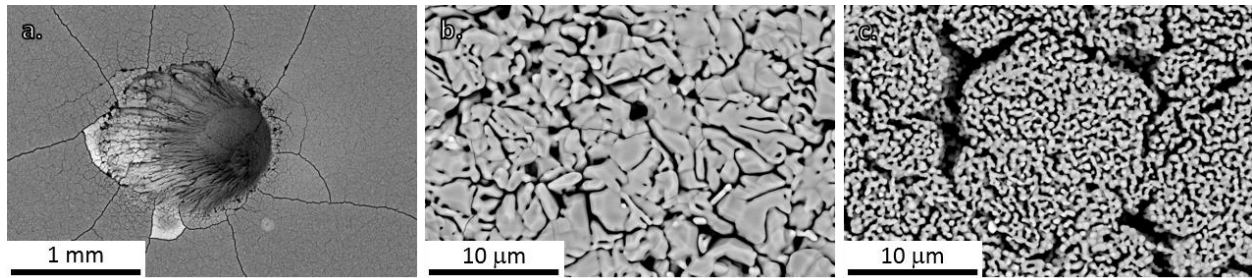


Figure 3-30. Plan view SEM images of $\text{Sc}_2\text{Si}_2\text{O}_7$ after steam exposure for 125 hours at 1400 °C, displaying a. material mechanical erosion at the highest velocity impingement site (200-235 m/s), b. Sc_2O_3 formation in the stagnant gas velocity region, and c. Sc_2O_3 reaction product in the high steam velocity region (165-185 m/s).

A representative backscattered SEM image of the reaction depth for $\text{Sc}_2\text{Si}_2\text{O}_7$ after steam exposure is shown in Figure 3-31a. Sc_2O_3 formation on $\text{Sc}_2\text{Si}_2\text{O}_7$ did not show notable velocity dependence across the majority of the sample, where gas velocities were calculated to be 80-200 m/s. The Sc_2O_3 morphology was additionally constant throughout the thickness of the reaction layer. Figure 3-31b displays sub-micron Sc_2O_3 particulate formed with orientation preference perpendicular to the reaction interface. An EDS linescan across the reaction interface in Figure 3-31c confirmed that Sc_2SiO_5 was not forming at the reaction interface and that Sc_2O_3 was the dominant reaction product for the $\text{Sc}_2\text{Si}_2\text{O}_7$ -steam reaction.

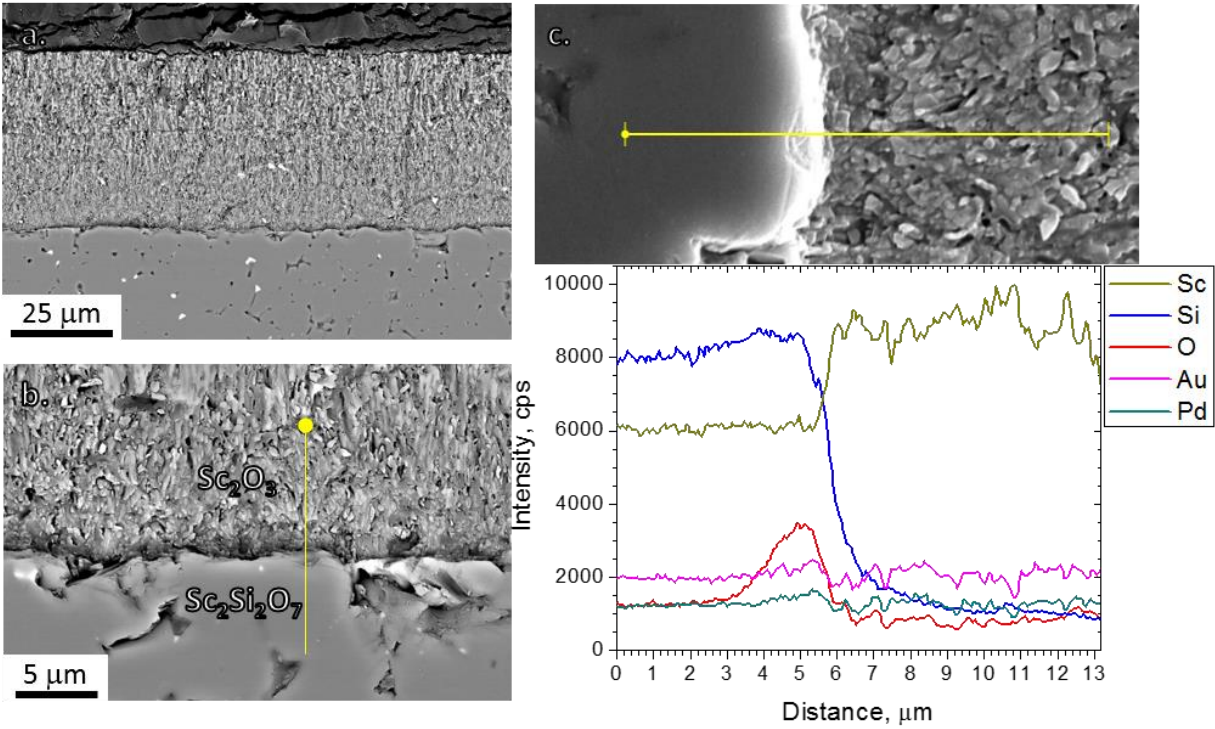


Figure 3-31. Cross-section SEM images of $Sc_2Si_2O_7$ after steam exposure for 125 hours at 1400 °C. a. Sc_2O_3 reaction product thickness at steam velocities 80-180 m/s, b. $Sc_2Si_2O_7$ - Sc_2O_3 reaction interface, and c. EDS linescan across the reaction interface (yellow bar).

3.3.3.4. Steam Exposure of $Nd_2Si_2O_7$

XRD results of the $Nd_2Si_2O_7$ surface before and after steam exposure for 124 hours at 1400 °C are shown in Figure 3-32. A-phase $Nd_2Si_2O_7$ readily reacted with steam to form peaks that match with the apatite phase, $Nd_{9.33}\square_{0.67}Si_6O_{26}$. Other XRD pattern matches included $Nd_{9.35}Si_6O_{26}$ and $Nd_{9.37}Si_6O_{26}$, implying that the Nd concentration could not be precisely determined with the given experimental procedure. While $Nd_4Si_3O_{12}$ ($2Nd_2O_3 \cdot 3SiO_2$) rather than $Nd_{9.33}\square_{0.67}Si_6O_{26}$ ($7Nd_2O_3 \cdot 9SiO_2$) was shown on the Nd_2O_3 - SiO_2 phase diagram, $Nd_{9.33}\square_{0.67}Si_6O_{26}$ is extensively analyzed in the XRD database and the literature as the most commonly accepted Nd silicate cation deficient apatite phase [116], [117]. Texturing of the (100) hkl plane was seen for $Nd_{9.33}\square_{0.67}Si_6O_{26}$, with preferential orientation of (200), (300), (400),

(500), and (600) hkl peaks with relative peak intensities 2.5-3.3 times greater than the reference pattern.

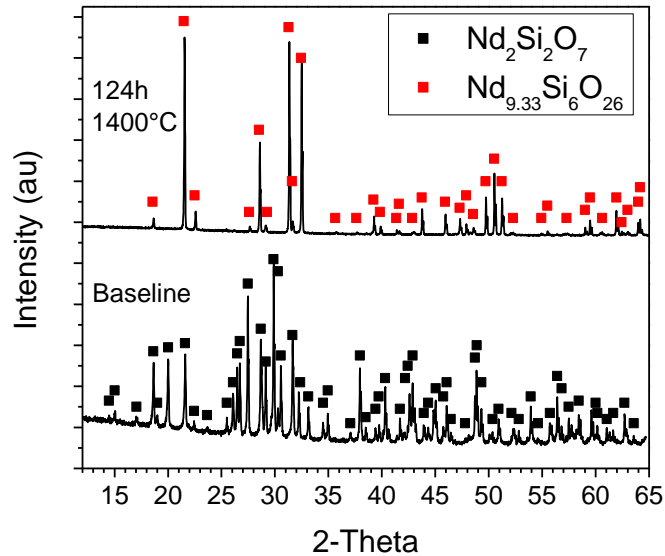


Figure 3-32. XRD of $\text{Nd}_2\text{Si}_2\text{O}_7$ baseline and after steam exposure at 1400 °C for 124 hours.

The impingement site, stagnant velocity region under the platinum foil sample holder, and the high velocity regions of the sample are shown in backscattered electron images in Figure 3-33. The impingement site showed extensive material loss and a large crack that extended completely through the coupon. Under the platinum foil, the hexagonal structure $\text{Nd}_{9.33}\square_{0.67}\text{Si}_6\text{O}_{26}$ phase was present as a dense and heavily faceted reaction layer. All high velocity regions (80-190 m/s) exhibit a porous $\text{Nd}_{9.33}\square_{0.67}\text{Si}_6\text{O}_{26}$ product phase where the grains are interconnected, analogous to faceting planes viewed in Figure 3-33b.

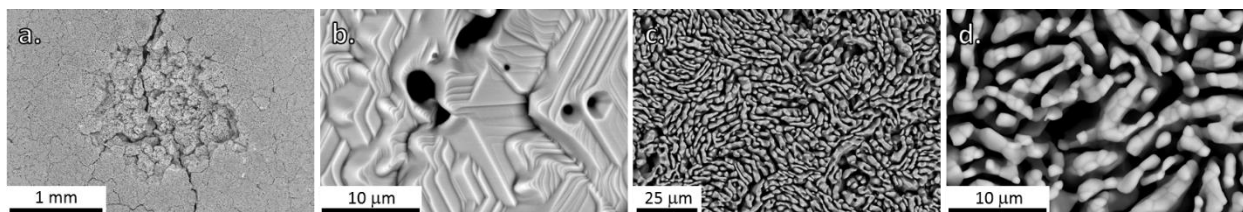


Figure 3-33. Plan view SEM images of $\text{Nd}_2\text{Si}_2\text{O}_7$ after steam exposure at 1400 °C for 124 hours, a. material mechanical erosion at the highest velocity impingement site (200-240 m/s), b. dense hexagonal $\text{Nd}_{9.33}\square_{0.67}\text{Si}_6\text{O}_{26}$ formation in the stagnant gas velocity region, and c./d. $\text{Nd}_{9.33}\square_{0.67}\text{Si}_6\text{O}_{26}$ reaction product in the high steam velocity region (165-185 m/s).

Cross-section analysis of $\text{Nd}_2\text{Si}_2\text{O}_7$ after steam exposure is shown in Figure 3-34. An excessively large porosity network was quickly visible for both velocity regions displayed. Similar to $\text{RE}_2\text{Si}_2\text{O}_7$ (RE = Er, Yb, Lu), densification of the top-layer of the $\text{Nd}_{9.33}\square_{0.67}\text{Si}_6\text{O}_{26}$ product phase was seen when gas velocities are 150-190 m/s that resulted in a slightly decreased total reaction thickness compared to intermediate velocities of 80-115 m/s. Figure 3-34c shows EDS of the densified region in Figure 3-34b, where peaks for C and Au/Pd are present from the epoxy and conductive sample coating, respectively. EDS identification confirmed a Nd/Si at. % ratio of 1.56, which agrees with the Nd/Si ratio of 1.56 for the $\text{Nd}_{9.33}\square_{0.67}\text{Si}_6\text{O}_{26}$ pattern determined by XRD. No other significant variations in Nd/Si ratios were determined by EDS in both plan view or cross-section across the $\text{Nd}_2\text{Si}_2\text{O}_7$ coupon, further affirming that $\text{Nd}_{9.33}\square_{0.67}\text{Si}_6\text{O}_{26}$ was the only product phase forming upon steam reaction.

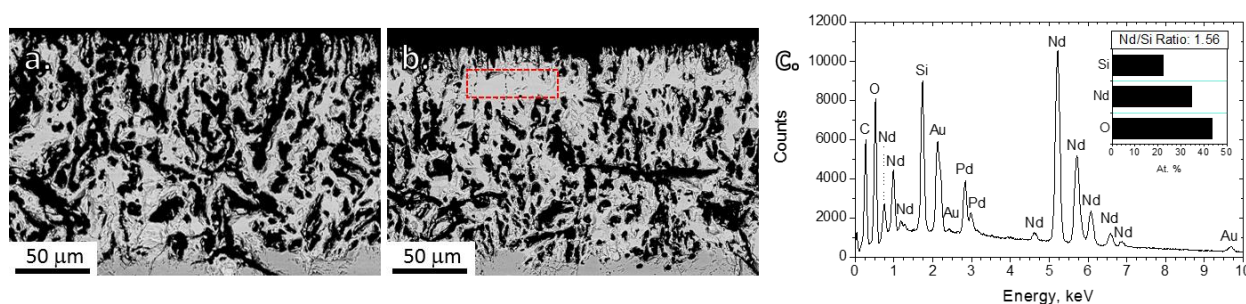


Figure 3-34. Cross-section SEM images of $\text{Nd}_2\text{Si}_2\text{O}_7$ after steam exposure at 1400 °C for 124 hours, a. $\text{Nd}_{9.33}\square_{0.67}\text{Si}_6\text{O}_{26}$ reaction product thickness at steam velocities 80-130 m/s, b. $\text{Nd}_{9.33}\square_{0.67}\text{Si}_6\text{O}_{26}$ reaction product thickness at steam velocities 165-185 m/s, and c. EDS of the reaction product zone marked by the red box in Figure 3-34b.

3.3.4. Analysis

All five silicate materials in this study ($\text{RE}_2\text{Si}_2\text{O}_7$, RE = Sc, Nd, Er, Yb, Lu) displayed porosity increases from a chemical reaction with high-velocity steam. Steam reaction products were rare earth rich phases, representative of silica volatility as $\text{Si}(\text{OH})_4$ (g). $\text{RE}_2\text{Si}_2\text{O}_7$ (RE = Er, Yb, Lu) and $\text{Nd}_2\text{Si}_2\text{O}_7$ displayed densification of the RE_2SiO_5 and $\text{Nd}_{9.33}\square_{0.67}\text{Si}_6\text{O}_{26}$ phases, respectively, where local gas velocities exceeded ~ 150 m/s. $\text{Sc}_2\text{Si}_2\text{O}_7$ uniquely did not display a silicate reaction product, and did not show signs of microstructural evolution due to the high melting temperature of Sc_2O_3 (2472°C). The product phase morphologies were consistently denser in the stagnant gas velocity regions for all tested samples, indicating a change in the reaction process compared to regions exposed to high-velocity steam.

A summation of the measured mass loss, average reaction depths for the steam velocity regions, and porosity production for the steam reaction products are presented in Table 3-9. It should be noted that mass loss data should be treated as qualitative since it includes mass uptake around the edges of the samples where the gas velocity was not high enough to inhibit contamination from the alumina tube furnace. Due to the lack of microstructural evolution and reaction depth changes for $\text{Sc}_2\text{Si}_2\text{O}_7$ (Figure 3-31), the average reaction depth for $\text{Sc}_2\text{Si}_2\text{O}_7$ reaction was presented over the entire 80-200 m/s gas velocity range. The average reaction depth for the 80-115 m/s steam velocity range was analogous to the regions where a porous reaction product forms on the surface without microstructural evolution (Figure 3-28b, Figure 3-31a, Figure 3-34a). The average reaction depth for the 150-200 m/s steam velocity range corresponds to both the densification of the reaction layer (RE = Nd, Er, Yb, Lu) and subsequent reaction to form a second outer product phase, such as rare earth oxides for RE = Er, Yb, and Lu (Figure 3-28c, Figure 3-33b). For each region, the average porosity area fraction was calculated to

compare to theoretical volume changes for the expected steam reactions. The volatilization/erosion behavior at the highest velocity impingement site was recorded, since the direct impingement of high velocity steam provided qualitative information on the resistance to mechanical erosion for each material.

*Table 3-9. Summary of measured mass loss, reaction depths, and area fractions of porosity produced for RE₂Si₂O₇ (RE = Sc, Nd, Er, Yb, and Lu) after high velocity steam exposure at 1400 °C for 125 hours. *Sc₂Si₂O₇ reaction depth and produced porosity amount are averages value over the entire 80-200 m/s steam velocity range.*

Sample	Mass Loss mg/cm ²	Average Reaction Depth 80-115 m/s, µm	Porosity %, 80-125 m/s	Average Reaction Depth 150-200 m/s, µm	Porosity % 150- 200 m/s	Impingement Depth 200-235 m/s, µm
Sc ₂ Si ₂ O ₇	7.49	44 ± 2 *	49% *	44 ± 2 *	49% *	241 ± 10
Nd ₂ Si ₂ O ₇	11.36	155 ± 5	47%	142 ± 7	47%	n/a
Er ₂ Si ₂ O ₇	2.98	50 ± 3	29%	16 ± 3	36%	42 ± 7
Yb ₂ Si ₂ O ₇	3.07	51 ± 2	23%	22 ± 3	43%	37 ± 6
Lu ₂ Si ₂ O ₇	2.69	32 ± 2	24%	22 ± 3	39%	90 ± 4

Both RE₂Si₂O₇ (RE = Sc, Nd) showed larger amounts of mass loss than RE = Er, Yb, Lu). For Sc₂Si₂O₇, the cause of the mass loss was due to increased SiO₂ loss to directly form Sc₂O₃ instead of Sc₂SiO₅ formation. The formation of a fine Sc₂O₃ reaction product also resulted in decreased structural integrity at the highest velocity impingement site, resulting in a mechanical erosion depth of 241 ± 10 µm after steam exposure at 1400 °C for 125 hours.

Nd₂Si₂O₇ uniquely formed a reaction product Nd_{9.33}□_{0.67}Si₆O₂₆, which has a higher SiO₂ concentration than the RE₂SiO₅ product phase. Excess mass loss and microstructural evolution through formation of porosity and porosity channels may be indicative of the lower melting temperature of Nd₂Si₂O₇ compared to other rare earth silicates in this study. The lower melting

temperature (higher homologous temperature) increases atom mobility and may encourage both higher steam reaction rates and rapid coarsening of the porous network. An accurate impingement erosion depth for $\text{Nd}_2\text{Si}_2\text{O}_7$ was not measurable due to a through-thickness crack after steam exposure.

$\text{RE}_2\text{Si}_2\text{O}_7$ (RE = Er, Yb, Lu) all displayed comparable steam reaction products, mass loss, average reaction depths, porosity formation, and impingement erosion depths. Each coupon produced RE_2SiO_5 as the major product phase at gas velocities of 80-115 m/s. From 125-150 m/s, densification of the RE_2SiO_5 layer resulted in decreased total reaction thicknesses. RE_2O_3 was seen to form from the dense RE_2SiO_5 layer when gas velocities exceeded 150 m/s, which further decreased the total reaction depth. The theoretical volume difference between $\text{Yb}_2\text{Si}_2\text{O}_7$ and Yb_2SiO_5 is -24%, between Yb_2SiO_5 and Yb_2O_3 is -32%, and between $\text{Yb}_2\text{Si}_2\text{O}_7$ and Yb_2O_3 is -52%. Initial porosity in each material was subtracted from the porosity area fraction measured after steam exposure to give the porosity production values presented in Table 3-9. Measured average porosity concentrations after steam exposure correlate well with the predicted volume changes. The thickness of the densified intermediate RE_2SiO_5 layer for Er was measurably denser than that of Yb and Lu, which resulted in decreased steam ingress to the reaction interface and thus a decreased total reaction depth in the 150-200 m/s steam velocity range. The cause of increased densification at higher velocities for $\text{Er}_2\text{Si}_2\text{O}_7$ is currently unknown, but may be a result of the lower melting temperature of $\text{Er}_2\text{Si}_2\text{O}_7$ (1800 °C) compared to RE = Yb, Lu (1850 °C, 1860 °C, respectively).

Using XRD and SEM/EDS analysis, the chemical reactions in Eq. 3-3 and 3-4 for RE = Er, Yb, and Lu were confirmed, consistent with the literature. For RE = Sc and Nd (Eq. 3-5 and 3-6), chemical reactions are proposed based on characterization of steam testing performed in

this work. Theoretical volume changes are used for determining porosity production for the given reactions.



The formation of Sc_2O_3 directly from $Sc_2Si_2O_7$ requires increased $H_2O (g)$ usage in the chemical reaction compared to Eq. 3-5 with a larger theoretical volume change of 53%. The chemical reaction for $Nd_2Si_2O_7$ is considered hypothetical due to the complexity of the reaction product. The theoretical porosity formation from $Nd_2Si_2O_7$ to $Nd_{9.33}\square_{0.67}Si_6O_{26}$ is 15%, which is much smaller than the measured porosity area fraction of 47% after 1400 °C steam exposure.

3.3.5. Discussion

XRD and SEM/EDS analysis showed $RE_2Si_2O_7$ ($RE = Er, Yb, Lu$) react with steam after 125 hours at 1400 °C to produce both RE_2SiO_5 and RE_2O_3 product phases. Each material also displayed similar microstructural changes across local regions of the sample surfaces. Near-stagnant steam velocity regions showed dense RE_2SiO_5 formation at $RE_2Si_2O_7$ grain boundaries for all three materials. Porous RE_2SiO_5 formed as the stable surface product at intermediate gas velocities (80-115 m/s). All three materials showed densification of this product layer in the 125-150 m/s steam velocity range. The densified RE_2SiO_5 product layer further reacted to form RE_2O_3 in the high velocity steam range of 150-200 m/s once gas transport to the disilicate interface was shut off. $Lu_2Si_2O_7$ showed the lowest specific mass loss and reaction depth for the 80-115 m/s steam velocity range compared to $RE = Er, Yb$. At higher velocities, Er_2SiO_5 product

layer densified better than RE = Yb, Lu, which resulted in $\text{Er}_2\text{Si}_2\text{O}_7$ displaying smaller total reaction depths at steam velocities of 150-200 m/s. At the highest velocity impingement site, $\text{Yb}_2\text{Si}_2\text{O}_7$ displayed the smallest total reaction thickness with minimal mechanical erosion, while RE = Er and Lu did show mechanical erosion. Average steam reaction depth, the rate of microstructural evolution such as product phase densification, and high-velocity mechanical erosion are all important factors for consideration in EBC design against steam reaction.

Klemm et al. showed that the steam stability of bulk $\text{Sc}_2\text{Si}_2\text{O}_7$ was similar to bulk Sc_2SiO_5 after steam exposure in a burner rig at 1450 °C for 100 hours [48]. The results of the current study verify the lack of stability of Sc_2SiO_5 in steam environments. The $\text{Sc}_2\text{Si}_2\text{O}_7$ material reacted to directly form Sc_2O_3 instead of the expected reaction to form Sc_2SiO_5 . Sc_2SiO_5 was not seen at the reaction interface or at near stagnant gas velocity regions where initial Sc_2O_3 formation occurred at grain boundaries. While the total reaction depth of the $\text{Sc}_2\text{Si}_2\text{O}_7$ reaction was comparable to that of RE = Er, Yb, and Lu, the $\text{Sc}_2\text{Si}_2\text{O}_7$ material underwent twice the amount of silica loss to produce the Sc_2O_3 reaction product. Thus, the specific mass loss for $\text{Sc}_2\text{Si}_2\text{O}_7$ after 125 hours in steam at 1400 °C was much higher than RE = Er, Yb, Lu. As shown earlier with Figure 3-4, Sc_2SiO_5 displayed $33 \pm 2 \mu\text{m}$ total reaction thickness after exposure to steam at 1400 °C for 125 hours, which is comparable to the reaction depth seen here for $\text{Sc}_2\text{Si}_2\text{O}_7$ ($44 \pm 2 \mu\text{m}$). The results of this work are in agreement with the similar steam reaction rates of $\text{Sc}_2\text{Si}_2\text{O}_7$ and Sc_2SiO_5 discussed by Klemm et al. [48].

Unlike other $\text{RE}_2\text{Si}_2\text{O}_7$ in this work, the Sc_2O_3 product layer did not undergo densification in the 125-150 m/s steam velocity range, as was seen for the RE_2SiO_5 (RE = Er, Yb, Lu) product phases. The stability of Sc_2O_3 product layer may result from increased stability of the Sc_2O_3 oxide phase (2472 °C) compared to RE_2SiO_5 (1950-2000 °C), reflected in the

product phase melting temperatures. Additionally, extensive impingement site mechanical erosion was measured for the $\text{Sc}_2\text{Si}_2\text{O}_7$ sample. The erosion is presumably caused from the lack of structural integrity of the highly porous Sc_2O_3 product phase, analogous to the behavior of HfSiO_4 and the highly porous HfO_2 steam reaction product discussed in Chapter 2.2. Therefore, $\text{Sc}_2\text{Si}_2\text{O}_7$ is not recommended as a single-layer EBC material.

$\text{Nd}_2\text{Si}_2\text{O}_7$ was exposed to steam for 124 hours at 1400 °C and uniquely displayed a complex intermediate line compound, $\text{Nd}_{9.33}\square_{0.67}\text{Si}_6\text{O}_{26}$, as the steam reaction product. This apatite phase determined in this work is the same as in the literature, where slight variation in the Nd stoichiometry agrees with the compositionally variant nature of apatite structures [107].

A coarse pore network was seen in the $\text{Nd}_{9.33}\square_{0.67}\text{Si}_6\text{O}_{26}$ reaction layer, where total reaction thicknesses far exceeded all other $\text{RE}_2\text{Si}_2\text{O}_7$ samples tested in this study. The increased thicknesses of the pore channels may be associated with the structural nature of the rare earth apatites. Figure 3-35 displays the $\text{Nd}_{9.33}\square_{0.67}\text{Si}_6\text{O}_{26}$ unit cell and the c-direction view of the extended crystal structure with the (100) plane in black, as preferential growth of the (100) plane for the apatite structure was determined from XRD analysis. Slater et al. showed that oxide ion conductivity is particularly high for the rare earth apatite systems, and parallel to the c-axis, conductivity can be an order of magnitude higher parallel than the a- or b-axes [118]. Increased mobility of oxygen and vacancies along the c-axis, parallel to the sample surface, may be contributing to the increased porosity network. $\text{Nd}_2\text{Si}_2\text{O}_7$ showed the highest mass loss and largest average reaction depth, reinforcing the concept that $\text{Nd}_2\text{Si}_2\text{O}_7$ is not desirable as a single layer EBC material.

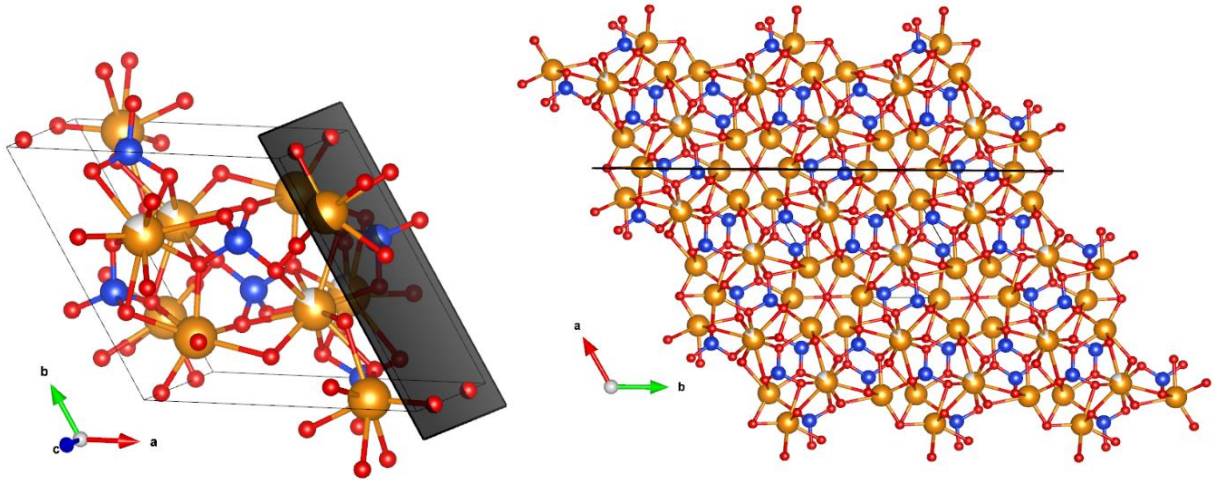


Figure 3-35. Unit cell and extended crystal structure of $\text{Nd}_{9.33}\square_{0.67}\text{Si}_6\text{O}_{26}$, with the (100) hkl plane in black, where the (100) plane was preferentially formed on the surface of $\text{Nd}_2\text{Si}_2\text{O}_7$ after steam exposure at 1400 °C for 124 hours.

The densification of steam product layers can be better understood through comparison of homologous temperatures for the reaction products after the 1400 °C steam exposures. Figure 3-36 displays the tested material and the steam reaction product and relates the coarsening behavior to the homologous temperature, or 1673 K divided by the reaction product melting temperature in Kelvin. Coarsening of the product layer was only seen for materials with a homologous temperature greater than 0.7.

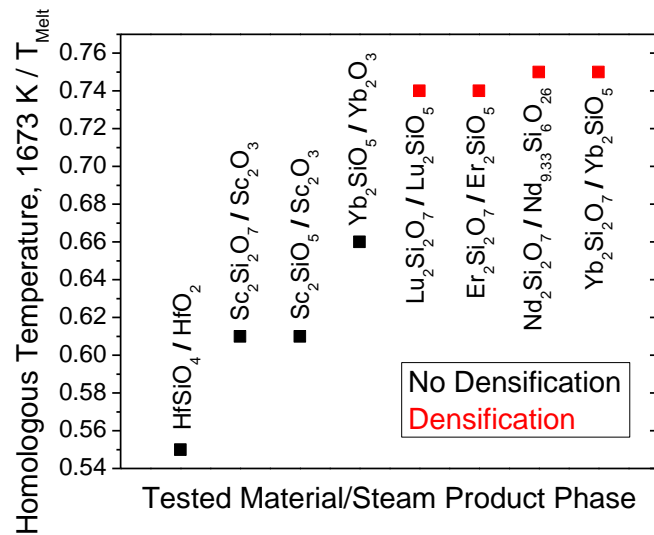


Figure 3-36. Homologous temperatures for each RE₂Si₂O₇ steam product phase. Reaction products that exhibited densification of the product layer are shown in red.

Homologous temperature was also utilized to compare the average reaction rates for EBC materials exposed to water vapor at 1400 °C for 125 hours, shown in Figure 3-37. Materials that displayed densification of the steam product phase are displayed in red, while materials that did not show major microstructural evolution of the steam product phase are presented in black. EBCs with the lowest homologous temperature, such as the rare earth monosilicates (RE₂SiO₅, RE = Sc and Yb), displayed the least degree of steam degradation. BSAS has the highest homologous temperature of the EBCs tested in this study (0.86) and was shown in Chapter 2.1 to volatilize all of its oxide constituents at 1400 °C. The RE₂Si₂O₇ materials tested in this study generally follow the same trend. Comparison of homologous temperatures for EBCs may represent a method for predicting the degree of water vapor reaction, although both scandium silicates (Sc₂SiO₅ and Sc₂Si₂O₇) do not fully agree with the hypothesis presented.

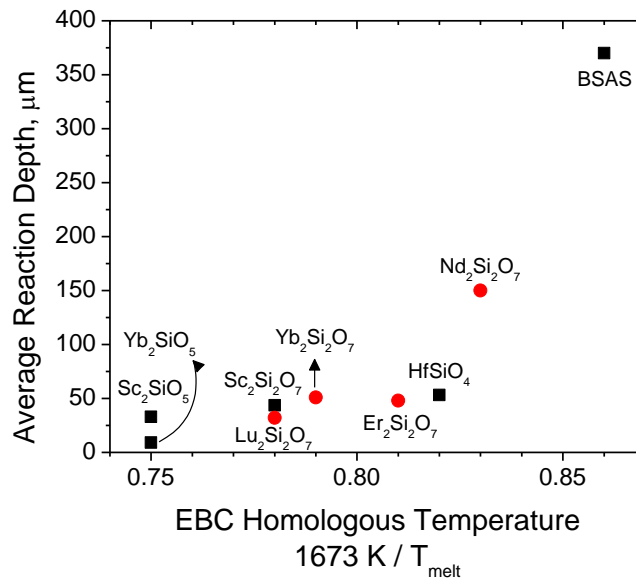


Figure 3-37. Average steam reaction depths compared to EBC homologous temperature for steam exposures at 1400 °C.

3.3.6. Conclusion

The high-velocity steam stability of single rare earth cation RE₂Si₂O₇ compounds is not universal, as suggested by available silica activity data. The reactivity of five RE₂Si₂O₇ (RE = Sc, Nd, Er, Yb, Lu) EBC candidates were compared after exposure to high-velocity H₂O (g) at 1400 °C for 125h. RE₂Si₂O₇ for RE = Er, Yb, and Lu displayed a primary reaction to form a porous silica-depleted RE₂SiO₅, similar to prior results in the literature. The RE₂SiO₅ further reacted with H₂O (g) to form porous RE₂O₃. RE = Sc and Nd both showed unique steam reactions, where Sc₂Si₂O₇ forms only a Sc₂O₃ layer and Nd₂Si₂O₇ readily forms Nd_{9.33}□_{0.67}Si₆O₂₆. Lu₂Si₂O₇ displayed the smallest average reaction depth of the present RE₂Si₂O₇, implying it may have increased steam resistance compared to the state-of-the-art EBC Yb₂Si₂O₇. This finding was supported by analysis of homologous temperatures of the EBCs and of their constituent reaction products. The steam reactivity of silicates was shown to trend with EBC homologous temperature, while beneficial microstructural changes such as densification

were found to be dependent on the reaction product homologous temperature. Rare earth cation considerations are thus important to consider for single rare earth cation EBC coatings as well as multi-component EBC candidate materials. It is possible that multi-component rare earth silicate mixtures could promote formation of certain steam reaction products, enhance structural integrity to limit high velocity mechanical erosion, and possibly tailor the steam reactivity for an optimized EBC material candidate. Particularly, formation of a multi-component $RE_2Si_2O_7$ with a high melting temperature, or a low homologous temperature, could result in an EBC with decreased steam reactivity relative to its individual constituents.

3.4. Multi-component $\text{RE}_2\text{Si}_2\text{O}_7$: Trends with Thermal Conductivity, Thermal Expansion, Young's Modulus, and High-velocity Steam Resistance

3.4.1. Introduction

Multi-component $\text{RE}_2\text{Si}_2\text{O}_7$ were produced to analyze thermal properties and phase stability through multiple rare earth cation solutions. The thermal expansion match between SiC and beta phase $\text{RE}_2\text{Si}_2\text{O}_7$, shown in Figure 3-38a, suggested the study of silicate solutions that incorporated RE = Sc, Lu, Yb, Er, and Y would be promising for EBCs. Beta phase $\text{RE}_2\text{Si}_2\text{O}_7$ for RE = Sc, Lu, and Yb do not display polymorphs at elevated temperatures which is also a desirable property for EBCs. Thermal expansion and phase stability are clear limitations for choice of rare earth elements as EBCs. Thus, stabilization of the beta phase was attempted through $\text{RE}_2\text{Si}_2\text{O}_7$ solutions with RE = Sc, Y, Nd, Er, Yb, and Lu powders. Steam reactions with phase pure $\text{Sc}_2\text{Si}_2\text{O}_7$ to form Sc_2O_3 and phase pure $\text{Nd}_2\text{Si}_2\text{O}_7$ to form $\text{Nd}_{9.33}\square_{0.67}\text{Si}_6\text{O}_{26}$ were considered undesirable product phases, as previously shown in Chapter 3.3. The ability to tailor the steam reaction product will be studied through Sc and Nd additions to multi-component solutions. $\text{Nd}_2\text{Si}_2\text{O}_7$ represents a traditionally undesirable EBC material, with a polymorph transition near 1400 °C and high CTEs for both stable phases. RE = Er and Y also display high-temperature polymorphs which make them undesirable as single layer EBCs.

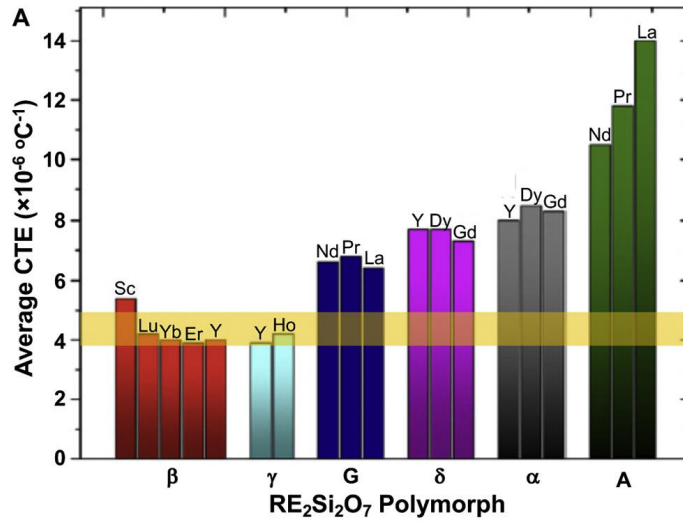


Figure 3-38. Thermal expansion of RE₂Si₂O₇ polymorphs compared to that of SiC (yellow bar) [105].

Research on (Y_xYb_{1-x})₂Si₂O₇ showed that the desired beta phase can be stabilized and that the undesired high-temperature polymorphs associated with Y₂Si₂O₇ can be avoided, depending on the ytterbium concentration [119]. A high entropy (Yb_{0.2}Y_{0.2}Lu_{0.2}Sc_{0.2}Gd_{0.2})₂Si₂O₇ was produced, where the low-CTE beta phase was stabilized for the solid solution [101] despite Gd₂Si₂O₇ being stable as the α-phase in the temperature range of interest. A 4-component disilicate (Er_{0.25}Tm_{0.25}Yb_{0.25}Lu_{0.25})₂Si₂O₇ was processed by Sun et al. and subjected to stagnant water vapor at 1400 °C for five hours [120]. The traditionally stable high-temperature polymorphs for Y₂Si₂O₇ and Tm₂Si₂O₇ were not present for the (Er_{0.25}Tm_{0.25}Yb_{0.25}Lu_{0.25})₂Si₂O₇ solution, further solidifying the concept of phase stabilization for rare earth silicates. The sample displayed large SiO₂ deposits on the sample surface after stagnant velocity steam exposure in a thermogravimetric analyzer, implying silica volatility from any steam reaction was not actually occurring during exposure [120]. While phase stabilization has been demonstrated in the literature, the impact of multi-component RE₂Si₂O₇ solutions on all pertinent EBC material properties is not yet fully understood.

The objective of this study is to address phase stability, thermochemical properties, and thermomechanical properties for the following sample solutions: $(\text{Sc}_{0.33}\text{Yb}_{0.67})_2\text{Si}_2\text{O}_7$, $(\text{Sc},\text{Y},\text{Yb})_2\text{Si}_2\text{O}_7$, $(\text{Er},\text{Yb},\text{Lu})_2\text{Si}_2\text{O}_7$, $(\text{Y},\text{Er},\text{Yb},\text{Lu})_2\text{Si}_2\text{O}_7$, $(\text{Sc}_{0.15}\text{Y}_{0.4}\text{Er}_{0.5}\text{Yb}_{0.5}\text{Lu}_{0.45})_2\text{Si}_2\text{O}_7$, and $(\text{Sc},\text{Nd},\text{Er},\text{Yb},\text{Lu})_2\text{Si}_2\text{O}_7$. Linear thermal expansion, Young's Modulus, thermal conductivity, and high-velocity steam reactivity were measured and assessed relative to the constituent single cation $\text{RE}_2\text{Si}_2\text{O}_7$.

3.4.2. Methods

Powders were weighed and annealed in air at 900 °C for 15 minutes to remove any organic binder on the powders, followed by ball milling with yttria-stabilized zirconia milling media for 24 hours. Samples were then consolidated with SPS between 1515-1620 °C with 65 MPa total pressure for 45 – 60 minutes in argon. Following sintering, samples were annealed in an open-air box furnace at either 1300 °C or 1500 °C for 24 hours. Sample densities were measured by Archimedes' method in deionized water four times and averaged.

Thermal expansion was determined using an Al_2O_3 pushrod dilatometer (Netzsch dil402c, Burlington, MA) with 25 cN applied force and 75 sccm flowing argon. An Al_2O_3 correction was performed for each material and subtracted from the final data. Sample rods of ~ 15 mm length and cross-section dimensions of approximately 3 mm x 5 mm were tested at 10 °C/min heating and cooling rates up to 1400 °C. Average linear thermal expansion was determined from the 200 °C – 1250 °C temperature range for the dilatometer heating curves.

Young's Modulus was measured via nanoindentation with an MTS Nano XP (MTS Systems Corporation, Eden Prairie, MN) at room temperature. Sample indents were taken 100 μm apart with 20-60 indents per sample with a constant strain rate of 0.1 /s to a maximum indentation depth of 2 μm . A Poisson's ratio of 0.3 was assumed for all silicate materials tested,

which was in general agreement with the literature [105]. Young's Modulus was averaged for each sample indentation with data from 100-200 nm indentation depths to minimize interaction with underlying porosity in the material.

Room temperature thermal conductivity was measured by Dr. Hans Olsen and Dr. Patrick Hopkins of the ExSITE research group at the University of Virginia via steady-state thermoreflectance (SSTR) laser technique [121]. SSTR utilizes a split-beam laser as both a steady state heat source for the sample and as a subsequent probing laser to discern changes in the sample reflectance, where thermoreflectance was correlated to thermal conductivity through an aluminum thin film transducer deposited on the sample surfaces. Samples were polished to less than 50 nm average surface roughness prior to aluminum deposition and SSTR measurements.

High-velocity water vapor testing was performed in the steamjet at 1400 °C for 125 hours. The steamjet setup has been described in Chapter 2.1.2.2. Sample mass change was recorded for each material exposure. Surface reactions were analyzed in plan view by XRD and SEM/EDS. Samples were then mounted in cross-section to analyze the reaction depth across the impingement site. ImageJ analysis suite was used to measure total reaction depths for various steam velocity regions.

3.4.3. Results

3.4.3.1. Starting Microstructure and Phase Stability

Initial characterization and starting microstructures of each multi-component RE₂Si₂O₇ are shown in Table 3-10 and in Figure 3-39 with backscattered electron SEM.

(Sc_{0.33}Yb_{0.67})₂Si₂O₇, (Sc,Y,Yb)₂Si₂O₇, (Er,Yb,Lu)₂Si₂O₇, (Y,Er,Yb,Lu)₂Si₂O₇, and

(Sc_{0.15}Y_{0.4}Er_{0.5}Yb_{0.5}Lu_{0.45})₂Si₂O₇ were found by XRD (shown later) and EDS, provided in Appendix 8.4, to be single phase β-RE₂Si₂O₇ with only minor rare earth cation clustering.

Table 3-10. Starting mixtures, stable phases, SEM area fractions, and densities for multi-component RE₂Si₂O₇ samples.

Sample RE ₂ Si ₂ O ₇	Stable Phase	Porosity Area Fraction	Measured Density, g/cm ³	Theoretical Density, Rule of Mixtures, g/cm ³
Sc _{0.33} Yb _{0.67}	β, C2/m	1.5 %	5.20 ± 0.02	5.22
Sc _{0.333} Y _{0.333} Yb _{0.333}	β, C2/m	5 %	4.49 ± 0.03	4.51
Er _{0.333} Yb _{0.333} Lu _{0.333}	β, C2/m	3 %	5.94 ± 0.01	6.09
Y _{0.25} Er _{0.25} Yb _{0.25} Lu _{0.25}	β, C2/m	8 %	5.44 ± 0.01	5.58
Sc _{0.15} Y _{0.4} Er _{0.5} Yb _{0.5} Lu _{0.45}	β, C2/m	5 %	5.21 ± 0.01	5.36
Sc _{0.2} Nd _{0.2} Er _{0.2} Yb _{0.2} Lu _{0.2}	β, C2/m + G, P2 ₁ /c	3 %	5.31 ± 0.01	5.42

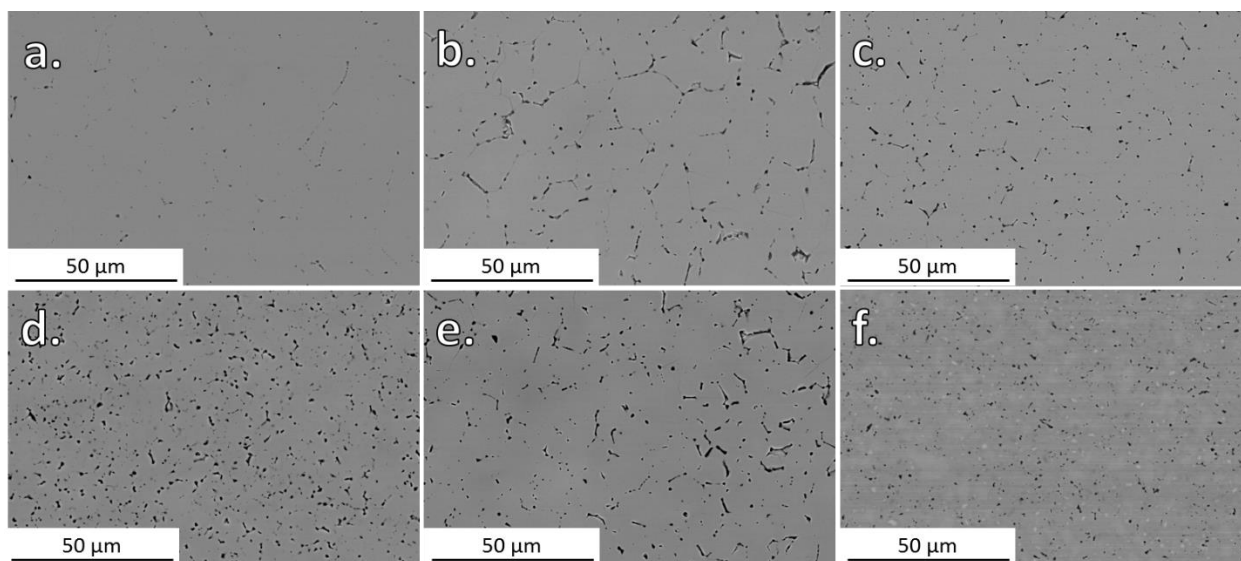


Figure 3-39. Starting microstructures of multi-component $RE_2Si_2O_7$, for RE = a. $Sc_{0.33}Yb_{0.67}$, b. $ScYb$, c. $ErYbLu$, d. $YErYbLu$, e. $Sc_{0.15}Y_{0.4}Er_{0.5}Yb_{0.5}Lu_{0.45}$, and f. $ScNdErYbLu$.

$(Sc,Nd,Er,Yb,Lu)_2Si_2O_7$ was found to be multi-phase and consisting of the β - and G- $RE_2Si_2O_7$ phases as shown in Figure 3-40. G- $RE_2Si_2O_7$ and γ - $RE_2Si_2O_7$ are both $P2_1/c$ space group monoclinic structures, and therefore differentiation between the two phases via XRD analysis was not possible for the multi-component $RE_2Si_2O_7$. The G- phase is the known stable high-temperature phase for $Nd_2Si_2O_7$, while the γ - phase is the stable high temperature phase for $Er_2Si_2O_7$. Both Nd and Er elements were concentrated in the secondary phase present in $(Sc,Nd,Er,Yb,Lu)_2Si_2O_7$, as will be shown with EDS data during the high-velocity steam section. Without conducting further higher resolution crystal analysis, the second phase will be referred to as G- phase throughout this work. The presence of G- $RE_2Si_2O_7$ represents phase stabilization of the Nd-rich phase, where the A- $RE_2Si_2O_7$ phase was predicted to be stable after annealing.

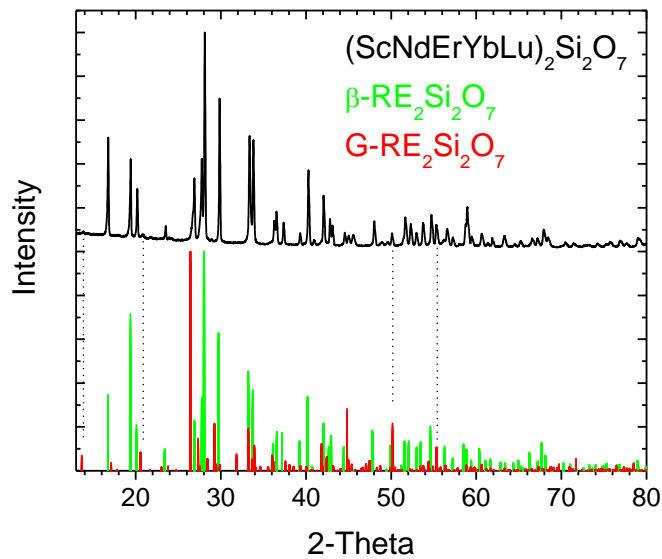


Figure 3-40. XRD of $(\text{ScNdErYbLu})_2\text{Si}_2\text{O}_7$ sample after 1300 °C anneal for 24 hours, displaying the presence of β - and G- $\text{RE}_2\text{Si}_2\text{O}_7$ phases.

3.4.3.2. Thermal Conductivity, Thermal Expansion, and Young's Modulus of Single and Multi-component $\text{RE}_2\text{Si}_2\text{O}_7$

Room temperature thermal conductivity values measured in this study and in the literature for single and multi-component $\text{RE}_2\text{Si}_2\text{O}_7$ are presented in Table 3-11. Presented literature comparisons were performed by laser flash technique, although no measurements, calculations, or estimations of thermal conductivity were found for $\text{Nd}_2\text{Si}_2\text{O}_7$ or $\text{Er}_2\text{Si}_2\text{O}_7$. The thermal conductivity of $\text{Lu}_2\text{Si}_2\text{O}_7$ measured in this study (8.7 ± 0.7) was double that of both measurements in the literature (4.4 W/mK [122] and 4.3 W/mK [105]).

Table 3-11. Room temperature thermal conductivity (κ) for single and multi-component $RE_2Si_2O_7$.

Material	κ (W/mK), 25 °C, This Study	κ (W/mK), 25 °C, Literature
$Sc_2Si_2O_7$	9.3 ± 0.5	9.4 [105]
β - $Y_2Si_2O_7$	6.3 ± 0.5	5.2 [105], 5.4 [122]
A- $Nd_2Si_2O_7$	1.2 ± 0.2	Data not available
β - $Er_2Si_2O_7$	4.6 ± 0.4	Data not available
$Yb_2Si_2O_7$	5.5 ± 0.5	4.3 [105], 4.45 [122]
$Lu_2Si_2O_7$	8.7 ± 0.7	4.3 [105], 4.4 [122]
$(Sc_{0.33}Yb_{0.67})_2Si_2O_7$	3.0 ± 0.3	
$(ScYYb)_2Si_2O_7$	2.2 ± 0.3	
$(ErYbLu)_2Si_2O_7$	6.3 ± 0.5	
$(YErYbLu)_2Si_2O_7$	4.3 ± 0.4	
$(Sc_{0.15}Y_{0.4}Er_{0.5}Yb_{0.5}Lu_{0.45})_2Si_2O_7$	2.5 ± 0.3	

Table 3-12 displays linear coefficients of thermal expansion for single and multi-component $RE_2Si_2O_7$ determined via dilatometry from heating curves in the temperature range of 200 °C - 1250 °C. Measured values were slightly higher than CTEs calculated from hot stage XRD in the literature [103], [123]. Raw dilatometer data for each tested material are presented in Appendix 8.5.

Table 3-12. Linear CTE for single and multi-component RE₂Si₂O₇.

Material	CTE x10 ⁶ /°C, 200-1250 °C, This Study	CTE x10 ⁶ /°C, Literature	Literature Temperature Range, °C
Sc ₂ Si ₂ O ₇	5.4 ± 0.7	5.4 [103]	30-1600
β-Y ₂ Si ₂ O ₇	5.2 ± 0.8	4.1 [123]	25-1400
A-Nd ₂ Si ₂ O ₇	12.5 ± 0.5	10.5 [103]	30-1200
β-Er ₂ Si ₂ O ₇	4.3 ± 0.8	3.9 [103]	30-1600
Yb ₂ Si ₂ O ₇	4.9 ± 0.4	4.0 [103]	30-1600
Lu ₂ Si ₂ O ₇	5.4 ± 0.8	4.2 [103]	30-1550
(Sc _{0.33} Yb _{0.67}) ₂ Si ₂ O ₇	4.7 ± 0.6		
(ScYYb) ₂ Si ₂ O ₇	4.5 ± 0.6		
(ErYbLu) ₂ Si ₂ O ₇	5.6 ± 0.7		
(YErYbLu) ₂ Si ₂ O ₇	4.9 ± 0.6		
(Sc _{0.15} Y _{0.4} Er _{0.5} Yb _{0.5} Lu _{0.45}) ₂ Si ₂ O ₇	4.1 ± 0.4		
(ScNdErYbLu) ₂ Si ₂ O ₇ multi-phase	4.8 ± 0.3		

Average room temperature Young's Modulus measurements of RE₂Si₂O₇ are displayed in Table 3-13. Calculated values from the literature are marked with an asterix, although it should be noted that A-Nd₂Si₂O₇ and δ-Er₂Si₂O₇ are determined from periodic trends in the Materials Project database and are only estimated [124], [125]. Given the high degree of anisotropy in Young's Modulus for RE₂Si₂O₇ materials [105], the values measured in the current study were considered comparable to both experimental and computational work performed in the literature.

Table 3-13. Room temperature Young's Modulus for single and multi-component $RE_2Si_2O_7$. *Values are calculated.

Material	Young's Modulus, GPa, 25 °C, This Study	Young's Modulus, GPa, 25 °C, Literature
$Sc_2Si_2O_7$	229 ± 14	200 [126], 202 [105]
β - $Y_2Si_2O_7$	188 ± 12	170* [122]
A- $Nd_2Si_2O_7$	153 ± 10	162* [124], [125]
β - $Er_2Si_2O_7$	182 ± 6	184* [125], [127]
δ - $Er_2Si_2O_7$	144 ± 19	190* [124], [125]
$Yb_2Si_2O_7$	195 ± 11	205 [126], 162* [122]
$Lu_2Si_2O_7$	198 ± 10	178* [122]
$(Sc_{0.33}Yb_{0.67})_2Si_2O_7$	206 ± 10	
$(Sc_{0.33}Y_{0.33}Yb_{0.33})_2Si_2O_7$	196 ± 15	
$(Er_{0.33}Yb_{0.33}Lu_{0.33})_2Si_2O_7$	191 ± 15	
$(Y_{0.25}Er_{0.25}Yb_{0.25}Lu_{0.25})_2Si_2O_7$	185 ± 15	
$(Sc_{0.15}Y_{0.4}Er_{0.5}Yb_{0.5}Lu_{0.45})_2Si_2O_7$	204 ± 17	
$(Sc_{0.2}Nd_{0.2}Er_{0.2}Yb_{0.2}Lu_{0.2})_2Si_2O_7$ multi-phase	179 ± 16	

3.4.3.3. Steamjet Exposures

High-velocity steam exposures were performed at 1400 °C for 125 hours for $(ScYYb)_2Si_2O_7$, $(ErYbLu)_2Si_2O_7$, $(YErYbLu)_2Si_2O_7$, and multi-phase $(ScNdErYbLu)_2Si_2O_7$. Figure 3-41 shows the XRD patterns before and after steam exposure for each sample. After steam exposures, $(ScYYb)_2Si_2O_7$, $(ErYbLu)_2Si_2O_7$, and $(YErYbLu)_2Si_2O_7$ displayed X2 phase RE_2SiO_5 and cubic RE_2O_3 peaks, while $(ScNdErYbLu)_2Si_2O_7$ only displayed matches to an X2 phase RE_2SiO_5 . All materials displayed peak shifting relative to the presented Yb_2O_3 , Yb_2SiO_5 , and $Yb_2Si_2O_7$ reference patterns due to the varied rare earth elements in solution.

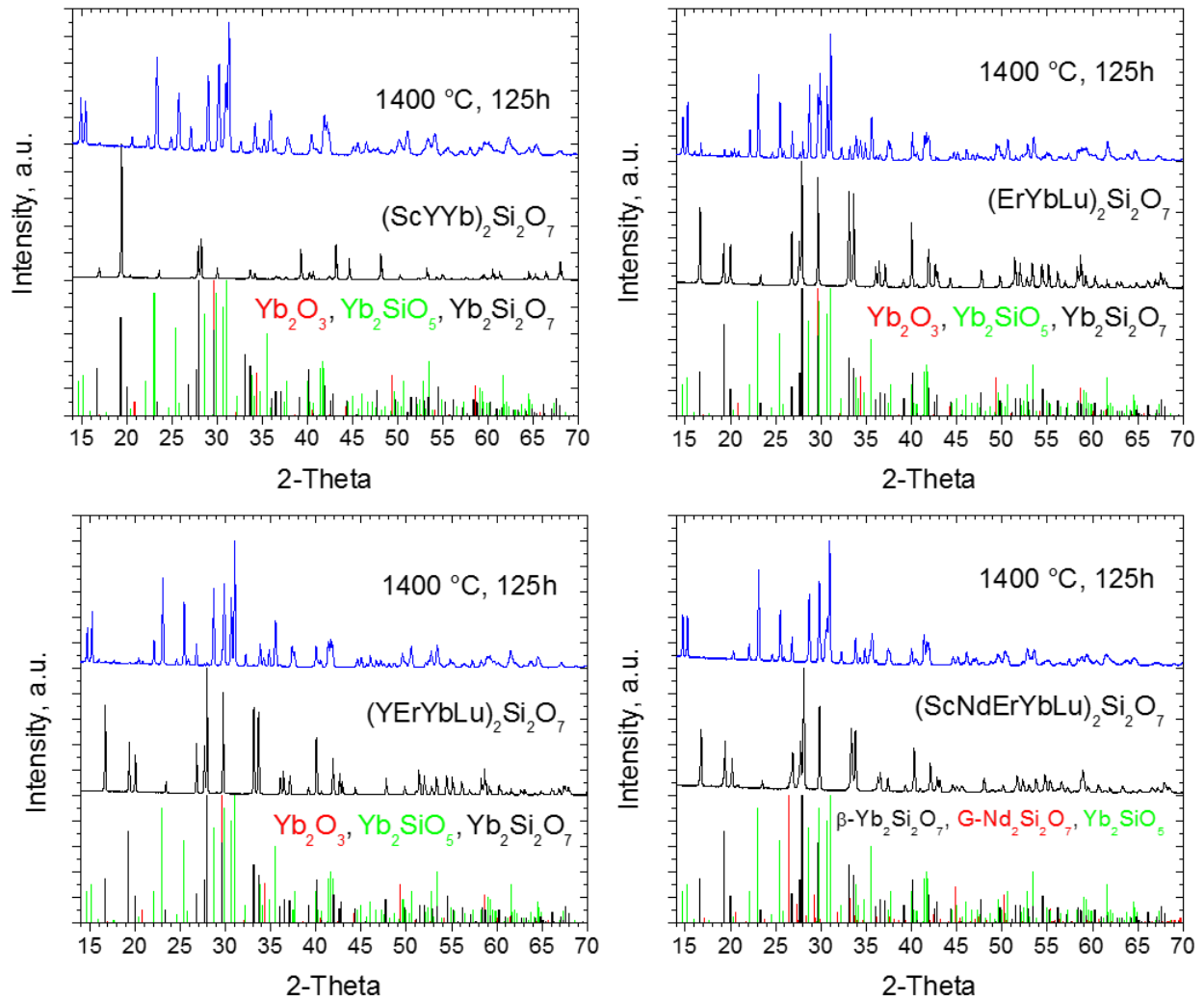


Figure 3-41. Pre- and post-steam test XRD patterns for $(\text{ScYb})_2\text{Si}_2\text{O}_7$, $(\text{ErYbLu})_2\text{Si}_2\text{O}_7$, $(\text{YErYbLu})_2\text{Si}_2\text{O}_7$, and $(\text{ScNdErYbLu})_2\text{Si}_2\text{O}_7$ after steam exposure for 125 hours at 1400 °C.

Figure 3-42 shows a macro image of the 4-component $(\text{Y,Er,Yb,Lu})_2\text{Si}_2\text{O}_7$ after steam exposure along with a low magnification SEM image of the impingement site. Higher magnification images were taken from the impingement site and following the white arrow to image changes in microstructure as the local steam velocity decreased.

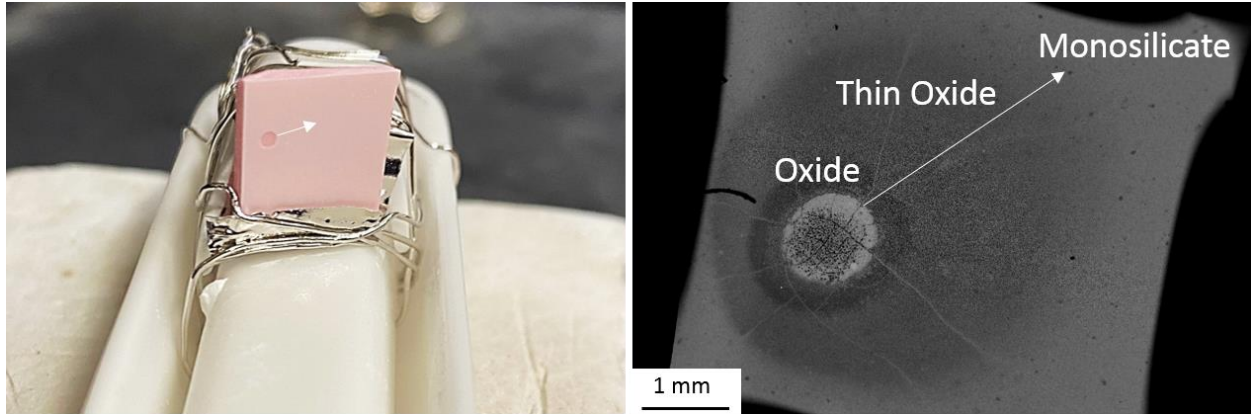


Figure 3-42. Macro image and low magnification SEM image of $(Y,Er,Yb,Lu)_2Si_2O_7$ after steam exposure at 1400 °C for 125h.

Figure 3-43 displays higher magnification images for $(ScYbLu)_2Si_2O_7$, $(ErYbLu)_2Si_2O_7$, and $(YErYbLu)_2Si_2O_7$ in three unique regions of the sample where each row corresponds to $(ScYbLu)_2Si_2O_7$, $(ErYbLu)_2Si_2O_7$, and $(YErYbLu)_2Si_2O_7$, respectively. Figure 3-43a display high velocity regions of the samples (165-185 m/s) where RE_2O_3 reaction products were visible on the surface, as determined by EDS. Figure 3-43b were taken downstream of the impingement site (80-115 m/s) and displayed the X2-phase RE_2SiO_5 reaction products. Figure 3-43c were representative of the steam reaction from stagnant steam conditions under the sample holder platinum foil. Unreacted $RE_2Si_2O_7$ grains were present with initial RE_2SiO_5 formation occurring along grain boundaries and sample defects.

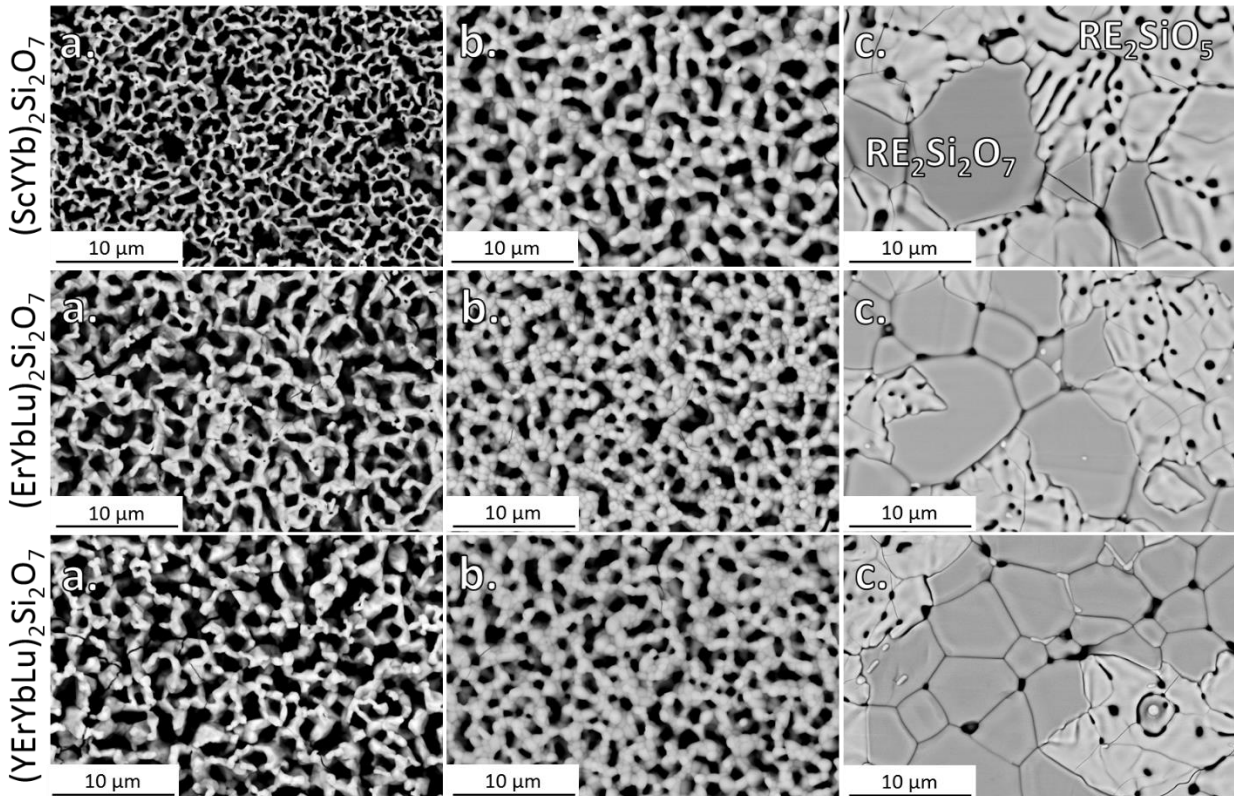


Figure 3-43. Plan view backscattered electron images of multi-component $RE_2Si_2O_7$ exposed to steam for 125 hours at 1400 °C, a. high velocity steam region where RE_2O_3 is the stable product phase (165-185 m/s), b intermediate steam velocity region where porous RE_2SiO_5 is the stable product phase (80-115 m/s), and c. stagnant steam velocity region showing the initial formation of RE_2SiO_5 (brighter phase).

Figure 3-44 shows EDS maps of $(YErYbLu)_2Si_2O_7$ in cross section after steam exposure at 1400 °C for 125 hours in the 90-110 m/s local gas velocity range. Minor clustering of rare earth cations, observed prior to steam testing during initial sample characterization, remained present after steam exposure, as marked with an arrow on the yttrium EDS map. Silica depletion from the steam reaction can be seen in the silicon EDS map, where a porous $(YErYbLu)_2SiO_5$ solid solution formed on $(YErYbLu)_2Si_2O_7$.

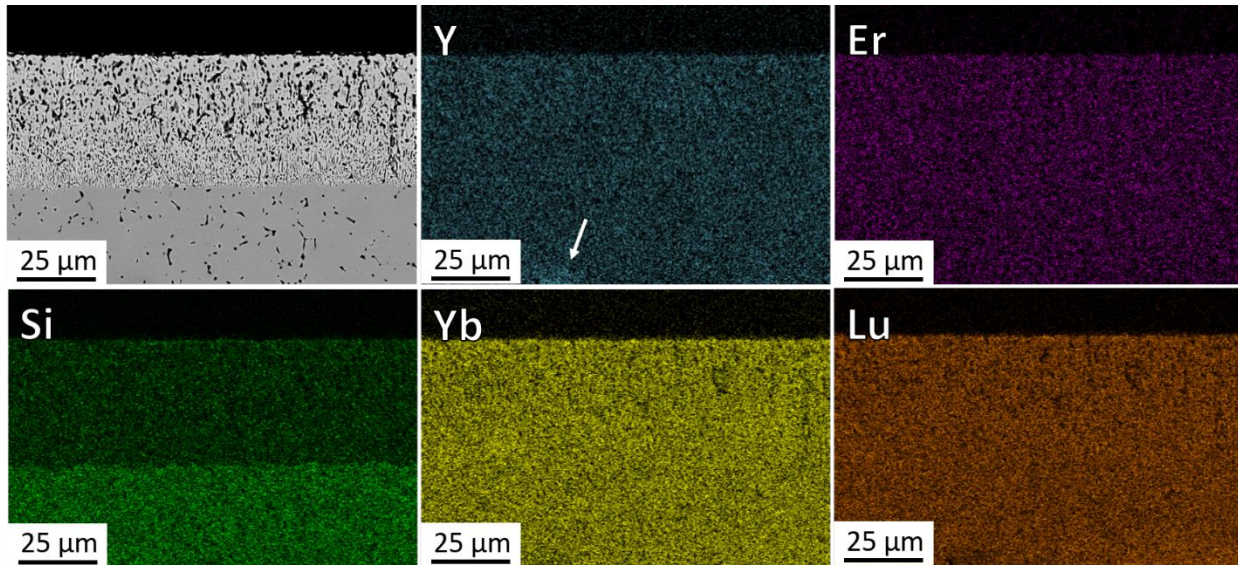


Figure 3-44. Cross section SEM and EDS of $(YErYbLu)_2Si_2O_7$ after steam exposure for 125 hours at 1400 °C and steam velocity of 90-110 m/s.

Representative cross-section SEM images of $(ScYYb)_2Si_2O_7$, $(ErYbLu)_2Si_2O_7$, and $(YErYbLu)_2Si_2O_7$ are displayed in Figure 3-45, where each row corresponds to a sample cross-section at a local steam velocity of: a. 80-115 m/s, b. 120-140 m/s, and c. 165-185 m/s. At the intermediate velocities, shown in the first row, a porous RE_2SiO_5 reaction product was seen on the surface of each material. The outer layer of the RE_2SiO_5 reaction products started to sinter and densify in the 120-140 m/s velocity range, shown in Figure 3-45b. A thin RE_2O_3 product was present on the outer layer for each sample at the highest gas velocities, shown in Figure 3-45c. $(ScYYb)_2Si_2O_7$ displayed a decreased amount of densification in the RE_2SiO_5 layer compared to the $(ErYbLu)$ and $(YErYbLu)$ samples, which subsequently led to increased reaction depths at the higher gas velocities.

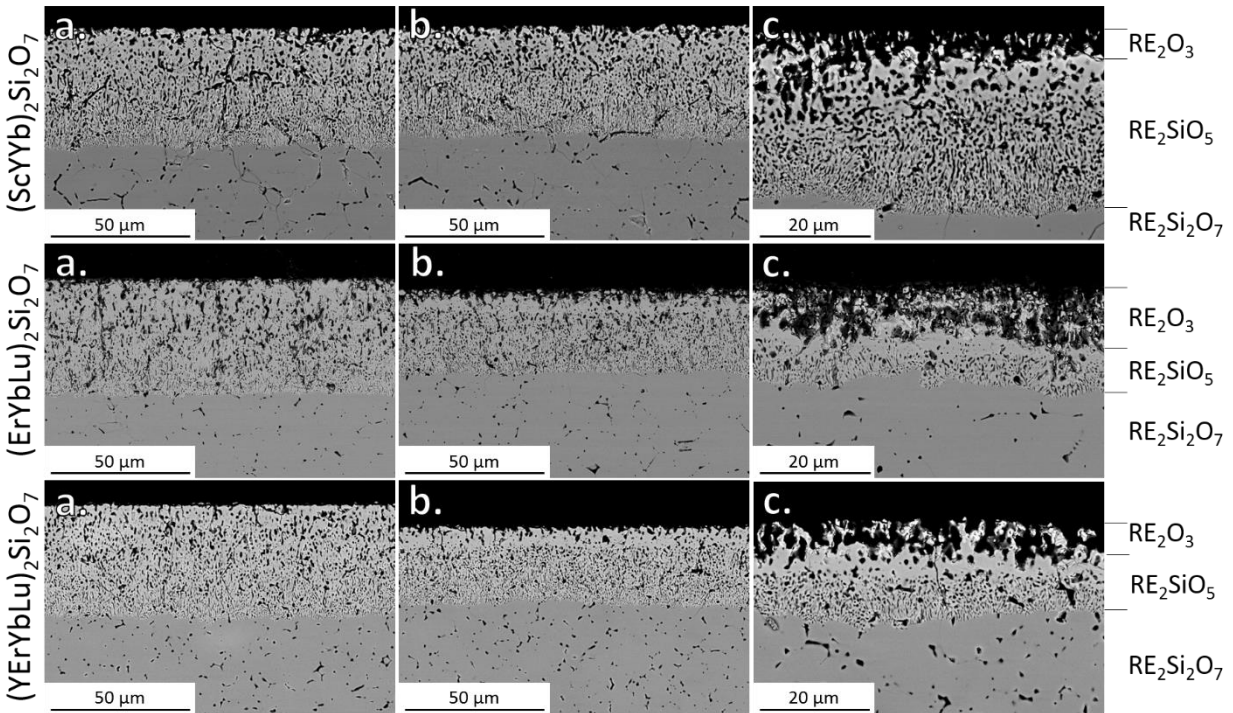


Figure 3-45. Cross-section SEM images of multi-component $RE_2Si_2O_7$ after steam exposure at 1400 °C for 125 hours for steam velocity regions of a. 80-115 m/s, b. 120-140 m/s, and c. 165-185 m/s. Respective images for c. are displayed at a higher magnification for visibility of the multi-layer reaction product.

Plan view images of the multi-phase $(Sc,Nd,Er,Yb,Lu)_2Si_2O_7$ after 125 hours of steam exposure at 1400 °C are shown in Figure 3-46, where backscattered electron images a, b, and c correspond to 180-200 m/s, 100-120 m/s, and 60-80 m/s, respectively. RE_2O_3 was present near the impingement site as a non-uniform surface layer, indicating a lack of reactivity of the RE_2SiO_5 phase. Formation of RE_2O_3 was seen on the RE_2SiO_5 reaction layer up to 4 mm downstream of the impingement site (~100 m/s), shown in Figure 3-46b as the small light grey nodules formed on the RE_2SiO_5 . Figure 3-46c displays the X2-phase RE_2SiO_5 primary steam reaction product.

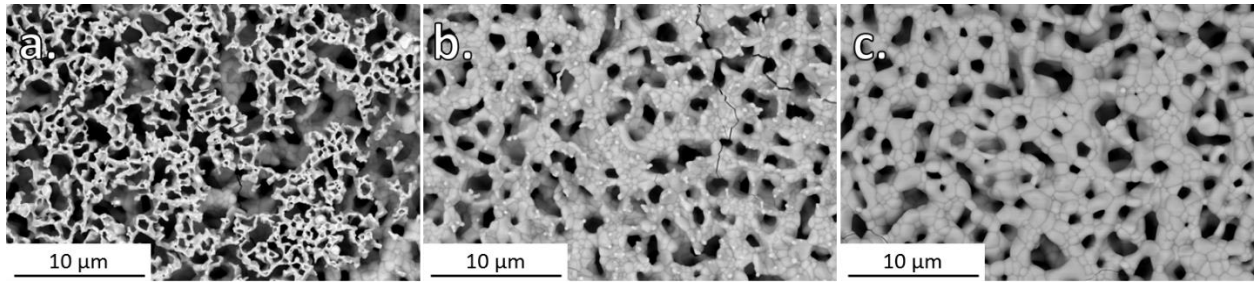


Figure 3-46. Plan view of $(\text{Sc,Nd,Er,Yb,Lu})_2\text{Si}_2\text{O}_7$ after steam exposure for 125 hours at 1400 °C, where local steam velocities were: a. 180-200 m/s, b. 100-120 m/s, and c. 60-80 m/s.

Cross-section EDS mapping of the $(\text{Sc,Nd,Er,Yb,Lu})_2\text{Si}_2\text{O}_7$ sample is shown in Figure 3-47. The RE_2SiO_5 reaction product displayed a solid solution of all cations, which is in agreement with the single X2-phase RE_2SiO_5 XRD pattern displayed earlier in Figure 3-41. Phase separation of Nd in the underlying $(\text{Sc,Nd,Er,Yb,Lu})_2\text{Si}_2\text{O}_7$ remained present after testing.

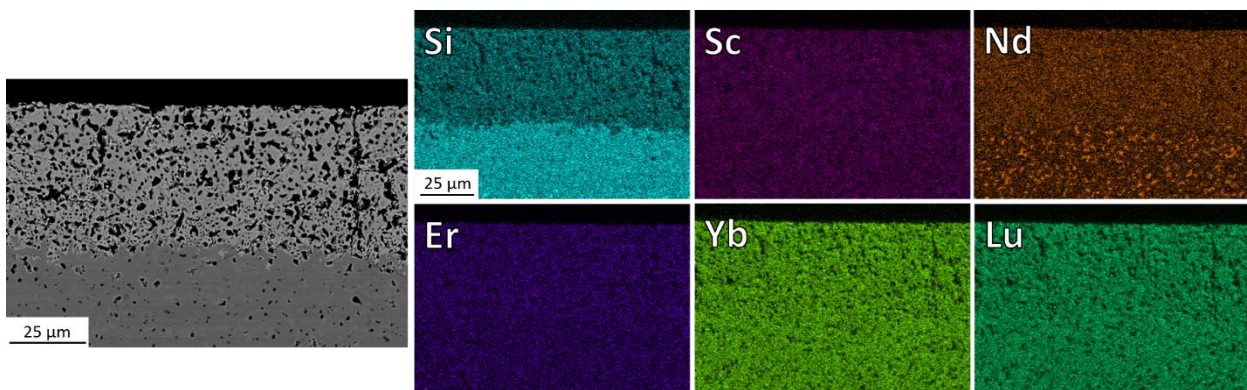


Figure 3-47. EDS mapping of $(\text{Sc,Nd,Er,Yb,Lu})_2\text{Si}_2\text{O}_7$ cross-section after steam exposure for 125 hours at 1400 °C and steam velocity 80-100 m/s, where the steam reaction product (RE_2SiO_5) formed as a solid solution of all rare earth cations.

Figure 3-48 displays the $(\text{Sc,Nd,Er,Yb,Lu})_2\text{Si}_2\text{O}_7$ cross-sections, where three distinct microstructural regions were observed: a. the intermediate steam velocity regime (80-120 m/s), b. the high velocity regime (150-180 m/s), and c. the steam impingement site (200-240 m/s). The steam reaction product, RE_2SiO_5 , showed slight coarsening with increasing gas velocity, resulting in decreased steam reaction depths in Figure 3-48b compared to intermediate velocities in Figure 3-48a. Extensive cracking was present at the impingement site, Figure 3-48c, where mechanical erosion led to material loss and sample cracking from high velocity impingement.

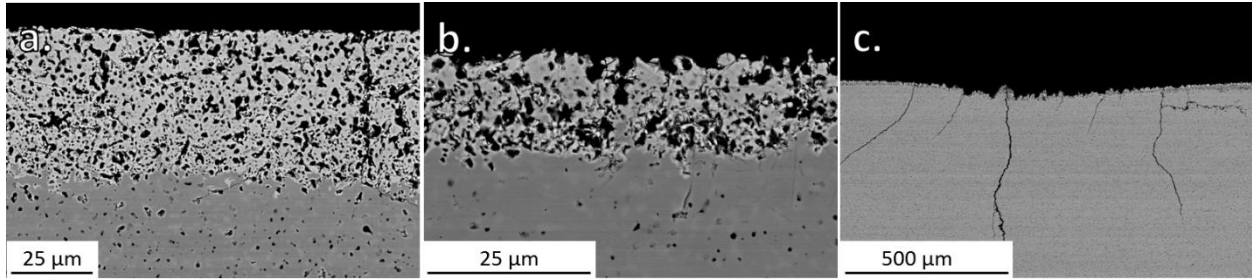


Figure 3-48. Cross-section SEM images of multi-phase $(Sc,Nd,Er,Yb,Lu)_2Si_2O_7$ after steam exposure for 125 hours at 1400 °C, where local steam velocities were: a. 80-120 m/s, b. 150-180 m/s, and c. 200-240 m/s.

The mass loss, average reaction depths, and impingement site mechanical erosion depths are presented in Table 3-14 for each multi-component $RE_2Si_2O_7$ tested in the steamjet. While mass loss data imply the $(ScNdErYbLu)_2Si_2O_7$ sample performed dramatically worse in steam than the other materials, all materials showed similar average reaction depths for the 80-115 m/s gas velocity range. Therefore, mass loss may not be an accurate comparison for each material, as it encompassed mechanical erosion and additional reactions with furnace ware at sample edges. $(ErYbLu)_2Si_2O_7$ and $(YErYbLu)_2Si_2O_7$ displayed clear densification of the RE_2SiO_5 product phase at gas velocities of 130-200 m/s, resulting in decreased average reaction depths at these higher velocities. $(ScYYb)_2Si_2O_7$ displayed excessive mechanical erosion at the impingement site, which agrees with the high erosion of phase pure $Sc_2Si_2O_7$. The multi-phase $(ScNdErYbLu)_2Si_2O_7$ sample displayed the least amount of mechanical erosion at the highest gas velocities.

Table 3-14. Specific mass loss and reaction depths for multi-component $RE_2Si_2O_7$ after steam exposure for 125h at 1400 °C.

$RE_2Si_2O_7$	Specific Mass Loss, mg/cm^2	Average Reaction Depth 80-115 m/s, μm	Average Reaction Depth 150-200 m/s, μm	Impingement Erosion Depth 200-235 m/s, μm
(Sc,Y,Yb)	3.87	45 ± 2	38 ± 3	100 ± 23
(Er,Yb,Lu)	2.99	41 ± 1	26 ± 5	53 ± 12
(Y,Er,Yb,Lu)	2.75	39 ± 2	18 ± 3	57 ± 8
(Sc,Nd,Er,Yb,Lu)	6.12	47 ± 3	29 ± 8	33 ± 16

3.4.4. Discussion

The rule of mixtures values for each multi-component material were determined from single rare earth cation $RE_2Si_2O_7$ values to determine any deviations from a predicted value. Figure 3-49 displays the ratio of the measured thermal conductivity divided by the rule of mixtures value on the y-axis, plotted against the standard deviation of the rare earth ionic radius and the standard deviation of the rare earth cation mass on the x-axes. As the measured thermal conductivity decreases compared to the rule of mixtures, the ratio decreases below a value of one. Thermal conductivity is thus clearly deviating from a rule of mixtures value as the differences in rare earth element size increase. A comparable trend was found for standard deviation of rare earth cation mass, such that lattice heterogeneity contributes to decreased thermal conductivity for multi-component $RE_2Si_2O_7$. Compared to similar plots in Figure 3-22 for multi-component RE_2SiO_5 , the $RE_2Si_2O_7$ displayed a greater decrease in thermal conductivity with cation mixing than the RE_2SiO_5 due to higher intrinsic thermal conductivities of $RE_2Si_2O_7$. The curvature of the plots presented in Figure 3-22 and Figure 3-49 imply that increasing ionic

radii disorder within a crystal lattice will result in a more rapid decrease in thermal conductivity than by introducing mass differences.

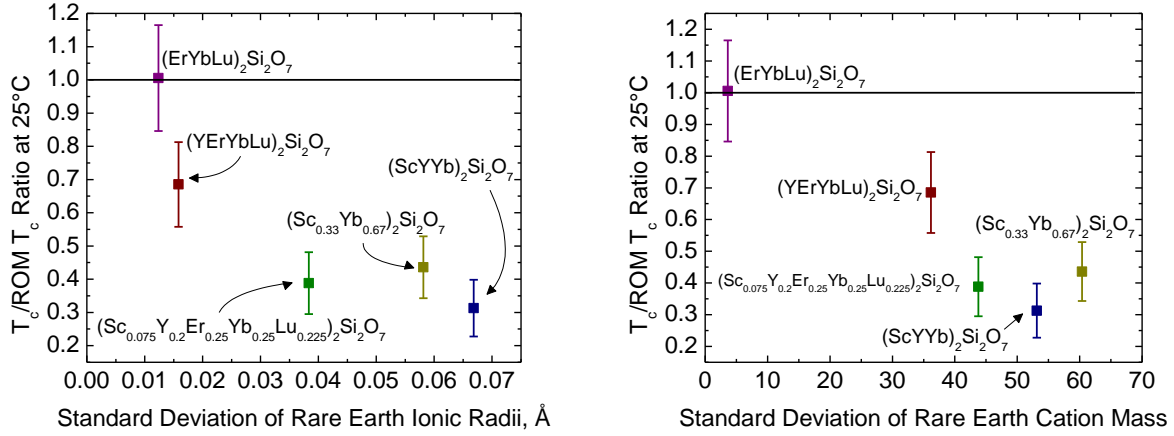


Figure 3-49. Ratio of rule of mixtures thermal conductivity values to the measured values for multi-component RE₂Si₂O₇, plotted against the standard deviation of rare earth ionic radius and the standard deviation of rare earth cation mass.

The ratio of measured values over rule of mixtures for thermal expansion and Young's Modulus are displayed in Figure 3-50. Ratios for all multi-component RE₂Si₂O₇ were near 1, representing minimal deviation from a rule of mixtures value. The CTE of the high-temperature G-phase for Nd₂Si₂O₇ [105] was used when calculating the rule of mixtures CTE for (ScNdErYbLu)₂Si₂O₇ to account for the stabilization of the G phase over the traditionally stable A phase at room temperature.

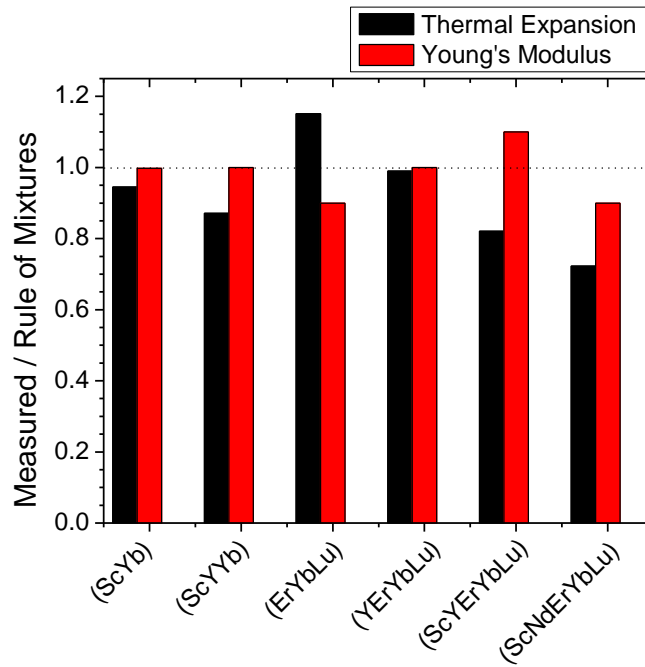


Figure 3-50. Thermal expansion and Young's Modulus ratios of measured values to rule of mixtures for multi-component $RE_2Si_2O_7$.

Young's Modulus was also found to trend with rare earth cation ionic radius for both single and multi-component $RE_2Si_2O_7$, shown in Figure 3-51. The δ phase $Er_2Si_2O_7$ and A phase $Nd_2Si_2O_7$ samples are outliers from the presented trend due to differing crystal structures from the β phase $RE_2Si_2O_7$.

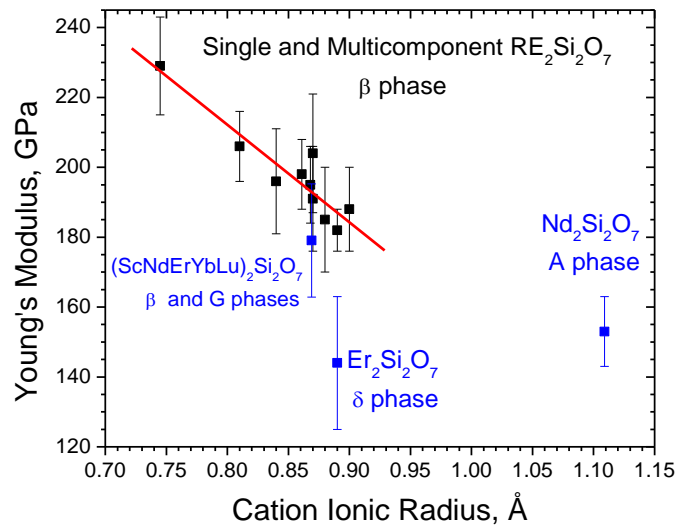


Figure 3-51. Young's Modulus (GPa) versus rare earth ionic radius for single and multi-component $RE_2Si_2O_7$ samples.

Comparable average reaction depths were measured for each multi-component $RE_2Si_2O_7$. Both solutions with Sc additions, $(ScYYb)_2Si_2O_7$ and $(ScNdErYbLu)_2Si_2O_7$, did not display densification of the product RE_2SiO_5 phase as was seen with the other multi-component $RE_2Si_2O_7$ materials. A Sc_2O_3 reaction product was not observed for $(ScNdErYbLu)_2Si_2O_7$, as was observed for phase pure $Sc_2Si_2O_7$. Additionally, the inclusion of Nd in $(ScNdErYbLu)_2Si_2O_7$ did not result in the formation of an apatite reaction product, as was seen for phase pure $Nd_2Si_2O_7$. Microstructural evolution of the RE_2SiO_5 steam product phase may be linked to the melting temperature of the EBC and its respective steam product phase, as discussed earlier in Figure 3-36.

Toropov et al. analyzed melting temperature through production of pseudobinary phase diagrams for the Y-Er silicate systems [128], where melting temperatures are shown in Table 3-15. The apatite compound was listed by Toropov as $RE_4Si_3O_{12}$, yet the accepted composition of the rare earth silicate apatite phase is now known to be $RE_{9.33}\square_{0.67}Si_6O_{26}$. The melting

temperatures of the Y-Er solutions were 100 °C – 200 °C lower than the constituent silicates for the yttrium and erbium disilicate, monosilicate, and apatite compounds.

Table 3-15. Melting temperatures of yttrium-erbium silicate compounds in solution [128].

Melting Temperatures, °C			
Compounds	RE = Y	RE = Er	RE = Y-Er solutions
RE ₂ Si ₂ O ₇	1830	1800	1624 (58/42 wt. %)
RE _{9.33} □ _{0.67} Si ₆ O ₂₆	1953	1900	1800 (53/47 wt. %)
RE ₂ SiO ₅	1980	1980	1844 (22/78 wt. %)

The decrease in melting temperature for binary rare earth cation RE₂Si₂O₇ was also confirmed in this work through the processing of equimolar (NdYb)₂Si₂O₇. While both Nd₂Si₂O₇ and Yb₂Si₂O₇ were processed by SPS in argon at 1575 °C and 1600 °C, respectively, the (NdYb)₂Si₂O₇ powder mixture displayed melting onset at ~1530 °C under 65 MPa applied pressure. The melt was recovered and is shown in Figure 3-52 after a 1430 °C anneal for 8 hours to restore oxygen stoichiometry. EDS point identification of multiple regions displayed a composition of (Nd_{0.22}Yb_{0.78})₂Si₂O₇ for the lighter greyscale phase, while the majority of the sample (darker phase) was (Nd_{0.58}Yb_{0.42})₂Si₂O₇ solution. Excess SiO₂ was present at the grain boundaries. Area EDS quantification of the entire view of Figure 3-52 displayed an average composition of (Nd_{0.50}Yb_{0.50})₂Si₂O₇, representing negligible compositional changes due to volatilization or reactions with the SPS graphite die set. Two component rare earth silicates thus stabilize the liquid phase relative to the solid phase.

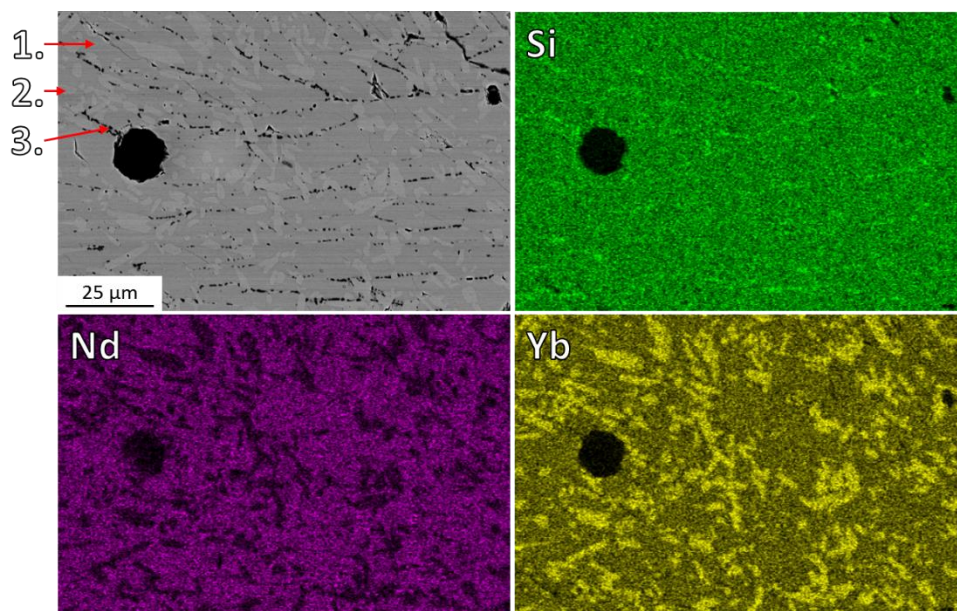


Figure 3-52. Equimolar $(NdYb)_2Si_2O_7$ recovered from sample melt during SPS processing and annealed at 1430 °C for 8 hours. EDS point identification of the marked phases were 1. $(Nd_{0.58}Yb_{0.42})_2Si_2O_7$, 2. $(Nd_{0.22}Yb_{0.78})_2Si_2O_7$, 3. SiO_2 with trace Nd and Yb signal.

Such decreases in binary rare earth silicate melting temperatures may become less prevalent with increasing additions of rare earth cations, as decreased concentrations of each rare earth will be present in solution. Rule of mixtures melting temperatures for multi-component $RE_2Si_2O_7$ (ScYb), (ErYbLu), (YErYbLu), and (ScNdErYbLu) are 1828 °C, 1837 °C, 1825 °C, and 1843 °C, respectively. Thus, homologous temperatures of the given materials are all similar, near 0.79-0.8. Figure 3-37 has been replotted to showcase the multi-component silicate homologous temperatures versus steam reaction depths, now in Figure 3-53. The similarities between the average steam reaction depth for the multi-component $RE_2Si_2O_7$ may be connected to the similar homologous temperatures of each multi-component materials, in addition to the hypothesized similar silica activities for all $RE_2Si_2O_7$. Additional $RE_2Si_2O_7$ (RE = La [128], Eu [129], Gd [61], and Dy [110]) homologous melting temperatures are presented in Figure 3-53 as dotted lines to illustrate candidates that would be expected to show increased steam reactivity based on the given trend. From available phase diagram information, $RE_2Si_2O_7$ (RE = La, Gd,

and Eu) are predicted to display an apatite steam reaction product, while $\text{Dy}_2\text{Si}_2\text{O}_7$ is expected to display Dy_2SiO_5 steam reaction product.

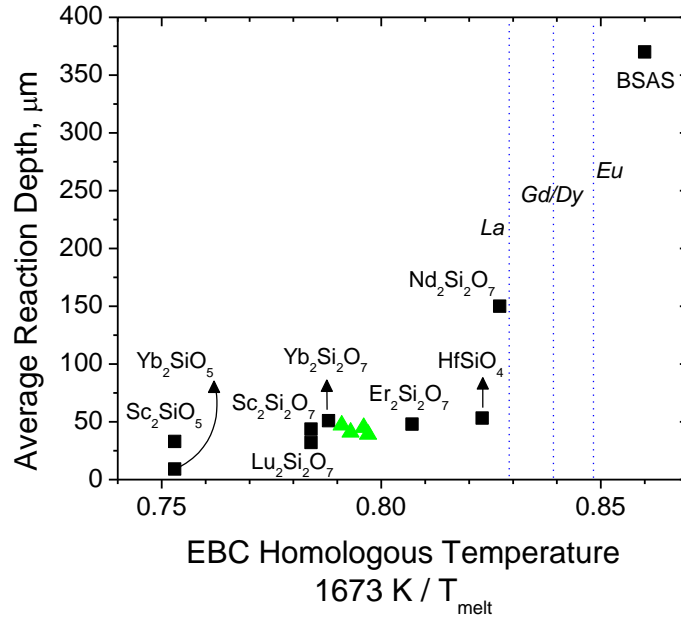


Figure 3-53. EBC homologous temperature compared to average steam reaction depths after 125 hours of steam exposure at 1400 °C. Green triangles represent the four multi-component $\text{RE}_2\text{Si}_2\text{O}_7$ samples tested in this study. Blue dashed lines represent homologous temperatures for $\text{RE}_2\text{Si}_2\text{O}_7$ (RE = La, Gd, Dy, and Eu).

A proposed effect of high entropy materials is the stabilization of a solid solution phase through increased entropic contribution to Gibbs free energy, suggesting an increase in the melting temperature (decrease in homologous temperature) for a high entropy solution relative to each constituent. Yet, high entropy by definition was only achieved in this work for the $(\text{ScNdErYbLu})_2\text{SiO}_5$ solid solution reaction product phase that formed on the multi-phase $(\text{ScNdErYbLu})_2\text{Si}_2\text{O}_7$ sample after steam exposure. Precise melting temperatures of optimized multi-component $\text{RE}_2\text{Si}_2\text{O}_7$ and RE_2SiO_5 systems should be explored in future research to improve understanding of the high-temperature stability of multi-component rare earth silicates as EBC candidates.

3.4.5. Conclusion

Multi-component $\text{RE}_2\text{Si}_2\text{O}_7$ were synthesized and characterized in terms of thermal conductivity, thermal expansion, Young's Modulus, and steam reactivity. Thermal conductivity of multi-component $\text{RE}_2\text{Si}_2\text{O}_7$ solution was greatly decreased relative to the constituents with increasing the lattice disorder. Thermal expansion and Young's Modulus were considered to follow a rule of mixtures, where trends in both properties correlated to the average rare earth cation ionic radius.

The high-velocity steam reactivity of multi-component $\text{RE}_2\text{Si}_2\text{O}_7$ at 1400 °C for 125 hours was analyzed. Additions of Sc did not result in destabilization of the RE_2SiO_5 product phase, as was seen with pure $\text{Sc}_2\text{Si}_2\text{O}_7$. Yet, additions of Sc to (ScYYb) and (ScNdErYbLu) disilicates did result in a decreased amount of sintering and densification for the RE_2SiO_5 product phase. Additions of Nd to $(\text{ScNdErYbLu})_2\text{Si}_2\text{O}_7$ did not result in formation of an apatite phase, as was seen with bulk $\text{Nd}_2\text{Si}_2\text{O}_7$. Multi-phase $(\text{ScNdErYbLu})_2\text{Si}_2\text{O}_7$ did not produce a stable RE_2O_3 layer, presumably due to lack of densification of the RE_2SiO_5 product phase. Additions of rare earth cations that individually displayed poor steam behavior ($\text{RE} = \text{Sc}, \text{Nd}$) were not detrimental to multi-component EBC stability in high-velocity steam. Thus, minor additions of rare earth elements can be used in solution to tailor thermal and mechanical properties, such as thermal conductivity, CTE, and Young's Modulus, without greatly diminishing high-temperature stability in steam.

3.5. CTE Prediction for High-temperature Silicate Materials

3.5.1. Introduction

Silicate materials show varied CTE even though the Si-O bond in ceramics is rigid with a thermal expansion near zero [130]. An assumption can be made that the Si-O tetrahedra in rare earth silicate materials do not contribute to thermal expansion, and therefore the metal-oxygen bonding may govern thermal expansion behavior. Hazen and Prewitt utilized this concept to create a model for thermal expansion of silicates and oxides up to 1000 °C [131]. The metal-oxygen bond expansion, $\langle a \rangle$, was estimated based on the cation charge, Z , and cation coordination number, p , to develop an empirical relationship shown in Eq. 3-7 [131].

$$\langle a \rangle = 32.9(0.75 - Z/p) \times 10^{-6} / ^\circ\text{C} \quad 3-7$$

3.5.2. Results

This empirical relation has been adapted in this work to better model silicate materials specifically for high-temperature applications. Both measured and literature data were compiled from dilatometry and high-temperature XRD techniques for $\text{RE}_2\text{Si}_2\text{O}_7$ [103], [132], [133], RE_2SiO_5 [35], [95], apatite silicates [134], [135], and non-rare earth silicates such as HfSiO_4 [136], ZrSiO_4 [136], SrSiO_3 [137], and Sr_2SiO_4 [137]. The 56 compiled material CTEs are presented in Figure 3-54, where a modified Hazen-Prewitt model was determined to produce Equation 3-8.

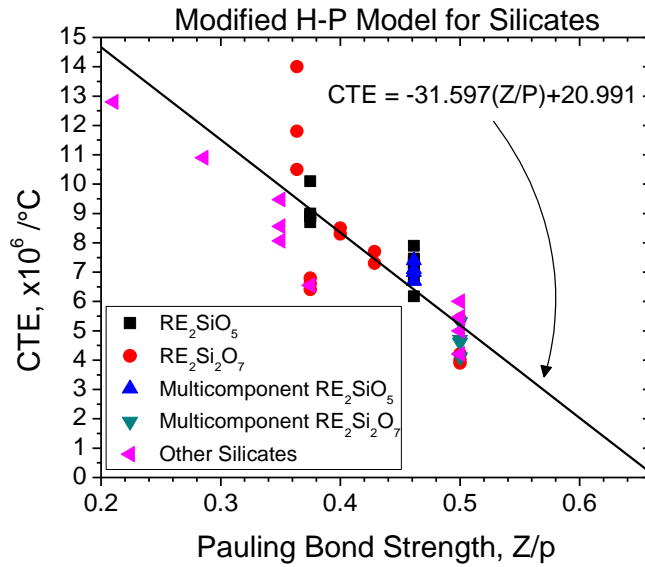


Figure 3-54. Linear thermal expansion of high-temperature silicates as a function of Pauling bond strength.

$$\langle a \rangle = 25.3(0.75 - Z/p) \times 10^{-6} / ^\circ\text{C} \quad 3-8$$

The average linear thermal expansion decreases with increasing Pauling bond strength, as stronger metal-oxygen bonds are less prone to expansion upon heating. Clear discrepancies are present for materials that exhibit the same bond strength, yet differing CTE values. For example, beta phase $\text{RE}_2\text{Si}_2\text{O}_7$ show a Pauling bond strength of 0.5, yet thermal expansion values vary with changing rare earth cation from $3.8\text{-}5.6 \times 10^{-6} / ^\circ\text{C}$. A-Phase $\text{RE}_2\text{Si}_2\text{O}_7$, such as $\text{RE} = \text{Nd}, \text{Ce}, \text{La}, \text{and Pr}$, show a Pauling bond strength of 0.36 with CTEs varying from $10.5\text{-}14 \times 10^{-6} / ^\circ\text{C}$. While differences may be accentuated by varying test temperatures and sample microstructures from data in the literature, a minor trend in thermal expansion for a given crystal structure may exist to accommodate for these differences. Both distortion and rotation of the Si-O tetrahedra and M-O polyhedra may be dependent on the M-O bond strength. Future work should investigate the cause of the minor shifts in CTE for a given crystal structure with changes in metal cation on the lattice as a means to increase the accuracy of predictions for high-temperature CTE of EBC candidates.

The metal-oxygen bond strength should be directly correlated to the ionic radius for a given charged ion and coordination number. Therefore, an alternative view of the compiled CTE data is presented in Figure 3-55. Here, CTE is plotted against the average ionic radius of each metal cation, where ionic radii data were compiled from Shannon database for each respective cation charge and coordination number [138]. Materials with a larger ionic radius correlate to a weaker metal-oxygen bond strength, and therefore thermal expansion of silicates increases with increasing average ionic radius. Thermal expansion of high-temperature silicate materials can be estimated from Equation 3-9 as a function of cation ionic radius, r .

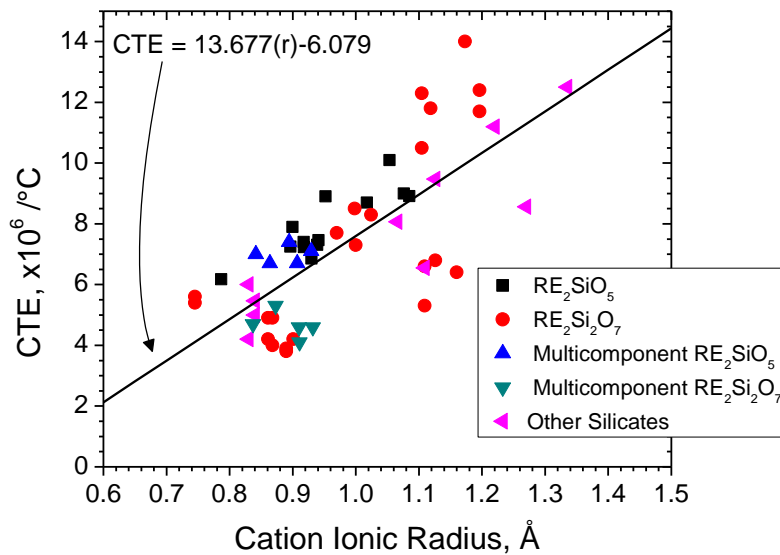


Figure 3-55. Linear thermal expansion of high-temperature silicates as a function of metal cation ionic radius, Å.

$$\langle a \rangle = 13.677(r) - 6.079 \times 10^{-6} / ^\circ\text{C} \quad 3-9$$

3.5.3. Conclusion

In the search for next generation EBC candidates, promising candidates should include those with smaller metal ionic radii, or a higher Pauling bond strength. Materials with higher cation charge (Z) or lower coordination number (p) should result in the higher bond strengths

that produce low CTE materials desirable for EBC applications. Multi-component silicates represent an avenue of future research for tailoring low CTE environmental barrier coatings.

3.6. Summary

Multi-component rare earth silicates can be used to tailor thermal, mechanical, and chemical properties of EBC materials. Thermal expansion and Young's Modulus were shown to generally follow a rule of mixtures, such that these properties of a multi-component material could be estimated prior to experimental testing. Quantitative empirical relationships have been developed for the rare earth silicates, correlating thermal expansion for silicate materials to both the Pauling bond strength and the rare earth cation ionic radius. Thermal conductivity deviated from a rule of mixtures due to increased phonon scattering as rare earth cations with more unique atomic masses and ionic radii were introduced into solution.

The steam reactivities of rare earth silicates were found to be generally similar, in agreement with the hypothesis that all $\text{RE}_2\text{Si}_2\text{O}_7$ should show similar silica activities. Although, different reaction products and microstructural evolution resulted in unique properties for rare earth silicates with varied rare earth cations. While most $\text{RE}_2\text{Si}_2\text{O}_7$ in this study produced both RE_2SiO_5 and RE_2O_3 product phases, $\text{Sc}_2\text{Si}_2\text{O}_7$ and $\text{Nd}_2\text{Si}_2\text{O}_7$ samples rapidly reacted with steam to form Sc_2O_3 and $\text{Nd}_{9.33}\square_{0.67}\text{Si}_6\text{O}_{26}$, respectively. Both $\text{Sc}_2\text{Si}_2\text{O}_7$ and Sc_2SiO_5 displayed similar reaction rates to both form Sc_2O_3 after steam exposures, indicating that Sc silicates are not stable in high-velocity steam.

Solutions of $\text{RE}_2\text{Si}_2\text{O}_7$ that comprised of beta phase rare earth silicates [RE = (ScYYb), (ErYbLu), and (YErYbLu)] displayed similar reaction depths and microstructures as their silicate constituents. When rare earth size differences were large, such as with $(\text{ScNdErYbLu})_2\text{Si}_2\text{O}_7$, a single solid solution was not achievable. Still, some Nd concentration was partially stabilized as the beta phase, implying small quantities of the large rare earth cations, such as Nd, can be used in multi-component silicate solutions. The thermal expansion of multi-phase

(ScNdErYbLu)₂Si₂O₇ displayed minimal CTE mismatch to that of SiC, suggesting multi-phase disilicate EBCs may be an alternative to traditional β phase EBCs. The steam reaction product for the (ScNdErYbLu)₂Si₂O₇ was the X2 phase RE₂SiO₅ solid solution, showing how X1 phase Nd₂SiO₅ can be stabilized as the X2 phase in a high entropy monosilicate solid solution. As stated earlier, phase pure Sc₂Si₂O₇ and Nd₂Si₂O₇ displayed Sc₂O₃ and Nd_{9.33}□_{0.67}Si₆O₂₆ steam reaction products, respectively. The lack of stability of these product phases for (ScNdErYbLu)₂Si₂O₇ demonstrates the ability to tailor steam reaction products and microstructure for multi-component EBCs.

4. Objective 3: Design and Comparison of Next Generation Environmental Barrier Coating Materials

Complex oxide systems can be represented by $A_xB_yO_z$, where ‘A’ and ‘B’ represent metals on different lattice sites and ‘O’ represents oxygen. In Objective 2, rare earth silicates (rare earth elements = A, silicon = B) were explored in terms of changes to the ‘A’ site to tailor material properties. Objective 3 allows for exploration of non-silicate systems, where the ‘B’ site is changed. Rare earth phosphates (A = rare earth elements, B = phosphorous) represent an avenue of interest for extending compositional design space beyond silicate materials. A review of known ytterbium phosphate ($YbPO_4$) properties, a novel EBC material candidate, will be provided, followed by analysis of thermal expansion and thermal expansion anisotropy, high-velocity steam resistance, and CaO-MgO- Al_2O_3 - SiO_2 (CMAS) molten glass resistance. Results will be qualitatively compared to $Yb_2Si_2O_7$ and Yb_2SiO_5 systems.

Introductory analysis of a novel EBC candidate, $YbPO_4$, requires a method for holistic comparison to past and present EBC materials, yet simultaneous optimization of all required EBC properties has not been attempted from a fundamental perspective. EBC research is conducted by laboratory teams often focused on specific individual failure mechanisms. The industry standard lifetime for gas turbine components is 25,000 hours [54], which implies all EBC failure mechanisms should be considered when designing next-generation EBCs. Therefore, a figure of merit (FoM) is desirable to most effectively design, test, and compare EBC candidates. BSAS, $HfSiO_4$, and the compounds of the Yb_2O_3 - SiO_2 system (Yb_2O_3 , Yb_2SiO_5 , and $Yb_2Si_2O_7$) will be compared to SiO_2 , the thermally grown oxide on SiC. $YbPO_4$ will also be presented as a novel EBC material for comparison, as $YbPO_4$ represents an avenue of interest for

extending the figure of merit beyond silicate materials. Each major failure mode for EBCs will be discussed. Measurable material properties and relevant criteria for EBC success will be presented as data inputs to address each major failure mode. Fruitful avenues of future research by the EBC community will be identified using the figure of merit.

4.1. Evaluation of YbPO₄ as an Environmental Barrier Coating

Candidate

4.1.1. Introduction

Current generation EBC candidates consist of both rare earth disilicates, RE₂Si₂O₇, and rare earth monosilicates, RE₂SiO₅ [139]. RE₂Si₂O₇ have better thermomechanical stability with SiC than RE₂SiO₅ due to lower thermal expansion mismatch and lower coefficient of thermal expansion (CTE) anisotropy. The thermal expansion anisotropy of RE₂SiO₅ results from crystal structure asymmetries and the rigid nature of Si-O tetrahedra bonding. Prior studies have shown that RE₂Si₂O₇ reacts with steam and CMAS (calcium magnesium aluminosilicate) more readily than RE₂SiO₅ due to a higher silica activity in the RE₂Si₂O₇ [51], [53]. The tradeoff between the two silicate compounds is thus the thermochemical reactivity and the thermal expansion behavior. Because of these known limitations in the high-temperature combustion environment, this work investigated ytterbium phosphate YbPO₄, wherein the SiO₄ sub-framework common to rare earth silicates was replaced with PO₄ tetrahedra, as an alternative EBC material with potentially improved thermomechanical and thermochemical stability.

The rare earth phosphates exist as either a monazite phase (RE=La-Gd) or as a xenotime crystal structure (RE=Gd-Lu, Sc, Y). The monazite REPO₄ are monoclinic crystal structures that have CTE values, ranging from 8–10 x10⁻⁶/°C [140], which present too large of a CTE mismatch with SiC (4.5-5.5 x10⁻⁶/°C) to be considered as single layer EBC materials [3]. Xenotime phosphates, such as YbPO₄ investigated in this present study, are tetragonal and analogous in crystal structure to ZrSiO₄ and HfSiO₄. Each rare earth atom has eightfold coordination with oxygen atoms which connect with a PO₄ tetrahedral sub-network. The CTEs of xenotime

orthophosphates are similar to SiC, which is desirable for environmental barrier coating applications [141]. The linear CTE of YbPO₄ measured by dilatometry is $\sim 5.85 \times 10^{-6}/^{\circ}\text{C}$ from 200 °C–1300 °C [142]. While no phase diagram or melting temperature is available for YbPO₄, other xenotime REPO₄ do not show high-temperature polymorphs and have high melting temperatures (e.g., YPO₄ = 2150 °C [143] or 1995 ± 20 °C [140], ErPO₄ = 1896 ± 20 °C [140]) making them suitable candidates for EBC applications. No known determination of CTE anisotropy has been made available for any xenotime rare earth orthophosphate in the literature.

Little research has been conducted on the steam resistance of rare earth phosphates. AlPO₄ exposed to a 50% H₂O (g) / 50% O₂ (g) environment with a steam flow rate of 8.5×10^{-4} m/s at 1350 °C for 200 hours in a TGA reacted to form a porous Al₂O₃ reaction product after exposure, where AlPO₄ decomposition to form Al₂O₃ and PO_x (g) was hypothesized [59]. Wang et al. studied YPO₄ powders as a potential EBC candidate by conducting thermogravimetric analysis (TGA) in a 50% H₂O (g) / 50% O₂ (g) environment with a steam flow rate of 8.5×10^{-4} m/s at 1350 °C for 300 hours [144]. In their study, a linear weight loss of 1.25×10^{-5} mg/cm²h was measured. Post-exposure characterization did not show the presence of reaction products, and therefore no hypothesis was made to explain the weight loss recorded during testing. In a separate study, TGA was conducted on REPO₄ (RE=Sc, Y, Er, Yb, Lu) in a 50% H₂O (g) / 50% O₂ (g) environment with a flow rate of 3.0×10^{-3} m/s at 1500 °C for 80 hours [142]. In contrast to the aforementioned study on YPO₄, the REPO₄ compounds were observed to gain weight. Post-exposure characterization showed a RE₃Al₅O₁₂ reaction product present on all sample surfaces, ascribed to sample reaction with alumina contaminants from the furnace ware. YbPO₄ had an averaged positive reaction rate of $4.31 \pm 1.92 \times 10^{-4}$ mg/cm²h for aluminate formation.

While the steam reaction for complex phosphates has not been definitively identified, the steam reaction products for AlPO_4 have been hypothesized to consist of porous alumina and $\text{PO}_2(\text{OH})$ (g) [13]. Table 4-1 displays steam reactions and hydroxide partial pressures for SiO_2 , AlPO_4 and Y_2O_3 , at 1200 °C, where gaseous metal hydroxide partial pressures from reactions with AlPO_4 and Y_2O_3 reactions are estimated [13]. Both $\text{Si}(\text{OH})_4$ (g) and $\text{PO}_2(\text{OH})$ (g) partial pressures for the given reactions are of the same order of magnitude, implying the steam reactivity of SiO_2 and AlPO_4 may also be comparable. It should be noted that AlPO_4 is a different crystal structure from the rare earth phosphates such as YbPO_4 , therefore the present data are not sufficient to approximate REPO_4 stabilities or to assume $\text{PO}_2(\text{OH})$ (g) would be the dominant gas species for REPO_4 in steam environments. $\text{Ca}_2\text{P}_2\text{O}_7$ reaction with $\sim 10^{-6}$ atm of water vapor at 1397 °C showed $\text{PO}(\text{OH})$ (g), $\text{PO}_2(\text{OH})$ (g), and $\text{P}(\text{OH})$ (g) reaction products at partial pressures of 1.6×10^{-7} atm, 2.3×10^{-8} atm, and 6.6×10^{-10} atm, respectively [145]. The dominant phosphorous hydroxide gas species remains unknown at high water vapor partial pressures for phosphate materials.

Alternatively, as shown in Table 4-1, Y_2O_3 is much more stable in steam compared to both pure SiO_2 and AlPO_4 , seen from the low partial pressure of $\text{Y}(\text{OH})_3$ (g) at 1200 °C. In experimental testing, no measurable volatilization of Y_2O_3 in high velocity steam has been recorded, suggesting that the rare earth elements in rare earth oxides do not volatilize at a measurable rate in the presence of steam under relevant furnace conditions [27]. While the reactivity of Yb_2O_3 with high-temperature steam is not presently known, Yb_2O_3 is predicted to show similar behavior as Y_2O_3 . This is corroborated by the formation and stability of Yb_2O_3 from $\text{Yb}_2\text{Si}_2\text{O}_7$ in Chapter 2.3 of this dissertation and in published work [29]. Thus, it is

hypothesized that the rare earth phosphates such as YbPO_4 will display a porous RE_2O_3 steam reaction product similar to the Al_2O_3 steam reaction product predicted for AlPO_4 .

Table 4-1. Steam chemical reaction to form hydroxide gaseous species for silica, yttria, and aluminum phosphate [13].

Steam Reaction	Hydroxide partial pressures (atm) for $p_{\text{H}_2\text{O}} = 1 \text{ atm}$, $p_{\text{O}_2} = 0.5 \text{ atm}$, 1473 K
$\text{SiO}_2(\text{c}) + 2\text{H}_2\text{O}(\text{g}) = \text{Si}(\text{OH})_4(\text{g})$	4×10^{-6}
$\text{AlPO}_4(\text{c}) + 0.5\text{H}_2\text{O}(\text{g}) = 0.5\text{Al}_2\text{O}_3 + \text{PO}_2(\text{OH})(\text{g})$	8×10^{-6}
$0.5\text{Y}_2\text{O}_3(\text{c}) + 1.5\text{H}_2\text{O}(\text{g}) = \text{Y}(\text{OH})_3(\text{g})$	9×10^{-11}

Corrosion mechanisms and corrosion rates of EBCs from molten salts and glasses represent an active area of research. Siliceous debris, such as small particulate, sand, dirt, or ash can be ingested by turbines, resulting in molten glass formation. The molten glass is termed CMAS due to the most common constituent oxides ($\text{CaO-MgO-Al}_2\text{O}_3\text{-SiO}_2$) although CMAS is compositionally variant, often with additional oxide constituents. There is no literature on YbPO_4 stability with molten salts and glasses. Other REPO_4 have been tested for stability with various salt chemical reactions. YPO_4 showed excellent stability against a Na_2SO_4 melt, with no reaction product formed after a 900 °C test for 100 hours [144]. CMAS (22CaO-19MgO-15AlO_{1.5}-44SiO₂) exposure of monazite REPO_4 (RE=Nd, Sm, Gd) was performed at 1250 °C for 4 hours [146]. CMAS resistance was shown to be superior to yttria stabilized zirconia due to both the rapid formation of a dense layer composed primarily of an apatite-type phase, $\text{Ca}_3\text{RE}_7(\text{PO}_4)(\text{SiO}_4)_5\text{O}_2$, and the hydrophobic properties of the rare earth phosphates. Apatite formation kinetics were shown to increase with decreasing size of the rare earth cation, such that GdPO_4 displayed the greatest CMAS resistance and the least total CMAS penetration depth for RE = Nd, Sm, and Gd. The presented phosphate apatite trend is in direct contradiction with rare

earth silicate apatite formation, where silicate apatite stabilities increase with increasing rare earth cation size. High-temperature calorimetry of rare earth silicate apatites, $\text{RE}_{9.33}\text{□}_{0.67}\text{Si}_6\text{O}_{26}$, showed decreased thermodynamic stability as the rare earth ionic radius decreases, where rare earth apatites of Tb-Lu are expected to not be stable [147]. Additionally, a claim that PO_4 is more polar than SiO_4 may contribute to more rapid formation of a protective apatite layer than silicate-based coating materials [146]. However, all materials tested were the high-CTE monazite phase, and are thus not suitable as EBC candidates. The trend presented by Wang et al. suggested that a smaller RE cation could contribute to faster apatite formation may also translate into the xenotime structures [146].

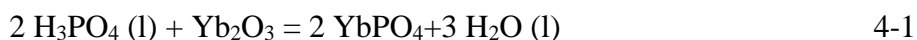
CMAS resistance of LuPO_4 , a xenotime rare earth phosphate, was studied as an EBC candidate [148]. LuPO_4 was exposed to CMAS ($33\text{CaO}-9\text{MgO}-13\text{AlO}_{1.5}-45\text{SiO}_2$) at $1300\text{ }^\circ\text{C}$, resulting in formation of $\text{Ca}_8\text{MgLu}(\text{PO}_4)_7$, $\text{CaAl}_2\text{Si}_2\text{O}_8$, $\text{CaMgSi}_2\text{O}_6$ and $\text{Lu}_2\text{Si}_2\text{O}_7$ phases. LuPO_4 was predicted to show greater CMAS resistance than $\text{Lu}_2\text{Si}_2\text{O}_7$ due to the formation of a protective layer occurring with less LuPO_4 dissolving in the molten CMAS. YbPO_4 is expected to behave similarly to LuPO_4 in regards to CMAS reactivity, given the similarities between the ytterbium and lutetium cations.

The objectives of this present study are to determine the suitability of YbPO_4 as an EBC through lab scale testing. The thermomechanical stability of YbPO_4 was investigated by high-temperature x-ray diffraction to confirm the thermal expansion of YbPO_4 and to report the first data on thermal expansion anisotropy of the tetragonal REPO_4 structure. Studies on YbPO_4 thermochemical stability were conducted by high-temperature high-velocity steam testing up to 235 m/s to determine steam reaction products in a fully saturated environment without surface contamination. Resistance to CMAS degradation was tested at $1300\text{ }^\circ\text{C}$ for 4, 24, and 96 hours in

stagnant air. The ability of YbPO₄ to form a protective layer against further CMAS penetration and the kinetics for growth of the protective layer were determined for the first time. The results of YbPO₄ thermal expansion anisotropy, stability in steam, and CMAS reactivity are compared to properties of state-of-the-art EBC Yb₂Si₂O₇.

4.1.2. Methods

YbPO₄ powders were produced via liquid chemical attack method between Yb₂O₃ and H₃PO₄ (15 wt.% H₂O) [146], [149]. The chemical reaction is presented in Equation 4-1.



A solution of 50 wt. % H₂O and the balanced wt. % of H₃PO₄ and Yb₂O₃ from Equation 4-1 were combined in a beaker attached to a water-cooled reflux tube to minimize any volatilization. Excess H₃PO₄ was added to the solution to ensure Yb₂O₃ would be the limiting reactant. The solution beaker was placed in a water bath at 65 °C and continuously stirred with a magnetic stir rod for 18 hours. Two powder batches were synthesized: one powder batch for the samples exposed to steam and the other powder batch for the samples exposed to CMAS.

Following synthesis, the solid YbPO₄ reaction product was filtered from the remaining liquid using Grade 5 Whatman filter papers under low vacuum at 381 torr. The powder was then washed with deionized water several times to ensure removal of any excess H₃PO₄, followed by drying at 300 °C to evaporate the water and annealed at 1100 °C in an open-air box furnace (CM Rapid Furnace, Bloomsfield NJ) for 12 hours in an Al₂O₃ crucible. The synthesized powder was then characterized for structure, phase, and composition using X-ray diffraction (XRD: Panalytical Empyrean Diffractometer, Westborough, MA) and scanning electron microscopy

(SEM: FEI Quanta 650, Hillsboro, OR) with energy dispersive spectroscopy (EDS: Oxford Instruments, Abingdon, UK).

Thermal expansion was measured on the YbPO_4 powder from room temperature to 1200 °C using a Panalytical Empyrean diffractometer with a hot stage attachment (Anton Paar HTK 1200N non-ambient stage, Graz, Austria) and spinning sample stage. The sensitivity of the diffractometer was ~ 5 wt.%. Scans were taken from 11-65° upon heating every 100 °C after a 1-minute equilibration hold at each temperature. HighScore Plus software was used to analyze peak shifting via Rietveld refinement to determine unit cell expansion with increasing temperature.

The powder batch for steam testing was loaded into a 20 mm diameter graphite die and sintered via spark plasma sintering (SPS DCS 25-10, Thermal Technologies, Santa Rosa, CA) for 15 minutes at a maximum temperature and pressure of 1600 °C and 65 MPa, respectively. The powder batch for CMAS studies was sintered for 25 minutes at 1550 °C and 65 MPa. The SPS process was conducted in an argon atmosphere for both powder batches, and therefore the consolidated sample pucks were oxygen deficient after sintering. Sample pucks were annealed in air at 1400 °C for 24 hours to restore oxygen stoichiometry to the material and remove residual carbon from the SPS process. The YbPO_4 puck was then sectioned into 10x10x1 mm coupons and polished to 0.25 μm with diamond suspension prior to steam testing and material characterization. Samples for CMAS exposure were 20 mm diameter disks with thicknesses of 1.25 mm and were finished to a surface polish of 1200 grit prior to testing.

The steamjet setup has been described in Chapter 2.1.2.2. Isothermal steam testing was conducted at 1400 °C for 60, 125, and 250 hours. Sample mass was recorded before and after steam testing with a microbalance (MS105DU, Mettler-Toledo, Columbus, OH) with an

accuracy of ± 0.05 mg to determine weight change from steam degradation. XRD and SEM were performed on the samples after steam exposure in plan view to show structural, chemical, and morphological changes in the sample. Optical profilometry (Zygo: NewView 7300: Middlefield, CT) was used to measure surface topology after exposure. Coupons were then mounted in epoxy and polished in cross section for SEM. Reaction layer thickness was measured using ImageJ Analysis Suite software (National Institutes of Health, Bethesda, Maryland) on micrographs acquired by SEM in cross-section as a function of position and local steam velocity determined from computational fluid dynamics software (ANSYS, Canonsburg, PA). An average reaction depth was calculated from at least 80 measurements spaced $75 \mu\text{m}$ apart to provide an accurate representation of the YbPO_4 degradation by exposure to steam at high-temperature and velocity as a function of time.

YbPO_4 reactions with CMAS were conducted using a composition of $33\text{CaO}-9\text{MgO}-13\text{AlO}_{1.5}-45\text{SiO}_2$, commonly used in the literature [150]–[153]. This composition of CMAS has a melting temperature around $1235 \text{ }^\circ\text{C}$ [150]. CMAS was prepared by mixing the correct ratios of the oxide constituents in a high purity Pt crucible and heating to $1300 \text{ }^\circ\text{C}$ for 24 hours to produce a transparent glass. The CMAS glass was quenched, crushed to a powder by ball milling with YSZ ball mill media, and cold pressed into pellets with approximately 40 mg/cm^2 relative to the YbPO_4 sample face surface area. Green body pellets were sintered at $1200 \text{ }^\circ\text{C}$ for 4 hours to create solid CMAS pellets for testing. Sintered CMAS pellets were then placed in the center of the 20 mm diameter YbPO_4 disks. The samples with CMAS pellets were then heated in an open-air box furnace at a rate of $10 \text{ }^\circ\text{C}/\text{min}$ to a maximum exposure temperature of $1300 \text{ }^\circ\text{C}$. YbPO_4 samples were exposed to CMAS for 4, 24, and 96 hours at $1300 \text{ }^\circ\text{C}$, then cooled to room temperature at $10 \text{ }^\circ\text{C}/\text{min}$. Both the sample and CMAS pellet masses were recorded before and

after each exposure. After exposure, the CMAS was adherent to the top of the YbPO_4 sample face. XRD was performed on the surface of each exposed specimen to determine reaction products within the residual CMAS glass and the reaction layer at the CMAS/ YbPO_4 interface. Samples were then sectioned in half and polished to 0.25 micron with diamond suspension for SEM/EDS analysis in cross-section. ImageJ Analysis Suite was used to measure CMAS reaction layer thicknesses on YbPO_4 and CMAS penetration depths from micrographs acquired by SEM using backscattered electrons.

4.1.3. Results

4.1.3.1. Pre-characterization of the Synthesized YbPO_4 Powder

Figure 4-1 shows the diffraction pattern of the synthesized YbPO_4 powder. The results show pure YbPO_4 powder was produced within the sensitivity of XRD, based on YbPO_4 ICDD pattern # 04-007-7022.

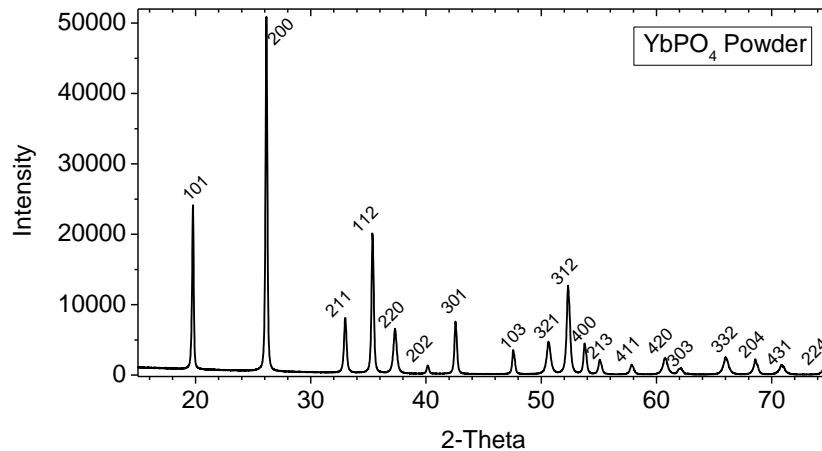


Figure 4-1. X-ray diffraction of initial YbPO_4 powder with hkl planes from ICDD pattern # 04-007-7022.

Fine YbPO_4 platelets were produced, shown in the backscattered electron SEM image in Figure 4-2. Energy dispersive spectroscopy (EDS) analysis showed an average Yb/P ratio near 1, which is consistent with YbPO_4 . A slightly higher Yb EDS signal was attributed to minor Yb_2O_3 present in the starting powder below the resolution of XRD.

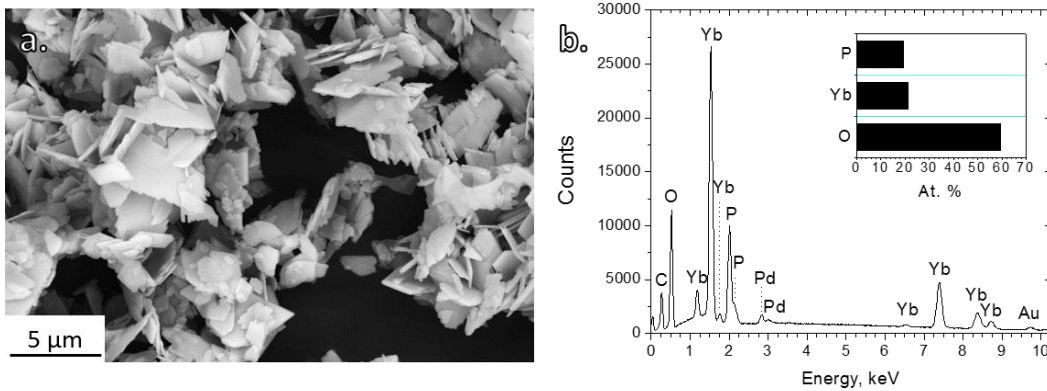


Figure 4-2. a. Backscattered SEM image of starting YbPO_4 powder and b. EDS spectra of YbPO_4 powder.

Figure 4-3a. shows the surface of a polished YbPO_4 coupon prepared for steam testing. Uniform porosity of 8-10% area fraction was present in the starting material. Additionally, SEM/EDS showed trace inclusions of Yb_2O_3 that were visibly present in the coupons (Figure 4-3b). The sample coupons processed for CMAS studies contained 5% Yb_2O_3 and 15% porosity.

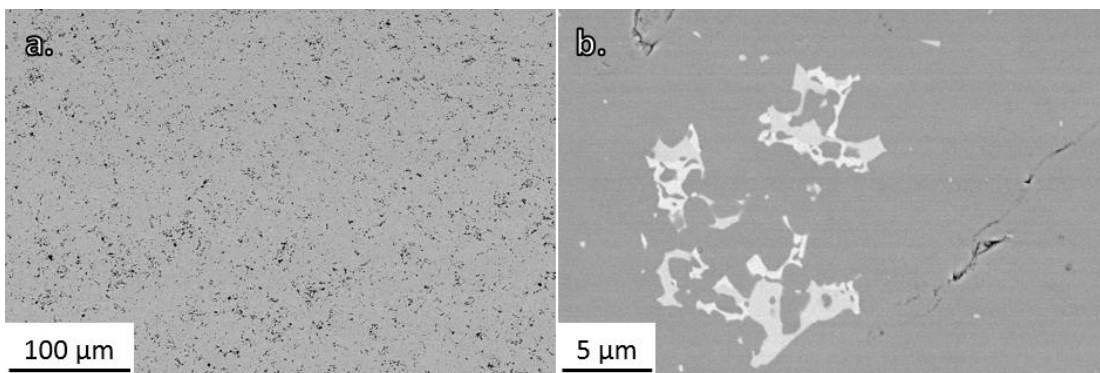


Figure 4-3. Backscattered electron SEM images a. of the sintered YbPO_4 after open air annealing at 1400 $^{\circ}\text{C}$ for 24 hours, and b. showing <1 at. % Yb_2O_3 inclusions (white).

4.1.3.2. Thermal Expansion and Thermal Expansion Anisotropy

All peaks in the YbPO₄ powder were matched to tetragonal YbPO₄ with no evidence of additional phases from room temperature up to 1200 °C. The hkl planes and d-spacings of the indexed diffraction peaks allowed for determination of unit cell lengths and angles. The unit cell was calculated through Rietveld refinement in HighScore Software for each temperature as a method for tracking unit cell growth with increasing temperature. Normalized unit cell growth is displayed in Figure 4-4a. for the a=b axis, c axis, and the total unit cell volume. Resulting unit cell parameters were used in Equation 4-2 to determine thermal expansion coefficients. CTE relates to the change in unit cell volume, ΔV , the change in temperature, ΔT , and the original unit cell volume at room temperature, V . Thermal expansion specifically along the a=b axis and c-axis were calculated with Eq. 4-2, with Δa and a or Δc and c substituted for ΔV and V terms, respectively.

$$CTE = \frac{1}{3} \frac{\Delta V}{V \Delta T} \quad 4-2$$

The thermal expansion along the a=b axis, c-axis, and the linear CTE are also presented in Figure 4-4b. from 100 °C to 1200 °C. The average values for the given temperature range are $a=5.4 \pm 0.4 \times 10^{-6} / ^\circ\text{C}$, $c= 7.3 \pm 0.1 \times 10^{-6} / ^\circ\text{C}$, and linear CTE = $6.0 \pm 0.3 \times 10^{-6} / ^\circ\text{C}$. An average difference of $1.9 \times 10^{-6} / ^\circ\text{C}$ was calculated between the a=b and c axes thermal expansion. The minor thermal expansion anisotropy of YbPO₄ supports the use of tetragonal REPO₄ as an EBC candidate for SiC/SiC CMCs.

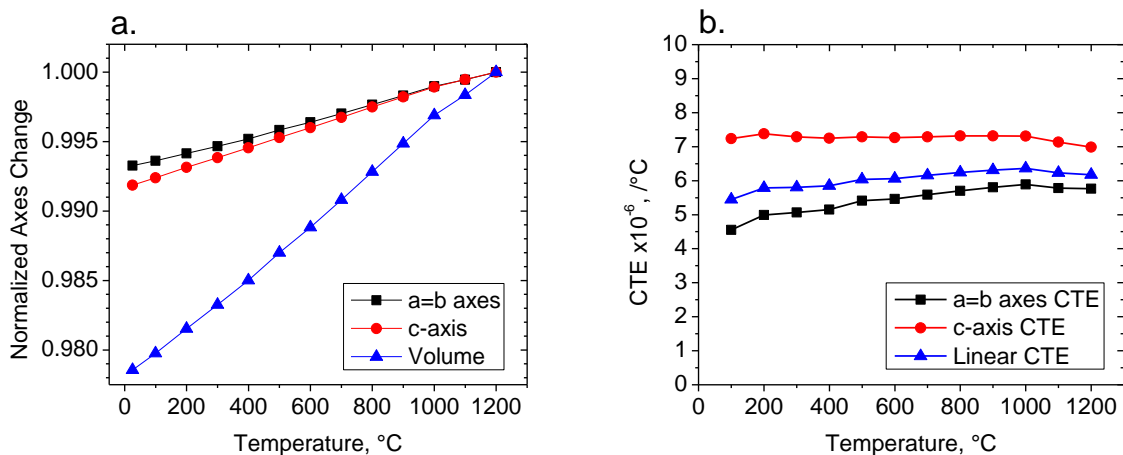


Figure 4-4. a. Normalized unit cell parameters for tetragonal YbPO_4 powder from XRD scans at 25-1200 °C and b. thermal expansion measurements for the linear CTE, a=b axis, and c-axis from 100-1200 °C.

4.1.3.3. Steamjet Results

4.1.3.3.1. YbPO_4 Compositional Changes

The position of each coupon in the steamjet provided the opportunity for dynamic study of YbPO_4 response to a variety of steam environments. The gas velocity distribution across the sample face varied from near stagnant velocities under the platinum sample holder region to a maximum water vapor velocity at the impingement site, near 235 m/s. Figure 4-5 displays three primary regions that can be separated on the YbPO_4 coupon surface analyzed after 60 hours of exposure to steam at 1400 °C. Figure 4-5a represents a stagnant gas velocity region, where the sample was held in place on the sample holder with a platinum foil covering. The initial material porosity of 8-10% was observed in this region. However, YbPO_4 did undergo initial surface reactions even with near stagnant gas velocities. The initial formation of Yb_2O_3 (light grey) occurred primarily at YbPO_4 (dark gray) grain boundaries.

The microstructure of the sample where gas velocities were less than ~80 m/s can be seen in Figure 4-5b. Elemental analysis conducted by EDS mapping of this region showed the presence of Al and trace Si (<5 at. %) in addition to Yb and O. The presence of Al and Si was

ascribed to contamination from the surrounding alumina furnace ware. SEM/EDS analysis was consistent with $\text{Yb}_4\text{Al}_2\text{O}_9$ as the stable phase on these surfaces. The porosity content, quantified by image analysis, was near 30% area fraction in this region and was attributed to the volatilization of a phosphorous hydroxide gas species, which explains why P was not detected by EDS analysis. Figure 4-5c is representative of the highest gas velocity regions near the gas impingement site where velocities are 80-200 m/s and water vapor partial pressures were assumed to be 1 atm. EDS analysis on this region detected only Yb and O, suggesting Yb_2O_3 formed on the surface with the volatilization of PO_4 as gaseous hydroxide reaction products. No other secondary phases or impurities were observed. The microstructure was consistently composed of fine-grained Yb_2O_3 crystallites with an average grain size of $0.4 \pm 0.1 \mu\text{m}$. Porosity was further increased in this highest velocity region to 45% area fraction, quantified by image analysis. By subtracting the initial 8-10% porosity, the presented results indicated that the YbPO_4 reaction with steam to form Yb_2O_3 resulted in a volume loss near 35-37%. Differences in theoretical density between YbPO_4 (6.414 g/cm^3) and Yb_2O_3 (9.216 g/cm^3) predicted a 44% porosity increase upon transformation, which was comparable with the results of this work. At the impingement site, above 200 m/s, material mechanical erosion was present for all exposed samples.

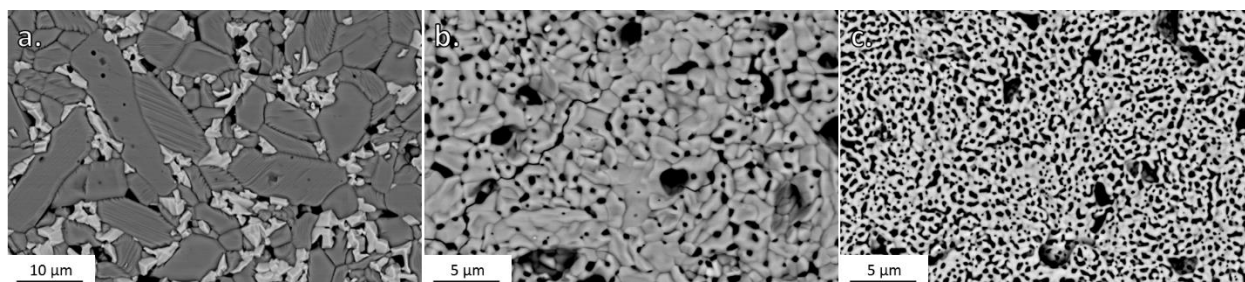


Figure 4-5. SEM of YbPO_4 after 1400°C steam exposure for 60 hours, a. stagnant steam velocity region underneath the platinum sample holder away from the impingement site ($10 \mu\text{m}$ scale bar), b. intermediate velocity regime where alumina contamination uptake occurs ($\sim 80 \text{ m/s}$), and c. high velocity region where Yb_2O_3 forms as the only stable reaction product ($120\text{-}150 \text{ m/s}$).

XRD patterns of YbPO_4 after steam exposure at $1400\text{ }^\circ\text{C}$ for 60, 125, and 250 hours are shown in Figure 4-6, plotted as log of the intensities to emphasize the presence of minor phases. The dashed box in Figure 4-6 displays the primary hkl peaks for the measured phases. Yb_2O_3 formed as a primary reaction product. Alumina contamination from furnace ware produced noticeable concentrations of $\text{Yb}_4\text{Al}_5\text{O}_{12}$ and $\text{Yb}_3\text{Al}_2\text{O}_9$ on sample surfaces outside of the high velocity (80-235 m/s) region. The high Al concentration phase, $\text{Yb}_3\text{Al}_5\text{O}_{12}$, was only present after the longer exposure times of 125 and 250 hours.

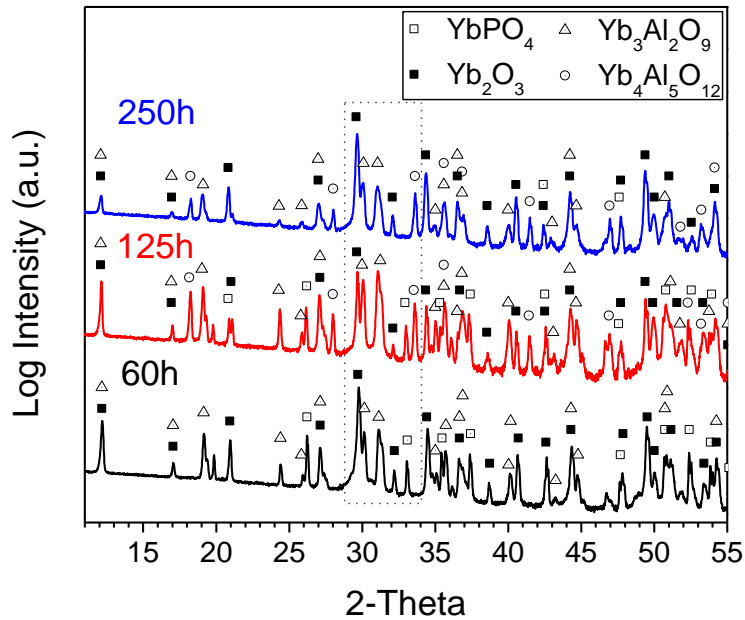


Figure 4-6. Logarithmic XRD patterns of the sample surfaces after steam exposure for 60, 125, and 250 hours at $1400\text{ }^\circ\text{C}$.

Optical profilometry allowed for depth profiling the surface to determine any special dependences on sample height. Figure 4-7 displays the surface map for YbPO_4 after 60 hours of steam exposure at $1400\text{ }^\circ\text{C}$. The surface appeared to be fairly uniform in height, with minor fluctuations between $5 - 15\text{ }\mu\text{m}$ in sample height. There was no correlation to local sample

position relative to the steam outlet and the profilometry surface height variations, which implied that Yb_2O_3 was not volatilizing by any detectable amount during testing.

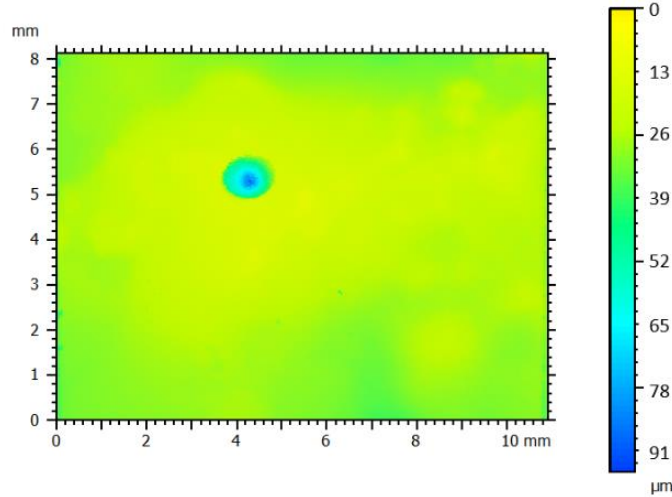


Figure 4-7. Zygo optical profilometry of the YbPO_4 surface after exposure to steam for 60 hours at 1400 °C.

At intermediate velocity regions below 80 m/s, alumina and minor silica uptake was present in the reaction layer. Figure 4-8a displays the plan view backscattered electron image of this region, and Figure 4-8b shows a comparable region in cross-section. The $\text{Yb}_4\text{Al}_2\text{O}_9$ reaction product with trace silica signal measured by EDS was seen to form on top of Yb_2O_3 . The reaction between Yb_2O_3 and $\text{Al}(\text{OH})_3$ (g) led to a volume increase, seen by the decreased porosity between the Yb_2O_3 and $\text{Yb}_4\text{Al}_2\text{O}_9$ layers in Figure 4-8b.

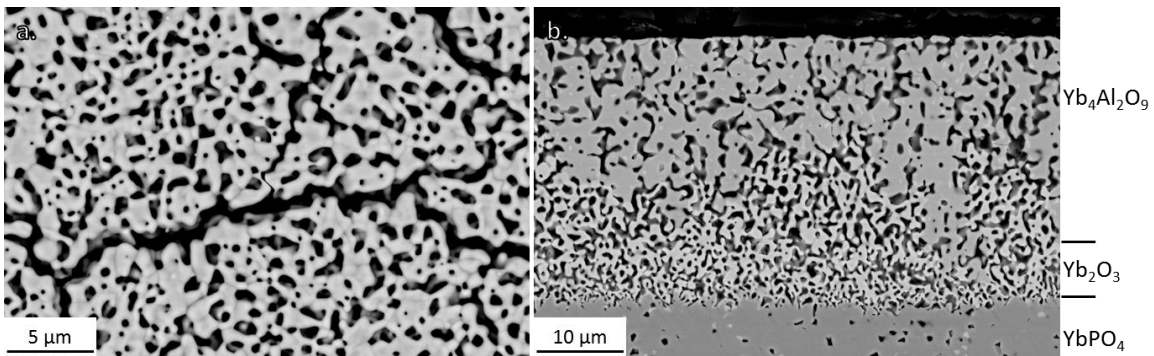


Figure 4-8. a. Plan view and b. Cross-section view of YbPO_4 after 250 hours at 1400 °C in the lower steam velocity range (~80 m/s) where Al_2O_3 and minor SiO_2 contamination react with Yb_2O_3 .

4.1.3.3.2. Steam Reaction Kinetics

The YbPO_4 steam reaction kinetics were determined from microstructural analysis of the coupon cross-sections following isothermal exposures to steam at 1400 °C for 60, 125, and 250 hours. Figure 4-9 shows representative SEM images of the YbPO_4 cross sections at the impingement site where the steam velocity ranged from 80–200 m/s. For this work, reaction kinetics were determined from these highest velocity regions (80-200 m/s) where only Yb_2O_3 formed as the stable product phase. The YbPO_4 microstructure following 60, 125, and 250 hours of steam exposure at 1400 °C is shown by Figure 4-9a, Figure 4-9b, and Figure 4-9c, respectively. Yb_2O_3 was the stable reaction product at the high velocity steam impingement site, represented by the layer of porous material that had formed on each of the coupon surfaces during exposure. The micrographs show the depth of this Yb_2O_3 reaction layer increased with increasing exposure time. The thickness of the reaction layer was measured for each exposure time. Yb_2O_3 showed slight coarsening from the reaction interface up to the reaction surface (high magnification images not shown here) yet no major microstructural differences were observed across all exposed samples. The YbPO_4 sample exposed to steam for 60 hours (Figure 4-9a) showed lateral cracks present along the Yb_2O_3 - YbPO_4 reaction interface, resulting from either rapid sample cooling or mechanical polishing damage of the sample.

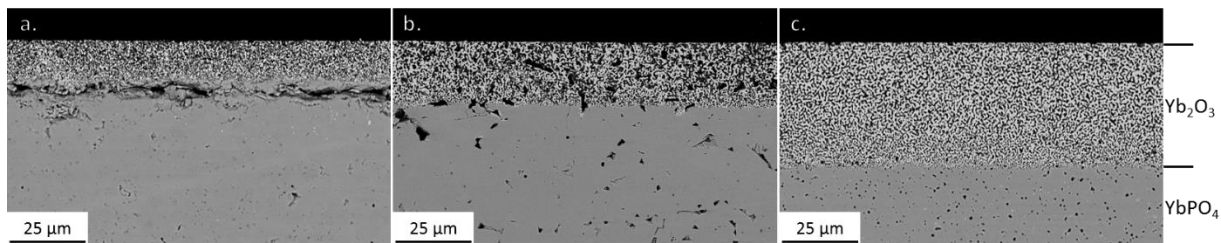


Figure 4-9. YbPO_4 cross-sections displaying the Yb_2O_3 reaction layer for a. 60h, b. 125h, and c. 250h at 1400 °C in the 80-200 m/s steam velocity regime.

The average steam reaction depth for the 80-200 m/s velocity range and the depth of mechanical erosion at the highest velocity impingement site for YbPO_4 exposed to water vapor

are plotted in Figure 4-10 as a function of the square root of exposure time at 1400 °C. The reaction depth and impingement erosion depth increased with increasing exposure time at 1400 °C. Specific mass loss data for YbPO₄ specimens after steam exposure also displayed linear fit to the square root of exposure time, although due to alumina uptake at intermediate steam velocities and sample edges, mass loss data are not presented as part of this work. Two comparisons are also presented for the Yb₂Si₂O₇ reaction with high velocity water vapor from a prior study [29]. Previous studies on Yb₂Si₂O₇ show that Yb₂Si₂O₇ reacts to form Yb₂SiO₅ at steam velocities of 80-115 m/s. Yb₂Si₂O₇ underwent microstructural changes and a secondary reaction to form Yb₂O₃ when water vapor velocities were greater than 150 m/s [29]. The secondary reaction and microstructural changes associated with it resulted in lower total reaction depths for Yb₂Si₂O₇ at higher velocities than in the 80-115 m/s velocity range. Further information on the microstructural evolution of Yb₂Si₂O₇ in high velocity steam can be found in Chapter 2.3 [29].

Similar to Yb₂Si₂O₇ in previous work, YbPO₄ shows a parabolic time dependence for the steam reaction, indicative of a diffusion-controlled process. The YbPO₄ reaction thickness, YbPO₄ erosion depth at the impingement site, and the data for Yb₂Si₂O₇ all showed an incubation period (4-25 hours) prior to establishing parabolic reaction kinetics. Thus, impingement mechanical erosion was believed to follow parabolic reaction kinetics due to required formation of porous Yb₂O₃ before onset of erosion. The average YbPO₄ reaction depth with steam over the 80-200 m/s velocity range was significantly less than Yb₂Si₂O₇ for both the 80-125 m/s and 150-200 m/s water vapor velocity ranges, suggesting YbPO₄ has enhanced steam resistance compared to Yb₂Si₂O₇.

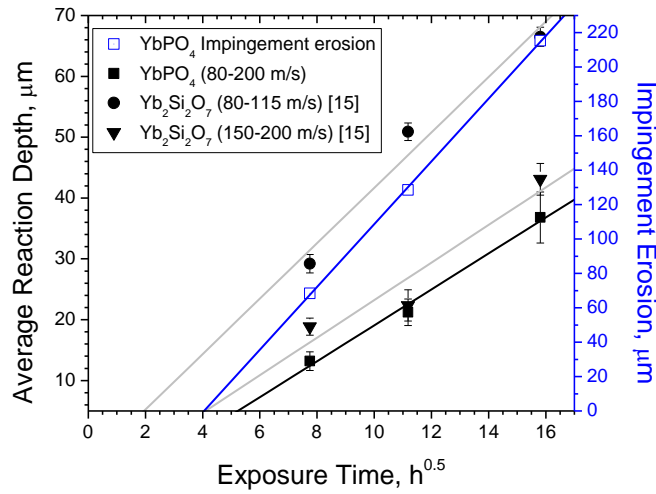


Figure 4-10. Average reaction depth and impingement erosion depths versus the square root of time for YbPO₄ in this study and Yb₂Si₂O₇ (previous study) at 1400 °C [29] and Chapter 2.3.

4.1.3.4. YbPO₄ Resistance to CMAS attack

Figure 4-11 shows macro images of the YbPO₄ samples after exposure to CMAS for 4, 24, and 96 hours. No mass change was observed after each exposure. This was indicative of both negligible volatilization of CMAS or loss of molten CMAS from flowing off of the YbPO₄ substrate surfaces. The macrographs show that molten CMAS did not spread to the edges of the YbPO₄ substrates. The YbPO₄ edges free from interaction with the molten CMAS allowed for comparison of YbPO₄ consumption by CMAS where they were in contact to the initial YbPO₄ substrate thickness.



Figure 4-11. Macro images of YbPO₄ samples after CMAS exposure for 4, 24, and 96 hours at 1300 °C.

4.1.3.4.1. YbPO₄ structural changes

XRD patterns of each sample surface after CMAS exposure for 4, 24, and 96 hours are shown in Figure 4-12. Reaction products that formed from YbPO₄ exposure to CMAS were Ca₈MgYb(PO₄)₇, Ca₂Yb₃(SiO₄)₂(PO₄)O, Ca₂Yb₈(SiO₄)₆O₂. Each sample displayed numerous minor peaks which were likely obscured by background signal from residual amorphous CMAS. Additionally, peak intensities were not well matched with database patterns, suggesting preferred growth directions of reaction products. The sample exposed to CMAS for 96 hours displayed Yb₂Si₂O₇ as the primary surface product. The high intensity of the primary Yb₂Si₂O₇ peak may have obscured identification of other phases that possibly formed by exposure to CMAS. The silicate apatite phase, Ca₂Yb₈(SiO₄)₆O₂, commonly formed from rare earth silicate reaction with CMAS, was only determined for the CMAS exposures after 4 and 24 hours at 1300 °C.

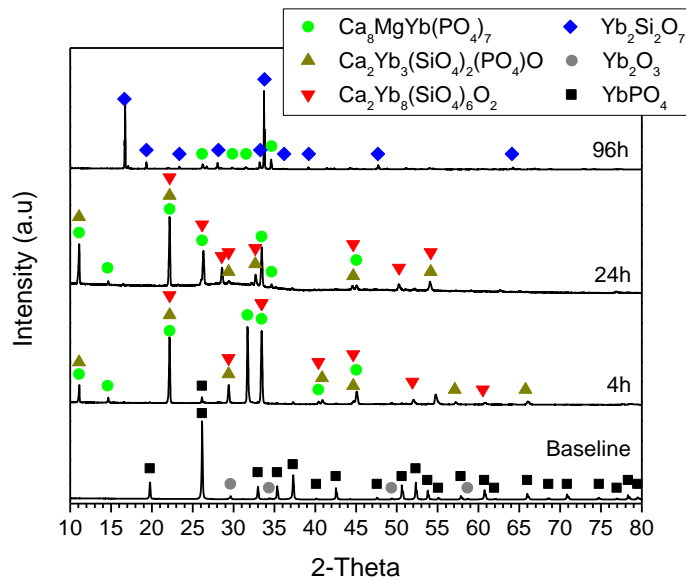


Figure 4-12. Plot of XRD patterns for the starting YbPO₄ material and after CMAS exposure for 4, 24, and 96 hours at 1300 °C.

Extended backscattered electron SEM images for each sample cross-section are presented in Figure 4-13. The residual CMAS glass increasingly wet the YbPO₄ surfaces with longer

exposure times. Large crystals were observed to have formed in the CMAS melt on the sample exposed for 96 hours, which supported the residual CMAS glass on the sample surface.

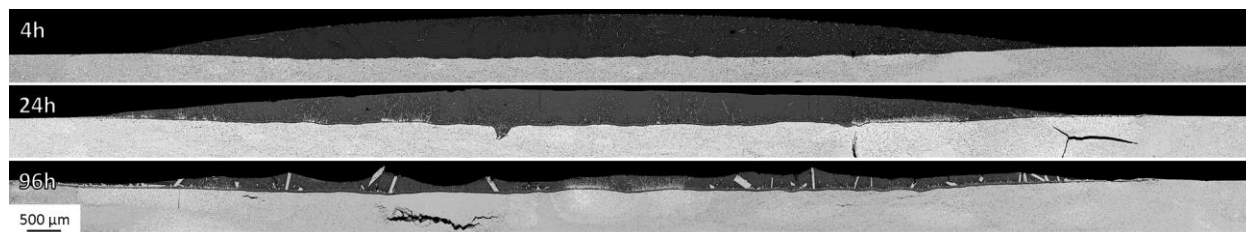


Figure 4-13. Stitched backscattered SEM images showing cross-sections of YbPO_4 after CMAS exposure for 4, 24, and 96 hours at $1300\text{ }^\circ\text{C}$ in stagnant air.

Higher magnification SEM images of the CMAS- YbPO_4 interface are displayed in Figure 4-14. A multi-level reaction layer was present that increased in thickness with increasing exposure time for 4, 24, and 96 hours at $1300\text{ }^\circ\text{C}$. The presence of porosity from YbPO_4 processing observed directly below the reaction front was generally free of CMAS glass, suggesting that the reaction layer was effective at halting CMAS infiltration into the sample. At the YbPO_4 interface, a continuous reaction layer was present that limited CMAS penetration into the substrate. A secondary reaction layer of lighter greyscale was observed on top of the continuous reaction layer. Finally, a dendrite-type phase was seen both in the residual glass and connecting to the outer layer of the reaction layer, as shown best in Figure 4-14b. Two other precipitate phases were also present in the CMAS melt. Figure 4-14c also displays one of the large crystallites in the CMAS glass that was supporting the residual glass in Figure 4-13 for the 96-hour exposure. Phase identification will be discussed in more detail in Figure 4-15.

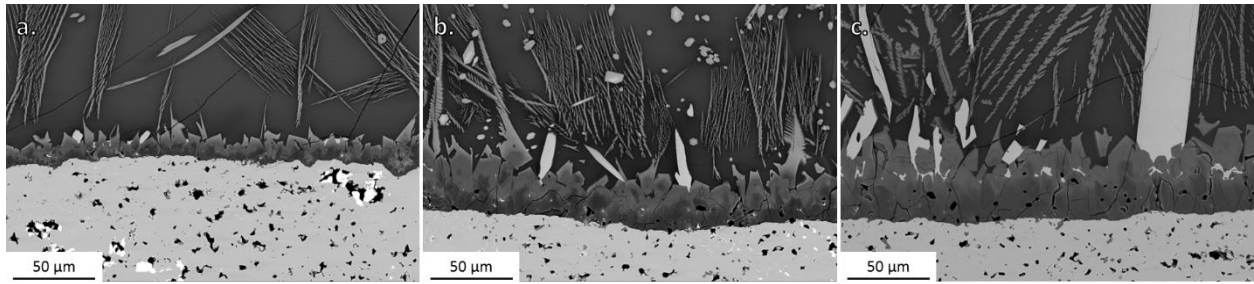


Figure 4-14. Higher magnification SEM images acquired with backscattered electrons of the YbPO_4 -CMAS tri-layer reaction product for a. 4h, b. 24h, and c. 96 hours of exposure at 1300 °C.

EDS mapping was used in combination with XRD to determine the phases formed after CMAS reaction. Figure 4-15 shows the EDS maps and point identification at the CMAS- YbPO_4 interface following exposure for 96 hours at 1300 °C. EDS showed that Al and Mg signals were confined to the continuous reaction layer, where below the continuous reaction layer, Al background signal was only present due to EDS peak overlap with Yb. Both Ca and trace Si signal from the CMAS melt occasionally penetrated into the YbPO_4 substrate below the continuous reaction layer into the sample pores. The continuous reaction layer was concentrated in Ca and P. EDS signal showed that Mg was present in the continuous reaction layer at only minor concentrations and that Al was not present outside of the residual CMAS glass.

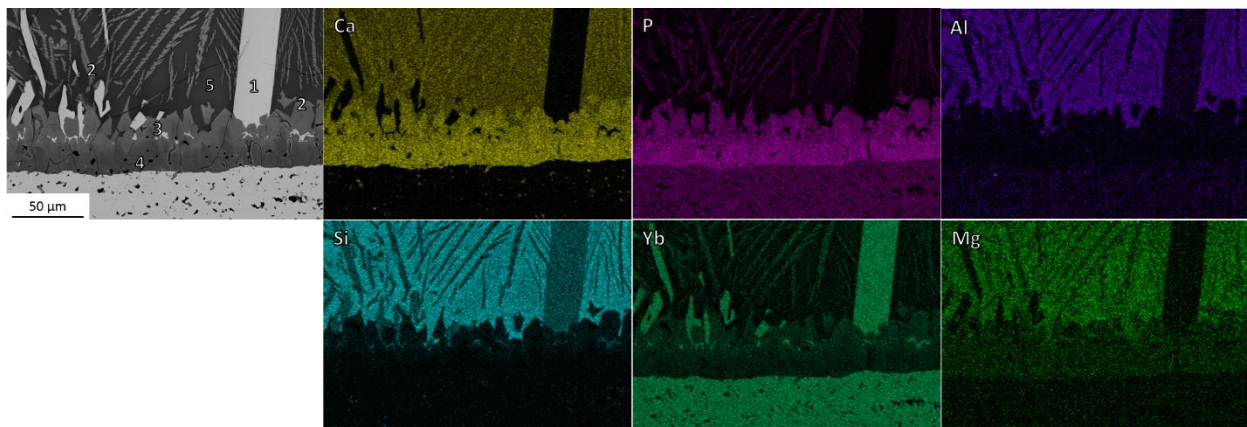


Figure 4-15. Energy Dispersive Spectroscopy of the YbPO_4 tri-layer reaction product after CMAS exposure for 96 hours at 1300 °C. Numbered areas in the image correspond to EDS results in Table 4-2.

Table 4-2 shows point identification of various regions labelled numerically from one to five in Figure 4-15. The large crystallites present after 96 hours in the glass (1) were matched

with $\text{Yb}_2\text{Si}_2\text{O}_7$. The composition of dendrite precipitates (2) and the multi-level reaction layer (2,3,4) are presented in the table. These phases showed a gradient in Ca, P, Si, and Yb signal. Ca and P increased in concentration closer to the reaction interface, while Si and Yb decreased in concentration from the dendritic precipitate phase to the reaction interface. The Ca content in the residual glass (5) decreased from the original CMAS composition as a result of forming Ca-rich phases during reaction.

Table 4-2. Energy Dispersive Spectroscopy area phase identification of the positions labelled in Figure 4-15.

No.	Position	Average EDS Signal
1	Glass Precipitate	$\text{Yb}_2\text{Si}_2\text{O}_7$
2	Dendrite Precipitate	$\text{Ca}_{0.35}\text{P}_{0.25}\text{Si}_{0.2}\text{Yb}_{0.15}\text{Mg}_{0.05}\text{O}_x$
3	Middle Reaction Layer	$\text{Ca}_{0.4}\text{P}_{0.35}\text{Yb}_{0.1}\text{Si}_{0.1}\text{Mg}_{0.05}\text{O}_x$
4	Lower Reaction Layer	$\text{Ca}_{0.45}\text{P}_{0.4}\text{Yb}_{0.075}\text{Mg}_{0.05}\text{Si}_{0.025}\text{O}_x$
5	Residual CMAS Glass	$\text{Si}_{0.45}\text{Ca}_{0.25}\text{Al}_{0.15}\text{Mg}_{0.1}\text{Yb}_{0.05}\text{P}_{0.025}\text{O}_x$

An EDS linescan is presented in Figure 4-16 through the reaction layer for the YbPO_4 sample exposed to CMAS for 96 hours at 1300 °C. The linescan starts with 0 μm at the residual CMAS glass and ends with 51 μm at the continuous reaction layer near the YbPO_4 substrate. The Ca and P signal clearly decreased in concentration from the substrate interface up to the CMAS glass, while the opposite behavior was noticed for both Si and Yb signal. The dendrite phase (outer edge of reaction layer) showed a large gradient in element concentrations. The Mg signal was constant as a minor element in all three layers of the reaction products. The Al signal was negligible through the reaction layers.

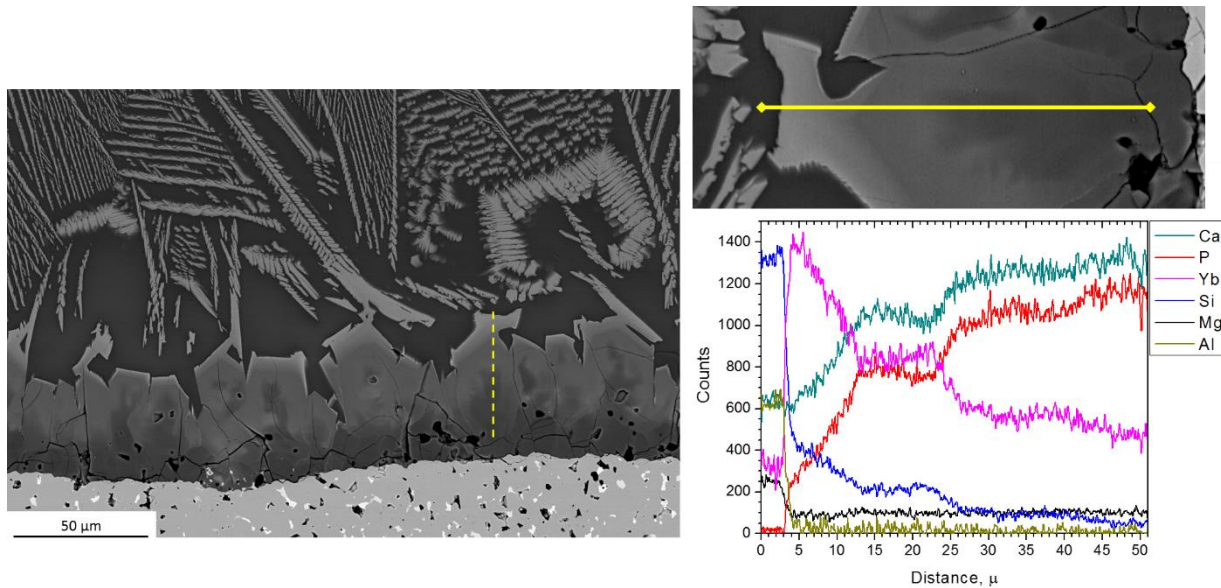


Figure 4-16. Energy Dispersive Spectroscopy linescan of the tri-layer reaction product after exposure to 1300 °C for 96 hours. The linescan starts with 0 μm at the residual CMAS glass and ends with 51 μm at the continuous reaction layer near the YbPO₄ substrate.

The total reaction layer thickness was measured across the samples to determine the reaction kinetics for CMAS attack on YbPO₄. The average reaction layer thickness is plotted in Figure 4-17 as a function of the square root of exposure time with a comparison to LuPO₄ samples exposed at 1300 °C to the same CMAS composition as used in this present work [148]. The reaction layer increased in thickness with a parabolic rate, consistent with a diffusion-controlled process. Using data presented by Hu et al. [148], a reaction rate was calculated to be $25 \pm 1 \mu\text{m}^2/\text{h}$ for LuPO₄ upon exposure, which was similar to the reaction rate of $28 \pm 1 \mu\text{m}^2/\text{h}$ for YbPO₄ in this present work. The results from this present study indicated that YbPO₄ is a strong EBC candidate based on the production of a dense continuous interfacial layer that halted CMAS penetration into the samples.

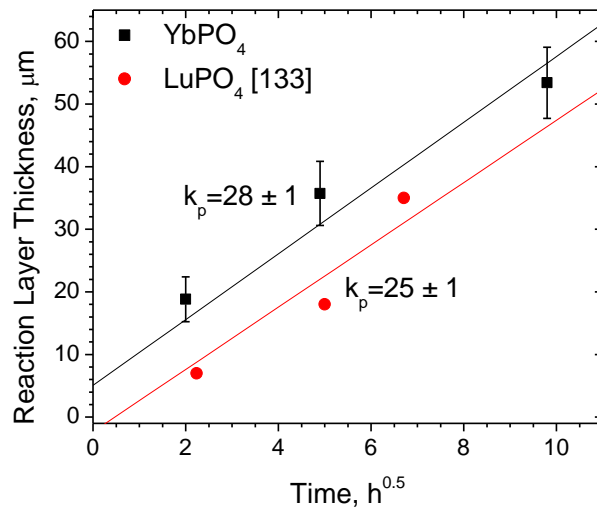


Figure 4-17. Tri-layer reaction product average thickness plotted against the square root of time for the rare earth phosphate – CMAS reaction at 1300 °C.

4.1.4. Discussion

4.1.4.1. Thermal Expansion and Thermal Expansion Anisotropy

The coefficient of thermal expansion of tetragonal YbPO₄ was measured to be 6.0×10^{-6} /°C with axial expansions of $a = 5.4 \times 10^{-6}$ /°C and $c = 7.3 \times 10^{-6}$ /°C for the 100 - 1200 °C temperature range, which is slightly higher than that of SiC. While Yb₂Si₂O₇ has a lower linear CTE of 4.2×10^{-6} /°C, it also displays a greater amount of anisotropy in its' axial CTE (a-axis: 5.7×10^{-6} /°C, b-axis: 3.7×10^{-6} /°C, and c-axis: 3.2×10^{-6} /°C) [50] than YbPO₄. Therefore, YbPO₄ may show decreased amounts of stress buildup upon thermal cycling as an EBC compared to Yb₂Si₂O₇.

The thermal expansion mismatch between EBC materials and their steam reaction products should also be considered. Yb₂SiO₅, the steam reaction product for Yb₂Si₂O₇, is highly anisotropic and prone to stress cracking, with CTEs: Linear = 7.25×10^{-6} /°C, a-axis = 2.2×10^{-6} /°C, b-axis = 6.6×10^{-6} /°C, and c-axis = 10.3×10^{-6} /°C [35]. Yb₂O₃, the steam reaction product

for YbPO₄, is cubic in structure with no anisotropy, yet has a higher linear CTE of 6.8-8.4 x10⁻⁶ /°C [49]. Additionally, both YbPO₄ and Yb₂O₃ have higher melting points than Yb₂Si₂O₇ and Yb₂SiO₅, which is advantageous as engine operating temperatures increase. The tradeoff between limiting thermal expansion mismatch and minimizing thermal expansion anisotropies between Yb₂Si₂O₇ and YbPO₄ EBC candidates and their respective reaction products is thus worthy of further research.

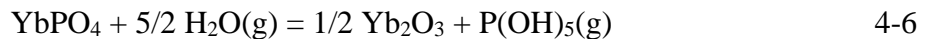
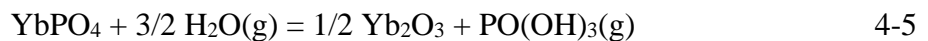
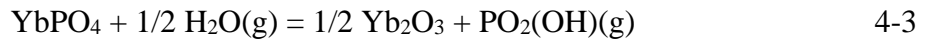
4.1.4.2. YbPO₄ Reaction with High-velocity Water Vapor

YbPO₄ reacted to form a Yb₂O₃ reaction product for all exposure times and gas velocities at 1400 °C. The Yb₂O₃ product layer showed minimal grain growth and coarsening at 1400 °C, indicative of the high melting temperature of Yb₂O₃. Below ~ 80 m/s, alumina and minor silica impurities in the furnace steam environment reacted with the surface Yb₂O₃ product phase to form Yb₄Al₂O₉ type compounds.

The YbPO₄ reaction depth showed a parabolic relationship to exposure time, indicative of a diffusion-controlled process. Similarly, the impingement erosion depth also displayed parabolic kinetics with a comparable incubation time to the average reaction depth data. Both factors indicate that mechanical erosion at the impingement site only occurs for the Yb₂O₃ product phase and that YbPO₄ does not experience mechanical erosion at steam gas velocities in the 200-245 m/s range. The average reaction rate and impingement erosion rate at 1400 °C were determined to be 8.70 μm²/h and 333 μm²/h, respectively. The high rate of mechanical erosion at the impingement site represents a concern for use of REPO₄ facing direct impact in combustion environments, and therefore warrants additional research.

YbPO₄ in this study showed lower steam reactivity than Yb₂Si₂O₇ for the 80-200 m/s gas velocity range at 1400 °C. The experimentally estimated equilibrium partial pressure of the P-O-

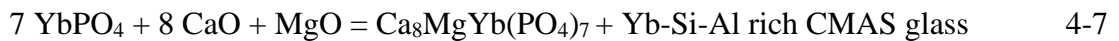
H gas is lower than that of Si(OH)₄ (g) for the Yb₂Si₂O₇ reaction with H₂O (g). Therefore, the P₂O₅ activity in YbPO₄-Yb₂O₃ dual phase field may also be lower than the SiO₂ activity for Yb₂Si₂O₇/Yb₂SiO₅ two-phase field, which has been measured to be a(SiO₂) = 0.194 at 1600 K [51]. The dominant gaseous product species for the YbPO₄ – H₂O (g) has not been confirmed. Hildenbrand et al. showed that PO₂(OH) or PO(OH) are dominant hydroxide species for Ca₂P₂O₇ when exposed to 10⁻⁶ atm of water vapor [145], which suggests both hydroxide phases may be present in this work with YbPO₄. Yet, Hildenbrand has also shown that the dominant manganese hydroxide species increases its (OH)_x group with increasing water vapor pressure [154]. This trend is believed to be consistent for many metal hydroxide groups, suggesting that other hydroxide gas species such as PO(OH)_x (x>1) may be present during this study where water vapor pressure is assumed to be 1 atm. For example, Ta₂O₅, a pentoxide analogous to P₂O₅, displayed TaO(OH)₃ (g) and Ta(OH)₅ (g) species after reaction with water vapor in the temperature range of 1250 °C-1450 °C [155]. Future work is needed to better understand the hydroxide species that form for REPO₄ in high water vapor partial pressure environments. Some predicted reactions are presented below for YbPO₄ and water vapor, assuming various phosphorous hydroxide species form as the dominant gaseous product species.



4.1.4.3. *YbPO₄ Reaction with CMAS*

The YbPO₄ reaction with CMAS for 4, 24, and 96 hours at 1300 °C resulted in formation of a tri-layer reaction product that inhibited CMAS penetration further into the bulk of the

material. XRD analysis showed that Ca-Yb-P rich phases formed upon reaction as well as $\text{Yb}_2\text{Si}_2\text{O}_7$, a precipitate phase found in the residual glass. The continuous reaction layer was composed primarily of a protective $\text{Ca}_8\text{MgYb}(\text{PO}_4)_7$ phase at the reaction interface, with a structure analogous to that of tricalcium phosphate (TCP), $\beta\text{-Ca}_3(\text{PO}_4)_2$. Further towards the residual glass and away from the reaction interface, the phase became rich in Si and Yb and depleted in P and Ca. EDS results are consistent with $\text{Ca}_8\text{MgYb}(\text{PO}_4)_7$ as the dense continuous phase present at the base of the reaction interface that limited CMAS infiltration. Due to limited patterns in the available XRD database, $\text{Ca}_2\text{Yb}_8(\text{SiO}_4)_6\text{O}_2$ and $\text{Ca}_2\text{Yb}_3(\text{SiO}_4)_2(\text{PO}_4)\text{O}$ were found to be the best matches to the rest of the XRD peaks after CMAS exposure. These two XRD phases did not fully match EDS phase analysis, which showed the middle and upper reaction layers to be $\text{Ca}_{0.4}\text{P}_{0.35}\text{Yb}_{0.1}\text{Si}_{0.1}\text{Mg}_{0.05}\text{O}_x$ and $\text{Ca}_{0.35}\text{P}_{0.25}\text{Si}_{0.2}\text{Yb}_{0.15}\text{Mg}_{0.05}\text{O}_x$, respectively. The trends presented suggest that element concentration varies throughout the entirety of the reaction layer, where Ca and P are rich at the substrate reaction interface while Yb and Si are more prevalent in the outer reaction layer and in the dendrites precipitated in the residual CMAS glass. The proposed initial CMAS reaction with YbPO_4 is shown in Eq. 4-7:



where this likely initial reaction product is Ca- and P-rich. Subsequent reaction with the Yb-Si-Al rich CMAS glass resulted in formation of an off-stoichiometry phase, $\text{Ca}_{8-x}\text{MgYb}_{1+x}(\text{SiO}_4)_x(\text{PO}_4)_{7-x}$. The Mg signal remained constant in the reaction phases and in the CMAS residual glass, and did not contribute to any changes in composition. Additionally, the Al signal by EDS was only present in the glass, and therefore was not participating in the formation of a protective reaction layer.

The TCP-type continuous reaction product determined in this work, $\text{Ca}_8\text{MgYb}(\text{PO}_4)_7$, has increased Ca content and reduced Yb content compared to the typical apatite reaction product, $\text{Ca}_2\text{RE}_8(\text{SiO}_4)_6\text{O}_2$, seen for $\text{RE}_2\text{Si}_2\text{O}_7$ and RE_2SiO_5 after exposure to CMAS. The chemical reaction for rare earth silicates to form silicate-base apatites is presented in Equation 4-8.



Increased removal of CaO and MgO from the CMAS occurs for production of the TCP-type phase compared to the silicate apatite. Unpublished work by Webster and Opila showed that glass viscosity was increased through decreased concentrations of CaO, decreased concentrations of MgO, and increased concentrations of Al_2O_3 [156]. Removal of additional CaO and MgO for the YbPO_4 -CMAS reaction increases viscosity of the melt and further decreases the penetration ability of the residual glass compared to the CMAS reaction with silicate EBCs.

Growth of the total reaction layer displayed parabolic behavior with a growth rate of $28 \pm 1 \mu\text{m}^2/\text{h}$, which is comparable to that of LuPO_4 found in the literature. Hu et al. determined the LuPO_4 -CMAS reaction layer consisted of rhombohedral $\text{Ca}_8\text{MgLu}(\text{PO}_4)_7$, with an apatite $\text{Ca}_2\text{Lu}_8(\text{SiO}_4)_6\text{O}_2$ dendrite phase and $\text{Lu}_2\text{Si}_2\text{O}_7$ crystals forming above the reaction interface in the residual glass [148]. The phases presented in the study by Hu et al. agree with those determined in this present study by XRD and EDS analysis, suggesting that tetragonal structure REPO_4 may all display similar reaction mechanisms with CMAS. The linear fit to parabolic reaction layer growth kinetics for YbPO_4 implies about a $5 \mu\text{m}$ thick reaction layer at zero hours of exposure time. It is unknown if this is an artifact of the testing performed in this work, or if YbPO_4 reacted with CMAS during furnace heating before reaching the exposure temperature of $1300 \text{ }^\circ\text{C}$. Future work should include other temperatures and exposure times to determine the onset of CMAS reaction with YbPO_4 .

In a separate study by Webster and Opila, $\text{Yb}_2\text{Si}_2\text{O}_7$ was exposed to the same CMAS composition, CMAS loading, and furnace exposure time as was used in this present study for YbPO_4 [151]. $\text{Yb}_2\text{Si}_2\text{O}_7$ after 96 hours of CMAS exposure displayed glass penetration through the entirety of the 1 mm thick sample. Blistering and large porosity production were also observed with the $\text{Yb}_2\text{Si}_2\text{O}_7$ samples post exposure, indicating that a protective Yb-apatite reaction layer was slow to form during exposure to CMAS. Large amounts of porosity production have also been reported in a study by Liu et al. for $\text{Yb}_2\text{Si}_2\text{O}_7$ exposed to CMAS at 1400 °C in a steam environment, although the reaction layer could not be identified [157]. The blister cracking behavior for $\text{Yb}_2\text{Si}_2\text{O}_7$ exposed to CMAS has been linked to a dilatation gradient through the $\text{Yb}_2\text{Si}_2\text{O}_7$ from CMAS infiltration and results from grain boundary transport of CMAS rather than chemical reaction to form a protective apatite reaction layer [126]. Stokes et al. annealed pellets of 50% $\text{Yb}_2\text{Si}_2\text{O}_7$ /50% CMAS at 1200-1400 °C to determine the primary reaction products for three CMAS compositions with varying CaO and SiO_2 content [158]. It was seen that an apatite phase, $\text{Ca}_2\text{Yb}_8(\text{SiO}_4)_6\text{O}_2$, was the primary product phase, yet as the CaO content decreased in the CMAS glass, $\text{Yb}_2\text{Si}_2\text{O}_7$ resulted as the dominant phase produced. The results by Stokes et al. may explain the rapid growth of $\text{Yb}_2\text{Si}_2\text{O}_7$ crystals seen in this present study for YbPO_4 exposed to CMAS for 96 hours at 1300 C.

Webster and Opila also exposed phase pure Yb_2SiO_5 to CMAS for up to 200 hours at 1300 °C [151]. A dense reaction layer consisting of apatite, $\text{Ca}_2\text{Yb}_8(\text{SiO}_4)_6\text{O}_2$, formed that halted further CMAS penetration into the bulk of the samples. Both apatite and garnet phases were present in the residual glass. While Yb_2SiO_5 displayed excellent CMAS resistance compared to $\text{Yb}_2\text{Si}_2\text{O}_7$, microcracking from the Yb_2SiO_5 thermal expansion anisotropy presented fast pathways for CMAS infiltration.

Results presented here suggest that YbPO_4 is more resistant to CMAS compared to phase pure $\text{Yb}_2\text{Si}_2\text{O}_7$ due to the rapid formation of a continuous reaction layer and consumption of CaO and MgO from the melt. While YbPO_4 may have comparable CMAS resistance compared to phase pure Yb_2SiO_5 , the thermomechanical properties of Yb_2SiO_5 are unsuitable as a standalone EBC material. The known presence of Yb_2SiO_5 in air plasma sprayed $\text{Yb}_2\text{Si}_2\text{O}_7$ coatings would result in increased CMAS resistance compared to phase pure Yb silicates. The CMAS resistance of APS YbPO_4 and APS $\text{Yb}_2\text{Si}_2\text{O}_7$ should be compared directly for a more robust understanding of EBC performance against CMAS attack.

4.1.5. Conclusion

YbPO_4 was synthesized to determine its relevance as an EBC candidate material for SiC-based turbine applications. The thermal expansion anisotropy was measured with hot stage XRD and determined to be less than the anisotropy of current EBC materials with reasonable CTE match to SiC. High velocity steam exposures at 1400 °C showed that YbPO_4 reacts to form Yb_2O_3 with a reaction rate lower than that of state-of-the-art EBC $\text{Yb}_2\text{Si}_2\text{O}_7$. CMAS exposures at 1300 °C resulted in formation of a tri-layer reaction product that successfully limited further CMAS ingress into the bulk of the YbPO_4 , while CMAS penetration in $\text{Yb}_2\text{Si}_2\text{O}_7$ was rapid for comparable studies with the same CMAS composition, CMAS loading, and furnace exposure times. The combined results suggest that YbPO_4 and other monazite structure REPO_4 be considered as novel EBC candidates for future coating applications in combustion turbines.

4.2. Holistic Comparison of Environmental Barrier Coating Material Candidates through Design of a Figure of Merit

4.2.1. Introduction

Silicon carbide ceramic matrix composites (SiC CMCs) entered commercial aircraft use as of 2016 in the GE LEAP engine [159]. Environmental barrier coatings (EBCs) are required for application of CMCs at high temperatures to minimize SiC interaction with the combustion environment. EBC material design initially focused on silicate materials to maintain chemical compatibility with both a required silicon intermediate bond coat and the SiC, to provide greater stability than thermally grown SiO₂, and to uphold an acceptable thermal expansion match with Si and SiC. While EBCs are a supportive technology to enable CMC usage, an understanding of EBC failure modes in service are critical for lifetime prediction of CMC components. Knowledge of EBC failure modes has led to the identification of other critical EBC properties required for extended coating lifetimes.

The well-known failure modes for EBCs in service consist of the following: reactivity with steam, oxidation of the silicon bond coat, CaO-MgO-Al₂O₃-SiO₂ (CMAS) molten glass infiltration, thermal stresses, mechanical erosion, and foreign object damage [139]. Even though significant research is underway by many research teams on individual EBC failure modes, no holistic comparison or figure of merit has been designed for EBC candidate materials. For example, the thermoelectric community utilizes a figure of merit for comparison of the Seebeck coefficient, electrical conductivity, and thermal conductivity with changes in temperature through a unified numerical value, ZT [160]. The complexity of EBCs limits the ability to produce a singular numerical model for comparison of EBC materials across all required

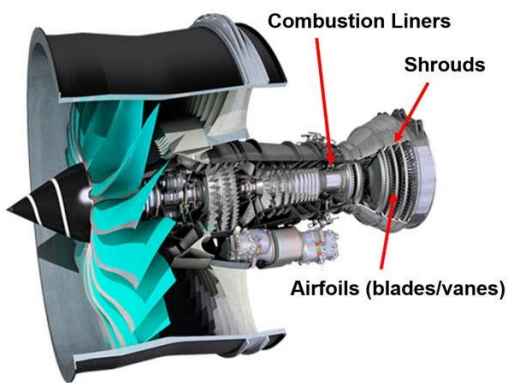
properties. This work constructs the first method for comparison of complex materials property requirements for EBC applications through a ranking system and graphical approach, accounting for all significant EBC failure modes. Past, present, and novel EBC candidate materials are compared: SiO_2 , $\text{Ba}_{0.75}\text{Sr}_{0.25}\text{Al}_2\text{Si}_2\text{O}_8$ (BSAS), HfSiO_4 , $\text{Yb}_2\text{Si}_2\text{O}_7$, Yb_2SiO_5 , Yb_2O_3 , and YbPO_4 . The complex interconnectivity of the turbine environment, coating fabrication on CMCs, and general material properties to the EBC failure modes will be discussed. Thermochemical and thermomechanical properties of candidate materials that best mitigate EBC failure modes were utilized in creation of an EBC ranking system. Employing the presented holistic approach provides a potential aid to the high-temperature coatings community for design of next generation EBC materials.

4.2.2. Background

4.2.2.1. Gas Turbine/Air Plasma Spray Conditions

The use of CMCs as hot section turbine components benefits fuel consumption through increased fuel burn temperatures above the melting temperatures of traditionally used superalloy components. Additionally, the lower material density of CMCs relative to superalloys leads to decreased component weight. CMC/EBC application are being pursued for static hot section components of gas turbines such as combustor liners, shrouds, and nozzles, as well as dynamic components such as turbine blades in the high-pressure regions of the engine [2], [161], [162]. Figure 4-18 displays the hot section of a Rolls-Royce turbofan, alongside expected environmental conditions in gas turbines. Operating conditions for the hot section of gas turbines can vary from 6 to 31 atm of pressure in high pressure turbine outlet and combustor outlet, respectively [163]. Typical material temperatures after combustion can be 1100°C - 1300°C for

commercial applications, depending on both position from the combustor outlet and stage of flight (take-off, cruise) [21], [163]. Turbine gas temperatures of turbines for Army applications routinely operate above 1400 °C with ongoing efforts to approach 1800 °C through additional support of component cooling channels and optimized CMC/EBC materials [162]. Fuel combustion results in approximately 10% partial pressure of H₂O (g) as a gaseous byproduct in the compressor region under high pressure, which translates to 0.6-3.1 atm of H₂O (g) [7], [21]. Gas velocities for a Model 501-K turbine (Rolls-Royce, Indianapolis, IN) have been measured to be 160 m/s-575 m/s from vane mid-span to the vane exit [21]. The gas velocity has also been calculated for a CFM56 turbine (CFM International, France) to range from 100-668 m/s, depending on distance from the combustor outlet [163].



Material Temperature, °C	Combustor Total Pressure, atm	Gas Velocity, m/s	P(H ₂ O) Partial Pressure, atm
1100-1400 [21], [162], [163]	6-31 [163]	100-668 [21], [163]	0.6-3.1 [21]

Figure 4-18. Rolls-Royce Inc. Turbofan [164] and general industrial gas turbine environmental conditions.

Turbine conditions are further exacerbated during take-off and landing, where rapid temperature and pressures changes are placed on components. An expectation with increasing fuel burn temperatures for next generation gas turbines involves further adaptations in pressure and gas velocity values. Therefore, EBCs must withstand extreme temperatures, pressures, gas chemistries, and gas velocities through multiple thermal cycles to support CMC components.

EBCs are applied to CMCs through air plasma spray (APS) process, where pre-reacted powder granule feedstock is ejected from a plasma onto the CMC/bond coat. EBC candidates are traditionally silicate materials for chemical compatibility with SiC and SiO₂. The high velocities of the APS process induce a splat-like EBC microstructure along with cracks and porosity. The EBC is deposited as a partially amorphous layer that is non-stoichiometric in composition [165]. Loss of SiO₂ from the powder interaction with the plasma results in silica deficient phases present, such as non-stoichiometric Yb₂SiO₅ and Yb₂O₃. An example of the sprayed EBC microstructure is shown for Yb₂Si₂O₇ in Figure 4-19 after annealing at 1200 °C for 2 hours in air [166]. Upon heating, the EBC is crystallized and approaches equilibrium phase composition. EBC candidate materials must be able to withstand the APS process without extensive decomposition and volatilization of components from interaction with the high-temperature plasma.

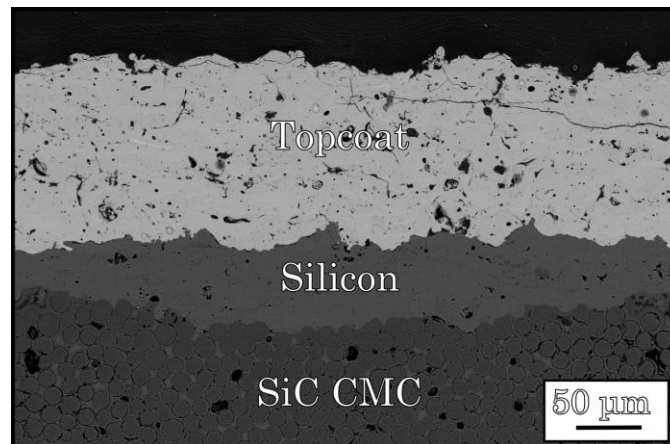


Figure 4-19. APS Yb₂Si₂O₇ topcoat with silicon bond coat on a SiC CMC substrate after annealing for 2h at 1200 °C in air [166].

4.2.3. EBC Failure Modes

Figure 4-20 relates EBC failure modes in service to the resultant phase distribution and microstructure from APS processing. Thermochemical (steam reaction, CMAS infiltration, and

bond coat oxidation) and thermomechanical (thermal stresses, mechanical erosion, and foreign object damage) failure modes are all interconnected with each other as discussed below.

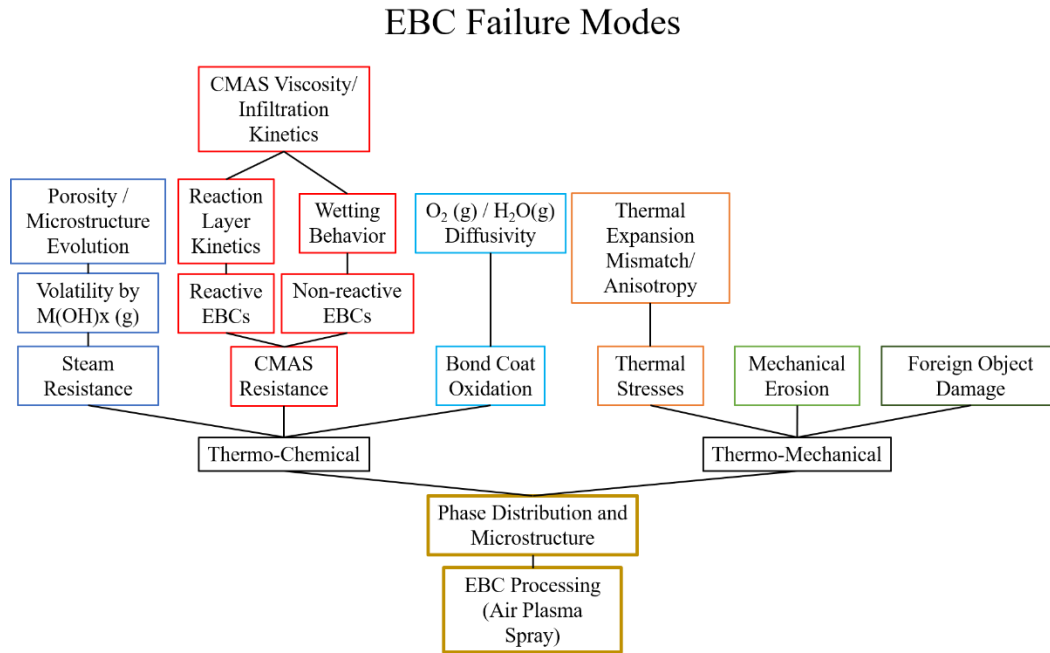


Figure 4-20. EBC failure modes and their respective causations.

4.2.3.1. Steam Resistance

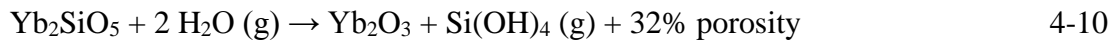
Steam resistance is a vital characteristic of EBCs due to the known volatility of SiO_2 , a thermally grown oxide (TGO) on SiC in a turbine environment. SiC is known to react with steam to concurrently produce SiO_2 and a volatile silicon hydroxide gas species [7]. The volatilization of SiO_2 in steam leads to recession of the SiC. The primary role of EBCs is to provide additional steam resistance to enable CMC technology. Calculated partial pressures of volatile gas species for simple oxides are provided in Table 4-3 at 1200 °C. EBC candidates are often complex rare earth silicate compounds such as $\text{Y}_2\text{O}_3 \cdot 2\text{SiO}_2$ ($\text{Y}_2\text{Si}_2\text{O}_7$). Individual constituents of these complex compounds are expected to selectively volatilize at rates related to their constituent oxide volatility. For example, the extremely low hydroxide partial pressure of Y_2O_3 compared to that of SiO_2 implies that $\text{Y}_2\text{Si}_2\text{O}_7$ will show almost exclusively SiO_2 volatilization in a steam

environment, leaving behind a Y₂O₃-rich reaction product. This has been proven experimentally for many silicate EBC candidates [16], [19], [27], [29], [167], [168].

Table 4-3. Partial pressures of metal hydroxide species (atm) at 1200 °C with P(H₂O)=1. * Estimated metal hydroxide partial pressures.

Material	Reaction	P(Hydroxide) at 1200 °C, atm
BaO	BaO+H ₂ O(g)→Ba(OH) ₂ (g)	8x10 ⁻⁴ [13]
SiO ₂	SiO ₂ +2H ₂ O(g) →Si(OH) ₄ (g)	4x10 ⁻⁶ [13]
Al ₂ O ₃	0.5Al ₂ O ₃ (c)+1.5H ₂ O(g) →Al(OH) ₃ (g)	1x10 ⁻⁷ [13]
TiO ₂	TiO ₂ +H ₂ O(g) →TiO(OH) ₂ (g)	8x10 ⁻⁹ [169]
ZrO ₂	ZrO ₂ (c)+2H ₂ O(g) →Zr(OH) ₄ (g)	8x10 ⁻⁹ [170] *
Y ₂ O ₃	0.5Y ₂ O ₃ (c)+1.5H ₂ O(g) →Y(OH) ₃ (g)	1x10 ⁻⁹ [170] *

EBC candidates thus should produce a reaction layer upon reaction with steam that is rich in an oxide that has very low volatility in a steam environment. State-of-the-art EBC Yb₂Si₂O₇ has been shown to undergo the following subsequent reactions in high-velocity steam:



where Yb₂O₃ is stable in steam [29]. Production of a porous product layer slows H₂O (g) transport to the EBC and leads to parabolic reaction kinetics, where the rate of volatilization decreases with increasing exposure time. A cross-section SEM image of Yb₂Si₂O₇ is shown in Figure 4-21 after exposure to 1 atm, 190-210 m/s steam for 250 hours at 1400 °C [29]. This image demonstrates the formation of reaction products Yb₂SiO₅ and Yb₂O₃ and associated porosity after exposure. Beneficial densification of the Yb₂SiO₅ microstructure further limited H₂O (g) reactant transport to the Yb₂Si₂O₇ interface, resulting in parabolic reaction kinetics.

Through-cracking of the Yb_2SiO_5 reaction layer was indicative of the high thermal expansion anisotropy of Yb_2SiO_5 , highlighting the interconnected relationship between thermochemical and thermochemical response.

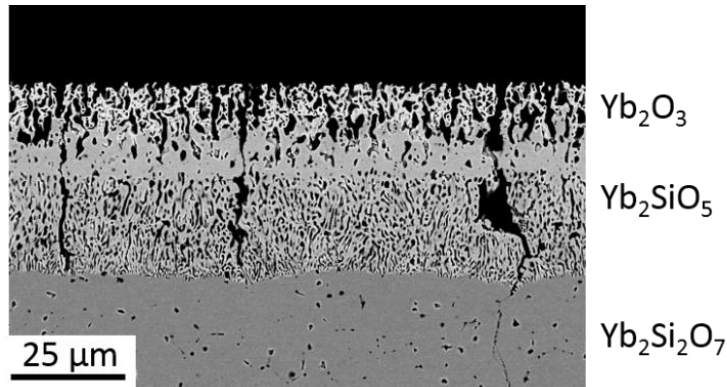


Figure 4-21. Backscattered electron SEM cross section of bulk $\text{Yb}_2\text{Si}_2\text{O}_7$ after a 1400 °C exposure to 1 atm $\text{H}_2\text{O}(\text{g})$ at 190-210 m/s for 250 hours, adapted from [29].

4.2.3.2. Oxidant Diffusion/Silicon Bond Coat Oxidation Resistance

Oxidation of the silicon bond coat produces an amorphous SiO_2 film at the EBC/silicon interface. The formation of a thermally grown oxide (TGO) can cause new thermal stresses upon cycling. If devitrified during service, SiO_2 can undergo phase transitions with subsequent volume changes, further damaging the EBC-bond coat interface. EBC candidates should have low oxygen and water vapor diffusivity, where an industry limit has been proposed at a maximum oxygen diffusion coefficient of $1 \times 10^{-11} \text{ cm}^2/\text{s}$ [171]. However, the oxidant can also quickly reach the bond coat through microstructural defects, such as porosity or cracks, resulting from either the APS process, cracks formed from the thermal stress release upon engine cycling, or from the porosity created through the EBC-steam reaction processes.

Utilization of $^{18}\text{O}_2$ (g) for oxygen exchange studies is commonly used for determination of diffusion coefficients of high-temperature materials [172]–[174]. Oxygen self-diffusion in bulk materials is lower than that of APS coatings and of materials in service, due to starting

microstructural defects, induced thermal stress cracking, production of porosity upon EBC reaction with steam, and oxidant chemical potential gradients present in service. To the author's knowledge, no reliable published data are known for oxygen transport rates through EBCs. In addition, high water vapor pressure in industrial gas turbines implies that oxidant transport to the interface may be governed by water vapor. Wada et al. have shown that oxidant transport through phase pure $\text{Yb}_2\text{Si}_2\text{O}_7$ is increased in a water vapor environment compared to a dry oxygen environment [175]. Zircon (ZrSiO_4) at 1100 °C has shown an ^{18}O (g) diffusivity of $1.2 \times 10^{-17} \text{ cm}^2/\text{s}$ at 1 atm total pressure, compared to an H_2^{18}O (g) diffusivity of $5.6 \times 10^{-16} \text{ cm}^2/\text{s}$ at 69 atm total pressure [31], although the pressure differences between testing prevents a direct comparison between water vapor and oxygen diffusion in zircon. To the author's knowledge, no water vapor diffusion studies in APS materials have been published to date.

4.2.3.3. CMAS Resistance

Siliceous debris can be ingested to the engine during use as small particulate, sand, dirt, or ash and melted within the turbine. Due to the natural variability of ingested debris across the world, $\text{CaO-MgO-Al}_2\text{O}_3\text{-SiO}_2$ (CMAS) molten glass can show a wide range of compositional variance in its primary components as well as in additional oxide constituents (Fe_2O_3 , TiO_2 , Na_2O , K_2O), leading to unique properties of the glass [9], [176], [177]. Current safe gas turbine operating conditions are established at a concentration of ingested CMAS debris $\leq 0.002 \text{ g/m}^3$, which is considered below a visible concentration [178]. A CMAS loading estimate for coated hot section components is determined from typical CMAS ingestion in the engine core in Dubai to be $< 1 \text{ mg/cm}^2$ [179], [180], yet most commonly, experimental methods utilize an excessively high CMAS loading in the range of 10–40 mg/cm^2 to study the CMAS reaction process, crystallization behavior, and infiltration kinetics [126], [146], [151], [176], [181], [182]. With

increasing engine operating temperatures, CMAS viscosity will decrease and reactivity will increase, such that CMAS degradation could become more prevalent in the future as a primary EBC failure mode.

CMAS mitigation strategies are proposed in which EBCs are either reactive or unreactive with CMAS. The unreactive EBC approach relies on surface tension, similar to hydrophobicity, to limit CMAS reaction, repel molten CMAS from coating adherence, and keep the CMAS in the gas stream [183]. Reactive EBCs represent the more common mitigation approach. The EBC outer layer becomes a sacrificial coating that promotes rapid formation of a CMAS reaction layer at the surface to produce a barrier for further CMAS ingress [148], [151], [184].

SEM cross-sections of $\text{Yb}_2\text{Si}_2\text{O}_7$ with 20 volume % Yb_2SiO_5 to model air plasma spray microstructures by Webster and Opila [185] and novel EBC candidate YbPO_4 [181] are presented in Figure 4-22 and Figure 4-23, respectively, after exposure to $\sim 40 \text{ mg/cm}^2$ of 33CaO-9MgO-13AlO_{1.5}-45SiO₂ composition CMAS for 96 hours at 1300 °C. The mixed phase $\text{Yb}_2\text{Si}_2\text{O}_7/\text{Yb}_2\text{SiO}_5$ reacted with CMAS to produce a semi-dense apatite reaction layer that limited CMAS penetration compared to phase pure $\text{Yb}_2\text{Si}_2\text{O}_7$ under the same conditions. An average CMAS infiltration depth was determined to be $\sim 360 \mu\text{m}$ after 96 hours, with preferential CMAS reaction with Yb_2SiO_5 “splats” to form apatite within the bulk of the material. Excessive infiltration of CMAS in $\text{Yb}_2\text{Si}_2\text{O}_7$ produces dilatation gradients, resulting in blister cracking and porosity production [184], although the presence of the secondary Yb_2SiO_5 phase was found to limit the presence of blister cracking in $\text{Yb}_2\text{Si}_2\text{O}_7$. The YbPO_4 EBC candidate under the same conditions readily formed a dense $\text{Ca}_8\text{MgYb}(\text{PO}_4)_7$ rhombohedral structure that effectively halted further CMAS infiltration, which can be seen by the large amount of residual glass left over on the YbPO_4 surface. The competing kinetics of CMAS infiltration versus CMAS/EBC

reaction rate has a clear connection to the ratio of CaO to SiO₂ in the CMAS melt [185]–[187]. As stated earlier, the high CMAS loading used for both experiments is not expected to be seen for EBC components in service. The CMAS composition, loading rate, viscosity, and exposure temperature are thus vital parameters for determining stability of EBCs against molten CMAS attack.

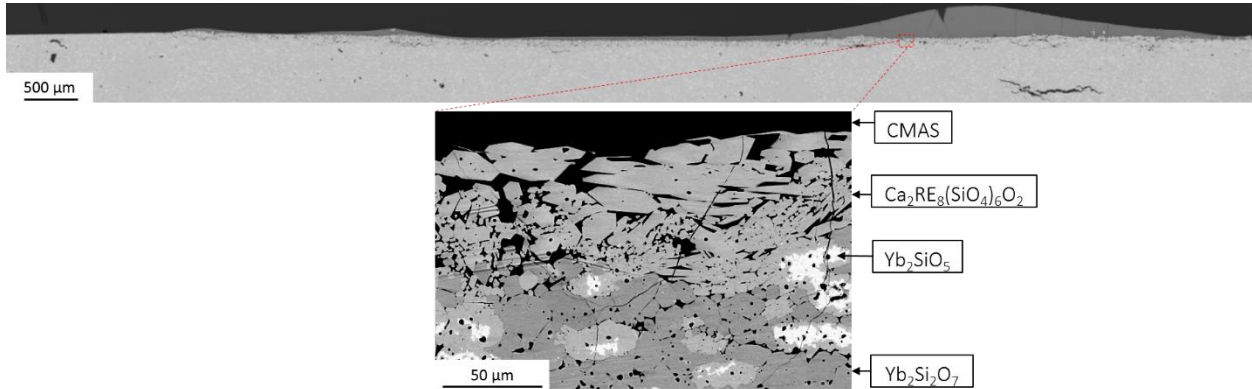


Figure 4-22. Mixed phase Yb₂Si₂O₇ with 20 volume % Yb₂SiO₅ “splat” like microstructure after exposure to ~40 mg/cm² of 33CaO-9MgO-13AlO_{1.5}-45SiO₂ composition CMAS for 96 hours at 1300 °C, adapted from [185].

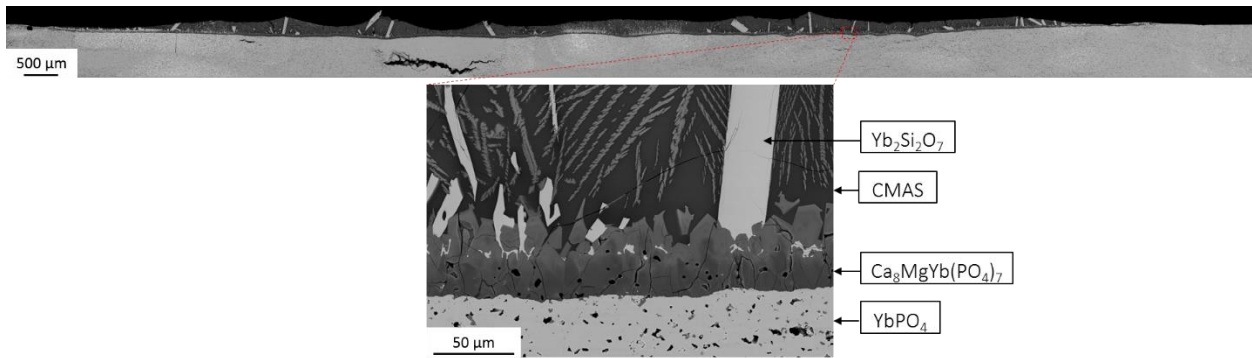


Figure 4-23. Phase-pure YbPO₄ after exposure to ~40 mg/cm² of 33CaO-9MgO-13AlO_{1.5}-45SiO₂ composition CMAS for 96 hours at 1300 °C, adapted from [181].

4.2.3.4. Thermal Stresses

Coefficient of thermal expansion (CTE) mismatch between the SiC CMC, silicon bond coat, thermally grown SiO₂, and the EBC can lead to stress buildup upon thermal cycling, inducing interfacial cracking and eventually material spallation. The CTEs of SiC, silicon, and thermally grown amorphous SiO₂ are 4.5-5.5x10⁻⁶ /°C [3], 3.5-4.5x10⁻⁶ /°C [32], and 0.5x10⁻⁶

$^{\circ}\text{C}$ [188], respectively. Therefore, EBC candidates require a CTE in the general range of $3.5\text{-}6.5 \times 10^{-6} / ^{\circ}\text{C}$ to minimize stress buildup at the EBC/silicon interface. Minimization of CTE mismatch between the layers is also directly correlated to the thermally grown oxide (TGO) growth rate and hence the oxidant permeability of the EBC. Additionally, the presence of polymorphs is detrimental to coating lifetimes in terms of thermal stresses. Figure 4-24 displays the polymorph transitions for the rare earth silicates, $\text{RE}_2\text{Si}_2\text{O}_7$ (RE = Sc, Y, La-Lu). It can be seen that for $\text{RE}_2\text{Si}_2\text{O}_7$ (RE = Y, La-Er), polymorph transitions are found in the temperature ranges of interest. Each polymorph change has an associated volume change leading to material cracking, in addition to each polymorph having unique thermal properties such as thermal expansion coefficients. Only $\text{RE}_2\text{Si}_2\text{O}_7$ (RE = Sc, Tm, Yb, Lu) are stable as the low CTE β -phase with no polymorph transitions.

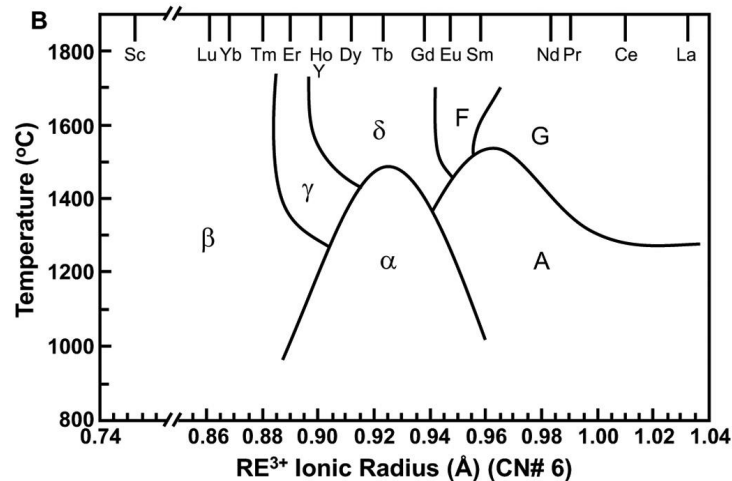


Figure 4-24. Phase stability of $\text{RE}_2\text{Si}_2\text{O}_7$ relative to rare earth ionic radius [105].

The thermal expansion anisotropy of EBCs should be considered, as coatings with highly anisotropic CTE will likely experience accelerated failure through microcracking. Figure 4-21 displays the Yb_2SiO_5 steam reaction product, which contains a high degree of CTE anisotropy. In the figure, Yb_2SiO_5 experienced stress cracking down to the $\text{Yb}_2\text{Si}_2\text{O}_7$ substrate even with the added compliance from surrounding porosity [29]. Microcracking upon thermal cycling

represents yet another pathway for steam transport, oxidant transport, and CMAS infiltration towards the CMC.

4.2.3.5. Mechanical Erosion and Foreign Object Damage

Reaction products from both steam and CMAS interactions with EBCs can be present at the gas/EBC interface with increased porosity and cracking relative to the bulk EBC. Mechanical erosion of the EBC reaction layer(s) can result from the turbine environment after a loss of structural integrity as surface pore formation and cracking occurs. Mechanical erosion was evident with HfSiO_4 (Figure 4-25) during exposure to high velocity steam for 250 hours at 1400 °C, where the erosion depth of the highly porous HfO_2 steam reaction product (~625 μm) exceeded that of typical EBC thicknesses in service (100-300 μm) at the 200-240 m/s velocity range [167]. In this process, the total thickness of the EBC is decreased over time, and unreacted EBC material is continually exposed to the turbine environment for further reaction or erosion. Foreign object damage produces a similar result for the EBC, although the damage arises not from a loss of structural integrity of the EBC, but from particulate impact ingested into the turbine [189].

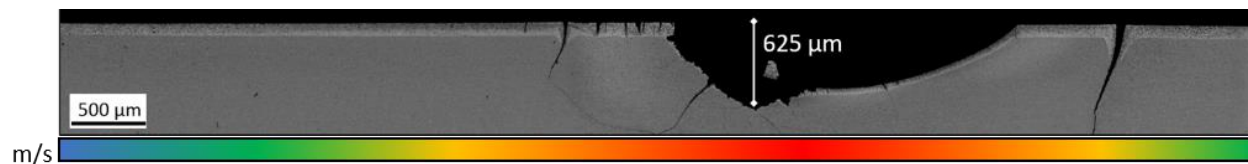


Figure 4-25. Backscattered electron SEM cross section of bulk HfSiO_4 after a 1400 °C exposure to 1 atm $\text{H}_2\text{O}(\text{g})$ for 250 hours. Excessive stress cracking and mechanical erosion of ~625 μm was measured at the impingement site (200-240 m/s water vapor velocity). Adapted from [167].

4.2.4. Results

A figure of merit (FOM) is developed utilizing the known failure modes of EBCs and the parameters in Table 4-4, which describe the phase stability, steam reactivity, CMAS reactivity,

oxidation character, and thermal stresses induced for various past, present, and novel EBC material candidates. Here, smaller values of FOM represent better EBC candidates. SiO₂ is presented as the baseline material, as SiO₂ is the thermally grown oxide for both SiC and silicon without a protective EBC. Other materials for comparison include EBC candidates Ba_{0.75}Sr_{0.25}Al₂Si₂O₈ (BSAS), HfSiO₄ (hafnon), Yb₂O₃, Yb₂SiO₅, state-of-the-art EBC Yb₂Si₂O₇, and novel EBC candidate YbPO₄.

Experimental and computational data were used to best fill in each material property in the table. Due to the novelty of EBC materials research, many material properties listed are not yet available. Detailed explanation of provided data, data manipulation, and approximations are represented by superscript letters in the text and are discussed in Appendix 8.6. For each failure mode category, a conditional value has been established as a method for appropriately differentiating between a successful (value = 0) and unsuccessful (value = 1) EBC candidate. For example, the presence of polymorphs is undesirable in the temperature range of interest to gas turbines, as polymorph transitions include volume changes that induce material cracking. The conditional statement for *Phase Stability* assigns a value of 1 to crystalline SiO₂, which shows unfavorable polymorphs (cristobalite) in the temperature range of interest. All other materials were assigned a value of 0, as they do not show unfavorable phase changes. In terms of *Thermal Stresses*, EBC CTEs with a value > 25% difference from the CTE of SiC (5x10⁻⁶ /°C) are assigned a conditional binary value of 1 to demonstrate that the value of this property is unacceptable for a successful EBC candidate.

Sub categories for *Phase Stability*, material melting temperature and nearby eutectic temperatures, are referenced from pseudo-binary phase diagrams for each respective material. A

conditional statement was placed to determine if a material has polymorphs in the temperature range of interest.

Steam Reactivity has been represented by three sub-categories. First, through the activity of the volatile component metal oxide species, such as the silica activity for silicate EBC candidates. Additionally, the amount of porosity produced upon steam reaction has been determined from known high-velocity water vapor chemical reactions. The steam reaction product melting temperature was also used to represent each steam product phase stability.

CMAS Reactivity has been represented by the changes in CMAS viscosity upon reaction as a simple metric for both CMAS infiltration rates and EBC/CMAS reaction rates. A starting SiO₂/CaO ratio of 45/33 was used, based on a common CMAS composition used in literature studies. A conditional statement was used to favor EBCs that produce a protective reaction layer to prevent further CMAS ingress.

EBC Diffusivity and resulting *Silicon Bond Coat Oxidation* was represented by the bulk EBC oxygen diffusion coefficients at 1400 °C in addition to a conditional statement based on the maximum diffusion coefficient standard already described [171]. Values of $-\log_{10}(D_{\text{Bulk}})$ were used as the input into the figure of merit so that all data can be compared without spanning multiple orders of magnitude.

The *Thermal Stresses* represent thermo-mechanical behavior of EBCs and includes the CTE, CTE anisotropy of the EBC, and the CTE of the steam reaction product. A final conditional statement was used to ensure EBCs have minimal CTE mismatch with SiC.

Table 4-4. Thermo-chemical and thermo-mechanical properties of selected high-temperature EBC materials. Conditional binary values are denoted with *. Footnotes a-m are provided in Appendix 8.6.

Thermo-chemical	SiO ₂	Yb ₂ O ₃	Yb ₂ SiO ₅	Yb ₂ Si ₂ O ₇	BSAS	HfSiO ₄	YbPO ₄
<u>Phase Stability</u>							
Melting point of EBC, °C	1723 [190]	2250 [112]	1950 [112]	1850 [112]	1680 [191]	1770 [36]	1896 ^a [140]
* More than one stable phase? Yes = 1, No = 0	1	0	0	0	0	0	0
Nearby eutectic temperature, °C	1723 [190]	1850 [112]	1850 [112]	1650 [112]	1300 [12]	1650 [36]	1450 ^b [192]
<u>Steam Reactivity</u>							
Oxide activity in H ₂ O (g), a(MO _x)	1 [7]	0 ^c [27]	0.003 ^d [51]	0.2 ^e [51]	1 ^f [193]	0.55 [194]	0.2 ^g [181]
Volume loss upon H ₂ O (g) reaction, %	100 [27]	0 [27]	32 [29]	24 [29]	100 [193]	45 [167]	44 [181]
Melting point of H ₂ O (g) reaction product	1723 [190]	2250 [112]	2250 [112]	1850 [112]	1680 [191]	2758 [36]	2250 [112]
* High-velocity H ₂ O (g) reaction kinetics, linear = 1, parabolic = 0	1 [27]	0 ^c [27]	0 [29]	0 [29]	1 [193]	0 [167]	0 [181]
<u>CMAS Reactivity</u>							
SiO ₂ /CaO ratio changes upon CMAS reaction	0.030 ^h	-0.106 ^h	0.023 ^h	0.152 ^h	0.061 ^h	0.030 ^h	0.436 ^h
* Formation of a protective reaction layer, Yes = 0, No = 1	1	0 [195], [196]	0 [151]	0 [151]	1 [197]	1 [198]	0 [181]
<u>Bond Coat Oxidation</u>							
O ₂ (g) Self diffusion D _{Bulk} in EBC, 1400 °C, cm ² /s	2.3x10 ⁻¹⁰ [199]	8.0x10 ⁻¹² ⁱ [200]	8.3x10 ⁻¹⁴ [172]	1.3x10 ⁻¹⁴ [173]	4.7x10 ⁻¹⁵ ^j [171]	1.3x10 ⁻¹⁴ ^k [31]	1.3x10 ⁻¹⁴ ^k [31]

* EBC requirement that $D_{Bulk} < 1 \times 10^{-11} \text{ cm}^2/\text{s}$, Yes = 0, No = 1	0	0	0	0	0	0	0
Thermo-mechanical	SiO₂	Yb₂O₃	Yb₂SiO₅	Yb₂Si₂O₇	BSAS	HfSiO₄	YbPO₄
<i>Thermal stresses</i>							
Linear CTE $\times 10^{-6} / ^\circ\text{C}$	0.5 ^l [188]	8.4 [49]	7.25 [35]	4.5 [50]	5.3 [201]	4 [136]	6 [181]
CTE anisotropy, max-min CTE axes, $\times 10^{-6} / ^\circ\text{C}$	0	0 [49]	8.1 [35]	2.5 [50]	2.6 ^m [202]	3 [136]	1.9 [181]
CTE of steam reaction product, $\times 10^{-6} / ^\circ\text{C}$	0.5 ^l [188]	8.4 [49]	8.4 [49]	7.25 [35]	5.3 [201]	6.1 [203]	8.4 [49]
* Is linear CTE of EBC within 25% of SiC ($4.5\text{-}5.5 \times 10^{-6} / ^\circ\text{C}$), Yes = 0, No = 1	1	1	1	0	0	0	0

Raw material property data from Table 4-4 were normalized between 0 and 1 for each sub category. Each material property was scaled so that 0 and 1 represented the most desired and least desired material property value, respectively. These normalized values can be summed together for each material to receive a figure of merit (FoM) score for each material, shown in Table 4-5, where a smaller score represents a better EBC material candidate. It was seen that state-of-the-art EBC material Yb₂Si₂O₇ and novel EBC candidate YbPO₄ displayed the smallest FoM scores, which implies that Yb₂Si₂O₇ and YbPO₄ are the optimum EBC candidates from the materials used in this study. Contrarily, SiO₂, which is representative of the SiC thermally grown oxide without an EBC, displayed the highest FoM score; the least desirable EBC material candidate.

Table 4-5. Figure of Merit score for each material, determined from summation of Table 4-4 after normalization of each sub category with values from 0 to 1. Smaller FoM scores represent the most desirable EBC material candidate.

Figure of Merit Score						
SiO ₂	Yb ₂ O ₃	Yb ₂ SiO ₅	Yb ₂ Si ₂ O ₇	BSAS	HfSiO ₄	YbPO ₄
7.99	6.47	6.16	3.78	7.62	5.82	3.78

Each normalized subcategory can also be summed to produce numerical values for the categories of *Phase Stability*, *Steam Reactivity*, *CMAS Reactivity*, *Bond Coat Oxidation*, and *Thermal Stresses*. These groupings are plotted in Figure 4-26 as a radar plot. Smaller FoM scores for each leg of the plot represent a more desirable material property for EBC application. Thus, materials that encompass a smaller area of the plot are qualitatively better EBC candidates. It should be noted that the arrangement of properties around the circumference of the radar plot affects the total encompassed area. Thus, the numerical figure of merit is more quantitative, whereas the plot provides easy visual comparison of EBC candidate material properties. For example, Yb₂O₃ displays highly desired phase stability, steam resistance, and CMAS resistance, yet a single layer Yb₂O₃ EBC would be expected to quickly fail through its high thermal stresses and/or through gas transport to the EBC/Silicon bond coat interface for rapid SiO₂ TGO formation. Both Yb₂Si₂O₇ and YbPO₄ encompass the smallest areas on the plot, and thus represent the better EBC candidates of the materials presented here. Each of these properties should then be investigated in more detail, as many are estimates. The radar plot provides a visual representation for the FoM score results in Table 4-4, where EBC candidates can be holistically compared.

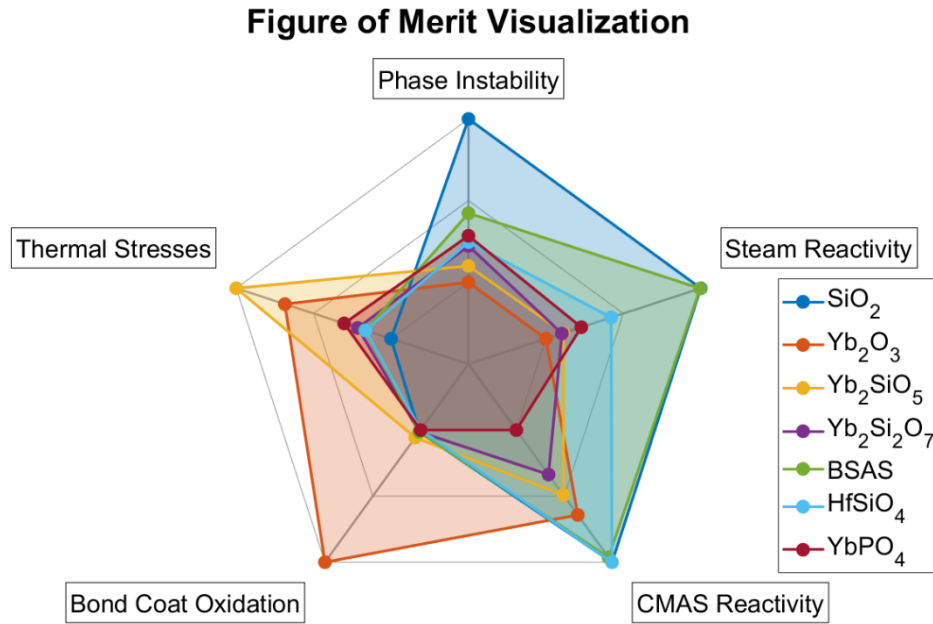


Figure 4-26. Figure of merit visualization for EBC material candidates. Smaller encompassed area on the figure indicates increased overall stability as an EBC material.

4.2.5. Discussion

Candidate materials in this study can be ranked from most desirable to least desirable EBC candidates, based in Table 4-4 and Figure 4-26: $\text{Yb}_2\text{Si}_2\text{O}_7$, YbPO_4 , Yb_2O_3 , HfSiO_4 , Yb_2SiO_5 , BSAS, and SiO_2 . Of the materials used in this work, Yb_2O_3 , HfSiO_4 , Yb_2SiO_5 , BSAS, and SiO_2 are known to be unacceptable single-layer EBC material candidates. The thermal expansion of Yb_2O_3 is far greater than that of SiC [49]. HfSiO_4 exposed to steam results in a highly porous and weakly connected HfO_2 reaction layer that undergoes mechanical erosion at gas velocities relevant to turbine conditions [167]. Yb_2SiO_5 has an unacceptably high CTE anisotropy that leads microcracking upon thermal cycling [35], [204]. BSAS reacts with SiO_2 , the thermally grown oxide, to form a liquid eutectic above 1300 °C and therefore cannot be considered as an EBC due to this maximum use temperature [12]. The use of legacy EBC material candidates in this study, however, provides insight on acceptable material property

values required for current generation EBCs and enables identification of estimated or missing EBC properties which should be studied in detail.

The state-of-the-art EBC $\text{Yb}_2\text{Si}_2\text{O}_7$ was verified through Table 4-4 as the most desirable material candidate. YbPO_4 , a novel EBC material, had the same FoM score as $\text{Yb}_2\text{Si}_2\text{O}_7$, which suggested rare earth orthophosphates (REPO_4) should be further studied as EBC material candidates. Still, five of the 15 data inputs for YbPO_4 in Table 4-4 were unknown and were roughly estimated based on similar materials and experimental comparison. Further research is needed to accurately determine the data inputs for YbPO_4 . Particularly, the Yb_2O_3 - P_2O_5 phase diagram with material melting temperatures, the $a(\text{P}_2\text{O}_5)$ value for YbPO_4 , and the oxygen diffusion coefficient in phase pure YbPO_4 need to be determined for accurate ranking of YbPO_4 phase stability, steam reactivity, and oxidation resistance, respectively.

Determination of a figure of merit for EBCs remains a challenge due to the complexity of the EBC failure modes and the lack of available data on high-temperature ceramic materials for comparison. The steam reaction parameter should eventually incorporate kinetic data as well as information on microstructural evolution of the product phase with increasing operating time. CMAS reaction thermodynamics, reaction kinetics, and infiltration kinetics are also needed to further understand and compare EBC materials. EBC diffusivity data, and resulting silicon bond coat oxidation kinetics, are particularly lacking. Furthermore, H_2O (g) diffusion coefficients should be determined for all materials in phase-pure and APS condition, as water vapor partial pressures in turbine environments are 0.6-3.1 atm or greater. It is unknown if O_2 (g) or H_2O (g) represents the primary silicon bond coat oxidant in turbine environments.

Nevertheless, the presented method for material comparison may prove useful for more similar materials, such as comparison of various single component and multi-component rare

earth disilicates ($\text{RE}_2\text{Si}_2\text{O}_7$) to the state-of-the-art $\text{Yb}_2\text{Si}_2\text{O}_7$. Future work most certainly requires computational methods for both determination of material properties as well as prediction of materials that fit specified property requirements of EBCs. Particularly, compositionally complex ceramics and high entropy ceramic materials should be researched to determine the overall impact of tailoring EBC properties through cation substitutions [35]. Additional secondary properties of interest to EBC material performance should also be considered for inclusion in the figure of merit, such as thermal conductivity, modulus, and the processability by APS technique. The stability of YbPO_4 powders during air plasma spray has not been experimentally determined, and the instability of P_2O_5 at elevated temperatures may require novel EBC processing techniques to be utilized. The presented figure of merit shows promise for comparison of other high-temperature materials such as thermal barrier coatings (TBCs) for use on superalloys and for EBCs on novel CMC designs, such as eutectic oxide-based CMCs.

4.2.6. Conclusion

Criteria for development of next generation EBCs were defined and explored. The first figure of merit for environmental barrier coating candidates was presented as a method for holistic comparison of materials against significant failure modes experienced by coatings in service. Available data for legacy, present, and novel EBC candidates were utilized to rank material candidates. State-of-the-art $\text{Yb}_2\text{Si}_2\text{O}_7$ was determined to be the most viable EBC, along with a novel and much less studied EBC candidate, YbPO_4 . Many material properties estimated in this work still need to be experimentally measured, yet oxidant diffusivity data for all bulk EBC materials represents a critical research avenue for holistic comparison of EBC candidates. The figure of merit can be used alongside experimental and computational methods to compare

properties of known materials, determine avenues for future EBC research, and predict the stability of complex materials for long term use in combustion environments.

4.3. Summary

YbPO₄, a novel EBC candidate, was explored in terms of thermal expansion behavior, steam resistance, and CMAS resistance. Thermal expansion data validated the minimal mismatch with SiC addressed in the literature. The thermal expansion anisotropy was reported for the first time for YbPO₄. The YbPO₄ tetragonal crystal structure and less rigid P-O bonding in YbPO₄ resulted in decreased thermal expansion anisotropy compared to many rare earth silicates, whose rigid Si-O bonding was discussed in Chapter 3.2.

YbPO₄ was shown to react with steam to form Yb₂O₃, even though comparable RE₂O₃-P₂O₅ phase diagrams suggest that multiple complex RE_xP_yO_z compounds could be stable at temperatures of interest. While the parabolic steam reaction rate for YbPO₄ was measurably lower than that of Yb₂Si₂O₇ presented in Chapter 2.3, the highly porous Yb₂O₃ product phase displayed an unacceptably high rate of mechanical erosion at 1400 °C. The lack of microstructural evolution of the Yb₂O₃ product layer can be explained through the high melting temperature of Yb₂O₃ (2250 °C) and is analogous to the HfSiO₄ system in Chapter 2.2, where the HfO₂ product layer (2758 °C) could not densify to provide structural integrity against mechanical erosion at the highest steam velocities. Increased turbine operating temperatures may support sintering and densification of the Yb₂O₃ product phase through increasing the steam reaction product homologous temperature.

YbPO₄ was shown to outperform state-of-the-art EBC Yb₂Si₂O₇ in terms of CMAS corrosion resistance, and was comparable to the CMAS behavior of Yb₂SiO₅. A tri-layer reaction product limited CMAS infiltration through rapid formation of a dense TCP-type continuous reaction layer, rich in Ca, that was stable in the presence of CMAS. Formation of the continuous reaction layer also resulted in consumption of CaO and MgO from the melt, which increased the

glass viscosity to further limit the penetration of CMAS through cracks, pores, or grain boundaries.

The first EBC figure of merit was presented as a method for comparison of multiple materials against the primary EBC failure modes in service. SiO_2 , BSAS, HfSiO_4 , Yb_2O_3 , Yb_2SiO_5 , $\text{Yb}_2\text{Si}_2\text{O}_7$, and YbPO_4 were compared to verify the figure of merit, as it is well known that $\text{Yb}_2\text{Si}_2\text{O}_7$ outranks the other candidates as the state-of-the-art EBC material. YbPO_4 was placed alongside the other silicate and oxide materials as a novel EBC candidate. The results of the figure of merit indicate that $\text{Yb}_2\text{Si}_2\text{O}_7$ and YbPO_4 are the optimal EBC candidates for the given materials selection. Pertinent data inputs to the figure of merit were not all known. Specifically, oxidant diffusivity in bulk and air plasma sprayed EBC materials has not been studied, and remains a vital research avenue for developing a holistic understanding of EBC stability. Additional categories should also be included to the figure of merit to address other EBC requirements such as processability by air plasma spray, thermomechanical stability, and a material's T/EBC capability through high-temperature thermal conductivity determination. The figure of merit provides guidance on materials processing, laboratory testing, and characterization necessary for accurate comparison of EBC material properties.

5. Final Remarks

The thermochemical stability of environmental barrier coating candidates was explored through high-velocity steam exposures in the temperature range of 1200 °C – 1400 °C. BSAS, HfSiO₄, and Yb₂Si₂O₇ were characterized in terms of microstructural evolution and reaction kinetics. The reaction process for BSAS was determined, where all oxide constituents volatilize at their own respective rates. An unprotective silica-depleted reaction product was seen for temperatures below 1300 °C, while at 1400 °C no solid reaction products were present on the surface. Even though initial materials characterization and stagnant water vapor testing in the literature implied that HfSiO₄ would be an excellent EBC candidate, this work displayed unacceptable amounts of mechanical erosion of the HfO₂ reaction product that inhibits the use of HfSiO₄ as an EBC in high-velocity environments. For the first time, state-of-the-art EBC Yb₂Si₂O₇ was characterized under high-velocity steam to display beneficial microstructural evolution of the Yb₂SiO₅ reaction product, where densification of the outer Yb₂SiO₅ layer occurred at 1300 °C and 1400 °C. Densification of the Yb₂SiO₅ product layer resulted in decreased reaction kinetics at the highest steam velocities by closure of the pore network and prevention of steam transport to the Yb₂Si₂O₇ interface.

Parabolic reaction kinetics were displayed for HfSiO₄ and Yb₂Si₂O₇, which is more desirable than the linear reaction kinetics of BSAS due to the thousands of hours required for EBC operation in service. The reaction rates for 1200 °C, 1300 °C, and 1400 °C were used to calculate the first temperature dependences for each steam reaction. The reaction enthalpy for BSAS agrees well with an estimated reaction enthalpy from thermodynamic data for volatilization of each oxide constituent. The quantitative nature of the steamjet was verified through (0001) plane sapphire steam testing, although reaction enthalpies for HfSiO₄, Yb₂Si₂O₇,

and Yb_2SiO_5 were much higher than the predicted value from volatilization of pure SiO_2 . It is proposed that complex compounds which react with steam to form a porous product layer do not have the same reaction enthalpies as their individual volatile component species, although this remains a point for further research.

Fundamental relationships between rare earth elements and respective rare earth silicate material properties were determined for pertinent properties such as thermal expansion, phase stability, steam resistance, thermal conductivity, and Young's Modulus. A rule of mixtures relation was determined for thermal expansion and Young's Modulus, meaning that these properties could be accurately predicted for novel materials before being experimentally measured. Trends with ionic radius and bond strength were also presented for tailoring CTE and modulus. The thermal conductivity of multi-component rare earth silicates can easily be tailored below a rule of mixtures through increasing lattice disorder, such that rare earth silicate EBCs are multi-functional T/EBC material systems.

Steam exposures of single cation and multi rare earth cation silicates did not all display the same reaction products or reaction rates after exposure to high-velocity steam, as previously believed. $\text{Sc}_2\text{Si}_2\text{O}_7$ exposed to high velocity steam highlighted the instability of Sc_2SiO_5 , where previously it was believed that all RE_2SiO_5 had excellent stability in steam. $\text{Nd}_2\text{Si}_2\text{O}_7$ did not form the expected Nd_2SiO_5 product phase but extensively reacted with steam to produce a highly porous apatite phase, $\text{Nd}_{9.33}\square_{0.67}\text{Si}_6\text{O}_{26}$. High-velocity steam exposure of a two-phase $(\text{Sc,Nd,Er,Yb,Lu})_2\text{Si}_2\text{O}_7$ displayed comparable reaction kinetics to other $\beta\text{-RE}_2\text{Si}_2\text{O}_7$, with production of a single phase $(\text{Sc,Nd,Er,Yb,Lu})_2\text{SiO}_5$ reaction product. Minor additions of both Sc and Nd to the mixture did not result in rapid formation of Sc_2O_3 or $\text{Nd}_{9.33}\square_{0.67}\text{Si}_6\text{O}_{26}$, as was seen with phase pure $\text{Sc}_2\text{Si}_2\text{O}_7$ and $\text{Nd}_2\text{Si}_2\text{O}_7$, respectively. EBC homologous temperature was

related to the average reaction depth for silicate EBCs, where a higher homologous temperature corresponded to increased steam reactivity.

A novel EBC candidate, YbPO_4 , was analyzed in terms of thermomechanical stability through linear CTE and CTE anisotropy measurements, high-velocity steam resistance, and CMAS resistance. Despite the extreme instability of P_2O_5 , YbPO_4 displayed enhanced steam resistance and CMAS resistance compared to state-of-the-art EBC material $\text{Yb}_2\text{Si}_2\text{O}_7$.

The first figure of merit was developed for a holistic comparison of EBC materials based on the substantial failure modes that EBCs can experience in service: water vapor reaction, CMAS reaction, oxidant transport through the EBC and subsequent bond coat oxidation, thermomechanical fatigue, mechanical erosion, and foreign object damage. Novel EBC candidate YbPO_4 was compared against past and present high-temperature EBC candidates, where $\text{Yb}_2\text{Si}_2\text{O}_7$ and YbPO_4 were determined to be the most optimal EBC candidates. Through analysis of the figure of merit, a clear lack of oxidant diffusivity data for all EBC candidates was observed. The figure of merit can guide the EBC community towards relevant processing, characterization, and laboratory testing of materials necessary for accurate comparison of next generation EBCs to the current state-of-the-art candidates.

Together, these studies provide new insight to the degradation mechanisms of EBCs and provide novel strategies for tailoring properties of next-generation EBCs.

6. Future Work

6.1. Objective 1

The ANSYS model should be updated to include water vapor partial pressure mapping in addition to the steam velocity mapping that was utilized throughout this work.

A quantitative study of $\text{SrAl}_2\text{Si}_2\text{O}_8$ (SAS) in the steamjet should be performed to improve understanding of BSAS reactivity in steam, as thermodynamic data are available for SAS in the FactSage thermodynamic database. The reaction enthalpies determined for HfSiO_4 and $\text{Yb}_2\text{Si}_2\text{O}_7$ were much higher than the expected reaction enthalpy for pure SiO_2 , and therefore further study is needed to determine the rate limiting mechanism for silica depletion.

Additional high-velocity steam testing of various metal oxides should be performed to verify the expected reaction enthalpies and confirm the quantitative abilities of the steamjet. Ga_2O_3 represents an oxide of interest for steamjet temperature analysis due to its uniquely high reaction enthalpy compared to most oxides found in the literature (499.61 kJ/mol, indirectly calculated via transpiration method [205]), high melting temperature (1725 °C), slow reaction kinetics with Al_2O_3 to form complex compounds [205], and limited polymorph changes in the temperatures of interest.

Additionally, high-velocity steam analysis of rare earth oxides should be pursued, such as Yb_2O_3 , as RE_2O_3 have been predicted to volatilize in steam to form $\text{RE}(\text{OH})_3$ (g) species [206], [207] with an estimated temperature dependence of 290.24 kJ/mol for $\text{Y}(\text{OH})_3$ (g) formation [13]. Volatilization of RE_2O_3 was not seen as part of this work with single rare earth and multi-component rare earth silicates, suggesting the reaction is negligible compared to SiO_2 volatilization. Thus, longer steam exposure times and increased exposure temperatures for Yb_2O_3 in steam may be needed to display hydroxide volatilization. Parker and Opila showed how high-

velocity steam reactions for Y_2O_3 resulted in rapid reactions with Al_2O_3 furnace ware and trace SiO_2 to form yttrium aluminates and silicates on sample regions outside of the highest steam velocities [27]. Future steam testing of Yb_2O_3 would require that the upstream sample edges are wrapped in platinum foil to prevent direct sample contamination from furnace ware such that a reliable baseline sample height could be determined during sample analysis. Determination of the temperature dependence for $\text{Yb}(\text{OH})_3$ (g) formation should provide insight to the unexpected temperature dependences determined in this work for $\text{Yb}_2\text{Si}_2\text{O}_7$.

6.2. Objective 2

It is unknown if the increased steam reactivity of Sc_2SiO_5 is representative of other RE_2SiO_5 or if it is only related to the scandium rare earth cation. Future work should investigate the changes in steam reactivity for an equimolar RE_2SiO_5 with both $\text{RE} = \text{Sc}, \text{Yb}$ to determine trends in steam reactivity and to optimize rare earth monosilicate stability for use in combustion environments.

The thermodynamic stability of all single cation $\text{RE}_2\text{Si}_2\text{O}_7$ is needed for each polymorph to more accurately predict the stable phases that would be produced for multi-component $\text{RE}_2\text{Si}_2\text{O}_7$ materials. Specifically, a lack of thermodynamic data limits the ability to determine effects of entropic and enthalpic stabilization of $\text{RE}_2\text{Si}_2\text{O}_7$ polymorphs for multi-component and high entropy solid solutions. Additionally, thermal, mechanical, and chemical properties of single cation $\text{RE}_2\text{Si}_2\text{O}_7$ are needed for all polymorphs for determination of a rule of mixtures, especially when multi-component $\text{RE}_2\text{Si}_2\text{O}_7$ result in stabilized crystal structures that would traditionally be unfavorable.

Binary mixtures of $(\text{RE}_1, \text{RE}_2)_2\text{Si}_2\text{O}_7$ have been shown to display depressed melting temperatures compared to their constituent disilicate line compounds. Melting temperatures of

optimized multi-component $\text{RE}_2\text{Si}_2\text{O}_7$ and RE_2SiO_5 systems should be explored in future research to improve understanding of the high-temperature stability of multi-component rare earth silicates as EBC candidates. The ability for high entropy mixtures to increase the solution melting point relative to the individual constituents remains an important question for further research.

$\text{Nd}_2\text{Si}_2\text{O}_7$ displayed a large volume increase upon steam reaction, while the expected reaction given in Equation 3-3 predicted a volume change of -15%. The steam reaction for $\text{Nd}_2\text{Si}_2\text{O}_7$ should be studied for an initially denser sample with additional variation in time and exposure temperature to determine formation onset of $\text{Nd}_{9.33}\square_{0.67}\text{Si}_6\text{O}_{26}$, Nd_2SiO_5 , and Nd_2O_3 . The apatite phase also formed on single crystal $\delta\text{-Y}_2\text{Si}_2\text{O}_7$ as $\text{Y}_{9.33}\square_{0.67}\text{Si}_6\text{O}_{26}$. Additional study should include analysis of the requirements for formation of the rare earth apatite phases in steam environments, as well as the stability of the apatite phase in the 1200 °C-1500 °C temperature range. Testing of $\text{Lu}_2\text{Si}_2\text{O}_7$ should be explored with variation in exposure time and temperature, as $\text{Lu}_2\text{Si}_2\text{O}_7$ displayed the lowest average reaction depth for all rare earth disilicate samples. The reaction enthalpy should be determined for $\text{Lu}_2\text{Si}_2\text{O}_7$ as a comparison to the high reaction enthalpy that was determined for $\text{Yb}_2\text{Si}_2\text{O}_7$ through this work.

Future work should investigate phase stabilization of various rare earth crystal structures through multi-component rare earth silicate mixtures as another means to deviate from a rule of mixtures for EBC material properties. Traditionally, β phase $\text{RE}_2\text{Si}_2\text{O}_7$, the stable phase for the smaller rare earth elements, are pursued for EBCs due to the lack of polymorph transitions in addition to the low CTE associated with this phase. Stabilization of other low CTE phases, such as the γ - or G- $\text{RE}_2\text{Si}_2\text{O}_7$ high temperature polymorphs (γ -: RE = Y, Ho and G-: RE=Nd, Pr, La), would increase the materials options for next generation EBCs through incorporation of

increasingly larger rare earth cations. New cation additions should not be limited to rare earth elements. Additions of cation elements into solution with differing charge from the +3 rare earth cation is expected to impact bond strength and bonding heterogeneity, thus allowing for further tailoring of thermal expansion, Young's Modulus, and thermal conductivity.

6.3. Objective 3

Analysis of YbPO_4 stability against steam and CMAS attack showed promise for rare earth phosphates as EBC material candidates. The volatilization reaction for YbPO_4 is still unknown, and the P-O-H gas product species forming for the steam reaction needs to be investigated. Future work should include time and temperature dependences for the YbPO_4 – steam reaction. The YbPO_4 -CMAS reaction layer kinetics should be investigated for other exposure temperatures, lower CMAS loads, and CMAS compositions to determine a minimum local concentration of Ca to lead to formation of a dense protective layer at the surface.

Reliable data for oxygen and water vapor diffusion pathways and diffusion rates in EBC material candidates are urgently needed to mitigate the TGO growth and EBC delamination mechanism as well as for data input for the figure of merit. Additionally, the results of Objective 2 should be utilized to create an optimized multi-component $\text{RE}_2\text{Si}_2\text{O}_7$, for which all properties of the figure of merit should be measured to compare to state-of-the-art $\text{Yb}_2\text{Si}_2\text{O}_7$. Additions to the figure of merit should include secondary properties relevant to EBC application, such as high-temperature thermal conductivity, Young's Modulus, and material stability and processability through the traditional air plasma spray process for applying EBC materials to CMCs.

7. Resulting Presentations, Publications, Patents, and Awards from this Work

7.1. Presentations:

1. Synthesis and Thermal Properties of Multi-component Rare Earth Silicates, Gordon Research Conference, Solid State Studies in Ceramics, *Poster*, South Hadley, MA. 2018.
2. Microstructural Evolution of Silicate-based Environmental Barrier Coatings in Combustion Environments, Materials Science and Technology, *Oral Presentation*, Columbus, OH. 2018.
3. Tailoring Thermal Properties of Rare Earth Silicates, International Conference on Advancement of Ceramic Composites, *Oral Presentation*, Daytona Beach, FL. 2019.
4. Microstructural Evolution of EBCs in High-temperature High Velocity Water Vapor, Gordon Research Conference, High-temperature Oxidation, *Poster*, New London, NH. 2019.
5. Microstructural Evolution of EBCs in High-temperature High Velocity Water Vapor, Materials Science and Technology, *Oral Presentation*, Seattle, WA. 2019.
6. Tailoring Thermal Properties of EBCs in High Entropy Rare Earth Monosilicates, Rolls-Royce Inc., *Oral Presentation*, Indianapolis, IN. 2019.

7.2. Publications:

1. Mackenzie Ridley, John Gaskins, Patrick Hopkins, Elizabeth Opila, Tailoring thermal properties of multi-component rare earth monosilicates, *Acta Materialia*, Volume 195, 2020, Pages 698-707, ISSN 1359-6454, <https://doi.org/10.1016/j.actamat.2020.06.012>.

2. Mackenzie Ridley, Elizabeth Opila, Thermochemical stability and microstructural evolution of $\text{Yb}_2\text{Si}_2\text{O}_7$ in high-velocity high-temperature water vapor, *Journal of the European Ceramic Society*, 2020, ISSN 0955-2219, <https://doi.org/10.1016/j.jeurceramsoc.2020.05.071>.
3. Zhidong Ding, Mackenzie Ridley, Jeroen Deijkers, Naiming Liu, Md Shafkat Bin Hoque, John Gaskins, Mona Zebarjadi, Patrick E. Hopkins, Haydn Wadley, Elizabeth Opila, Keivan Esfarjani, The thermal and mechanical properties of hafnium orthosilicate: Experiments and first-principles calculations, *Materialia*, Volume 12, 2020, 100793, ISSN 2589-1529, <https://doi.org/10.1016/j.mtla.2020.100793>.
4. Mackenzie Ridley, Elizabeth Opila, Thermomechanical and thermochemical stability of HfSiO_4 for environmental barrier coating applications, *Journal of the American Ceramic Society*, 2021, <https://doi.org/10.1111/jace.17729>.
5. Mackenzie Ridley, Elizabeth Opila, High-temperature water vapor reaction mechanism of barium strontium aluminosilicate (BSAS), *Manuscript in Progress*.
6. Mackenzie Ridley, Elizabeth Opila, High-velocity steam resistance of $\text{RE}_2\text{Si}_2\text{O}_7$ (RE = Sc, Nd, Er, Yb, and Lu) at 1400 °C, *Manuscript in Progress*.
7. Mackenzie Ridley, Cormac Toher, Elizabeth Opila, Experimental and computational thermomechanical properties of multi-component rare earth disilicates, *Manuscript in Progress*.
8. Mackenzie Ridley, Bohuslava McFarland, Cameron Miller, Elizabeth Opila, Evaluation of YbPO_4 as an environmental barrier coating candidate, *Manuscript in Progress*.

9. Mackenzie Ridley, Dominic Pinnisi, Elizabeth Opila, Holistic comparison of environmental barrier coating material candidates through design of a figure of merit, *Manuscript in Progress*.

7.3. Patents:

1. Chamberlain, A.L., Opila, E.J. and Ridley, M.J., University of Virginia Licensing, Ventures Group, Rolls Royce Corp and University of Virginia, 2020. Thermal and/or environmental barrier coating system. U.S. Patent Application 16/723,675.

<https://patents.google.com/patent/US20200199027A1/en>

7.4. Awards:

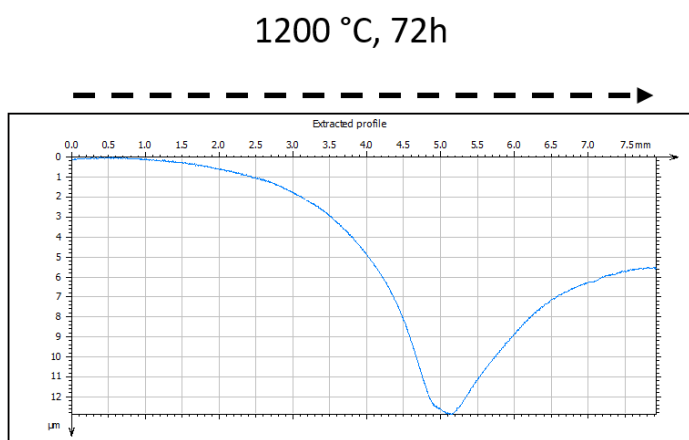
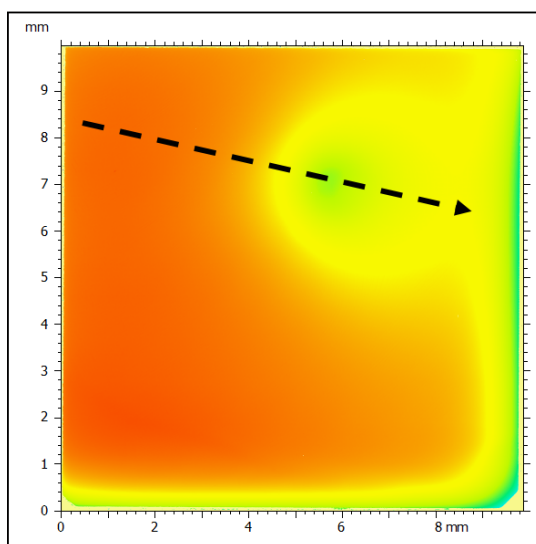
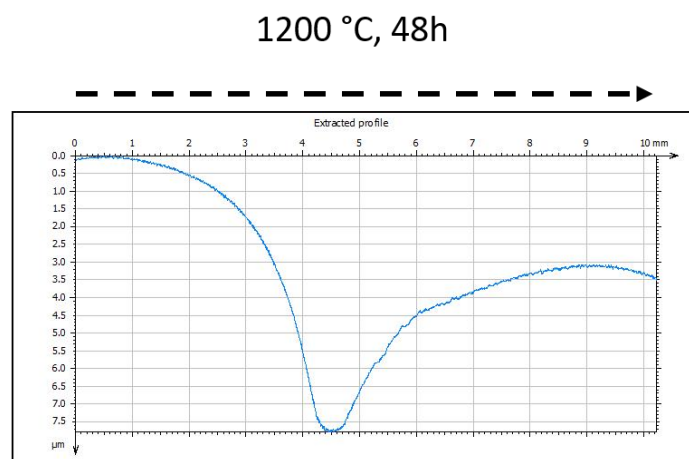
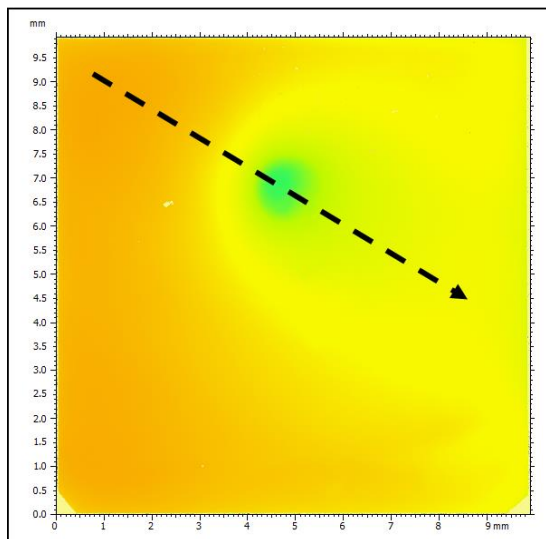
1. Virginia Space Grant Consortium (VSGC) Graduate Research Fellowship, 2020-2021.

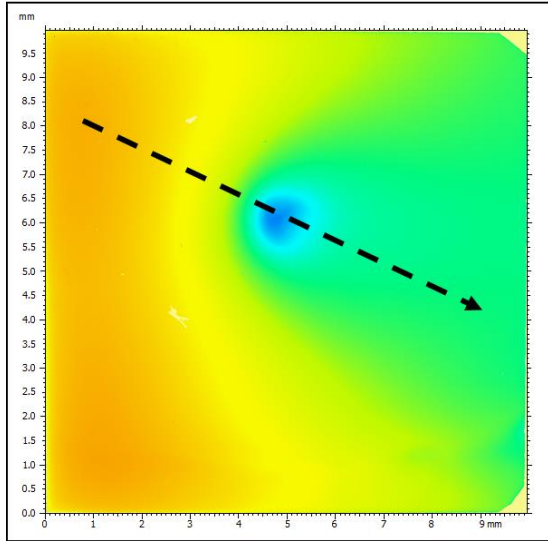
8. Appendices

8.1. Profilometry Mapping and Linescan Analysis of Al₂O₃ (0001)

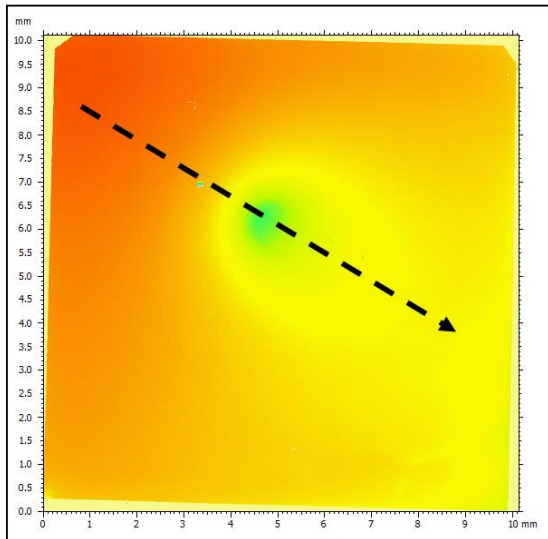
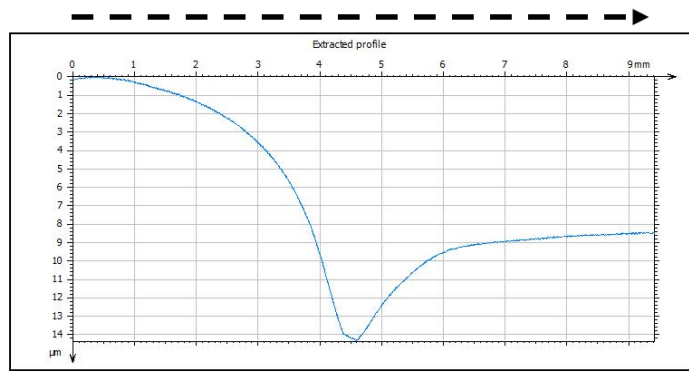
Exposures to Steam

Each test sample is represented by the profilometry map, each with unique color scaling. A linescan was taken through the impingement site, and is displayed as recession depth on the y-axis versus position in mm on the x-axis.

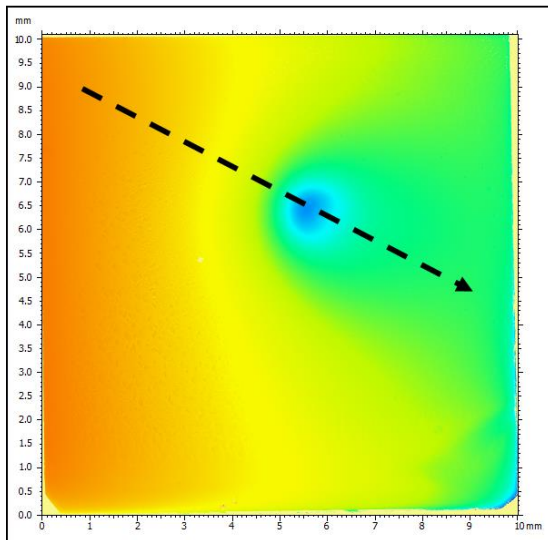
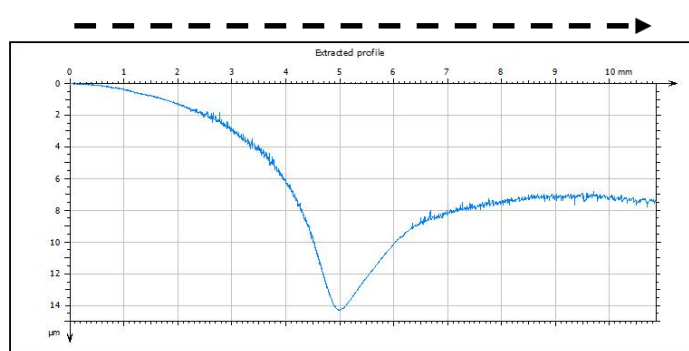




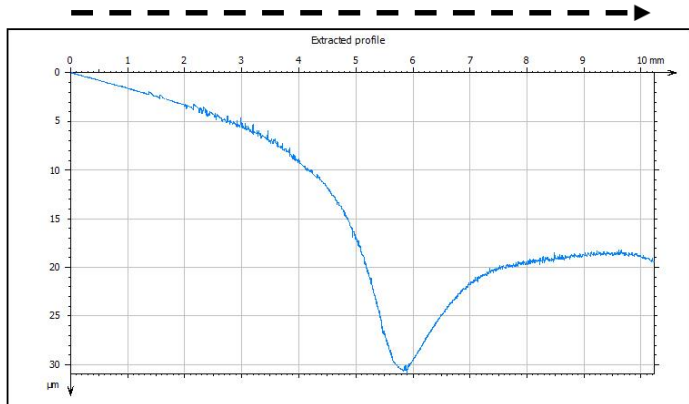
1200 °C, 84h

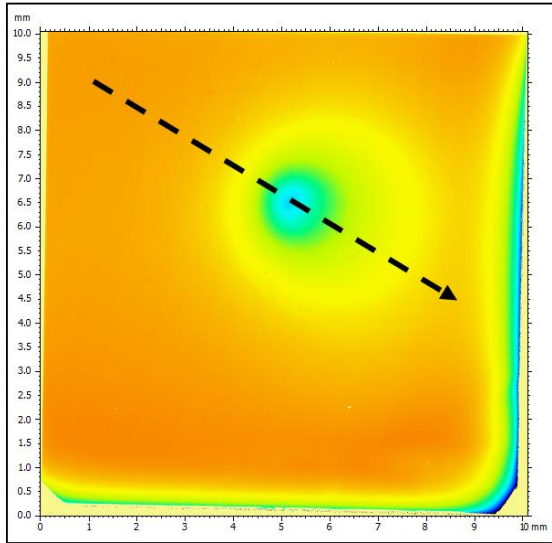


1300 °C, 24h

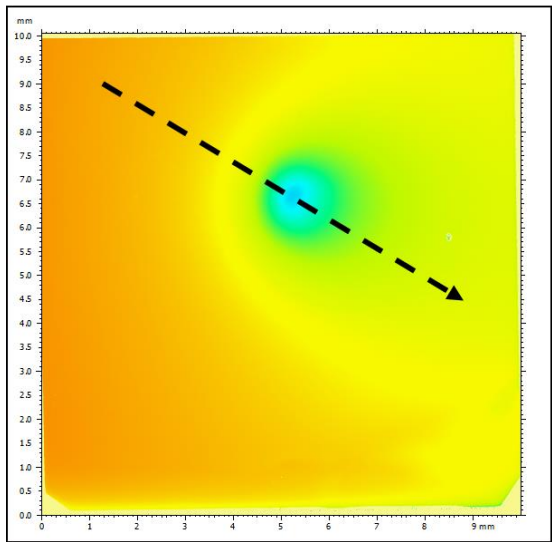
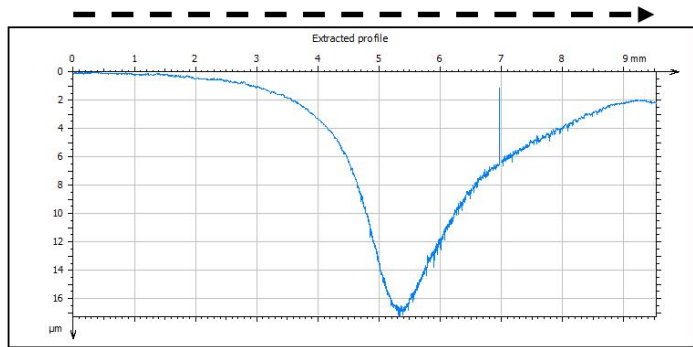


1300 °C, 48h

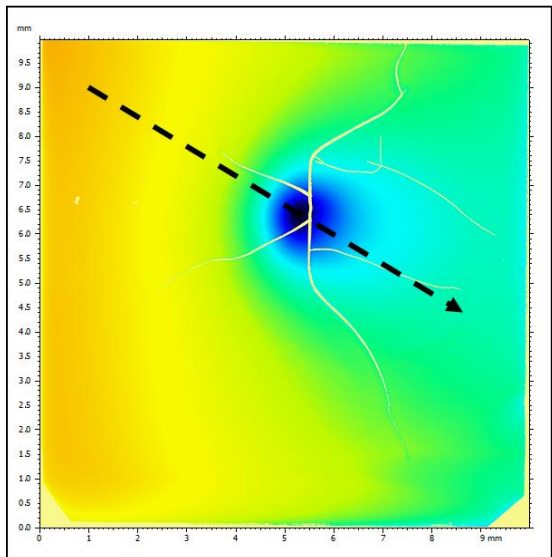
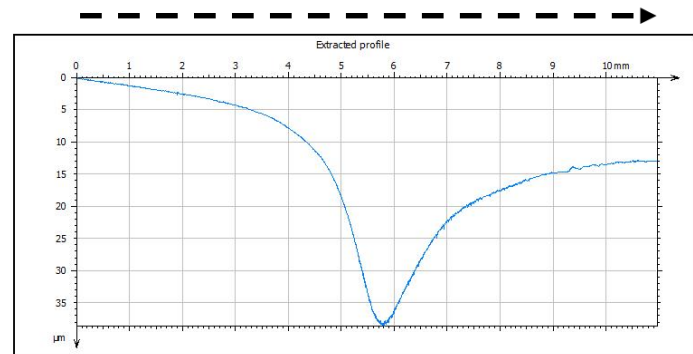




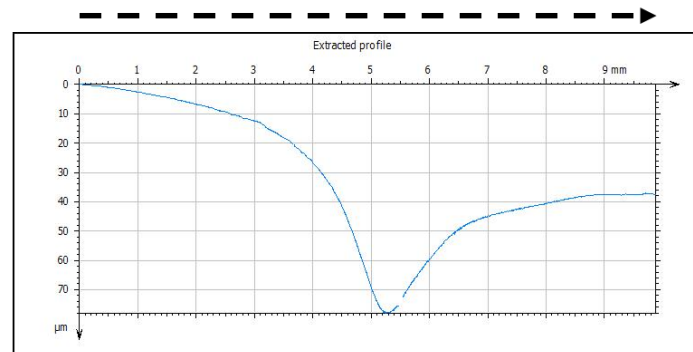
1400 °C, 12h

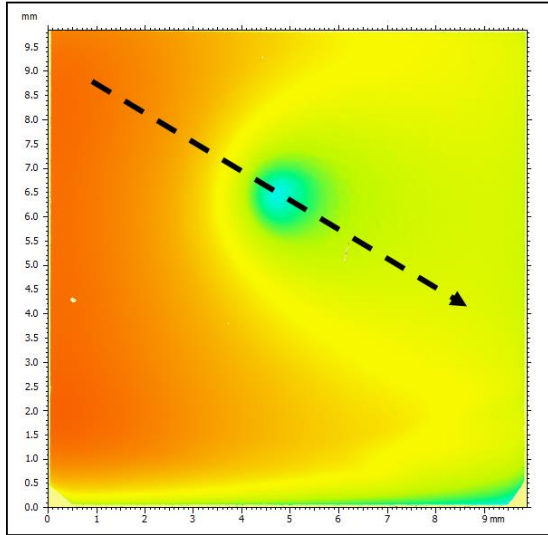


1400 °C, 24h

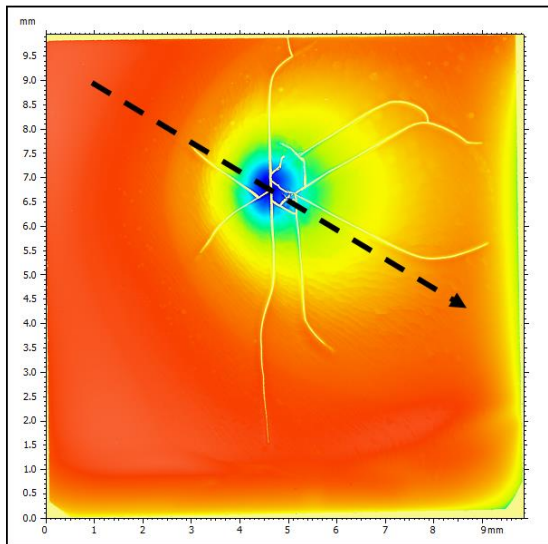
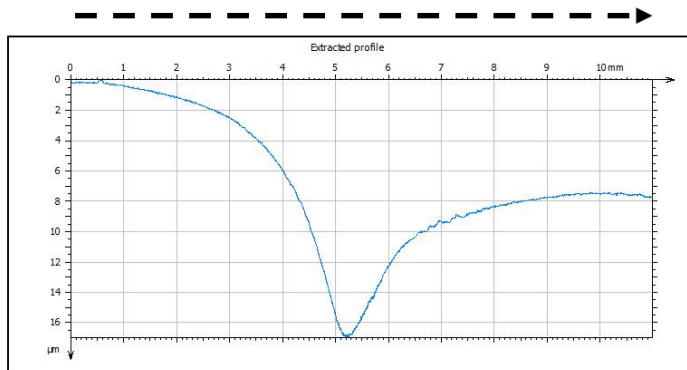


1400 °C, 48h

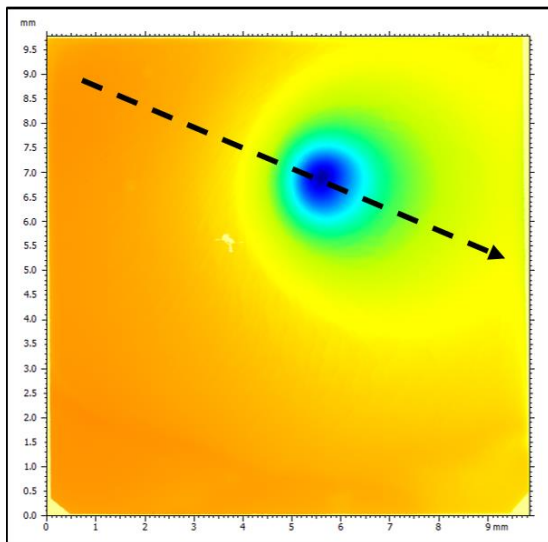
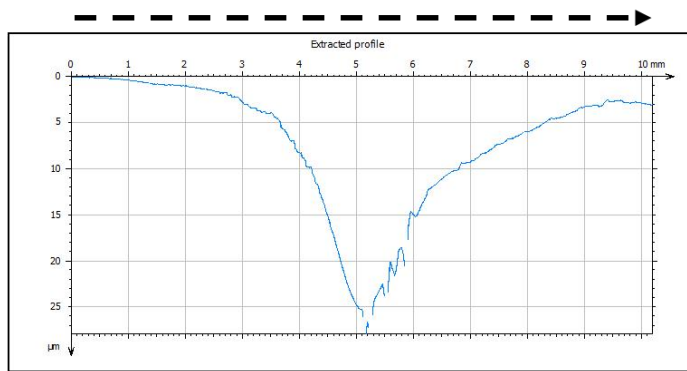




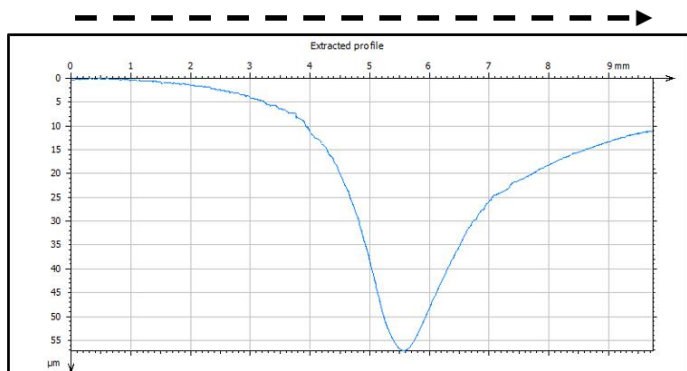
1450 °C, 6h



1450 °C, 12h



1450 °C, 24h



8.2. Crystal Data for δ -Y₂Si₂O₇ from single crystal X-ray Diffraction

Table 1. Sample and crystal data for Y₂Si₂O₇

Identification code	Y ₂ Si ₂ O ₇	
Chemical formula	O ₇ Si ₂ Y ₂	
Formula weight	346.00 g/mol	
Temperature	299(2) K	
Wavelength	0.71073 Å	
Crystal size	0.130 x 0.138 x 0.215 mm	
Crystal system	orthorhombic	
Space group	P n m a	
Unit cell dimensions	a = 13.6788(15) Å	α = 90°
	b = 8.1574(9) Å	β = 90°
	c = 5.0243(5) Å	γ = 90°
Volume	560.63(10) Å ³	
Z	4	
Density (calculated)	4.099 g/cm ³	
Absorption coefficient	21.010 mm ⁻¹	
F(000)	648	

Table 2. Atomic coordinates and equivalent isotropic atomic

**displacement parameters (\AA^2) for
 $\text{Y}_2\text{Si}_2\text{O}_7$.**

U(eq) is defined as one third of the trace of the orthogonalized U_{ij} tensor.

	x/a	y/b	z/c	U(eq)
Y1	0.87435(2)	0.49071(4)	0.33932(7)	0.00438(17)
Si1	0.68084(9)	0.75	0.3765(3)	0.0043(3)
Si2	0.45954(9)	0.75	0.6250(3)	0.0039(3)
O1	0.73258(17)	0.5859(3)	0.4869(5)	0.0069(5)
O2	0.6550(2)	0.75	0.0656(7)	0.0070(7)
O3	0.5795(2)	0.75	0.5600(7)	0.0059(7)
O4	0.3994(3)	0.75	0.3493(6)	0.0067(7)
O5	0.45234(16)	0.9187(3)	0.7904(5)	0.0073(5)

Table 3. Bond lengths (\AA) for $\text{Y}_2\text{Si}_2\text{O}_7$

Y1-O1	2.217(2)	Y1-O5	2.268(2)
Y1-O2	2.3042(19)	Y1-O4	2.3429(15)
Y1-O1	2.380(2)	Y1-O5	2.455(2)
Y1-O3	2.495(2)	Y1-Si1	3.1356(11)
Y1-Si2	3.1904(11)	Y1-Si2	3.3575(11)
Y1-Si1	3.4221(12)	Y1-Y1	3.8009(7)

Si1-O2	1.602(4)	Si1-O1	1.613(2)
Si1-O1	1.613(2)	Si1-O3	1.665(3)
Si2-O5	1.611(2)	Si2-O5	1.611(2)
Si2-O4	1.611(4)	Si2-O3	1.673(3)

Table 4. Bond angles (°) for Y₂Si₂O₇

O1-Y1-O5	91.32(8)	O1-Y1-O2	88.91(10)
O5-Y1-O2	87.41(10)	O1-Y1-O4	86.97(10)
O5-Y1-O4	88.21(10)	O2-Y1-O4	173.91(11)
O1-Y1-O1	78.65(5)	O5-Y1-O1	169.96(8)
O2-Y1-O1	92.09(10)	O4-Y1-O1	91.49(10)
O1-Y1-O5	164.20(8)	O5-Y1-O5	72.89(9)
O2-Y1-O5	90.78(9)	O4-Y1-O5	91.96(10)
O1-Y1-O5	117.15(8)	O1-Y1-O3	133.27(9)
O5-Y1-O3	126.77(9)	O2-Y1-O3	69.57(10)
O4-Y1-O3	116.49(10)	O1-Y1-O3	62.00(9)
O5-Y1-O3	60.71(9)	O1-Y1-Si1	104.88(7)
O5-Y1-Si1	157.73(6)	O2-Y1-Si1	77.90(8)
O4-Y1-Si1	107.50(8)	O1-Y1-Si1	30.23(6)
O5-Y1-Si1	90.49(6)	O3-Y1-Si1	31.89(7)
O1-Y1-Si2	162.10(6)	O5-Y1-Si2	98.18(6)

O2-Y1-Si2	76.48(8)	O4-Y1-Si2	108.35(8)
O1-Y1-Si2	91.43(6)	O5-Y1-Si2	29.67(5)
O3-Y1-Si2	31.28(7)	Si1-Y1-Si2	62.34(3)
O1-Y1-Si2	108.39(6)	O5-Y1-Si2	101.62(6)
O2-Y1-Si2	160.07(8)	O4-Y1-Si2	25.78(7)
O1-Y1-Si2	82.06(6)	O5-Y1-Si2	75.29(6)
O3-Y1-Si2	90.98(6)	Si1-Y1-Si2	87.87(3)
Si2-Y1-Si2	84.606(16)	O1-Y1-Si1	75.17(6)
O5-Y1-Si1	69.13(6)	O2-Y1-Si1	23.57(8)
O4-Y1-Si1	150.37(7)	O1-Y1-Si1	107.49(6)
O5-Y1-Si1	98.90(6)	O3-Y1-Si1	92.75(6)
Si1-Y1-Si1	99.931(17)	Si2-Y1-Si1	94.03(3)
Si2-Y1-Si1	170.40(3)	O1-Y1-Y1	129.43(7)
O5-Y1-Y1	38.11(6)	O2-Y1-Y1	88.96(8)
O4-Y1-Y1	90.20(9)	O1-Y1-Y1	151.92(6)
O5-Y1-Y1	34.77(6)	O3-Y1-Y1	92.37(7)
Si1-Y1-Y1	123.90(3)	Si2-Y1-Y1	61.56(2)
Si2-Y1-Y1	87.48(3)	Si1-Y1-Y1	83.53(2)
O2-Si1-O1	115.62(11)	O2-Si1-O1	115.62(11)
O1-Si1-O1	112.22(18)	O2-Si1-O3	110.86(18)
O1-Si1-O3	100.08(12)	O1-Si1-O3	100.08(12)

O2-Si1-Y1	132.07(8)	O1-Si1-Y1	47.99(9)
O1-Si1-Y1	111.74(11)	O3-Si1-Y1	52.34(8)
O2-Si1-Y1	132.07(8)	O1-Si1-Y1	111.74(11)
O1-Si1-Y1	47.99(9)	O3-Si1-Y1	52.34(8)
Y1-Si1-Y1	77.54(3)	O2-Si1-Y1	96.81(10)
O1-Si1-Y1	32.78(9)	O1-Si1-Y1	101.19(10)
O3-Si1-Y1	132.85(7)	Y1-Si1-Y1	80.69(2)
Y1-Si1-Y1	128.24(4)	O2-Si1-Y1	35.118(18)
O1-Si1-Y1	147.61(11)	O1-Si1-Y1	83.79(9)
O3-Si1-Y1	104.65(10)	Y1-Si1-Y1	153.01(4)
Y1-Si1-Y1	99.932(17)	Y1-Si1-Y1	119.10(4)
O2-Si1-Y1	35.118(18)	O1-Si1-Y1	83.79(9)
O1-Si1-Y1	147.61(11)	O3-Si1-Y1	104.65(10)
Y1-Si1-Y1	99.932(17)	Y1-Si1-Y1	153.01(4)
Y1-Si1-Y1	76.76(2)	Y1-Si1-Y1	70.03(3)
O5-Si2-O5	117.38(19)	O5-Si2-O4	114.37(10)
O5-Si2-O4	114.37(10)	O5-Si2-O3	99.24(11)
O5-Si2-O3	99.24(11)	O4-Si2-O3	109.45(18)
O5-Si2-Y1	48.96(8)	O5-Si2-Y1	113.27(10)
O4-Si2-Y1	130.84(8)	O3-Si2-Y1	50.75(8)
O5-Si2-Y1	113.27(10)	O5-Si2-Y1	48.96(8)

O4-Si2-Y1	130.84(8)	O3-Si2-Y1	50.75(8)
Y1-Si2-Y1	75.97(3)	O5-Si2-Y1	151.11(10)
O5-Si2-Y1	78.41(9)	O4-Si2-Y1	39.23(2)
O3-Si2-Y1	101.82(10)	Y1-Si2-Y1	150.39(4)
Y1-Si2-Y1	95.395(16)	O5-Si2-Y1	78.41(9)
O5-Si2-Y1	151.11(10)	O4-Si2-Y1	39.23(2)
O3-Si2-Y1	101.82(10)	Y1-Si2-Y1	95.395(16)
Y1-Si2-Y1	150.39(4)	Y1-Si2-Y1	78.10(3)
Si1-O1-Y1	124.02(14)	Si1-O1-Y1	101.78(12)
Y1-O1-Y1	134.00(10)	Si1-O2-Y1	121.31(8)
Si1-O2-Y1	121.31(8)	Y1-O2-Y1	116.89(15)
Si1-O3-Si2	157.6(2)	Si1-O3-Y1	95.77(10)
Si2-O3-Y1	97.97(11)	Si1-O3-Y1	95.77(10)
Si2-O3-Y1	97.97(11)	Y1-O3-Y1	103.82(12)
Si2-O4-Y1	114.99(8)	Si2-O4-Y1	114.99(8)
Y1-O4-Y1	129.06(15)	Si2-O5-Y1	136.91(13)
Si2-O5-Y1	101.37(11)	Y1-O5-Y1	107.11(9)

Table 5. Torsion angles (°) for Y₂Si₂O₇

O2-Si1-O1-Y1	59.9(2)	O1-Si1-O1-Y1	-75.7(2)
O3-Si1-O1-Y1	178.97(16)	Y1-Si1-O1-Y1	-127.70(12)

Y1-Si1-O1-Y1 -175.5(2)	Y1-Si1-O1-Y1 -43.36(15)
Y1-Si1-O1-Y1 75.14(13)	Y1-Si1-O1-Y1 39.5(3)
O2-Si1-O1-Y1 -124.63(15)	O1-Si1-O1-Y1 99.81(15)
O3-Si1-O1-Y1 -5.53(14)	Y1-Si1-O1-Y1 47.80(11)
Y1-Si1-O1-Y1 132.14(7)	Y1-Si1-O1-Y1 -109.36(8)
Y1-Si1-O1-Y1 -144.98(12)	O1-Si1-O2-Y1 161.11(15)
O1-Si1-O2-Y1 27.1(3)	O3-Si1-O2-Y1 -85.91(17)
Y1-Si1-O2-Y1 -143.44(8)	Y1-Si1-O2-Y1 -28.4(3)
Y1-Si1-O2-Y1 132.97(16)	Y1-Si1-O2-Y1 -171.8(3)
O1-Si1-O2-Y1 -27.1(3)	O1-Si1-O2-Y1 -161.11(15)
O3-Si1-O2-Y1 85.91(17)	Y1-Si1-O2-Y1 28.4(3)
Y1-Si1-O2-Y1 143.44(8)	Y1-Si1-O2-Y1 -55.20(18)
Y1-Si1-O2-Y1 171.8(3)	O2-Si1-O3-Si2 0.0000(10)
O1-Si1-O3-Si2 122.53(10)	O1-Si1-O3-Si2 -122.53(10)
Y1-Si1-O3-Si2 127.72(7)	Y1-Si1-O3-Si2 -127.72(7)
Y1-Si1-O3-Si2 121.77(11)	Y1-Si1-O3-Si2 -36.38(3)
Y1-Si1-O3-Si2 36.38(3)	O2-Si1-O3-Y1 -127.72(7)
O1-Si1-O3-Y1 -5.19(13)	O1-Si1-O3-Y1 109.76(11)
Y1-Si1-O3-Y1 104.57(14)	Y1-Si1-O3-Y1 -5.95(17)
Y1-Si1-O3-Y1 -164.09(5)	Y1-Si1-O3-Y1 -91.34(9)
O2-Si1-O3-Y1 127.72(7)	O1-Si1-O3-Y1 -109.76(11)

O1-Si1-O3-Y1 5.19(13)	Y1-Si1-O3-Y1 -104.57(14)
Y1-Si1-O3-Y1 -110.52(6)	Y1-Si1-O3-Y1 91.34(9)
Y1-Si1-O3-Y1 164.09(5)	O5-Si2-O3-Si1 -120.05(10)
O5-Si2-O3-Si1 120.05(10)	O4-Si2-O3-Si1 0.0000(10)
Y1-Si2-O3-Si1 -127.37(8)	Y1-Si2-O3-Si1 127.37(8)
Y1-Si2-O3-Si1 40.06(3)	Y1-Si2-O3-Si1 -40.06(3)
O5-Si2-O3-Y1 7.32(14)	O5-Si2-O3-Y1 -112.58(12)
O4-Si2-O3-Y1 127.37(8)	Y1-Si2-O3-Y1 -105.26(15)
Y1-Si2-O3-Y1 167.43(6)	Y1-Si2-O3-Y1 87.31(10)
O5-Si2-O3-Y1 112.58(12)	O5-Si2-O3-Y1 -7.32(14)
O4-Si2-O3-Y1 -127.37(8)	Y1-Si2-O3-Y1 105.26(15)
Y1-Si2-O3-Y1 -87.31(9)	Y1-Si2-O3-Y1 -167.43(6)
O5-Si2-O4-Y1 -164.81(14)	O5-Si2-O4-Y1 -25.4(2)
O3-Si2-O4-Y1 84.90(15)	Y1-Si2-O4-Y1 139.33(8)
Y1-Si2-O4-Y1 30.5(2)	Y1-Si2-O4-Y1 169.8(3)
O5-Si2-O4-Y1 25.4(2)	O5-Si2-O4-Y1 164.81(14)
O3-Si2-O4-Y1 -84.90(15)	Y1-Si2-O4-Y1 -30.5(2)
Y1-Si2-O4-Y1 -139.33(7)	Y1-Si2-O4-Y1 -169.8(3)
O5-Si2-O5-Y1 -32.9(3)	O4-Si2-O5-Y1 105.3(2)
O3-Si2-O5-Y1 -138.38(19)	Y1-Si2-O5-Y1 -130.9(2)
Y1-Si2-O5-Y1 -87.27(18)	Y1-Si2-O5-Y1 85.2(3)

Y1-Si2-O5-Y1 121.34(18) O5-Si2-O5-Y1 98.00(15)
O4-Si2-O5-Y1 -123.88(15) O3-Si2-O5-Y1 -7.52(15)
Y1-Si2-O5-Y1 43.59(12) Y1-Si2-O5-Y1 -143.95(14)
Y1-Si2-O5-Y1 -107.80(9)

Table 6. Anisotropic atomic displacement parameters (\AA^2) for $\text{Y}_2\text{Si}_2\text{O}_7$

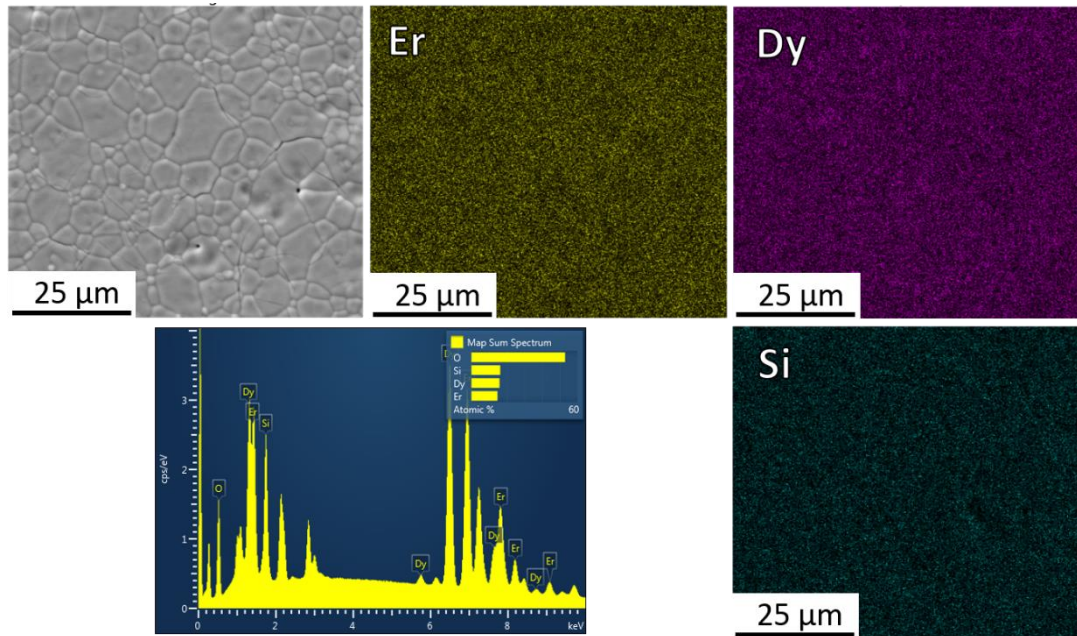
The anisotropic atomic displacement factor exponent takes the form: $-2\pi^2[h^2 a^{*2} U_{11} + \dots + 2 h k a^* b^* U_{12}]$

	U_{11}	U_{22}	U_{33}	U_{23}	U_{13}	U_{12}
Y1	0.0078(2)	0.0034(2)	0.0020(3)	-	-	0.00031(10)
				0.00039(10)	0.00031(11)	
Si1	0.0072(6)	0.0051(6)	0.0008(6)	0	0.0008(5)	0
Si2	0.0070(6)	0.0040(5)	0.0006(7)	0	-0.0004(5)	0
O1	0.0089(11)	0.0077(10)	0.0042(12)	0.0020(9)	0.0006(9)	0.0023(9)
O2	0.0121(15)	0.0049(14)	0.0040(18)	0	-0.0001(13)	0
O3	0.0060(15)	0.0076(14)	0.0042(19)	0	0.0019(13)	0
O4	0.0112(16)	0.0058(15)	0.003(2)	0	-0.0028(12)	0
O5	0.0098(11)	0.0060(10)	0.0061(13)	-0.0038(9)	0.0001(9)	0.0002(8)

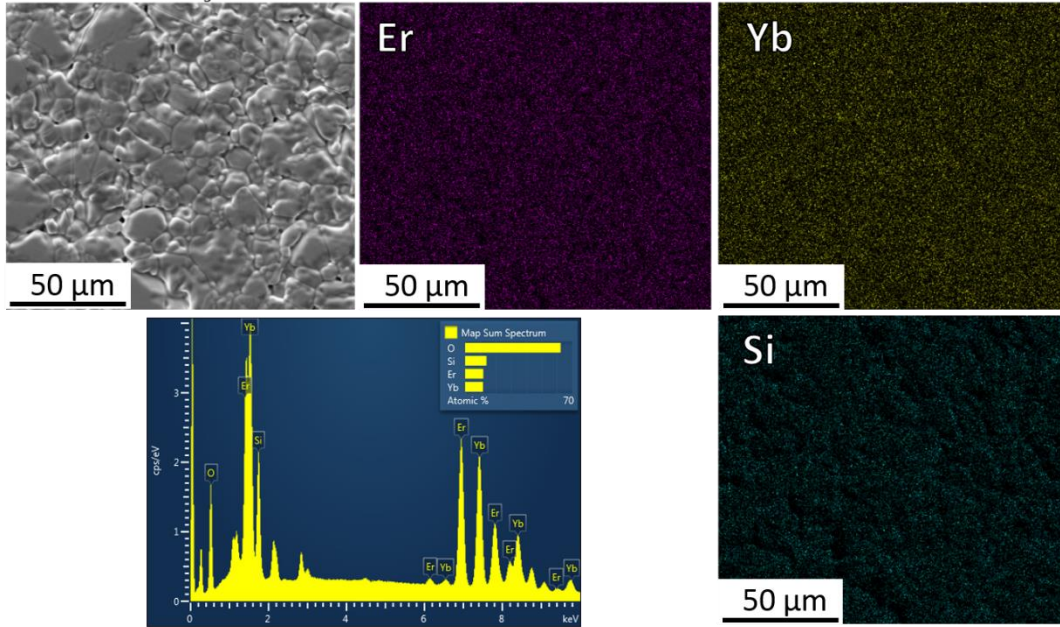
8.3. EDS Characterization of Multi-component Rare Earth

Monosilicates

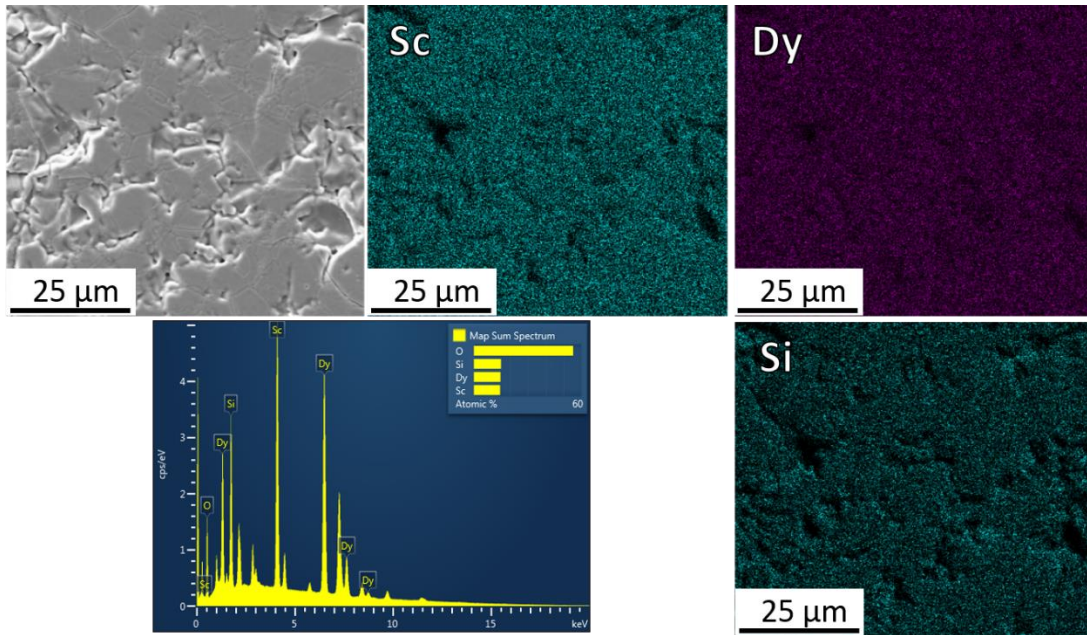
EDS of multicomponent RE_2SiO_5 was performed on samples after annealing at 1500 °C for 24 hours with a FEI Quanta LV200 scanning electron microscope.



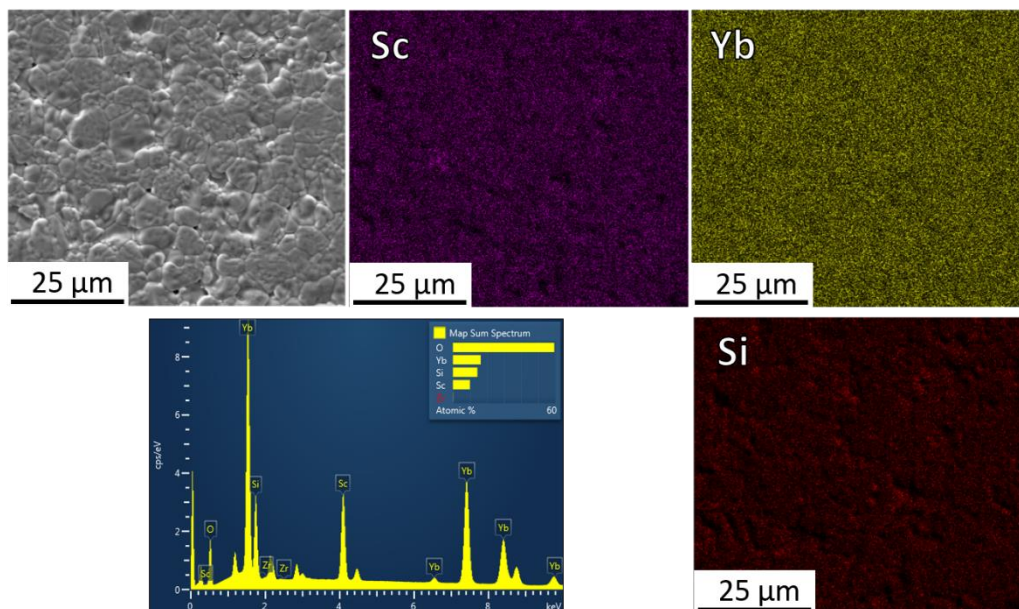
EDS of annealed $(\text{ErDy})_2\text{SiO}_5$ after processing.



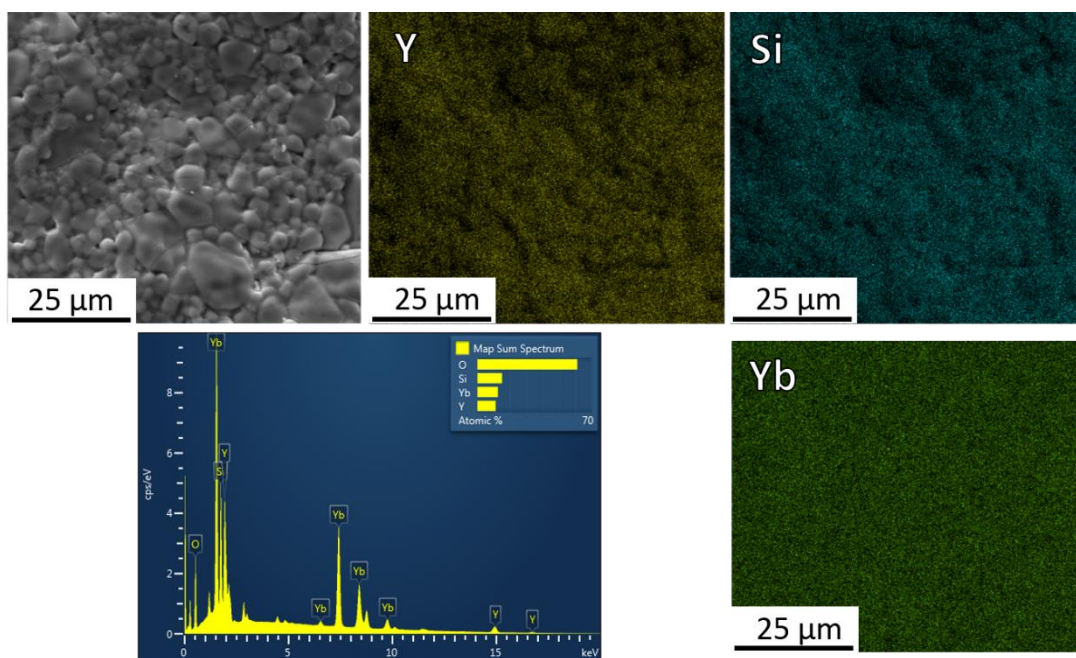
EDS of annealed $(ErYb)_2SiO_5$ after processing.



EDS of annealed $(ScDy)_2SiO_5$ after processing.

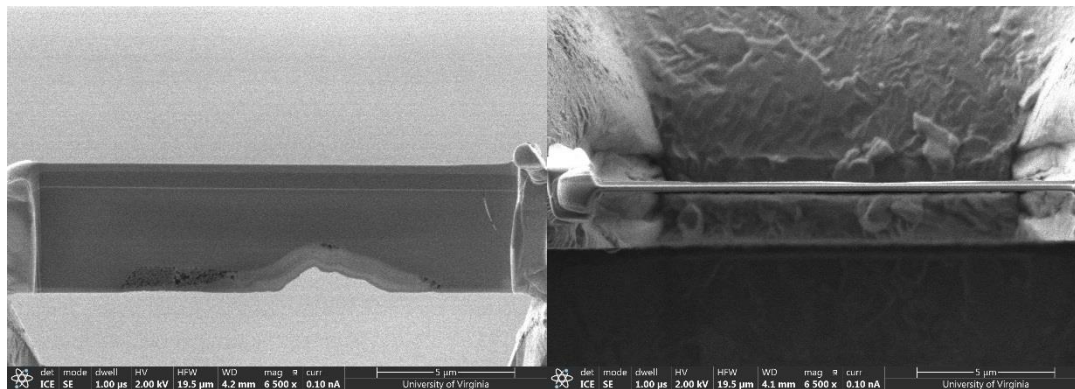


EDS of annealed (ScYb)₂SiO₅ after processing.

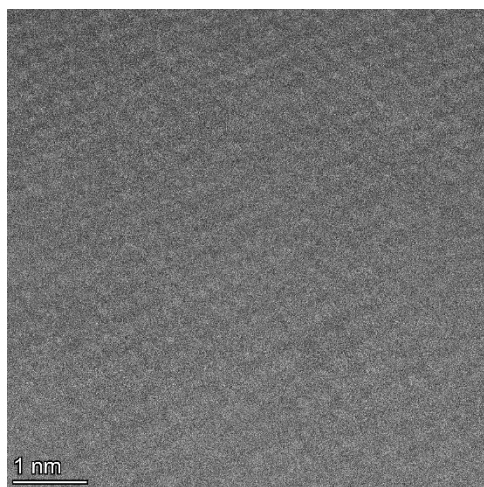


EDS of annealed (Yb)₂SiO₅ after processing.

TEM/EDS Analysis of $(\text{ScYDyErYb})_2\text{SiO}_5$ is presented below.

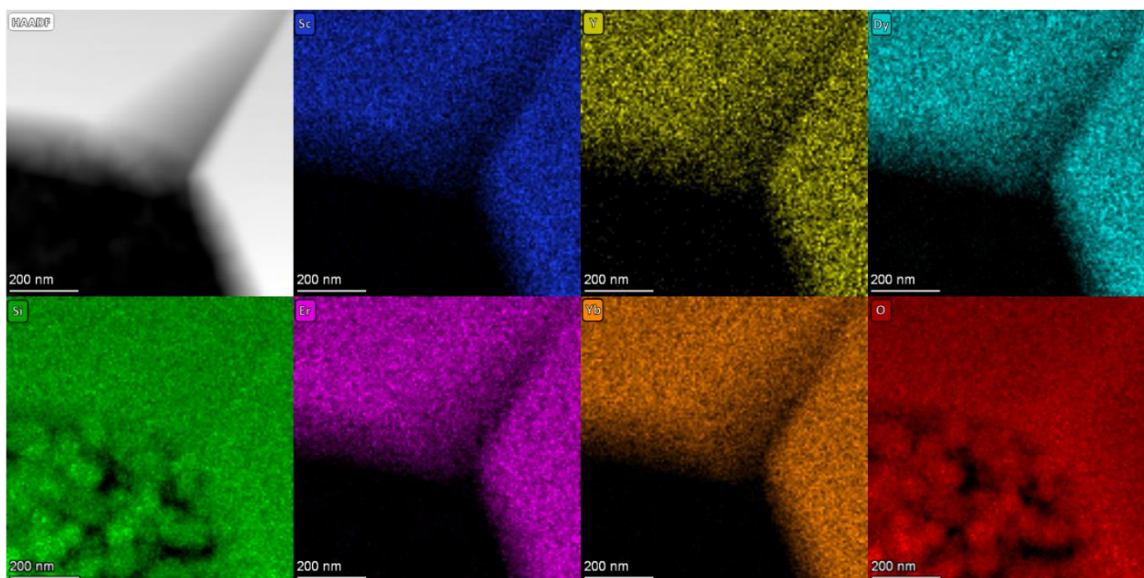


Focused ion beam images of the multi-component RE_2SiO_5 , sectioned from the bulk with a gallium ion source for Themis TEM and EDS analysis.



Element	Atomic fraction	Target Fraction
-	%	%
O	55.23	62.5
Si	13.60	12.5
Sc	5.15	5
Y	7.37	5
Dy	5.76	5
Er	6.92	5
Yb	5.98	5

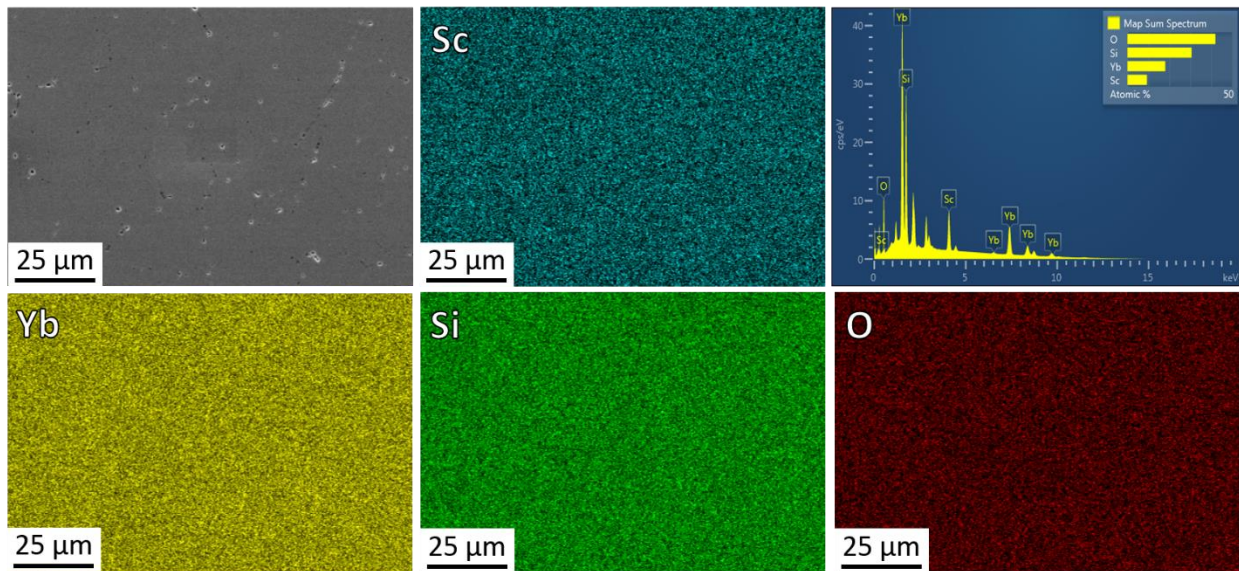
High angle annular dark field (HAADF) image of the multi-component RE_2SiO_5 and EDS statistics for the full region of the HAADF image.



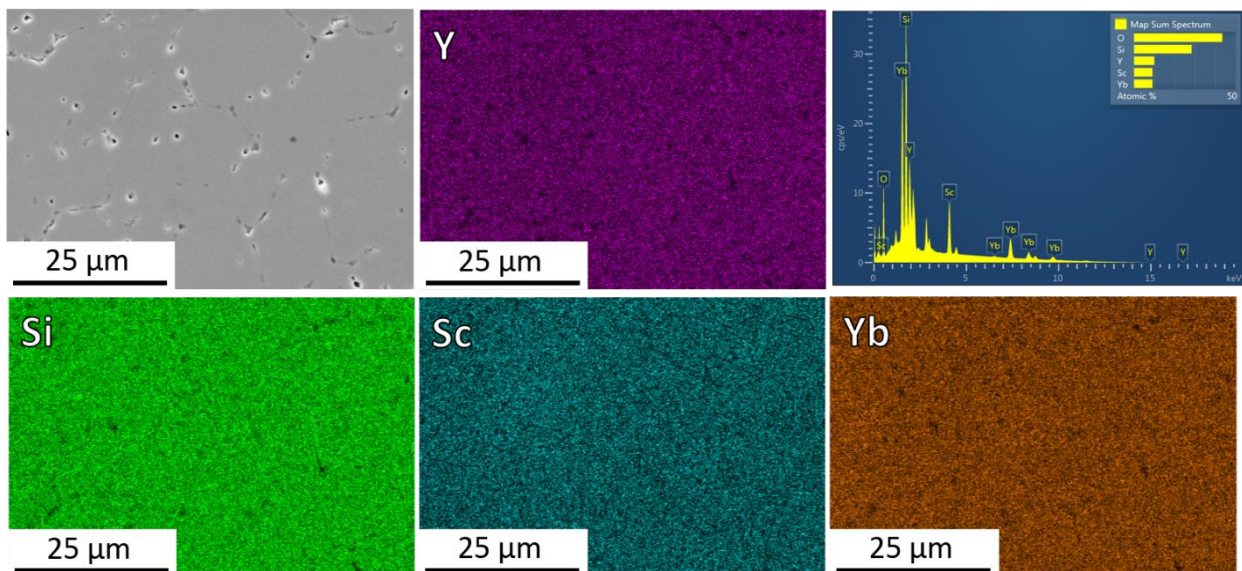
HAADF EDS maps of the multi-component RE_2SiO_5 . A grain boundary beside a pore is imaged, where the pore contains 50 nm colloidal silica from TEM sample preparation.

8.4. EDS Characterization of Multi-component Rare Earth Disilicates

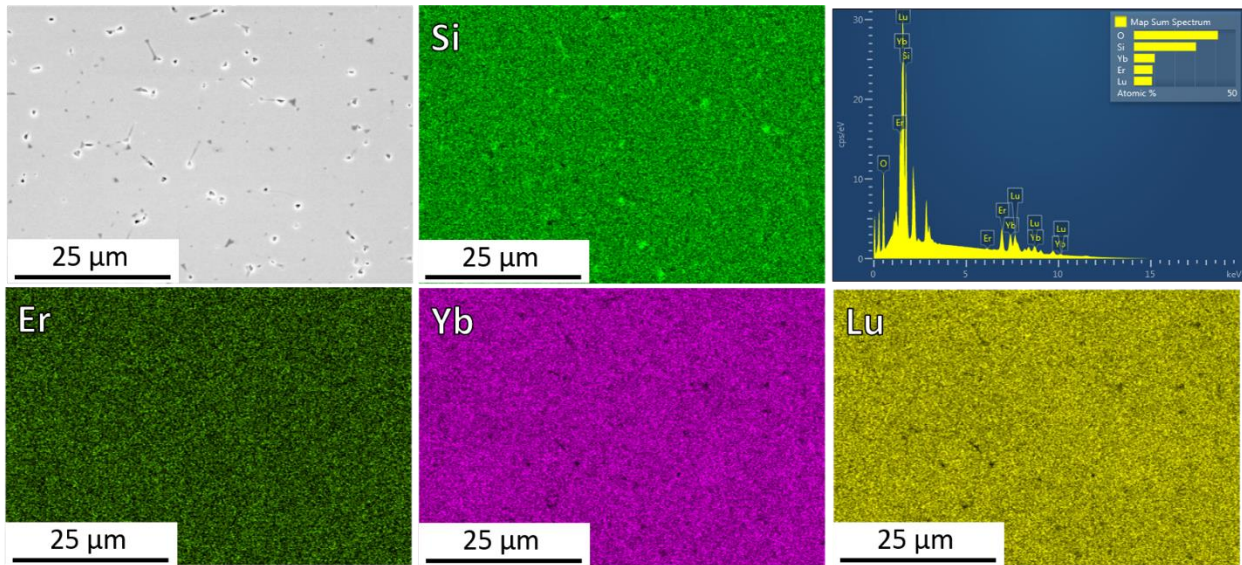
EDS characterization was performed on polished $\text{RE}_2\text{Si}_2\text{O}_7$ coupons after processing with a FEI Quanta 650 scanning electron microscope. While occasional rare earth cation clustering was present with all samples, the presented EDS maps are representative of the bulk of each material.



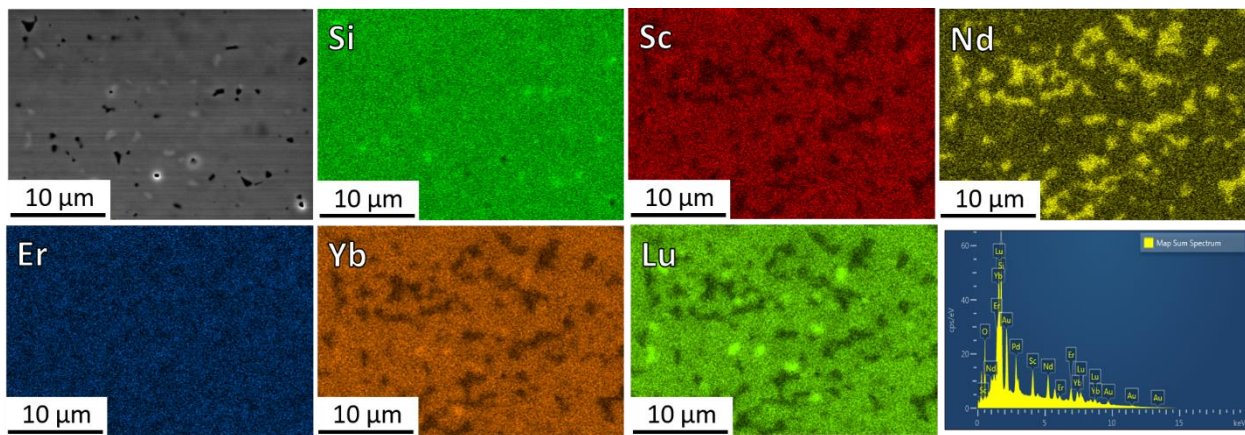
EDS of polished $(\text{Sc}_{0.33}\text{Yb}_{0.67})_2\text{Si}_2\text{O}_7$ after processing.



EDS of polished $(\text{ScYYb})_2\text{Si}_2\text{O}_7$ after processing.



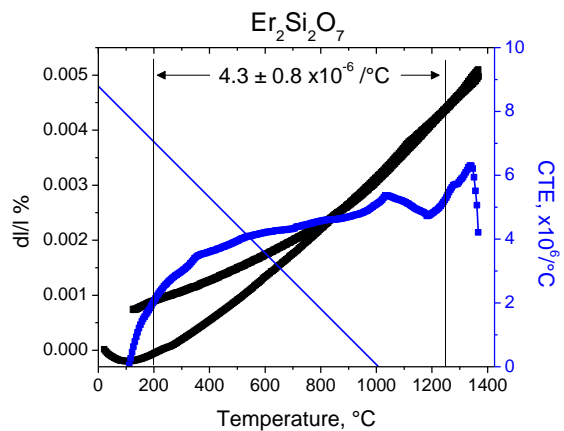
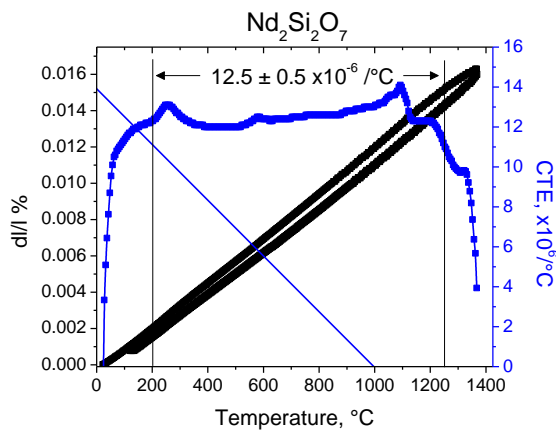
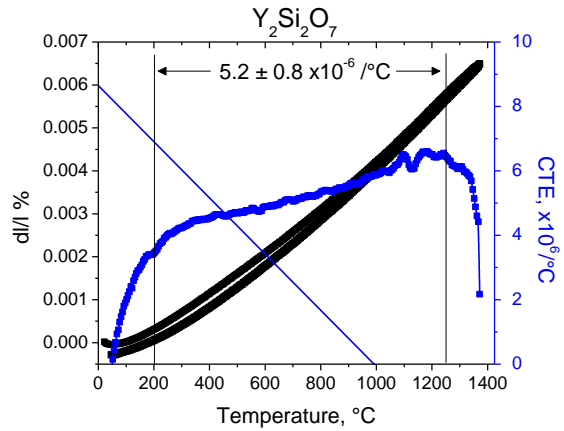
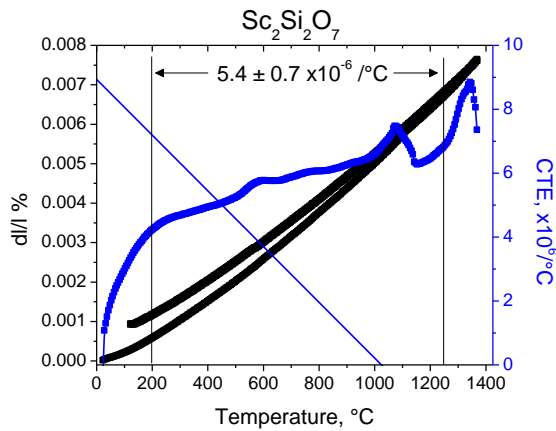
EDS of polished $(ErYbLu)_2Si_2O_7$ after processing. Free SiO_2 was observed at some of the sample grain boundaries.

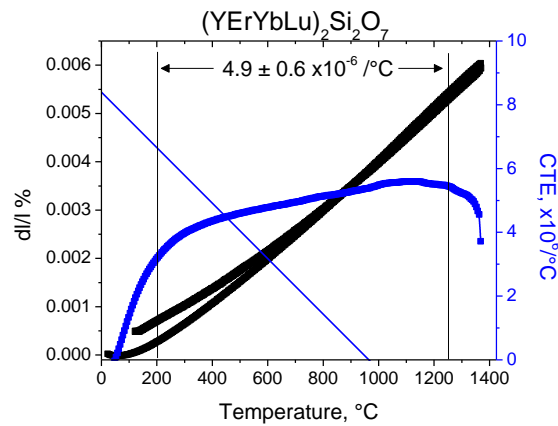
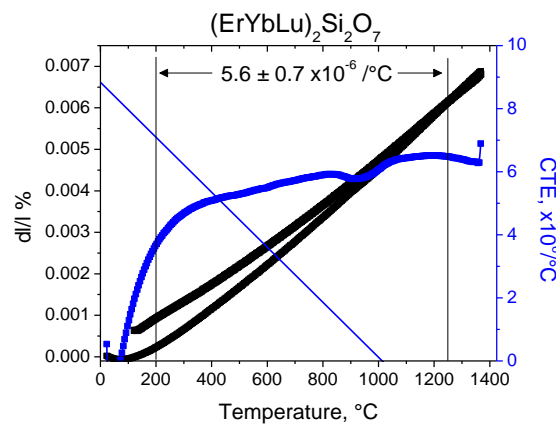
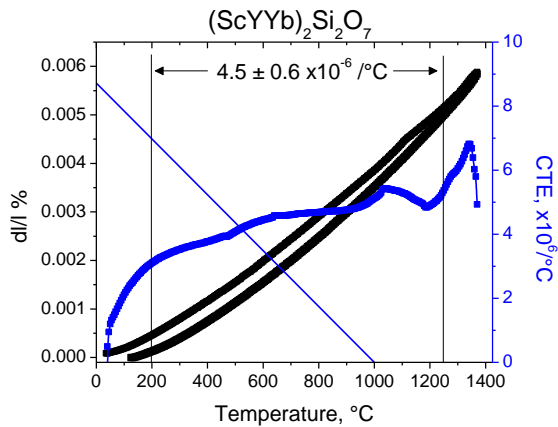
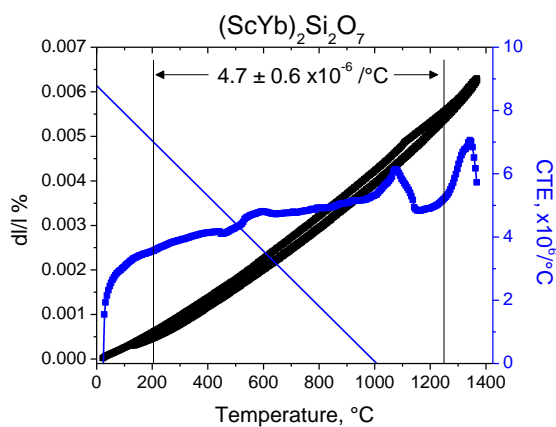
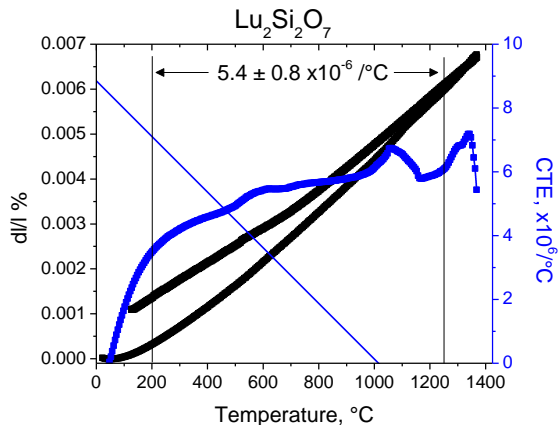
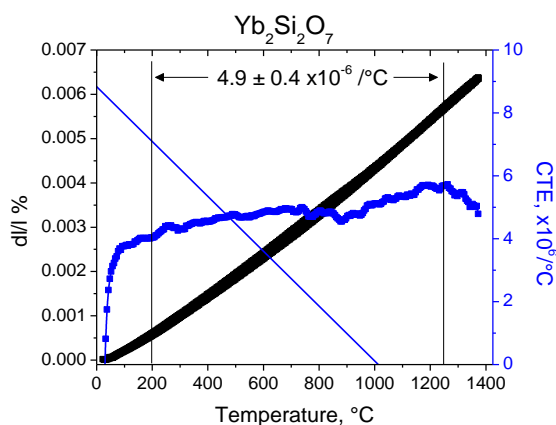


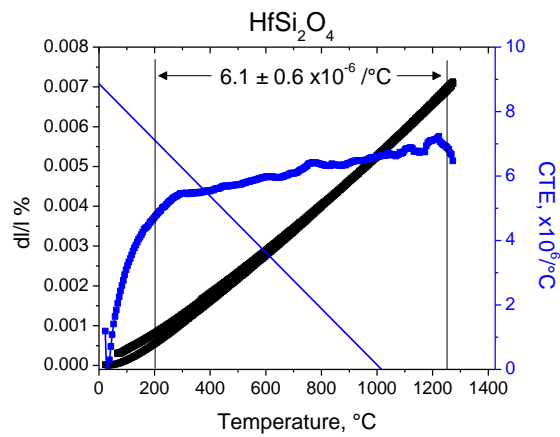
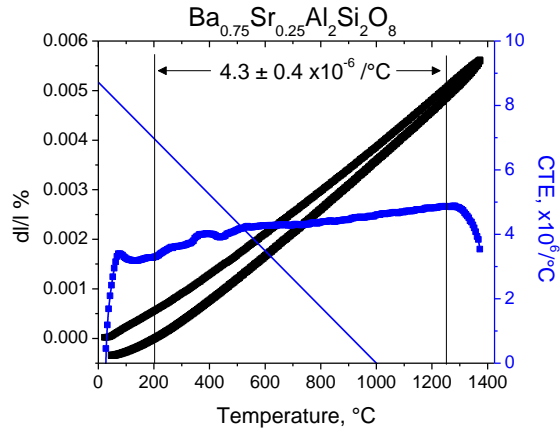
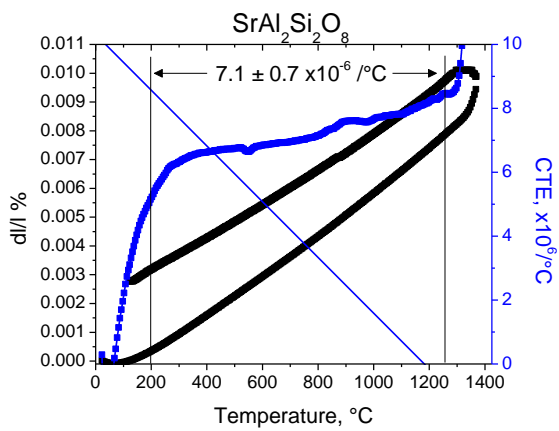
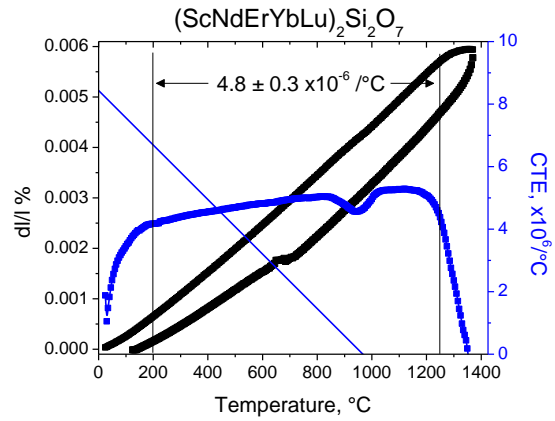
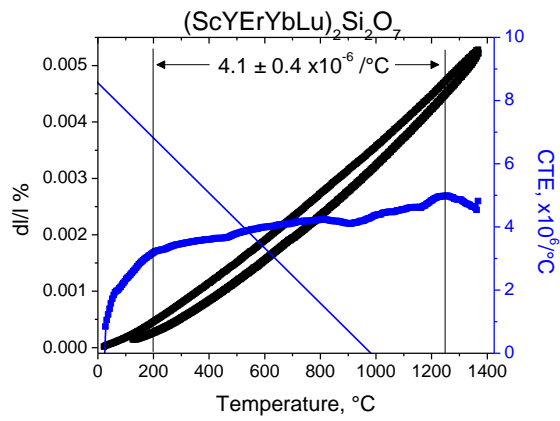
EDS of polished multi-phase $(ScNdErYbLu)_2Si_2O_7$ after processing. Lu cation clustering was not prevalent across the entire sample.

8.5. Dilatometry Data for Silicate Materials

Dilatometry of various silicate materials. The length change dl/l (black) is presented up to 1400 °C and the thermal expansion (blue) is averaged for the 200 °C – 1250 °C temperature range from heating curves at 10 °C/min.







8.6. Figure of Merit Data Manipulation

Assumptions and clarifications are as follows, where each letter corresponds with the subscript letter in Table 4-4:

- a: The YbPO_4 melting temperature is unknown. The ErPO_4 melt temperature was used to estimate that of YbPO_4 .
- b: The Yb_2O_3 - P_2O_5 phase diagram is unknown. The nearby eutectic temperature was estimated from the Y_2O_3 - P_2O_5 phase diagram.
- c: Volatility of Yb_2O_3 was estimated to be negligible based on high velocity steam testing of $\text{Yb}_2\text{Si}_2\text{O}_7$ [29] and high-velocity steam testing of Y_2O_3 [27].
- d: The $a(\text{SiO}_2)$ from the Yb_2O_3 - Yb_2SiO_5 two-phase field was presented.
- e: The $a(\text{SiO}_2)$ from the Yb_2SiO_5 - $\text{Yb}_2\text{Si}_2\text{O}_7$ two-phase field was presented.
- f: The $a(\text{MO}_x)$ consists of all oxide constituents (BaO , SrO , Al_2O_3 , SiO_2) since all components volatilize in high-velocity steam.
- g: The $a(\text{P}_2\text{O}_5)$ in rare earth orthophosphates is unknown. The $a(\text{P}_2\text{O}_5)$ was assumed to be near 0.2 based on comparable reaction rates to $\text{Yb}_2\text{Si}_2\text{O}_7$ in high-velocity steam testing at 1400 °C.
- h: The SiO_2/CaO ratio changes were determined from consumption of SiO_2/CaO upon reaction and introduction of additional SiO_2 into the residual melt:

$$\frac{\text{SiO}_2}{\text{CaO}} \text{ Ratio Changes} = \frac{(\text{SiO}_2_{\text{UCSB}} - \text{SiO}_2_{\text{EBC Reaction}})}{(\text{CaO}_{\text{UCSB}} - \text{CaO}_{\text{EBC Reaction}})}$$

The baseline CMAS composition used here was derived from commonly used synthetic CMAS (UCSB) with a SiO_2/CaO ratio of 45/33. HfSiO_4 reaction with CMAS is unknown; HfSiO_4 was assumed to donate SiO_2 to the melt and not produce a reaction product, based on the reaction between CMAS and ZrSiO_4 .

- i: The oxygen diffusion coefficient of Yb_2O_3 is unknown. The presented value was self-diffusion of single crystal Y_2O_3 at 1400 °C.
- j: The oxygen diffusion coefficient of $\text{Ba}_{0.75}\text{Sr}_{0.25}\text{Al}_2\text{Si}_2\text{O}_8$ (BSAS) is unknown. The oxygen diffusion coefficient for $\text{Al}_6\text{Si}_2\text{O}_{13}$ (mullite) at 1400 °C was extrapolated from 1119 °C -1319 °C data to be used as an estimate for BSAS.

k: The oxygen diffusion coefficient of HfSiO₄ and YbPO₄ are unknown. The oxygen diffusion coefficient for tetragonal ZrSiO₄ at 1400 °C was used as an estimate for HfSiO₄ and YbPO₄ since all materials exhibit the same space group.

l: The CTE of amorphous SiO₂ at 1027 °C.

m: The BSAS CTE anisotropy is unknown. The CTE anisotropy for BaAl₂Si₂O₈ (BAS) was used as an estimate for that of Ba_{0.75}Sr_{0.25}Al₂Si₂O₈ (BSAS).

Property values in Table 4-4 were normalized to develop the Figure of Merit, as shown in Table SM1. Raw data presented in Table 4-4 was normalized so that the largest comparing property value was denoted by a value of one (Value/Maximum Value). The oxygen diffusivity spans multiple order of magnitude; $-\log_{10}(D_{\text{Bulk}})$ was used as the values prior to scaling in Table SM1. For material properties where a high value is desired (melting temperature, nearby eutectic temperature, SiO₂/CaO ratio changes for the CMAS reaction, and $-\log_{10}(D_{\text{Bulk}})$ representing the oxygen diffusivity), the values were subtracted from one so that the most desired property value displayed a smaller normalized value $[1-(\text{Value}/\text{Maximum Value})]$. The Figure of merit score was determined by summation of all normalized property values from Table SM1. The result of this summation is presented in Table 4-5 as the sum of all normalized properties.

Table SM1. Normalized data from Table 2 with the given scaling method.

Thermo-chemical	SiO ₂	Yb ₂ O ₃	Yb ₂ SiO ₅	Yb ₂ Si ₂ O ₇	BSAS	HfSiO ₄	YbPO ₄	Scaling Method
<i>Phase Stability</i>								
Melting point of EBC	0.2387	0	0.1333	0.1778	0.2533	0.2133	0.1573	1-Val/Max
More than one stable phase? Yes = 1, No = 0	1	0	0	0	0	0	0	Val/Max
Nearby Eutectic temperature, C	0.1081	0	0	0.1081	0.2973	0.1081	0.2162	1-Val/Max
<i>Steam Reactivity</i>								
Oxide activity in H ₂ O (g), a(MO _x)	1	0	0.003	0.2	1	0.55	0.2	Val/Max

Volume loss upon H ₂ O (g) reaction, %	1	0	0.32	0.24	1	0.45	0.44	Val/Max
Melting point of H ₂ O (g) reaction product	0.621 1	0.8158	0.8158	0.6708	0.609 1	1	0.8158	Val/Max
* High-velocity H ₂ O (g) reaction kinetics, linear = 1, parabolic = 0	1	0	0	0	1	0	0	Val/Max
<i>CMAS Reactivity</i>								
SiO ₂ /CaO ratio changes upon CMAS reaction	0.930 6	1.2419	0.9462	0.6505	0.861 1	0.9306	0	1- Val/Max
* Formation of a protective reaction layer, Yes = 0, No = 1	1	0	0	0	1	1	0	Val/Max
<i>Bond Coat Oxidation</i>								
O ₂ (g) Self Diffusion D _{Bulk} in EBC, 1400 °C, cm ² /s	0.05	0.22	0.09	0.03	0.00	0.03	0.03	1- Val/Max
* EBC requirement that D _{Bulk} < 1x10 ⁻¹¹ cm ² /s, Yes = 0, No = 1	0	0	0	0	0	0	0	Val/Max
Thermo-mechanical	SiO₂	Yb₂O₃	Yb₂SiO₅	Yb₂Si₂O₇	BSAS	HfSiO₄	YbPO₄	Scaling Method
<i>Thermal stresses</i>								
Linear CTE x10 ⁻⁶ /°C	0.060	1	0.863	0.536	0.631	0.476	0.714	Val/Max
CTE Anisotropy, max-min CTE axes, x10 ⁻⁶ /°C	0	0	1	0.309	0.321	0.370	0.235	Val/Max
CTE of steam reaction product, x10 ⁻⁶ /°C	0.060	1	1	0.863	0.631	0.726	1	Val/Max
* Is Linear CTE of EBC within 25% of SiC (4.5-5.5 x10 ⁻⁶ /°C), Yes = 0, No = 1	1	1	1	0	0	0	0	Val/Max

Each normalized material property subcategory for the given EBC failure modes was summed to produce a visual representation of EBC candidates through the Figure of Merit. The results of the given summation are shown in Table SM2. Table SM2 was plotted in MATLAB with the maxima and minima for each EBC failure mode category as the maxima and minima for each leg of the radar plot.

Table SM2. Data used for plotting the visualization of the Figure of Merit for each EBC failure mode.

<u>EBC Failure Modes</u>	SiO₂	Yb₂O₃	Yb₂SiO₅	Yb₂Si₂O₇	BSAS	HfSiO₄	YbPO₄
Phase Stability	1.35	0.00	0.13	0.29	0.55	0.32	0.37
Steam Reactivity	3.62	0.82	1.14	1.11	3.61	2.00	1.46
CMAS Reactivity	1.93	1.24	0.95	0.65	1.86	1.93	0.00
Bond Coat Oxidation	0.05	0.22	0.09	0.03	0.00	0.03	0.03
Thermal Stresses	1.12	3.00	3.86	1.71	1.58	1.57	1.95

9. Bibliography

- [1] T. Ohji and M. Singh, *Engineered Ceramics: Current Status and Future Prospects*. John Wiley & Sons, 2015.
- [2] G. Gardiner, "Aeroengine Composites, Part 1: The CMC invasion," *Composites World*, 2015.
- [3] R. W. Olesinski and G. J. Abbaschian, "The C–Si (Carbon-Silicon) System," *Bulletin of Alloy Phase Diagrams*, no. 5, pp. 486–489, 1984.
- [4] F. Collier, "Concept and Technologies for Green Aviation - National Aeronautics and Space Administration," presented at the Green Engineering Masters Forum, Sep. 30, 2009, [Online]. Available: nasa.gov/pdf/395949main_collier.pdf.
- [5] E. J. Opila, J. L. Smialek, R. C. Robinson, D. S. Fox, and N. S. Jacobson, "SiC Recession Caused by SiO₂ Scale Volatility under Combustion Conditions: II, Thermodynamics and Gaseous-Diffusion Model," *Journal of the American Ceramic Society*, vol. 82, no. 7, pp. 1826–1834, 1999.
- [6] E. J. Opila, R. C. Robinson, and M. J. Verrilli, "Borosilicate Glass-Induced Fiber Degradation of SiC/BN/SiC Composites Exposed in Combustion Environments," *Int. J. Appl. Ceram. Technol.*, vol. 13, no. 3, pp. 434–442, May 2016, doi: 10.1111/ijac.12499.
- [7] E. J. Opila and R. E. Hann, "Paralinear Oxidation of CVD SiC in Water Vapor," *Journal of the American Ceramic Society*, vol. 80, no. 1, pp. 197–205, 1997, doi: 10.1111/j.1151-2916.1997.tb02810.x.
- [8] E. J. Opila, "Variation of the Oxidation Rate of Silicon Carbide with Water-Vapor Pressure," *Journal of the American Ceramic Society*, vol. 82, no. 3, pp. 625–636, 1999, doi: 10.1111/j.1151-2916.1999.tb01810.x.
- [9] C. Levi, J. Hutchinson, M. Vidal-Sétif, and C. Johnson, "Environmental Degradation of TBCs by Molten Deposits," *MRS Bulletin*, vol. 37, Oct. 2012, doi: 10.1557/mrs.2012.230.
- [10] V. L. Wiesner, B. J. Harder, and N. P. Bansal, "High-temperature interactions of desert sand CMAS glass with yttrium disilicate environmental barrier coating material," *Ceramics International*, vol. 44, no. 18, pp. 22738–22743, Dec. 2018, doi: 10.1016/j.ceramint.2018.09.058.
- [11] M. W. Hull, "Accuracy, Precision, and Confidence in X-ray Fluorescence for Positive Material Identification," *The NDT Technician*, vol. 16, no. 1, pp. 1–6, 2017.
- [12] K. N. Lee *et al.*, "Upper Temperature Limit of Environmental Barrier Coatings Based on Mullite and BSAS," *Journal of the American Ceramic Society*, vol. 86, no. 8, pp. 1299–1306, 2003, doi: 10.1111/j.1151-2916.2003.tb03466.x.
- [13] P. J. Meschter, E. J. Opila, and N. S. Jacobson, "Water Vapor–Mediated Volatilization of High-Temperature Materials," *Annu. Rev. Mater. Res.*, vol. 43, no. 1, pp. 559–588, Jul. 2013, doi: 10.1146/annurev-matsci-071312-121636.
- [14] K. N. Lee, D. S. Fox, and N. P. Bansal, "Rare earth silicate environmental barrier coatings for SiC/SiC composites and Si₃N₄ ceramics," *Journal of the European Ceramic Society*, vol. 25, no. 10, pp. 1705–1715, Jan. 2005, doi: 10.1016/j.jeurceramsoc.2004.12.013.
- [15] J. Welty, "Fundamentals of Momentum, Heat and Mass Transfer, 5th Edition," p. 729.
- [16] N. Al Nasiri, N. Patra, D. D. Jayaseelan, and W. E. Lee, "Water vapour corrosion of rare earth monosilicates for environmental barrier coating application," *Ceramics International*, vol. 43, no. 10, pp. 7393–7400, Jul. 2017, doi: 10.1016/j.ceramint.2017.02.123.

- [17] S. Ueno, D. D. Jayaseelan, H. Kita, T. Ohji, and H. T. Lin, "Comparison of Water Vapor Corrosion Behaviors of $\text{Ln}_2\text{Si}_2\text{O}_7$ (Ln=Yb and Lu) and ASiO_4 (A=Ti, Zr and Hf) EBC's," *Key Engineering Materials*, vol. 317–318, pp. 557–560, 2006, doi: 10.4028/www.scientific.net/KEM.317-318.557.
- [18] É. Darthout and F. Gitzhofer, "Thermal Cycling and High-Temperature Corrosion Tests of Rare Earth Silicate Environmental Barrier Coatings," *J Therm Spray Tech*, pp. 1–15, Sep. 2017, doi: 10.1007/s11666-017-0635-5.
- [19] S. Ueno, T. Ohji, and H.-T. Lin, "Recession behavior of $\text{Yb}_2\text{Si}_2\text{O}_7$ phase under high speed steam jet at high temperatures," *Corrosion Science*, vol. 50, no. 1, pp. 178–182, Jan. 2008, doi: 10.1016/j.corsci.2007.06.014.
- [20] N. Maier, K. G. Nickel, and G. Rixecker, "High temperature water vapour corrosion of rare earth disilicates (Y,Yb,Lu) $_2\text{Si}_2\text{O}_7$ in the presence of $\text{Al}(\text{OH})_3$ impurities," *Journal of the European Ceramic Society*, vol. 27, no. 7, pp. 2705–2713, Jan. 2007, doi: 10.1016/j.jeurceramsoc.2006.09.013.
- [21] M. K. Ferber and H. T. Lin, "Environmental Characterization of Monolithic Ceramics for Gas Turbine Applications," *Key Eng. Mat.*, vol. 287, pp. 367–380, Jun. 2005, doi: 10.4028/www.scientific.net/KEM.287.367.
- [22] A. V. Plyasunov, "Thermodynamic properties of H_4SiO_4 in the ideal gas state as evaluated from experimental data," *Geochimica et Cosmochimica Acta*, vol. 75, no. 13, pp. 3853–3865, Jul. 2011, doi: 10.1016/j.gca.2011.04.016.
- [23] C. V. Cojocar, D. Lévesque, C. Moreau, and R. S. Lima, "Performance of thermally sprayed Si/mullite/BSAS environmental barrier coatings exposed to thermal cycling in water vapor environment," *Surface and Coatings Technology*, vol. 216, pp. 215–223, Feb. 2013, doi: 10.1016/j.surfcoat.2012.11.043.
- [24] K. More *et al.*, "Evaluating Environmental Barrier Coatings on Ceramic Matrix Composites After Engine and Laboratory Exposures," *American Society of Mechanical Engineers, International Gas Turbine Institute, Turbo Expo (Publication) IGTI*, vol. 4, Jan. 2002, doi: 10.1115/GT2002-30630.
- [25] S. L. dos Santos e Lucato, O. H. Sudre, and D. B. Marshall, "A Method for Assessing Reactions of Water Vapor with Materials in High-Speed, High-Temperature Flow," *J. Am. Ceram. Soc.*, vol. 94, pp. s186–s195, Jun. 2011, doi: 10.1111/j.1551-2916.2011.04556.x.
- [26] R. A. Golden and E. J. Opila, "A method for assessing the volatility of oxides in high-temperature high-velocity water vapor," *Journal of the European Ceramic Society*, vol. 36, no. 5, pp. 1135–1147, Apr. 2016, doi: 10.1016/j.jeurceramsoc.2015.11.016.
- [27] C. G. Parker and E. J. Opila, "Stability of the Y_2O_3 - SiO_2 system in high-temperature, high-velocity water vapor," *J Am Ceram Soc*, p. jace.16915, Dec. 2019, doi: 10.1111/jace.16915.
- [28] C. W. Bale *et al.*, "FactSage Thermochemical Software and Databases, 2010-2016," *Calphad*, vol. 54, pp. 33–53, 2016.
- [29] M. Ridley and E. Opila, "Thermochemical stability and microstructural evolution of $\text{Yb}_2\text{Si}_2\text{O}_7$ in high-velocity high-temperature water vapor," *Journal of the European Ceramic Society*, vol. 41, no. 5, pp. 3141–3149, May 2020, doi: 10.1016/j.jeurceramsoc.2020.05.071.
- [30] E. J. Opila, "Oxidation and Volatilization of Silica Formers in Water Vapor," *Journal of the American Ceramic Society*, vol. 86, no. 8, pp. 1238–1248, Aug. 2003, doi: 10.1111/j.1151-2916.2003.tb03459.x.

- [31] E. B. Watson and D. J. Cherniak, "Oxygen diffusion in zircon," *Earth and Planetary Science Letters*, vol. 148, no. 3, pp. 527–544, May 1997, doi: 10.1016/S0012-821X(97)00057-5.
- [32] R. Hull, *Properties of crystalline silicon*. IET, 1999.
- [33] K. Nakano, N. Fukatsu, and Y. Kanno, "Thermodynamics of Zr/Hf-mixed silicates as a potential for environmental barrier coatings for Tyranno-hex materials," *Surface and Coatings Technology*, vol. 203, no. 14, pp. 1997–2002, Apr. 2009, doi: 10.1016/j.surfcoat.2009.01.035.
- [34] J. Varghese, T. Joseph, K. P. Surendran, T. P. D. Rajan, and M. T. Sebastian, "Hafnium silicate: a new microwave dielectric ceramic with low thermal expansivity," *Dalton Transactions*, vol. 44, no. 11, pp. 5146–5152, 2015, doi: 10.1039/C4DT03367A.
- [35] M. J. Ridley, J. Gaskins, P. Hopkins, and E. J. Opila, "Tailoring Thermal Properties of Multi-component Rare Earth Monosilicates," *Acta Materialia*, vol. 195, pp. 698–707, Aug. 2020, doi: 10.1016/j.actamat.2020.06.012.
- [36] D. Shin, R. Arróyave, and Z.-K. Liu, "Thermodynamic modeling of the Hf–Si–O system," *Calphad*, vol. 30, no. 4, pp. 375–386, Dec. 2006, doi: 10.1016/j.calphad.2006.08.006.
- [37] J. Fuhrmann and J. Pickardt, "On the formation of HfSiO₄ single crystals by chemical transport reactions," *Zeitschrift fuer Anorganische und Allgemeine Chemie (1950)*, vol. 532 pp. 171–174, 1986, Accessed: Dec. 17, 2019. [Online].
- [38] M. C. Morris, "Standard x-ray diffraction powder patterns: section 20- data for 71 substances," *National Bureau of Standards*, no. Monogram 25, p. 156, 1984.
- [39] M. Fritsch, H. Klemm, M. Herrmann, and B. Schenk, "Corrosion of selected ceramic materials in hot gas environment," *Journal of the European Ceramic Society*, vol. 26, no. 16, pp. 3557–3565, Jan. 2006, doi: 10.1016/j.jeurceramsoc.2006.01.015.
- [40] J. Chevalier and L. Gremillard, "The Tetragonal-Monoclinic Transformation in Zirconia: Lessons Learned and Future Trends," *Journal of the American Ceramic Society*, vol. 92, no. 9, p. 20, 2009.
- [41] D. W. Stacy, J. K. Johnstone, and D. R. Wilder, "Axial Thermal Expansion of HfO₂," *Journal of the American Ceramic Society*, vol. 55, no. 9, pp. 482–483, 1972, doi: 10.1111/j.1151-2916.1972.tb11347.x.
- [42] S. Ueno, D. D. Jayaseelan, T. Ohji, and H. T. Lin, "Corrosion and Oxidation Behavior of ASiO₄ (A=Ti, Zr, and Hf) and Silicon Nitride with an HfSiO₄ Environmental Battier Coating," *Journal of Ceramic Processing & Research*, vol. 6, no. 1, pp. 81–84, 2005.
- [43] S. Chapman and T. G. Cowling, *Mathematical theory non uniform gases account kinetic theory viscosity thermal conduction and diffusion gases*, 3rd Edition. Cambridge Mathematical Library: Cambridge University Press, 1991.
- [44] D. R. Poirier and G. H. Geiger, "Diffusion in Solids," in *Transport Phenomena in Materials Processing*, D. R. Poirier and G. H. Geiger, Eds. Cham: Springer International Publishing, 2016, pp. 463–507.
- [45] N. S. Jacobson, E. J. Opila, D. L. Myers, and E. H. Copland, "Thermodynamics of gas phase species in the Si–O–H system," *The Journal of Chemical Thermodynamics*, vol. 37, no. 10, pp. 1130–1137, Oct. 2005, doi: 10.1016/j.jct.2005.02.001.
- [46] I. Barin, "Thermochemical Data of Pure Substances," *VCH*, 1989, Accessed: Jan. 07, 2020. [Online]. Available: <https://ci.nii.ac.jp/naid/10006949556/>.
- [47] H. C. O'Neill, "Free energy of formation of zircon and hafnon," *American Mineralogist*, vol. 91, no. 7, pp. 1134–1141, 2015, doi: 10.2138/am.2006.2071.

- [48] H. Klemm, "Silicon Nitride for High-Temperature Applications," *Journal of the American Ceramic Society*, vol. 93, no. 6, pp. 1501–1522, Jun. 2010, doi: 10.1111/j.1551-2916.2010.03839.x.
- [49] S. Stecura and W. J. Campbell, "Thermal Expansion and Phase Inversion of Rare-Earth Oxides," BM-RI-5847, 4840970, Oct. 1960. doi: 10.2172/4840970.
- [50] C. G. Parker, "Unpublished work, Argonne National Laboratories Advanced Photon Source, University of Virginia." 2018.
- [51] C. Gustavo and N. S. Jacobson, "Mass spectrometric measurements of the silica activity in the Yb_2O_3 - SiO_2 system and implications to assess the degradation of silicate-based coatings in combustion environments," *Journal of the European Ceramic Society*, vol. 35, pp. 4259–4267, 2015.
- [52] R. A. Golden, K. Mueller, and E. J. Opila, "Thermochemical stability of $\text{Y}_2\text{Si}_2\text{O}_7$ in high-temperature water vapor," *Journal of the American Ceramic Society*, vol. 103, no. 8, pp. 4517–4535, 2020, doi: <https://doi.org/10.1111/jace.17114>.
- [53] N. Jacobson, "Silica Activity Measurements in the Y_2O_3 - SiO_2 System and Applications to Modeling of Coating Volatility," *Journal of American Ceramic Society*, vol. 97, no. 6, pp. 1959–1965, 2014.
- [54] G. Lipiak and A. Schroeder, "Lifetime extension for Siemens gas turbines," *VGB PowerRech*, vol. 87, no. 10, 2007, Accessed: Dec. 19, 2019. [Online]. Available: <https://www.osti.gov/etdeweb/biblio/20949978>.
- [55] M. D. Allendorf, C. F. Melius, B. Cosic, and A. Fontijn, "BAC-G2 Predictions of Thermochemistry for Gas-Phase Aluminum Compounds," *J. Phys. Chem. A*, vol. 106, no. 11, pp. 2629–2640, Mar. 2002, doi: 10.1021/jp013128r.
- [56] E. J. Opila and D. L. Myers, "Alumina Volatility in Water Vapor at Elevated Temperatures," *Journal of the American Ceramic Society*, vol. 87, no. 9, pp. 1701–1705, 2004, doi: <https://doi.org/10.1111/j.1551-2916.2004.01701.x>.
- [57] A. Hashimoto, "The effect of H_2O gas on volatilities of planet-forming major elements: I. Experimental determination of thermodynamic properties of Ca-, Al-, and Si-hydroxide gas molecules and its application to the solar nebula," *Geochimica et Cosmochimica Acta*, vol. 56, no. 1, pp. 511–532, Jan. 1992, doi: 10.1016/0016-7037(92)90148-C.
- [58] L. V. Gurvich, I. V. Veyts, and C. B. Alcock, "Thermodynamic Properties of Individual Substances," *Begell House*, vol. Vol. 3, no. Part 1, pp. 138, 150–151, 1996.
- [59] X.-H. Chen, L.-F. Cheng, Y.-G. Wang, L.-T. Zhang, Z.-L. Hong, and Y.-H. Wu, "Corrosion Behavior of AlPO_4 as Environmental Barrier Coating in Water Vapor Environment," *Journal of Inorganic Materials*, vol. 24, no. 2, pp. 397–401, 2009.
- [60] H. Mao, M. Selleby, and O. Fabrichnaya, "Thermodynamic reassessment of the Y_2O_3 - Al_2O_3 - SiO_2 system and its subsystems," *Calphad*, vol. 32, no. 2, pp. 399–412, Jun. 2008, doi: 10.1016/j.calphad.2008.03.003.
- [61] N. A. Toropov, "Some Rare Earth Silicates," *Trans. Int. Ceram. Congr., 7th, London, United Kingdom*, pp. 435–442, 1960.
- [62] G. M. Sheldrick, "SHELXT – Integrated space-group and crystal-structure determination," *Acta Cryst A*, vol. 71, no. 1, Art. no. 1, Jan. 2015, doi: 10.1107/S2053273314026370.
- [63] Bruker, *SADABS; APEX3*. Madison, Wisconsin, USA: Bruker AXS Inc., 2012.
- [64] O. V. Dolomanov, L. J. Bourhis, R. J. Gildea, J. a. K. Howard, and H. Puschmann, "OLEX2: a complete structure solution, refinement and analysis program," *J Appl Cryst*, vol. 42, no. 2, Art. no. 2, Apr. 2009, doi: 10.1107/S0021889808042726.

- [65] J. Gild *et al.*, “A High-entropy Silicide: $(\text{Mo}_{0.2}\text{Nb}_{0.2}\text{Ta}_{0.2}\text{Ti}_{0.2}\text{W}_{0.2})\text{Si}_2$,” *Journal of Materiomics*, vol. 5, no. 3, pp. 337–343, Sep. 2019, doi: 10.1016/j.jmat.2019.03.002.
- [66] J. Gild *et al.*, “High-entropy fluorite oxides,” *Journal of the European Ceramic Society*, vol. 38, no. 10, pp. 3578–3584, Aug. 2018, doi: 10.1016/j.jeurceramsoc.2018.04.010.
- [67] L. Backman and E. J. Opila, “Thermodynamic assessment of the group IV, V and VI oxides for the design of oxidation resistant multi-principal component materials,” *Journal of the European Ceramic Society*, vol. 39, no. 5, pp. 1796–1802, May 2019, doi: 10.1016/j.jeurceramsoc.2018.11.004.
- [68] B. Gorr *et al.*, “High temperature oxidation behavior of an equimolar refractory metal-based alloy 20Nb 20Mo 20Cr 20Ti 20Al with and without Si addition,” *Journal of Alloys and Compounds*, vol. 688, pp. 468–477, Dec. 2016, doi: 10.1016/j.jallcom.2016.07.219.
- [69] D. B. Miracle and O. N. Senkov, “A critical review of high entropy alloys and related concepts,” *Acta Materialia*, vol. 122, pp. 448–511, 2017.
- [70] R. DeHoff, *Thermodynamics in Materials Science, Second Edition*. CRC Press, 2006.
- [71] S. V. Ushakov, S. Hayun, W. Gong, and A. Navrotsky, “Thermal Analysis of High Entropy Rare Earth Oxides,” *Materials*, vol. 13, no. 14, Art. no. 14, Jan. 2020, doi: 10.3390/ma13143141.
- [72] Z. Tian, L. Zheng, J. Wang, P. Wan, J. Li, and J. Wang, “Theoretical and experimental determination of the major thermo-mechanical properties of RE_2SiO_5 (RE=Tb, Dy, Ho, Er, Tm, Yb, Lu, and Y) for environmental and thermal barrier coating applications,” *Journal of the European Ceramic Society*, vol. 36, no. 1, pp. 189–202, Jan. 2016, doi: 10.1016/j.jeurceramsoc.2015.09.013.
- [73] B. Abeles, “Lattice Thermal Conductivity of Disordered Semiconductor Alloys at High Temperatures,” *Phys. Rev.*, vol. 131, no. 5, pp. 1906–1911, Sep. 1963, doi: 10.1103/PhysRev.131.1906.
- [74] L. Turcer and N. P. Padture, “Towards multifunctional thermal environmental barrier coatings (TEBCs) based on rare-earth pyrosilicate solid-solution ceramics,” *Scripta Materialia*, no. 154, pp. 111–117, 2018, doi: 10.1016/j.scriptamat.2018.05.032.
- [75] A. Giri, J. Braun, C. Rost, and P. Hopkins, “On the minimum limit to thermal conductivity of multi-atom component crystalline solid solutions based on impurity mass scattering,” *Scripta Materialia*, no. 138, pp. 134–138, 2017, doi: 10.1016/j.scriptamat.2017.05.045.
- [76] J. Han, Y. Wang, R. Liu, and D. Jiang, “Study on water vapor corrosion resistance of rare earth monosilicates RE_2SiO_5 (RE = Lu, Yb, Tm, Er, Ho, Dy, Y, and Sc) from first-principles calculations,” *Heliyon*, vol. 4, no. 10, p. e00857, 2018, doi: <https://doi.org/10.1016/j.heliyon.2018.e00857>.
- [77] M. Głowacki, “Właściwości optyczne i strukturalne krzemianów ziem rzadkich i ich roztworów stałych,” 2012.
- [78] ASTM International, “Standard Test Methods for Density of Compacted or Sintered Powder Metallurgy (PM).” ASTM.
- [79] E. Gentner, *Mineral.-Petro. Institut, Univ. Heidelberg, Heidelberg, West Germany., ICDD Grant-in-Aid*, 1989.
- [80] H. F. McMurdie, M. C. Morris, E. H. Evans, B. Paretzkin, W. Wong-Ng, and C. R. Hubbard, “Standard X-Ray Diffraction Powder Patterns from The JCPDS Research Associateship,” *Powder Diffraction*, vol. 1, no. 3, pp. 265–275, Sep. 1986, doi: 10.1017/S0885715600011829.

- [81] Y. He, “Rapid Thermal Conductivity Measurement with a Hot Disk Sensor: Part 1. Theoretical Considerations,” *Thermochimica Acta*, vol. 436, no. 1, pp. 122–129, Oct. 2005, doi: 10.1016/j.tca.2005.06.026.
- [82] S. E. Gustafsson, “Transient plane source techniques for thermal conductivity and thermal diffusivity measurements of solid materials,” *Review of Scientific Instruments*, vol. 62, no. 3, pp. 797–804, Mar. 1991, doi: 10.1063/1.1142087.
- [83] S. Malinarič, “Uncertainty Analysis of Thermophysical Property Measurements of Solids Using Dynamic Methods,” *Int J Thermophys*, vol. 28, no. 1, pp. 20–32, Feb. 2007, doi: 10.1007/s10765-006-0134-2.
- [84] D. G. Cahill, “Thermal conductivity measurement from 30 to 750 K: the 3ω method,” *Review of Scientific Instruments*, vol. 61, no. 2, pp. 802–808, Feb. 1990, doi: 10.1063/1.1141498.
- [85] K. Liddell and D. P. Thompson, “X-ray diffraction data for yttrium silicates,” *Trans. J. Br. Ceram. Soc.*, vol. 85, no. 1, pp. 17–22, 1986.
- [86] K. A. Denault *et al.*, “Average and local structure, Debye temperature, and structural rigidity in some oxide compounds related to phosphor hosts,” *ACS applied materials & interfaces*, vol. 7, no. 13, pp. 7264–7272, 2015.
- [87] L. León-Reina, J. M. Porrás-Vázquez, E. R. Losilla, L. Moreno-Real, and M. A. Aranda, “Structure and oxide anion conductivity in $\text{Ln}_2(\text{TO}_4)_2$ ($\text{Ln} = \text{La}, \text{Nd}$; $\text{T} = \text{Ge}, \text{Si}$),” *Journal of Solid State Chemistry*, vol. 181, no. 9, pp. 2501–2506, 2008.
- [88] D. Zhu and L. Kang, “Thermal Expansion and Thermal Conductivity of Rare Earth Silicates,” presented at the ICACC, International Conference on Advanced Ceramics and Composites, 2006, Accessed: Jan. 08, 2018. [Online]. Available: <https://ntrs.nasa.gov/archive/nasa/casi.ntrs.nasa.gov/20060051745.pdf>.
- [89] N. Al Nasiri, N. Patra, D. Horlait, D. D. Jayaseelan, and W. E. Lee, “Thermal Properties of Rare-Earth Monosilicates for EBC on Si-Based Ceramic Composites,” *J. Am. Ceram. Soc.*, vol. 99, no. 2, pp. 589–596, Feb. 2016, doi: 10.1111/jace.13982.
- [90] K. Fukuda and H. Matsubara, “Anisotropic thermal expansion in yttrium silicate,” *Journal of Materials Research*, vol. 18, no. 07, pp. 1715–1722, Jul. 2003, doi: 10.1557/JMR.2003.0236.
- [91] Z. S. Khan *et al.*, “Synthesis and characterization of Yb and Er based monosilicate powders and durability of plasma sprayed Yb_2SiO_5 coatings on C/C–SiC composites,” *Materials Science and Engineering: B*, vol. 177, no. 2, pp. 184–189, Feb. 2012, doi: 10.1016/j.mseb.2011.12.004.
- [92] M.-H. Lu, H.-M. Xiang, Z.-H. Feng, X.-Y. Wang, and Y.-C. Zhou, “Mechanical and Thermal Properties of Yb_2SiO_5 : A Promising Material for T/EBCs Applications,” *Journal of the American Ceramic Society*, vol. 99, no. 4, pp. 1404–1411, 2016, doi: 10.1111/jace.14085.
- [93] C.-W. Nan, R. Birringer, D. R. Clarke, and H. Gleiter, “Effective thermal conductivity of particulate composites with interfacial thermal resistance,” *Journal of Applied Physics*, vol. 81, no. 10, pp. 6692–6699, May 1997, doi: 10.1063/1.365209.
- [94] Z. Sun, M. Li, and Y. Zhou, “Thermal properties of single-phase Y_2SiO_5 ,” *Journal of the European Ceramic Society*, vol. 29, no. 4, pp. 551–557, Mar. 2009, doi: 10.1016/j.jeurceramsoc.2008.07.026.
- [95] Al Nasiri Nasrin, Patra Niranjana, Horlait Denis, Jayaseelan Daniel Doni, Lee William E., and Smialek J., “Thermal Properties of Rare-Earth Monosilicates for EBC on Si-Based

- Ceramic Composites,” *Journal of the American Ceramic Society*, vol. 99, no. 2, pp. 589–596, Oct. 2015, doi: 10.1111/jace.13982.
- [96] X. Ren, Z. Tian, J. Zhang, and J. Wang, “Equiatomic quaternary $(Y_{1/4}Ho_{1/4}Er_{1/4}Yb_{1/4})_2SiO_5$ silicate: A perspective multifunctional thermal and environmental barrier coating material,” *Scripta Materialia*, vol. 168, pp. 47–50, Jul. 2019, doi: 10.1016/j.scriptamat.2019.04.018.
- [97] J. L. Braun *et al.*, “Charge-Induced Disorder Controls the Thermal Conductivity of Entropy-Stabilized Oxides,” *Advanced Materials*, vol. 30, no. 51, p. 1805004, 2018, doi: 10.1002/adma.201805004.
- [98] Y. Ogura, “ Y_2SiO_5 as Oxidation Resistant Coating for C/C Composites,” in *Proc. 10th, Whistler, Canada, 1995*, pp. 767–774.
- [99] S. Ramasamy, S. N. Tewari, K. N. Lee, R. T. Bhatt, and D. S. Fox, “EBC development for hot-pressed Y_2O_3/Al_2O_3 doped silicon nitride ceramics,” *Materials Science and Engineering: A*, vol. 527, no. 21–22, pp. 5492–5498, Aug. 2010, doi: 10.1016/j.msea.2010.05.067.
- [100] W. Hu and H. Nian, “Phase evolution of reactive sputtering synthesized holmium silicate coatings,” *Journal of The American Ceramic Society*, no. 102, 2018, doi: <http://dx.doi.org/10.1111/jace.15930>.
- [101] Y. Dong, K. Ren, Y. Lu, Q. Wang, J. Liu, and Y. Wang, “High-entropy environmental barrier coating for the ceramic matrix composites,” *Journal of the European Ceramic Society*, vol. 39, no. 7, pp. 2574–2579, Jul. 2019, doi: 10.1016/j.jeurceramsoc.2019.02.022.
- [102] J. Felsche, *The Crystal Chemistry of the Rare Earth Silicates*, Rare Earths. Berlin, Heidelberg: Springer, 1973.
- [103] A. J. Fernández-Carrión, M. Allix, and A. I. Becerro, “Thermal Expansion of Rare-Earth Pyrosilicates,” *Journal of the American Ceramic Society*, vol. 96, no. 7, pp. 2298–2305, 2013, doi: 10.1111/jace.12388.
- [104] *Thermo-calc Software TCOX Database Version 8*. Thermo-calc.
- [105] L. R. Turcer and N. P. Padture, “Towards multifunctional thermal environmental barrier coatings (TEBCs) based on rare-earth pyrosilicate solid-solution ceramics,” *Scripta Materialia*, vol. 154, pp. 111–117, Sep. 2018, doi: 10.1016/j.scriptamat.2018.05.032.
- [106] N. A. Toropov and M. V. Kougiya, *Inorganic Materials*, vol. 7, no. 7, pp. 1220–1223, 1971.
- [107] J. Felsche, “Rare Earth Silicates with the Apatite Structure,” *Journal of Solid State Chemistry*, vol. 5, pp. 266–275, 1972, doi: 10.1016/0022-4596(72)90039-4.
- [108] J. E. Saal, D. Shin, A. J. Stevenson, G. L. Messing, and Z.-K. Liu, “First-Principles Thermochemistry and Thermodynamic Modeling of the Al_2O_3 – Nd_2O_3 – SiO_2 – Y_2O_3 Pseudoquaternary System,” *Journal of the American Ceramic Society*, vol. 93, no. 12, pp. 4158–4167, 2010, doi: <https://doi.org/10.1111/j.1551-2916.2010.03993.x>.
- [109] T. Hoai Le, K. Tang, S. Arnout, A. Malfliet, B. Blanpain, and M. Guo, “Thermodynamic assessment of the Nd_2O_3 – CaO – SiO_2 ternary system,” *Calphad*, vol. 55, pp. 157–164, Dec. 2016, doi: 10.1016/j.calphad.2016.08.006.
- [110] N. A. Toropov, F. Ya. Galakhov, and S. F. Konovalova, *Bull. Acad. Sci. USSR, Div. Chem. Sci.*, vol. 8, pp. 1271–1277, 1961.
- [111] N. A. Toropov and V. A. Vasil’eva, “Phase Diagram of the Binary System of Scandium Oxide and Silica,” *Zh. Neorg. Khim.*, vol. 7, no. 8, pp. 1938–1945, 1962.
- [112] N. A. Toropov and I. A. Bondar, “High-Temperature Solid Solutions of Silicates of the Rare Earth Elements,” *Trans. Int. Ceram. Congr., 8th*, pp. 85–103, 1961.

- [113] X. Ye, Y. Luo, S. Liu, D. Wu, D. Hou, and F. Yang, “Experimental study and thermodynamic calculation of Lu_2O_3 - SiO_2 binary system,” *Journal of Rare Earths*, vol. 35, no. 9, pp. 927–933, Sep. 2017, doi: 10.1016/S1002-0721(17)60996-7.
- [114] B. T. Richards, K. A. Young, F. de Francqueville, S. Sehr, M. R. Begley, and H. N. G. Wadley, “Response of ytterbium disilicate–silicon environmental barrier coatings to thermal cycling in water vapor,” *Acta Materialia*, vol. 106, no. Supplement C, pp. 1–14, Mar. 2016, doi: 10.1016/j.actamat.2015.12.053.
- [115] S. Ueno, D. D. Jayaseelan, and T. Ohji, “Water vapor corrosion behavior of lutetium silicates at high temperature,” *Ceramics International*, vol. 32, no. 4, pp. 451–455, Jan. 2006, doi: 10.1016/j.ceramint.2005.03.022.
- [116] K. Kobayashi and Y. Sakka, “Rudimental research progress of rare-earth silicate oxyapatites: their identification as a new compound until discovery of their oxygen ion conductivity,” *J. Ceram. Soc. Japan*, vol. 122, no. 1428, pp. 649–663, 2014, doi: 10.2109/jcersj2.122.649.
- [117] Y. Masubuchi, M. Higuchi, and K. Kodaira, “Reinvestigation of Phase Relations around the Oxyapatite Phase in the Nd_2O_3 - SiO_2 System,” *Journal of Crystal Growth*, vol. 247, no. 1, pp. 207–212, Jan. 2003, doi: 10.1016/S0022-0248(02)01908-5.
- [118] P. R. Slater, J. E. H. Sansom, and J. R. Tolchard, “Development of Apatite-type Oxide Ion Conductors,” *Chem. Record*, vol. 4, no. 6, pp. 373–384, 2004, doi: 10.1002/tcr.20028.
- [119] A. J. Fernández-Carrión, M. D. Alba, A. Escudero, and A. I. Becerro, “Solid Solubility of $\text{Yb}_2\text{Si}_2\text{O}_7$ in β -, γ - and δ - $\text{Y}_2\text{Si}_2\text{O}_7$,” *Journal of Solid State Chemistry*, vol. 184, no. 7, pp. 1882–1889, Jul. 2011, doi: 10.1016/j.jssc.2011.05.034.
- [120] L. Sun *et al.*, “High temperature corrosion of $(\text{Er}_{0.25}\text{Tm}_{0.25}\text{Yb}_{0.25}\text{Lu}_{0.25})_2\text{Si}_2\text{O}_7$ environmental barrier coating material subjected to water vapor and molten calcium–magnesium–aluminosilicate (CMAS),” *Corrosion Science*, vol. 175, p. 108881, Oct. 2020, doi: 10.1016/j.corsci.2020.108881.
- [121] J. L. Braun, D. H. Olson, J. T. Gaskins, and P. E. Hopkins, “A steady-state thermoreflectance method to measure thermal conductivity,” *Review of Scientific Instruments*, vol. 90, no. 2, p. 024905, Feb. 2019, doi: 10.1063/1.5056182.
- [122] Z. Tian, L. Zheng, Z. Li, J. Li, and J. Wang, “Exploration of the low thermal conductivities of γ - $\text{Y}_2\text{Si}_2\text{O}_7$, β - $\text{Y}_2\text{Si}_2\text{O}_7$, β - $\text{Yb}_2\text{Si}_2\text{O}_7$, and β - $\text{Lu}_2\text{Si}_2\text{O}_7$ as novel environmental barrier coating candidates,” *Journal of the European Ceramic Society*, vol. 36, no. 11, pp. 2813–2823, Sep. 2016, doi: 10.1016/j.jeurceramsoc.2016.04.022.
- [123] M. D. Dolan *et al.*, “Structures and anisotropic thermal expansion of the α , β , γ , and δ polymorphs of $\text{Y}_2\text{Si}_2\text{O}_7$,” *Powder Diffraction*, vol. 23, no. 1, pp. 20–25, Mar. 2008, doi: 10.1154/1.2825308.
- [124] M. de Jong *et al.*, “Charting the complete elastic properties of inorganic crystalline compounds,” *Scientific Data*, vol. 2, no. 1, Art. no. 1, Mar. 2015, doi: 10.1038/sdata.2015.9.
- [125] A. Jain *et al.*, “Commentary: The Materials Project: A materials genome approach to accelerating materials innovation,” *APL Materials*, vol. 1, no. 1, p. 011002, Jul. 2013, doi: 10.1063/1.4812323.
- [126] L. R. Turcer, A. R. Krause, H. F. Garces, L. Zhang, and N. P. Padture, “Environmental-barrier coating ceramics for resistance against attack by molten calcia-magnesia-aluminosilicate (CMAS) glass: Part II, β - $\text{Yb}_2\text{Si}_2\text{O}_7$ and β - $\text{Sc}_2\text{Si}_2\text{O}_7$,” *Journal of the*

- European Ceramic Society*, vol. 38, no. 11, pp. 3914–3924, Sep. 2018, doi: 10.1016/j.jeurceramsoc.2018.03.010.
- [127] R. Gaillac, P. Pullumbi, and F.-X. Coudert, “ELATE: an open-source online application for analysis and visualization of elastic tensors,” *J. Phys.: Condens. Matter*, vol. 28, no. 27, p. 275201, May 2016, doi: 10.1088/0953-8984/28/27/275201.
- [128] N. A. Toropov, I. A. Bondar, and F. Ya. Galakhov, “High-Temperature Solid Solutions of Silicates of the Rare Earth Elements,” *Trans. Int. Ceram. Congr., 8th, Copenhagen, Denmark*, pp. 85–103, 1962.
- [129] I. A. Bondar, N. A. Toropov, and L. N. Koroleva, “Phase Equilibriums in Systems Containing Monoxides of Samarium and Europium, and Silicon Dioxide,” *Izv. Akad. Nauk SSSR, Neorg. Mater.*, no. 3, pp. 2034–2039, 1967.
- [130] M. Cameron, S. Sueno, C. T. Prewitt, and J. J. Papike, “High-Temperature Crystal Chemistry of Acmite, Diopside, Hedenbergite Jadeite, Spodumene and Ureyite,” *American Mineralogist*, vol. 58, no. 7–8, pp. 594–618, Aug. 1973.
- [131] R. M. Hazen and C. T. Prewitt, “Effects of temperature and pressure on interatomic distances in oxygen-based minerals,” *American Mineralogist*, vol. 62, no. 3–4, pp. 309–315, Apr. 1977.
- [132] A. C. Strzelecki *et al.*, “High-Temperature Thermodynamics of Cerium Silicates, $\text{A-Ce}_2\text{Si}_2\text{O}_7$, and $\text{Ce}_{4.67}(\text{SiO}_4)_3\text{O}$,” *ACS Earth Space Chem.*, vol. 4, no. 11, pp. 2129–2143, Nov. 2020, doi: 10.1021/acsearthspacechem.0c00231.
- [133] M. V. Ayyasamy, J. A. Deijkers, H. N. G. Wadley, and P. V. Balachandran, “Density functional theory and machine learning guided search for $\text{RE}_2\text{Si}_2\text{O}_7$ with targeted coefficient of thermal expansion,” *J Am Ceram Soc*, vol. 103, no. 8, pp. 4489–4497, Aug. 2020, doi: 10.1111/jace.17121.
- [134] T. S. Key, K. F. Presley, R. S. Hay, and E. E. Boakye, “Total Thermal Expansion Coefficients of the Yttrium Silicate Apatite Phase $\text{Y}_{4.69}(\text{SiO}_4)_3\text{O}$,” *Journal of the American Ceramic Society*, vol. 97, no. 1, pp. 28–31, 2014, doi: <https://doi.org/10.1111/jace.12619>.
- [135] A. V. Knyazev, E. N. Bulanov, A. O. Korshunov, and O. V. Krashenninnikova, “Synthesis and thermal expansion of some lanthanide-containing apatites,” *Inorganic Materials*, vol. 49, pp. 1133–1137, 2013, doi: <https://doi.org/10.1134/S0020168513110095>.
- [136] Z. Ding *et al.*, “The thermal and mechanical properties of hafnium orthosilicate: Experiments and first-principles calculations,” *Materialia*, vol. 12, 2020, doi: <https://doi.org/10.1016/j.mtla.2020.100793>.
- [137] C. Thieme and C. Rüssel, “Thermal expansion behavior of SrSiO_3 and Sr_2SiO_4 determined by high-temperature X-ray diffraction and dilatometry,” *J Mater Sci*, vol. 50, no. 16, pp. 5533–5539, Aug. 2015, doi: 10.1007/s10853-015-9100-3.
- [138] R. Shannon, “Shannon Radii,” *Database of Ionic Radii*. <http://abulafia.mt.ic.ac.uk/shannon/ptable.php> (accessed Dec. 27, 2017).
- [139] K. N. Lee, “ $\text{Yb}_2\text{Si}_2\text{O}_7$ Environmental barrier coatings with reduced bond coat oxidation rates via chemical modifications for long life,” *Journal of the American Ceramic Society*, vol. 102, no. 3, pp. 1507–1521, 2019, doi: <https://doi.org/10.1111/jace.15978>.
- [140] Y. Hikichi and T. Nomura, “Melting Temperatures of Monazite and Xenotime,” *J American Ceramic Society*, vol. 70, no. 10, p. C-252-C-253, Oct. 1987, doi: 10.1111/j.1151-2916.1987.tb04890.x.
- [141] P. Mogilevsky, “On the miscibility gap in monazite–xenotime systems,” *Phys Chem Minerals*, vol. 34, no. 3, pp. 201–214, Mar. 2007, doi: 10.1007/s00269-006-0139-1.

- [142] J. Han, Y. Wang, R. Liu, and F. Wan, "Theoretical and experimental investigation of Xenotime-type rare earth phosphate REPO₄, (RE = Lu, Yb, Er, Y and Sc) for potential environmental barrier coating applications," *Sci Rep*, vol. 10, no. 1, p. 13681, Dec. 2020, doi: 10.1038/s41598-020-70648-0.
- [143] W. Szuszkiewicz, E. Radomińska, T. Znamierowska, and P. Wilk, "Phase equilibria in the YPO₄-Rb₃PO₄ system," *J Therm Anal Calorim*, vol. 111, no. 1, pp. 63–69, Jan. 2013, doi: 10.1007/s10973-011-2172-7.
- [144] Y. Wang, X. Chen, W. Liu, L. Cheng, and L. Zhang, "Exploration of YPO₄ as a potential environmental barrier coating," *Ceramics International*, vol. 36, no. 2, pp. 755–759, Mar. 2010, doi: 10.1016/j.ceramint.2009.10.014.
- [145] D. L. Hildenbrand and K. H. Lau, "Thermochemical properties of gaseous POBr and some H–P–O species," *The Journal of Chemical Physics*, vol. 100, no. 11, pp. 8373–8376, Jun. 1994, doi: 10.1063/1.466782.
- [146] F. Wang, L. Guo, C. Wang, and F. Ye, "Calcium-magnesium-alumina-silicate (CMAS) resistance characteristics of LnPO₄ (Ln = Nd, Sm, Gd) thermal barrier oxides," *Journal of the European Ceramic Society*, vol. 37, no. 1, pp. 289–296, Jan. 2017, doi: 10.1016/j.jeurceramsoc.2016.08.013.
- [147] A. S. Risbud, K. B. Helean, M. C. Wilding, P. Lu, and A. Navrotsky, "Enthalpies of formation of lanthanide oxyapatite phases," *J. Mater. Res.*, vol. 16, no. 10, pp. 2780–2783, Oct. 2001, doi: 10.1557/JMR.2001.0381.
- [148] X. Hu, F. Xu, K. Li, Y. Zhang, Y. Xu, and X. Zhao, "Thermal properties and Calcium-Magnesium-Alumina-Silicate (CMAS) resistance of LuPO₄ as environmental barrier coatings," *Journal of the European Ceramic Society*, vol. 40, no. 4, pp. 1471–1477, Apr. 2020, doi: 10.1016/j.jeurceramsoc.2019.11.018.
- [149] J. M. Nedelec, D. Avignant, and R. Mahiou, "Soft Chemistry Routes to YPO₄ -Based Phosphors: Dependence of Textural and Optical Properties on Synthesis Pathways," *Chem. Mater.*, vol. 14, no. 2, pp. 651–655, Feb. 2002, doi: 10.1021/cm010572y.
- [150] H. Zhao, C. G. Levi, and H. N. G. Wadley, "Molten silicate interactions with thermal barrier coatings," *Surface and Coatings Technology*, vol. 251, pp. 74–86, Jul. 2014, doi: 10.1016/j.surfcoat.2014.04.007.
- [151] R. I. Webster and E. J. Opila, "Mixed phase ytterbium silicate environmental-barrier coating materials for improved calcium–magnesium–alumino-silicate resistance," *Journal of Materials Research*, vol. 35, no. 17, pp. 2358–2372, 2020, doi: 10.1557/jmr.2020.151.
- [152] J. M. Drexler, A. L. Ortiz, and N. P. Padture, "Composition effects of thermal barrier coating ceramics on their interaction with molten Ca–Mg–Al–silicate (CMAS) glass," *Acta Materialia*, vol. 60, no. 15, pp. 5437–5447, Sep. 2012, doi: 10.1016/j.actamat.2012.06.053.
- [153] D. L. Poerschke, G. G. E. Seward, and C. G. Levi, "Influence of Yb:Hf Ratio on Ytterbium Hafnate/Molten Silicate (CMAS) Reactivity," *Journal of the American Ceramic Society*, vol. 99, no. 2, pp. 651–659, 2016, doi: <https://doi.org/10.1111/jace.13964>.
- [154] D. L. Hildenbrand and K. H. Lau, "Thermochemistry of gaseous manganese oxides and hydroxides," *J. Chem. Phys.*, vol. 100, no. 11, pp. 8377–8380, Jun. 1994, doi: 10.1063/1.466783.
- [155] D. L. Myers, M. J. Kulis, J. P. Horwath, N. S. Jacobson, and D. S. Fox, "Interactions of Ta₂O₅ with water vapor at elevated temperatures," *Journal of the American Ceramic Society*, vol. 100, no. 6, pp. 2353–2357, 2017, doi: <https://doi.org/10.1111/jace.14796>.

- [156] R. I. Webster and E. J. Opila, “Viscosity of CaO-MgO-Al₂O₃-SiO₂ (CMAS) melts: Experimental measurements and comparison to model calculations,” *Manuscript in Progress*, 2021.
- [157] J. Liu, L. Zhang, Q. Liu, L. Cheng, and Y. Wang, “Calcium–magnesium–aluminosilicate corrosion behaviors of rare-earth disilicates at 1400°C,” *Journal of the European Ceramic Society*, vol. 33, no. 15, pp. 3419–3428, Dec. 2013, doi: 10.1016/j.jeurceramsoc.2013.05.030.
- [158] J. L. Stokes, B. J. Harder, V. L. Wiesner, and D. E. Wolfe, “High-Temperature thermochemical interactions of molten silicates with Yb₂Si₂O₇ and Y₂Si₂O₇ environmental barrier coating materials,” *Journal of the European Ceramic Society*, vol. 39, no. 15, pp. 5059–5067, Dec. 2019, doi: 10.1016/j.jeurceramsoc.2019.06.051.
- [159] J. Steibel, Z. Ren, G. Singh, A. Misra, K. N. Lee, and M. van Roode, “Ceramic matrix composites taking flight at GE aviation,” *American Ceramic Society Bulletin*, no. 98, pp. 30–33, 2019.
- [160] G. D. Mahan, “Figure of merit for thermoelectrics,” *Journal of Applied Physics*, vol. 65, no. 4, pp. 1578–1583, Feb. 1989, doi: 10.1063/1.342976.
- [161] “CMC materials applications to gas turbine hot section components | Joint Propulsion Conferences.” <https://arc.aiaa.org/doi/abs/10.2514/6.1998-3266> (accessed Dec. 19, 2020).
- [162] M. J. Walock, V. Heng, A. Nieto, A. Ghoshal, M. Murugan, and D. Driemeyer, “Ceramic Matrix Composite Materials for Engine Exhaust Systems on Next-Generation Vertical Lift Vehicles,” *Journal of Engineering for Gas Turbines and Power*, vol. 140, no. 102101, Jun. 2018, doi: 10.1115/1.4040011.
- [163] T. H. Nguyen, P. Tri Nguyen, and F. Garnier, “Evaluation of the relationship between the aerothermodynamic process and operational parameters in the high-pressure turbine of an aircraft engine,” *Aerospace Science and Technology*, vol. 86, pp. 93–105, Mar. 2019, doi: 10.1016/j.ast.2019.01.011.
- [164] “Rolls-Royce Inc.” <https://www.rolls-royce.com/> (accessed Dec. 19, 2020).
- [165] E. Garcia, H. Lee, and S. Sampath, “Phase and microstructure evolution in plasma sprayed Yb₂Si₂O₇ coatings,” *Journal of the European Ceramic Society*, vol. 39, no. 4, pp. 1477–1486, Apr. 2019, doi: 10.1016/j.jeurceramsoc.2018.11.018.
- [166] L. Herweyer, “The High Temperature Sodium Sulfate Interactions with Ytterbium Disilicate Environmental Barrier Coatings Systems and Silicon Carbide Ceramic Matrix Composite Materials,” University of Virginia, 2020.
- [167] M. J. Ridley and E. J. Opila, “Thermomechanical and Thermochemical Stability of HfSiO₄ for Environmental Barrier Coating Applications,” *J Am Ceram Soc*, 2020, doi: 10.1111/jace.17729.
- [168] E. Bakan, M. Kindelmann, W. Kunz, H. Klemm, and R. Vaßen, “High-velocity water vapor corrosion of Yb-silicate: Sprayed vs. sintered body,” *Scripta Materialia*, vol. 178, pp. 468–471, 2020, doi: <https://doi.org/10.1016/j.scriptamat.2019.12.019>.
- [169] Q. N. Nguyen, D. L. Myers, N. S. Jacobson, and E. J. Opila, “Experimental and Theoretical Study of Thermodynamics of the Reaction of Titania and Water at High Temperatures,” p. 28, 2014.
- [170] C. W. Bauschlicher, C. J. Bodenschatz, D. L. Myers, and N. S. Jacobson, “Thermodynamics of high-temperature aluminum, zirconium, and yttrium hydroxide and oxyhydroxide vapor species,” *Journal of the American Ceramic Society*, vol. 103, no. 10, pp. 5870–5880, 2020, doi: <https://doi.org/10.1111/jace.17213>.

- [171] R. A. Golden, “Matric Development for Water Vapor Resistant SiC-Based Ceramic Matric Composites,” Dissertation, University of Virginia, Charlottesville, Virginia, 2017.
- [172] T. Matsudaira *et al.*, “Mass transfer in polycrystalline ytterbium monosilicate under oxygen potential gradients at high temperatures,” *Journal of the European Ceramic Society*, Jul. 2020, doi: 10.1016/j.jeurceramsoc.2020.07.045.
- [173] S. Kitaoka *et al.*, “Mass Transfer Mechanism in Yb₂Si₂O₇ Under Oxygen Potential Gradients at High Temperatures,” in *Advances in High Temperature Ceramic Matrix Composites and Materials for Sustainable Development; Ceramic Transactions, Volume CCLXIII*, John Wiley & Sons, Ltd, 2017, pp. 187–195.
- [174] F. Nozahic, C. Estournès, A. L. Carabat, W. G. Sloof, S. van der Zwaag, and D. Monceau, “Self-healing thermal barrier coating systems fabricated by spark plasma sintering,” *Materials & Design*, vol. 143, pp. 204–213, Apr. 2018, doi: 10.1016/j.matdes.2018.02.001.
- [175] M. Wada *et al.*, “Effect of Water Vapor on Mass Transfer in Polycrystalline Yb₂Si₂O₇ under Oxygen Potential Gradients at High Temperatures,” *Acta Materialia*, vol. 201, pp. 373–385, Dec. 2020, doi: 10.1016/j.actamat.2020.10.002.
- [176] J. Sleeper, A. Garg, V. L. Wiesner, and N. P. Bansal, “Thermochemical interactions between CMAS and Ca₂Y₈(SiO₄)₆O₂ apatite environmental barrier coating material,” *Journal of the European Ceramic Society*, vol. 39, no. 16, pp. 5380–5390, Dec. 2019, doi: 10.1016/j.jeurceramsoc.2019.08.040.
- [177] L. Barbieri, A. Corradi, and I. Lancellotti, “Thermal and chemical behaviour of different glasses containing steel fly ash and their transformation into glass-ceramics,” *Journal of the European Ceramic Society*, vol. 22, no. 11, pp. 1759–1765, Oct. 2002, doi: 10.1016/S0955-2219(01)00492-7.
- [178] B. Weinzierl *et al.*, “On the visibility of airborne volcanic ash and mineral dust from the pilot’s perspective in flight,” *Physics and Chemistry of the Earth, Parts A/B/C*, vol. 45–46, pp. 87–102, Jan. 2012, doi: 10.1016/j.pce.2012.04.003.
- [179] R. Clarkson, “Volcanic Ash Impacts on Jet Engines and Developments Since 2010, Rolls-Royce Inc. (Aero Engines),” presented at the NAT 2030 / ACM, 2019, Accessed: Jan. 07, 2021. [Online]. Available: <https://www.icao.int/EURNAT/Other%20Meetings%20Seminars%20and%20Workshops/NAT%202030%20Vision%20Workshop/NAT2030%20PR10.pdf>.
- [180] R. A. Golden, “Personal Communication,” 2020.
- [181] M. J. Ridley, B. McFarland, C. Miller, and E. J. Opila, “Analysis of YbPO₄ as an Environmental Barrier Coating Candidate,” *Manuscript in Progress*.
- [182] S. Krämer, J. Yang, C. G. Levi, and C. A. Johnson, “Thermochemical Interaction of Thermal Barrier Coatings with Molten CaO–MgO–Al₂O₃–SiO₂ (CMAS) Deposits,” *Journal of the American Ceramic Society*, vol. 89, no. 10, pp. 3167–3175, 2006, doi: <https://doi.org/10.1111/j.1551-2916.2006.01209.x>.
- [183] A. Nieto, R. Agrawal, L. Bravo, C. Hofmeister-Mock, M. Pepi, and A. Ghoshal, “Calcium–magnesium–alumina–silicate (CMAS) attack mechanisms and roadmap towards Sandphobic thermal and environmental barrier coatings,” *International Materials Reviews*, vol. 0, no. 0, pp. 1–42, Oct. 2020, doi: 10.1080/09506608.2020.1824414.
- [184] L. R. Turcer and N. P. Padture, “Rare-earth pyrosilicate solid-solution environmental-barrier coating ceramics for resistance against attack by molten calcium–magnesium–

- aluminosilicate (CMAS) glass,” *J. Mater. Res.*, vol. 35, no. 17, pp. 2373–2384, Sep. 2020, doi: 10.1557/jmr.2020.132.
- [185] R. Webster, “Mitigation Strategies for Calcium-Magnesium-Aluminosilicate (CMAS) Attack on Environmental Barrier Coatings,” University of Virginia, 2019.
- [186] Z. Yan, X. Lv, J. Zhang, Y. Qin, and C. Bai, “Influence of MgO, Al₂O₃ and CaO/SiO₂ on the viscosity of blast furnace type slag with high Al₂O₃ and 5 wt-% TiO₂,” *Canadian Metallurgical Quarterly*, vol. 55, no. 2, pp. 186–194, Apr. 2016, doi: 10.1080/00084433.2015.1126903.
- [187] G. Urbain, Y. Bottinga, and P. Richet, “Viscosity of liquid silica, silicates and aluminosilicates,” *Geochimica et Cosmochimica Acta*, vol. 46, no. 6, pp. 1061–1072, Jun. 1982, doi: 10.1016/0016-7037(82)90059-X.
- [188] W. Y. Lee, E. Lara-Curzio, and K. L. More, “Multilayered Oxide Interphase Concept for Ceramic-Matrix Composites,” *Journal of the American Ceramic Society*, vol. 81, no. 3, pp. 717–720, 1998, doi: <https://doi.org/10.1111/j.1151-2916.1998.tb02396.x>.
- [189] N. Kedir *et al.*, “In situ characterization of foreign object damage (FOD) in environmental-barrier-coated silicon carbide (SiC) ceramic,” *Journal of the American Ceramic Society*, vol. 103, no. 8, pp. 4586–4601, 2020, doi: <https://doi.org/10.1111/jace.17165>.
- [190] R. B. Sosman, “System Si-SiO₂, at low p,” *Trans. Br. Ceram. Soc.*, vol. 54, no. 11, pp. 655–670, 1955.
- [191] I. G. Talmy, D. A. Haught, and J. A. Zaykoski, “Synthesis and Properties of BaO·Al₂O₃·2SiO₂ - SrO·Al₂O₃·2SiO₂ (BAS-SAS) Ceramics,” *The American Ceramic Society*, vol. 52, Art. no. CONF-940416-, Aug. 1995, Accessed: Dec. 17, 2020. [Online]. Available: <https://www.osti.gov/biblio/86594>.
- [192] W. Szuskiewicz and T. Znamierowska, “Y₂O₃-P₂O₅ Phase Diagram,” *Pol. J. Chem*, vol. 63, no. 4–12, pp. 381–391, 1989.
- [193] M. J. Ridley and E. J. Opila, “High-Temperature Water-Vapor Reaction Mechanism of Barium Strontium Aluminosilicate (BSAS),” *Manuscript in Progress*.
- [194] E. J. Opila, “Stability of Complex Silicate Environmental Barrier Coating Candidate Materials in High-Temperature Water Vapor,” presented at the Materials Science and Technology, Portland, OR, 2019.
- [195] C. Miller and R. Webster, “Unpublished work,” University of Virginia, 2018.
- [196] R. Webster and Commonwealth Center for Additive Manufacturing, “Unpublished Work,” University of Virginia, 2019.
- [197] K. M. Grant, S. Krämer, J. P. A. Löfvander, and C. G. Levi, “CMAS degradation of environmental barrier coatings,” *Surface and Coatings Technology*, vol. 202, no. 4, pp. 653–657, Dec. 2007, doi: 10.1016/j.surfcoat.2007.06.045.
- [198] C. B. Iyi, “CMAS reactivity with candidate ceramic oxides applicable in thermal barrier coatings,” M.S., University of California, Irvine, United States -- California, 2012.
- [199] M. A. Lamkin, “Oxygen Mobility in Silicon Dioxide and Silicate Glasses: a Review,” doi: 10.1016/0955-2219(92)90010-B.
- [200] K. Ando, Y. Oishi, H. Hase, and K. Kitazawa, “Oxygen Self-Diffusion in Single-Crystal Y₂O₃,” *Journal of the American Ceramic Society*, vol. 66, no. 12, p. C-222-C-223, 1983, doi: <https://doi.org/10.1111/j.1151-2916.1983.tb11012.x>.
- [201] N. P. Bansal, “Solid State Synthesis and Properties of Monoclinic Celsian,” *NASA Technical Memorandum 107355*.

- <https://ntrs.nasa.gov/archive/nasa/casi.ntrs.nasa.gov/19970010347.pdf> (accessed Jan. 10, 2018).
- [202] M. Kerstan, M. Muller, and C. Russel, “High temperature thermal expansion of $\text{BaAl}_2\text{Si}_2\text{O}_8$, $\text{CaAl}_2\text{Si}_2\text{O}_8$, and $\text{Ca}_2\text{Al}_2\text{SiO}_7$ studied by high-temperature X-ray diffraction (HT-XRD),” *Solid State Sciences*, vol. 38, pp. 119–123, 2014, doi: <https://doi.org/10.1016/j.solidstatesciences.2014.10.010>.
- [203] J. A. Deijkers, “Thermal and Environmental Barrier Coating Concepts for Silicon-based Ceramic Matrix Composites.” 2020.
- [204] X. Zhong *et al.*, “Thermal shock resistance of tri-layer $\text{Yb}_2\text{SiO}_5/\text{Yb}_2\text{Si}_2\text{O}_7/\text{Si}$ coating for SiC and SiC-matrix composites,” *Journal of the American Ceramic Society*, vol. 101, no. 10, pp. 4743–4752, 2018, doi: <https://doi.org/10.1111/jace.15713>.
- [205] M. Stanislawski, U. Seeling, D. Peck, S. Woo, L. Singheiser, and K. Hilpert, “Vaporization study of doped lanthanum gallates and GaO(s) in H/HO atmospheres by the transpiration method,” *Solid State Ionics*, vol. 176, no. 35–36, pp. 2523–2533, Nov. 2005, doi: [10.1016/j.ssi.2005.07.015](https://doi.org/10.1016/j.ssi.2005.07.015).
- [206] E. Courcot, F. Rebillat, F. Teyssandier, and C. Louchet-Pouillier, “Stability of rare earth oxides in a moist environment at elevated temperatures—Experimental and thermodynamic studies: Part II: Comparison of the rare earth oxides,” *Journal of the European Ceramic Society*, vol. 30, no. 9, pp. 1911–1917, Jul. 2010, doi: [10.1016/j.jeurceramsoc.2010.02.012](https://doi.org/10.1016/j.jeurceramsoc.2010.02.012).
- [207] E. Courcot, F. Rebillat, F. Teyssandier, and C. Louchet-Pouillier, “Thermochemical stability of the $\text{Y}_2\text{O}_3\text{--SiO}_2$ system,” *Journal of the European Ceramic Society*, vol. 30, no. 4, pp. 905–910, Mar. 2010, doi: [10.1016/j.jeurceramsoc.2009.09.007](https://doi.org/10.1016/j.jeurceramsoc.2009.09.007).